Cardiff University

# QUANTIFYING THE MECHANICAL PROPERTIES OF SKIN *IN VIVO* AND *EX VIVO* TO OPTIMISE MICRONEEDLE DEVICE DESIGN


Rachel Beth Groves (B.Eng)

PhD Thesis

Institute of Medical Engineering & Medical Physics
School of Engineering

# Declaration of Authorship

**DECLARATION**

This work has not been previously accepted in substance for any degree and is not concurrently in candidature from any degree.

Signed……(candidate) Date…….....

**STATEMENT 1**

This thesis is being submitted in partial fulfilment of the requirements for the degree of PhD

Signed……(candidate) Date…….....

**STATEMENT 2**

This thesis is the result of my own independent work/investigation, except where otherwise stated. Other sources are acknowledged by explicit references.

Signed……(candidate) Date…….....

**STATEMENT 3**

I hereby give consent for my thesis, it accepted, to be available for photocopying and for library loan, and for the title and summary to be made available outside organisations.

Signed……(candidate) Date…….....

# ABSTRACT

The transdermal delivery of therapeutics is limited to only a few molecules due to the outermost layer of skin, the stratum corneum, which acts as a barrier against the ingress of substances into the body. Microneedle arrays, which are commonly between 70μm and 900μm in length, have been developed as a method of promoting drug and vaccine delivery by creating microperforations in the stratum corneum to increase transport into the skin. The design of microneedle devices has significantly developed over recent years to allow for the delivery of numerous compounds into *in vivo* and *ex vivo* skin. Microneedle devices are now beginning to be taken away from the laboratory and towards clinical use but to achieve this it is desirable that all microneedles within the device penetrate skin *in vivo* to a sufficient depth. As microneedle devices have been extensively tested in cadaver tissue, a greater understanding of the mechanical properties of skin *in vivo* and *ex vivo* is required and to hypothesise whether animal models such as murine skin *ex vivo* serves as an appropriate model for human skin *ex vivo.*

Measurements were performed on human skin *in vivo* by applying small cylindrical and spherical indenters to the volar aspect of the forearm on 7 volunteers. The average Young's Modulus of the skin was 39.64kPa and 65.86kPa when applying the spherical and cylindrical indenters respectively. In a series of tensile measurements performed at three load axis orientations using *ex vivo* samples from human and murine donors, it was found that the key variation was attributed to the deformation experienced at initial low loads. This was shown to be significantly longer for human skin with an average of 5.10mm, when compared with murine skin which had an average of 1.61mm ($p<0.05$). Histological examination showed that human skin was far thicker, with an increased volume of dermal tissue, compared with murine skin, and this anatomical variation may have been the main reason why human and murine skin exhibited different mechanical properties.

Finite element models (FEMs) were established of skin indentation *in vivo*, which incorporated the epidermis, dermis and hypodermis, and of human and murine skin in tension. Appropriate boundary conditions and mesh densities were implemented and the geometries were taken from real life measurements where possible. The Ogden material model of hyperelasticity was chosen to represent the skin layers for the FEM of skin indentation and an anisotropic material was used to describe human and murine skin in tension by adapting the Weiss *et al* model of transverse isotropy.

Inverse finite element analysis was then used to match the FEMs with the experimental measurements. The multilayered FEM of skin was correlated against the *in vivo* indentation tests where model and experimental fit gave average root mean squared errors ($R^2_{ave}$) of between 0.00103 and 0.0488 for the 7 volunteers. The optimal material parameters showed correlations with experimental measurements, where volunteers 1, 6 and 7 were shown to have the stiffest skin through Young's Modulus calculations, which was reflected in the increased nonlinearity of the parameters extracted for the hypodermal layer. A stronger agreement between model and experiment for the anisotropic model of human and murine skin in tension was shown where the $R^2_{ave}$ was between 0.0038 and 0.0163. Again, model and experimental observations were shown to correlate where there was a significant difference ($p<0.05$) between 6 of the 14 average material parameters ($C_2$, $C_{3,1}$, $\lambda_1$, $C_{3,2}$, $C_{3,3}$, $\lambda_3$) when comparing human to murine skin.

The multilayered FEM of human skin *in vivo* was further validated by modelling the application of a single microneedle to skin, prior to penetration. The model was then correlated against *in vivo* measurements performed on one of the volunteers and it was found that the model provided a good approximation for the experimental measurements. Using the multilayered FEM of human skin indentation, it was possible to model the deflection of the skin during the application of a pressure load comparable to microneedle array application. This allowed for the development of several curved microneedle arrays which aimed to distribute the load over all microneedles to potentially create uniform skin penetration by all those within the array. The microneedles were manufactured simply and quickly using wire cutting technologies from stainless steel and tested in human skin *in vivo* and in *ex vivo* samples of human and murine skin, where methylene blue was applied to identify any microchannels created by the microneedles. Preliminary measurements taken from murine skin *ex vivo* were discounted as microchannel staining was not possible. Analyses performed on human skin *ex vivo* showed penetration at high loads (4-5N) for all four microneedle array designs and the microneedle array with the smallest curvature (0.95mm) had the most consistent puncture for all microneedles, however puncture *in vivo* was difficult to characterise using approach developed. Therefore further work is required to assess more volunteers and donors.

This study has highlighted the great differences in the mechanical properties of human and murine skin, suggesting that murine skin is not an appropriate model to assess microneedle puncture. It has also shown that the underlying tissues and hypodermis play a pivotal role in microneedle insertion mechanics.

# ACKNOWLEDGEMENTS

First and foremost I would like to express my deepest gratitude to my supervisors, Prof. Sam Evans and Dr. Sion Coulman, for all their consistent support, guidance and enthusiasm throughout the three years. I consider myself extremely lucky to have had such excellent supervision.

I would also like to thank Dr. James Birchall, Dr. Marc Pearton, Barbara Torris and all those within Welsh School of Pharmacy who have always been such a great help and a pleasure to work with.

I have greatly enjoyed working with all those within the Institutive of Medical Engineering and Medical Physics and would like to thank them all for their ideas and words of encouragement

I would like to thank everyone who volunteered and donated for any aspect of this study. I could not have done it without such generosity.

I would like to acknowledge Cardiff University and the EPSRC for funding my studies. Also, I would like to thank the IMechE and SWIEET for providing me with generous contributions towards various conference expenses.

For all my friends, I would like to say a huge thank you for continuously providing me with distractions away from the occasional misery of doing a PhD. To all of you who had been through it yourselves and understood, and to those who just listened, I honestly don't think I could have finished without such a great network of friends. I am very lucky to have you all.

To all of my family, especially my Mum, Dad and Christopher, I would like to say thank you for pretty much everything.

# CONTENTS

Page

## CHAPTER 2
## MEASURING THE MECHANICAL PROPERTIES OF SKIN *IN VIVO* AND *EX VIVO*

## CHAPTER 3
## FINITE ELEMENT MODELLING THE MECHANICAL PROPERTIES OF SKIN AS A MULTILAYER AND AS AN ANISOTROPIC MATERIAL

## CHAPTER 4
## INVERSE ANALYSIS TO DESCRIBE THE MECHANICAL PROPERTIES OF SKIN

## CHAPTER 5
## OPTIMISING MICRONEEDLE DEVICE DESIGN TO INCREASE SKIN PUNCTURE EFFICIENCY

# ABBREVIATIONS

| | |
|---|---|
| DIC | Digital Image Correlation |
| FEM | Finite Element Modelling |
| LB | Lower Back |
| M-R | Mooney Rivlin |
| MRI | Magnetic Resonance Imaging |
| OCT | Optimal Coherence Tomography |
| SC | Stratum Corneum |
| SD | Standard Deviation |
| UB | Upper Back |
| V-W | Veronda Westmann |

# NOMENCLATURE

| | |
|---|---|
| $a$ | Angle of fibre orientation relative to 0 axis on skin sample |
| $C_1$ | Material constant |
| $C_2$ | Material constant |
| $\lambda_m$ | Fibre stretch for straightened fibres |
| $C_3$ | Scales the exponential stresses |
| $C_4$ | Rate of un-crimping |
| $C_5$ | Modulus of the straightened fibres |
| $C_6$ | Determined from the requirement that the stress is continuous at $\lambda_m$ |
| $E_r$ | Reduced Young's Modulus |
| $E_i$ | Young's Modulus of indenting material |
| $E_s$ | Young's Modulus of skin |
| $f_i^{EXP}$ | Force reading from experimental data |
| $f_i^{FEM}$ | Force reading from finite element model |
| $N,\ n,\ i$ | Integer value |
| $F_1$ | Response of the isotropic matrix |
| $F_2$ | Contribution of the fibre family |
| $I_1,\ I_2$ | First and second invariant of the deviatoric of the right Cauchy Green deviatoric respectively |
| $J$ | Jacobian of the deformation (volume ratio) |
| $K$ | Bulk modulus |
| $\mu$ | Shear modulus |
| $\lambda_m$ | Stretch at which fibres are straightened |
| $\lambda$ | Stretch |
| $\lambda_1,\ \lambda_2,\ \lambda_3$ | Principle stretches |
| $r$ | Radius of indenter |
| $R^2$ | Coefficients of determinants |
| $R_0^2, R_{45}^2, R_{90}^2$ | Coefficients of determinants value calculated when load axes orientated at 0º, 45º and 90º for tensile tests respectively |

| | |
|---|---|
| $R^2_{cyl}, R^2_{sph}$ | Coefficients of determinants value calculated for model of indentation by cylindrical and spherical indenters respective |
| $R^2_{ave}$ | Average coefficients of determinants value comparing all three load axes. |
| $v_i$ | Poisson's Ratio of indenting material |
| $v_s$ | Poisson's Ratio of skin |
| $U(J)$ | Volumetric component |
| $W$ | Strain energy density function |

# CHAPTER 1

# INTRODUCTION AND LITERATURE REVIEW

## 1.1 General Introduction

The transdermal delivery of therapeutics into the body has several advantages when compared with other methods. The approach allows for increased patient compliance, reduced risk of gastrointestinal degradation and direct application to the treatment site. However, the transdermal delivery of compounds is severely limited by the outermost layer of skin called the stratum corneum (SC), and hence only a small number of therapeutics can currently be delivered via this route. Arrays of microneedles measuring between 70μm and 900μm in height have been developed to promote transdermal drug delivery by creating microperforations in the skin, hence allowing molecules to diffuse through the SC with more ease. Over the past decade, a range of microneedle array designs have been developed to allow for the delivery of several therapeutic compounds into / across the skin. However, designs are usually based on the manufacturing techniques available rather than development from biomechanical concepts, and without effective skin puncture whilst using the device, the microneedle array is relatively useless.

To establish designs which can allow for effective and repeatable microneedle puncture, a greater understanding of the mechanical characteristics of skin is required. Some studies have already begun to quantify the mechanics of skin penetration by microneedles in *ex vivo* and *in vivo* tissues, but there are some

concerns as to whether *ex vivo* tissue is a suitable model when assessing microneedle puncture, due to the different biomechanical properties between *ex vivo* and *in vivo*. This study therefore aimed to quantify the mechanical properties of *in vivo* human skin and laboratory models which have been used to examine skin puncture, to determine whether such alternatives serve as an appropriate model. Furthermore, by obtaining data relating to the mechanical properties of human skin *in vivo*, it was possible to establish more rationally designed microneedle arrays that potentially allow for effective skin puncture across all microneedles within the array. This was achieved by developing curved in plane microneedle arrays manufactured from stainless steel sheets, where the curvature was determined by modelling skin deformation at loads comparable to microneedle application. By using such a device, it was possible to determine whether skin puncture *in vivo* was uniform across all microneedles within the array, and whether such results were repeatable in *ex vivo* tissue to further the observations noted during the mechanical tests and models of *in vivo* and *ex vivo* skin.

## 1.2 Literature review

The following section will detail the relevant literature which has lead to the aims and objective of this study. The function of skin as an immune organ and the mechanical properties of the tissue will be presented, in addition to the various experimental methods and modelling techniques used to describe the mechanical behaviour. The implications of microneedle devices for transdermal drug delivery will also be detailed, along with the attempts made to characterise skin puncture by microneedles. The literature review provides an up-to-date overview of the microneedle concept and the attempts made to improve microneedle insertion into skin. However, there are notable gaps within current research which have also been highlighted.

### 1.2.1 Skin structure and function

Skin is a multilayered and highly organised thin membrane which covers the surface of the body. Skin must be flexible enough not to impair body motion, whilst being tough enough to resist tearing and piercing. It serves as a barrier protecting against the ingress of potentially harmful microbes and chemicals from the external environment, and cushions mechanical impact. Additionally, skin reduces heat and water loss, and contains nerve fibres and immune responsive cells. The structure can be split into three main layers as shown in Figure 1.1, which are the epidermis, dermis and hypodermis, all containing additional layers and structures. Within this section each separate skin layer will be discussed in terms of function.

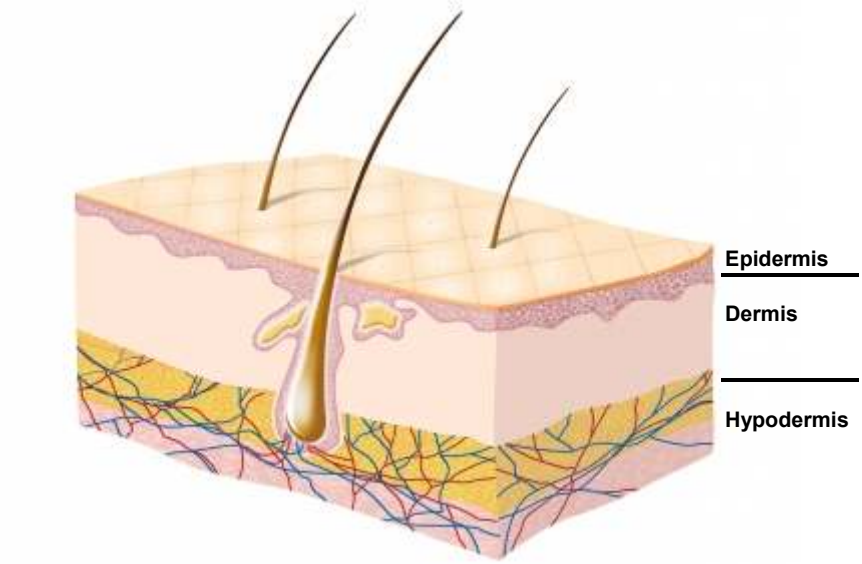


*Figure 1.1: Diagram of human skin, showing the three main skin layers (Figure reproduced from http://www.123rf.com).*

#### *1.2.1.1 Epidermis*

The epidermal layer is approximately 0.1mm thick in humans (Koehler et al., 2010) depending on the location, and consists of several separate layers of tissue, where the outermost is the waterproof covering of the SC, which prevents fluid ingestion and loss. This layer is usually around 25μm thick (Koehler et al., 2010) and is constructed of corneocytes, which lay flat and are held together by lipids, forming a “bricks and mortar” structure (Barry, 2001). The tissue is constantly being renewed by cell shedding from the surface and

the replacement by those beneath. As SC is in direct contact with the external environment, it is most influenced by factors such as humidity and temperature, compared with the other skin layers (Papir, Hsu and Wildnauer, 1975).

Beneath the SC is a layer of tissue called the viable epidermis, which has long been recognised as a highly immune reactive structure, as it contains antigen presenting cells (Babiuk et al., 2000). This function makes the skin a potential target for vaccination.

#### *1.2.1.2 Dermis*

The dermis can be split into two anatomical regions, which are the outermost papillary and underlying reticular dermis. Both structures have a total thickness of approximately 1mm in humans (Moore et al., 2003) containing elastin and collagen fibres within a matrix. The thinner papillary dermis contains smaller and more loosely connected fibres which are vertically arranged, connecting the epidermis to the reticular dermis. The reticular dermis consists of a fibre matrix which is orientated in plane with the skin (Silver, Siperko and Seehra, 2003). The fibre matrix direction is in part related to the Langer's lines on the body, which detail the orientation at which the skin has least flexibility. As a result of the collagen and elastin fibrils, the dermis has a mainly mechanical function, allowing for high levels of deformation, as the fibres stretch and re-orientate (Brown, 1973). The contribution of the fibre matrix within skin is discussed further in section 1.2.3. Depending on the skin site, the dermal layer also houses structures such as hair follicles, blood vessels and several glands which secrete sebum, cerumen and sweat (Scanlon and Sanders, 1997).

#### *1.2.1.3 Hypodermis*

The hypodermis is a layer of subcutaneous fat found below the dermis containing areolar connective and adipose tissues, which connects the underlying muscles to the skin (Scanlon and Sanders, 1997). The thickness of this layer varies substantially more than the outermost dermal and

epidermal layers. The areolar tissue consists of collagen and elastin fibres much like the dermis, and many migrating white blood cells which aim to destroy any pathogens which enter the body. The adipose tissue stores fats and nutrients as a potential energy source and provides cushioning for bony prominences (Scanlon and Sanders, 1997).

### 1.2.2 Transdermal drug delivery and the microneedle concept

Transdermal drug delivery of therapeutics has several advantages over other methods, including the avoidance of gastrointestinal degradation, improvement of patient compliance and the ability to apply treatment to a localised site (Coulman, Allender and Birchall, 2006). Within the viable epidermis are an abundance of Langerhans cells, which engulf and process microbial antigens within the tissue, hence becoming fully functioning antigen presenting cells (Ng et al., 2009). Due to this process, many have studied the implications of intradermal immunisation and have shown that vaccine doses can be reduced when administered transdermally as opposed to intramuscular injection (Hunsaker and Perino, 2001; Quan et al., 2010a). However, the skin acts as an excellent barrier between the body and harmful substances within the environment, therefore the transdermal diffusion of compounds can be difficult to achieve. As a result, intra-/transdermal delivery has been limited to only a few low molecular weight and high lipophilicity drugs.

As discussed previously, skin is a stratified tissue consisting of many layers, one in particular acts as the main barrier for invading chemicals. The very outer layer, the SC, provides a waterproof coating for the underlying skin tissue. Thus this layer predominantly hinders the transdermal administration of therapeutics. The few compounds which can bypass this layer usually do so via natural pathways such as intercellular and transcellular permeation, where the substance routes around or through the cells within the SC, or by migration down hair follicles and gland ducts (Barry, 2001). To increase the number of therapeutic substances which can be administered to the body, the

research community has developed several methods for circumventing the SC to increase skin permeability. Some of which aim to physically disrupt the skin barrier to increase permeation and activate immune responses (Nickoloff and Naidu, 1994) and other approaches have striped the SC entirely from the skin by using abrasive techniques (Andrews et al., 2011). This method has been proven to greatly improve passive diffusion of antigens to the body (Mikszta et al., 2002). An alternative method, which has received significant attention, is the microneedle array, which is an arrangement of needles with a total height ranging from 70μm (Wei-Ze et al., 2010) to 900μm (Donnelly et al., 2010). Such devices aim to perforate the SC to allow for the diffusion of therapeutics into the skin.

Microneedle arrays for transdermal drug delivery purposes were first patented in 1976 by Gerstel and Place (Gerstel and Place, 1976). Nonetheless, it was not until advancements were made in the microfabrication industry in the 1990's, that the devices could be manufactured and tested (Henry et al., 1998). Microneedle designs aim to either increase the permeability of skin to allow for more efficient transdermal delivery, or act as an instrument which not only punctures the skin but also carries the therapeutic substance into the tissue. Studies have shown that such devices have dramatically increased patient compliance when compared with hypodermic injection, as no / minimal pain and little irritation is experienced during application (Kaushik et al., 2001; Bal et al., 2008; Haq et al., 2009). When queried, both clinicians and the general public have been documented to be positive overall about the benefits of microneedles for drug delivery purposes (Birchall et al., 2011). As a result, development of the technology to increase the potential for such devices to be taken from a laboratory tool towards a clinically useful device, is beginning to take place.

Microneedle devices can be categorised into four main groups, which are shown in Figure 1.2 (Arora, Prausnitz and Mitragotri, 2008). The simplest method is to use solid microneedle arrays to puncture or disrupt the SC, after which a medicated substance is applied to the site and allowed to diffuse to the underlying tissue. An enhancement of this method is to add a coating to

the solid array, which contains the drug, vaccine or protein which is to be delivered to the body. The coating method usually involves the dipping or spraying of the drug solution onto the microneedle array, until the coat is of adequate thickness (Gill and Prausnitz, 2007 2008; Quan et al., 2010b; McGrath et al., 2011). Studies have shown that the coating volume can be increased by adding pockets or grooves to the individual microneedle design, which allows the solution to collect in the microconduits of the needle (Gill and Prausnitz, 2008; Han et al., 2009). The coated array are then inserted into the skin and removed, leaving the coating *in situ*, after which the drug solution dissolves over time. An adaptation of this method is biodegradable microneedles, where the entire needle is fabricated from a biodegradable material, into which the drug is encapsulated. A similar concept is used as with the coated microneedles, however the entire needle remains within the skin and dissolves over time, rather than the coating. The advantage of both biodegradable and coated microneedles is that both approaches provide an increased control over the drug volume delivered, also promoting the slow release of therapeutics (Zhang et al., 2010). However, there are concerns regarding the mechanical integrity of biodegradable microneedles as they have been found to fracture and buckle at comparatively low loads, due to the materials used during fabrication (Park, Allen and Prausnitz, 2005). Finally, by adapting the concept used for hypodermic injection, hollow microneedles allow for intradermal injection, providing control over the drug volume used in clinical practise.

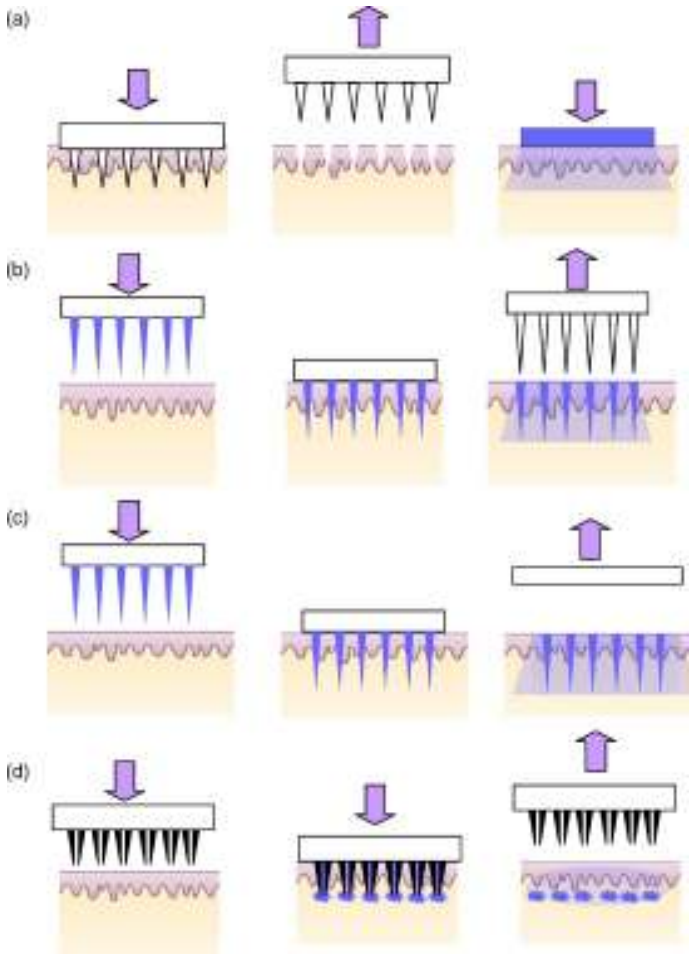


*Figure 1.2: The four main microneedle design variations:- a) solid array inserted into skin medicated substance is then applied, b) solid array coated with a therapeutic substance, c) microneedle fabricated from a biodegradable material and d) hollow microneedles for intradermal injection. (Figure reproduced from (Arora et al., 2008).)*

Table 1.1: Example of some of the published microneedle studies.

| Microneedle Design | Fabrication Methods | Fabrication Materials | Transport studies in human & animal skin | |
|---|---|---|---|---|
| | | | *In vivo* | *Ex vivo* |
| **Solid** | ***Reactive ion etching*** (Henry et al., 1998; Xie, Xu and Gao, 2005; Wei-Ze et al., 2010)<br>***Electrical discharge machining*** (McAllister et al., 2003; Zhou et al., 2009; Gomaa et al., 2010; Bystrova and Luttge, 2011; Donnelly et al., 2011)<br>***Photochemical etching*** (Martanto et al., 2004)<br>***Wet & dry etching*** (Morrissey et al., 2005; Wilke et al., 2005) | ***Silicone*** (Henry et al., 1998; Morrissey et al., 2005; Wilke et al., 2005; Xie et al., 2005; Ji et al., 2006; Wei-Ze et al., 2010; Yan et al., 2010)<br>***Stainless steel*** (Martanto et al., 2004; Chen et al., 2009; Bal et al., 2010b)<br>***Polymers*** (Gomaa et al., 2010; Donnelly et al., 2011)<br>***Polymer coated with metal*** (Zhou et al., 2010)<br>***Ceramics*** (Bystrova and Luttge, 2011) | ***Fluorescence and dyes*** (Bal et al., 2010a)<br>***Insulin vaccine*** (Martanto et al., 2004; Chen et al., 2009; Ding et al., 2009)<br>***Diphtheria vaccine*** (Ding et al., 2009) | ***Fluorescence and dyes*** (Henry et al., 1998; McAllister et al., 2003; Xie et al., 2005; Gomaa et al., 2010)<br>***Insulin*** (Chen et al., 2009) |
| **Coated** | ***Laser cutting*** (Shirkhansadeh, 2005; Gill and Prausnitz, 20072008; Quan et al., 2010a)<br>***Reactive ion etching*** (Crichton et al., 2011)<br>***Micromoulding*** (Han et al., 2009) | ***Silicone*** (Crichton et al., 2010)<br>***Stainless steel*** (Shirkhansadeh, 2005; Gill and Prausnitz, 20072008; Quan et al., 2010a; Kim et al., 2011)<br>***Polymers*** (Han et al., 2009) | ***Influenza vaccine*** (Quan et al., 2010a; Song et al., 2010; Kim et al., 2011)<br>***Ovalbumin*** (Han et al., 2009) | ***Influenza vaccine*** (Kim et al., 2011)<br>***Fluorescence and dyes*** (Gill and Prausnitz, 2007) |
| **Biodegradable** | ***Drawing material into needle*** (Lee, Lee and Jung, 2011)<br>***Micromoulding*** (Miyano et al., 2005; Park et al., 2005; Park, Allen and Prausnitz, 2006; Lee, Park and Prausnitz, 2008; Ito et al., 2011{Park, 2007 #6)}<br>***Solid, blunt microneedle fabricated by laser cutting of stainless steel, arrowhead made by micromoulding*** (Chu and Prausnitz, 2011) | ***Sugars*** (Miyano et al., 2005; Li et al., 2009; Lee et al., 2011)<br>***Biodegradable polymers*** (Park et al., 2005; Park et al., 2006; Park et al., 2007; Chu and Prausnitz, 2011; Ito et al., 2011)<br>***Organic compounds*** (Lee et al., 2008) | ***Hydrophilic molecules*** (Lee et al., 2011)<br>***Fluorescence and dyes*** (Miyano et al., 2005)<br>Antibodies (Li et al., 2009) | ***Drugs*** (Park et al., 2006; Lee et al., 2008) |
| **Hollow** | ***Micromoulding*** (Davis et al., 2005; Lippmann and Pisano, 2006; Lippmann, Geiger and Pisano, 2007; Hafeli, Mokhtari and Liepmann, 2009; Matteucci et al., 2009; Zhu et al., 2009; Bystrova and Luttge, 2011)<br>***Reactive Ion etching*** (Gardeniers et al., 2003; Mukerjee et al., 2004; Stoeber and Liepmann, 2005; Chen, Wei and Iliescu, 2010)<br>***Wet Etching*** (Gardeniers et al., 2003) | ***Polymers*** (Davis et al., 2005; Lippmann and Pisano, 2006; Lippmann et al., 2007; Matteucci et al., 2009; Zhu et al., 2009)<br>***Silicone*** (Gardeniers et al., 2003; Mukerjee et al., 2004; Stoeber and Liepmann, 2005; Hafeli et al., 2009; Chen et al., 2010)<br>Nickel (Zhu et al., 2009)<br>***Ceramics*** (Bystrova and Luttge, 2011) | ***Insulin*** (Davis et al., 2005)<br>***Fluorescence and dyes*** (Hafeli et al., 2009)<br>***Influenza vaccine*** (Van Damme et al., 2009) | ***Fluorescence and dyes*** (Chen et al., 2010) |

A summary of some of the associated studies for all four microneedle designs is shown in Table 1.1. The fabrication methods, materials, along with the *in vivo* and *ex vivo* transport studies of drugs, vaccines and dyes have been shown, where several common themes can be noted. Typically microneedles are predominantly manufactured from silicon, stainless steel and polymers, with the exception of biodegradable microneedles which have been manufactured from organic compounds and sugars. Microneedle arrays have been used to deliver a range of therapeutics including the influenza vaccine, insulin, drug compounds and fluorescent agents to detect skin penetration, both *in vivo* and *ex vivo*. Moreover, the micromanufacturing processes are similar when fabricating all four microneedle designs. This summary shows the diversity of the concept and the range of uses, hence a greater general understanding of microneedle design and the effects on skin puncture are required.

For microneedle devices to be successfully used as a method for promoting transdermal drug delivery, it is integral that skin penetration is achieved. As a result, numerous studies have attempted to quantify skin penetration by using various imaging methods and by performing penetration measurements using *in vivo* and *ex vivo* skin tissue. One of the simplest methods is to detect skin puncture by applying a dye to the skin post microneedle application, where the aqueous dye stains the nucleated cells within the epidermis, implying the SC barrier has been broken. This technique has been used *ex vivo* (Coulman et al., 2009; Haq et al., 2009; Zhang et al., 2010) and *in vivo* (Bal et al., 2010b), and when used in conjunction with microscopic imaging or histological examination, it is possible to quantify the staining distribution through the cross section and en face of the tissue, providing clues regarding penetration depth (Zhang et al., 2010). Transdermal water loss can also be used as a measurement for microneedle skin penetration, as successful skin puncture results in the disruption of the waterproof barrier, thus causing the tissue to dehydrate due to evaporation. The approach can also be used to measure microchannel closure after skin penetration (Gomaa et al., 2010; Kalluri and Banga, 2011).

Further quantification of microneedle puncture can be made by using several imaging techniques. One conventional approach is to use histological sectioning to examine the channels created after microneedle insertion (Kalluri and Banga, 2011). Optical coherence tomography is also a popular method and allows for a breadth of information from *in vivo* (Enfield et al., 2010; Coulman et al., 2011) and *ex vivo* (Donnelly et al., 2010) examination. Such approaches can be used to determine microchannel depth (Enfield et al., 2010) and the effect of insertion force into cadaver tissue on microneedle puncture (Donnelly et al., 2010). In an *in vivo* study by Coulman *et al*. in 2011, two microneedle devices were compared with hypodermic needle application to human skin. The investigation found that the elastic properties of skin caused a large amount of recoil once the micro and hypodermic needles had been removed. Only very small microchannels, predominantly confined to the epidermal region were found, suggesting that the mechanical properties of skin play a large role in skin penetration. Additionally, when quantifying array puncture it was noted that for in plane microneedle arrays, the outer needles penetrated to a significantly greater depth when compared with the internal microneedles within the array.

The measurement of microneedle insertion forces into *in vivo* and *ex vivo* skin have aided in the design of individual microneedles and predict fracture within the skin (Davis et al., 2004). To ensure sufficient puncture, some have established approaches to reduce application force by either vibrating the microneedle (Yang and Zahn, 2004), mounting the array onto a roller device (Badran, Kuntsche and Fahr, 2009; Park et al., 2010; Zhou et al., 2010), or by applying a consistent load onto an array (Verbaan et al., 2008; Donnelly et al., 2010). The measurement of insertion force can be achieved *in vivo* by observing the change in electrical resistance across the skin as a microneedle penetrates the skin barrier. Insertion forces of a single microneedle *in vivo* have varied from 0.1N-3.4N, where a strong relationship between insertion force and microneedle interfacial area have been documented (Davis et al., 2004). However, application of arrays containing 3364 short densely packed microneedles, measuring 60μm, into *ex vivo* murine skin have shown less force is required to create skin puncture, at only 0.6N over the entire array

(Crichton et al., 2010). This implies large discrepancies between human *in vivo* and animal *ex vivo* skin puncture measurements.

Several investigations have begun to develop more rational microneedle and array designs. Studies have replicated the shape of a mosquito's proboscis to form the geometry of single microneedles with the aim to aid skin penetration (Aoyagi, Izumi and Fukuda, 2008; Izumi et al., 2011). Additionally, some have used theoretical calculations to optimise the microneedle density within an array (Al-Qallaf and Das, 2008; Al-Qallaf and Das, 2009), to measure strain in *ex vivo* skin during microneedle application (Kendall, Chong and Cock, 2007) and to mimic skin deformation upon microneedle application using simple finite element models (FEMs) (Roxhed et al., 2007; Aoyagi et al., 2008; Kong, Zhou and Wu, 2011).

The range of approaches used to assess and describe skin puncture by microneedles is varied. However, some describe microneedle puncture within *ex vivo* skin tissue from animal donors such as murine (Crichton et al., 2010), so the data collected may not be truly representative of *in vivo* measurements performed on human skin. Therefore, the mechanical characteristics of human skin *in vivo* should be considered when evaluating microneedle puncture and establishing new microneedle designs. Furthermore, the comparison between the mechanical properties of *in vivo* and *ex vivo* skin would provide information that could be used when assessing *ex vivo* skin puncture by microneedles, to accommodate for the variations between the mechanical properties of the two tissue types.

### 1.2.3 The mechanical characteristics of skin

As discussed previously, skin is a complex multifunction organ which covers the entire surface of the body. To enable body motion, it must be flexible enough to facilitate large deformations in all directions, whilst maintaining the ability to return to its original state. This gives rise to a complicated range of mechanical properties. When considering the skin as a whole, incorporating

the epidermal, dermal and hypodermal layers, it can be described as anisotropic (Stark, 1977; Gerhard and Vogel, 1981), viscoelastic (Pereira, Mansour and Davis, 1991), nonlinear (Brown, 1973) and non homogenous, resulting in an ability to endure large deformations. Due to the viscoelastic properties, skin undergoes a phenomenon known as preconditioning, where under cyclic loads the stress-strain relationship continuously alters until a steady state is reached (Matsumura et al., 2001; Lui and Yeung, 2008). Additionally, *in vivo* the skin is subjected to a pre-stress which is present in varying degrees all over the body (Alexander and Cook, 1977; Jacquet et al., 2008).

The SC is the stiffest of the skin layers, therefore the least extendible under applied load. The layer exhibits less viscoelastic and preconditioning behaviour compared to other layers, but still maintains a nonlinear stress-strain relationship under applied tension (Koutroupi and Barbenel, 1990). The mechanical response of this layer can vary greatly depending upon environmental changes such as hydration, temperature, humidity and chemical treatments (Wildneuer, Bothwell and Douglass, 1971; Papir et al., 1975; Wu, van Osdol and Dauskardt, 2006b).

The underlying dermis contributes a large amount to the overall mechanical characteristics of skin. As described previously, this layer consists of a dense network of collagen and elastin fibres which allow for high levels of deformation. The overall mechanical response of skin tissue under applied tension can be divided into three main phases (Brown, 1973), shown in Figure 1.3.

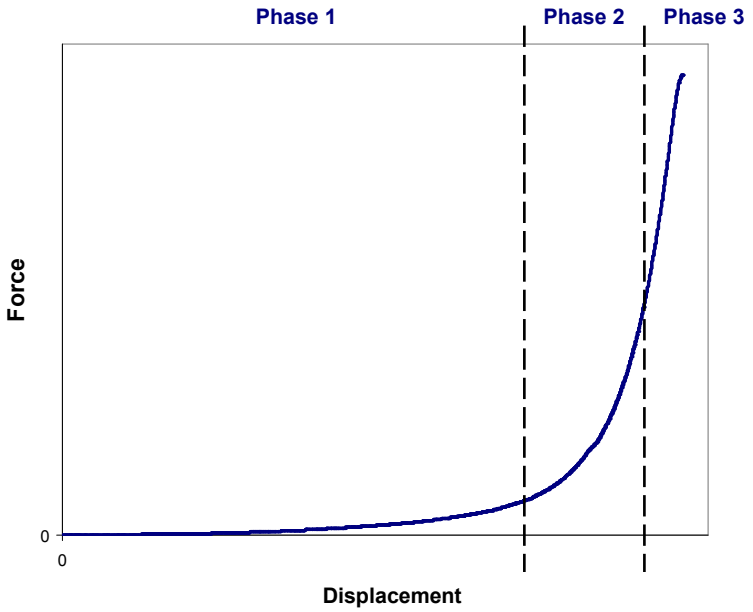


*Figure 1.3: Plot showing a typical force - displacement response for skin.*

Each phase can be related to the collagen and elastin fibres within the dermis. Phase one illustrates great extension at low load as the dermal fibres orientate towards the load axis, after which the dermal fibres begin to un-crimp and become progressively more aligned resulting in an increased stiffness. Finally the fibres come under direct load culminating in an almost linear third phase (Brown, 1973). It has been suggested that the dermal elastin fibres contribute to the mechanical response at low loads and during tissue recoil (Oxlund, Manschot and Viidik, 1988). The influence of the collagen fibres have been examined, by altering fibre diameter and density, on the biomechanical properties of skin tissue (Sanders and Goldstein, 2001), in addition to the properties of the individual collagen fibres themselves (Parkinson et al., 1997; Wenger et al., 2007). Hence this matrix of collagenous and elastic fibres held within a viscous material, provides the skin with the majority of the in plane flexibility during load application. This tissue also aids in the recoil once the stress has been removed (Brown, 1973). The underlying hypodermis is the softest of the three layers and evenly transfers loads from the upper skin layer to the underlying tissues. Hence is important when applying loads perpendicularly to the surface of the skin.

All layers collectively and independently exhibit different material characteristics but all still posses viscoelastic, non homogenous, anisotropic and nonlinear properties. A number of *in vivo* and *ex vivo* approaches have been developed to test these properties and sections 1.2.4 & 5 will discuss these methods. Furthermore sections 1.2.6 & 7 detail the theoretical models used to characterise such behaviours.

### 1.2.4 Testing the mechanical properties of skin *ex vivo*

Analysing the mechanical behaviour of *ex vivo* animal and human skin can allow for a wide range of characteristics to be explored, which may not be possible *in vivo.* As the tissue sample can be removed, it is possible to conduct destructive tests to determine the failure mechanisms and tensile strength of the sample. Furthermore, the tissue layers can be separated and evaluated independently.

The most commonly used materials test performed on *ex vivo* skin samples is the tensile test. Using this method, many have detailed the anisotropic (Lanir and Fung, 1974; Stark, 1977), nonlinear (Brown, 1973) and viscoelastic (Pereira et al., 1991) behaviour of skin, as well the effects under failure (Pereira, Lucas and Swee-Hin, 1997), creep (Del Prete et al., 2004), fatigue (Muñoz et al., 2008) and preconditioning (Matsumura et al., 2001; Lui and Yeung, 2008). This approach has also been used to characterise the variations between animal donor groups with scarred (Corr et al., 2009) and aged skin (Gerhard and Vogel, 1981).

The outermost SC layer can be removed by heat or chemical separation from *ex vivo* samples, however as a result the underlying epidermis and dermis can become damaged. Hence, these layers are not normally separated intact. Various tensile tests have been performed on the SC to determine the effects of temperature and hydration (Papir et al., 1975), in addition to the tensile strength of the tissue (Koutroupi and Barbenel, 1990). More recently, other materials testing techniques have been used to evaluate the properties of the

SC including nanoindentation (Yuan and Verma, 2006) and fracture mechanics theories such as the determination of delamination energies between cells to characterise the failure mechanisms (Wu et al., 2006b). Some researches have calculated the Young's Modulus of the SC for human, murine and porcine tissue using nanoindentation, where values of 0.5GPa - 1.4Mpa and 50 – 200MPa respectively, were found (Pailler-Mattei et al., 2007; Crichton et al., 2011; Yuan and Verma 2006), suggesting large variations between species.

The subcutaneous fat layer has highly viscous properties due to the loosely connected matrix, which allows the tissue to attach the dermis to the underlying tissues. Therefore tensile loading is not an appropriate testing technique. Thus the properties of the subcutaneous fat in compression (Miller-Young, Duncan and Baroud, 2002) and through the using rheometer, to obtain the shear modulus (Geerligs et al., 2008; Geerligs et al., 2010).

Another key advantage of using *ex vivo* skin tissue is that the effects of altering the skin's anatomical structure on the biomechanical behaviour can be evaluated. This approach has been used to vary the quantity of collagen (Del Prete et al., 2004), elastin (Oxlund et al., 1988) and proteoglycans (Eshel and Lanir, 2001) within the skin, as well the effects of blood flow (Tatlidede et al., 2009) and hormonal changes (Özyazgan et al., 2002) within rat and mouse models. In addition to the benefits discussed, *ex vivo* mechanical testing of skin has vast implications for the development of new tissue engineered scaffold, as it provides a basis for comparisons between actual tissue and engineered structures (Courtney et al., 2006). However examining the mechanical properties of skin *ex vivo* removes the tissue from the natural environment, thus removing the pre-stress and source of hydration, resulting in different mechanical characteristics when compared with *in vivo* analysis.

### 1.2.5 Testing the mechanical properties of skin *in vivo*

*In vivo* examination of the mechanical behaviour of skin allows for the characterisation of the properties whilst the skin is in a natural state of pretension and hydration. Four main mechanical tests have been developed to measure the properties of skin *in vivo*, these are torsion, tension, suction and indentation, which can be sub grouped into those methods which apply in plane strain and perpendicular strain to the skin's surface.

Torsion tests can be used to measure the anisotropic mechanical properties by adhering a solid disc to the skin and applying a prescribed torque (Sanders, 1973). Another commonly used technique is tensile loading, where two tabs are attached to the skin and an applied displacement is implemented (Wan Abas and Barbenel, 1982; Manschot and Brakkee, 1986; Lim et al., 2008). This approach can be used to show the formation of wrinkles in compression, as well as the tensile mechanical characteristics of *in vivo* skin. As both tension and torsion analysis of the skin's mechanical properties are performed in plane, the effects of the hypodermis and underlying tissues on the mechanical properties are minimal, attributing the majority of the measurements obtained to the properties of the dermis and epidermis. The Young's Modulus of human skin *in vivo* has been measured using both tension and torsion, with values of between 4.6-20MPa for tension (Manschot and Brakkee, 1986) and 420-850kPa for torsion (Agache et al., 1980), implying that the skin is stiffer in tension as apposed to torsion. When comparing such values with *ex vivo* Young's Modulus calculations shown in section 1.2.4, it can be seen that *ex vivo* skin has a significantly higher Young's Modulus.

Two approaches which load the skin perpendicular to the surface are suction and indentation. Suction measurements apply a vacuum to the surface of the skin, causing the tissue to deform due to the decrease in pressure (Hendriks et al., 2004). This relative displacement can then be quantified and used as a measurement for skin elasticity. Indentation measurements are a commonly

used technique within materials testing, where a rigid indenter is applied to the skin site and the relative load and displacement on the indenter is used to quantify the material properties of the tissue (Bader and Bowker, 1983; Pailler-Mattéi and Zahouani, 2006). With both suction and indentation assessments, the hypodermis and underlying tissues come under direct load, hence these tissues contribute to the mechanical response. The specific mechanical properties of a skin layer can be controlled by varying indenter and suction cup size. For example, a small indenter or suction cup could be used to characterise the upper skin layers, where as a larger indenter or suction cup could measure the mechanical response of the lower layers such as the hypodermis (Hendriks et al., 2004). Recently, new devices which were derived from indentation and suction methods include instruments which blow air onto the skin to measure the properties (Fujimura et al., 2008), and indentation devices which can apply loads to the skin under various orientations, giving anisotropic measurements (Flynn, Taberner and Nielsen, 2011).

With advancements in medical imaging techniques, many have further quantified skin deformation *in vivo* with the aid of magnetic resonance imaging (MRI) (Tran et al., 2007), optical coherence tomography (OCT) (Hendriks et al., 2006) and ultrasound (Hendriks et al., 2003; Hendriks et al., 2006). Such approaches provide deflection measurements for each skin layer (Hendriks et al., 2006), under applied suction and indentation. Surface examination has also been used for skin, detailing the level of strain under tension and compression. These include digital image correlation (DIC) (Evans and Holt, 2009), motion analysis (Mahmud, Holt and Evans, 2010) and the application of a simple grid formation to the skin (Wan Abas and Barbenel, 1982). These approaches use the displacement of the marker system, relative to the starting formation prior to skin deformation, to measure the strain distribution across the surface. Recently, ultrasound methods have also been used to measure the strain across skin under applied and natural in plane tension (Mofid et al., 2010).

*In vivo* methods to analyse the mechanical properties of skin allow the tissue to be assessed within its natural state of stress and strain. Measurements perpendicular and in plane to the skin surface can be made, providing data relative to each skin layer and across the skin respectively. With advancements in imaging techniques, more accurate measurements of surface and layer deformation have been achieved. However, only low loads can be applied to the tissue and even though some tests can be used to estimate the properties of each layer, these measurements can only ever be taken as estimates as the individual tissues cannot be removed and separately examined.

### 1.2.6 Constitutive models used to describe the mechanical behaviour of skin

The mechanical characteristics of skin are very complex, but if modelled using appropriate constitutive laws, it is possible to describe the properties more so than through mechanical testing alone. Moreover, relevant mathematical representations of skin can be implemented for many clinical and non clinical research purposes and within an industrial context, to aid in product development.

Hyperelastic materials are ideally elastic, and can be incompressible or compressible, where the constitutive equations can be derived from a strain energy density function. These functions are used to detail nonlinear and isotropic behaviour which is independent of strain rate. There are numerous hyperelastic models which describe the mechanical characteristics of soft solids which can also be used to represent biological tissues such as skin. Although such laws allow for nonlinear stress – strain behaviour, the research community has also established models which specifically depict the mechanical characteristics of biological tissues such as skin by allowing for anisotropic and viscoelastic characteristics. The appropriate constitutive models which can be used to detail the mechanical characteristics of skin will be discussed within this section. Later in this Chapter, studies which have

used the specified models to represent the mechanical behaviour of skin by inverse analysis and finite element modelling will be discussed.

### *1.2.6.1 Nonlinear models of hyperelasticity*

Nonlinear models of hyperelasticity have been widely used to characterise the mechanical behaviour of skin, many of which are available within finite element modelling software. The six main hyperelastic models which have been used to describe soft tissues and skin are presented in date order. All symbols are detailed in the Nomenclature on page xi.

**Neo-Hookean (1948)**

The neo-Hookean model is an extension of Hooke's Law for large deformations and can be used to describe the mechanical incompressible nonlinear isotropic response of rubber like materials and soft tissues. The strain energy density function for the incompressible neo-Hookean model is shown in Equation 1.1 (Holzapfel, 2006).

$$W = C_1\left(\lambda_1^2 + \lambda_2^2 + \lambda_3^2 - 3\right) = C_1\left(I_1 - 3\right) \qquad 1.1$$

$C_1 = \frac{\mu}{2}$, $\lambda_1, \lambda_2, \lambda_3$ = principal stretches and $I_1$ = first invariant

**Mooney – Rivlin (1952)**

An extension of the neo-Hookean material model is the Mooney –Rivlin (M-R) model of hyperelasticity. The M-R model describes the isotropic, nonlinear and incompressible response of rubber like materials, which uses the strain energy density function shown in Equation 1.2 (Holzapfel, 2006).

$$W = C_1\left(\lambda_1^2 + \lambda_2^2 + \lambda_3^2 - 3\right) + C_2\left(\lambda_1^{-2} + \lambda_2^{-2} + \lambda_3^{-2} - 3\right) = C_1\left(I_1 - 3\right) + C_2\left(I_2 - 3\right) \qquad 1.2$$

$C_1 = \frac{\mu_1}{2}$ and $C_2 = \frac{-\mu_2}{2}$ and the shear modulus given by $\mu = \mu_1 - \mu_2$. Note that when $C_2 = 0$, the model reduces to a neo – Hookean material.

**Veronda – Westmann (1970)**

The strain energy function for the incompressible Veronda – Westmann (V-W) model is shown in Equation 1.3. It is similar to that of the M-R model, however the strain energy is given in exponential form. As a result, the relationship allows for exponential stiffening at increased strain (Veronda and Westmann, 1970). The model again allows for nonlinear and isotropic behaviour

$$W = C_1\left[e^{(C_2(I_1-3))}-1\right]-\frac{C_1C_2}{2}(I_2-3) \qquad 1.3$$

$C_1 = \frac{\mu_1}{2}$ and $C_2 = \frac{-\mu_2}{2}$ and the shear modulus is $\mu = \mu_1 - \mu_2$.

**Ogden (1972)**

The Ogden material model describes the nonlinear isotropic behaviour of rubber like materials using the following incompressible strain energy function detailed in Equation 1.4 (Ogden, 1972). The model describes the changes in the principal stretches from reference to the current orientation.

$$W = W(\lambda_1,\lambda_2,\lambda_3)\sum_{i=1}^{N}\frac{\mu}{\alpha}\left(\lambda_1^{\alpha}+\lambda_2^{\alpha}+\lambda_3^{\alpha}-3\right) \qquad 1.4$$

**Arruda - Boyce (1993)**

The Arruda – Boyce model uses an eight polymer chain representation of the macromolecular network, allowing for nonlinear material behaviour. Each individual polymer chain is described by the non-Gaussian statistical theory and the strain energy density function is derived from the inverse Langevin function. Equation 1.5 shows the first three terms of the strain energy (Arruda and Boyce, 1993; Holzapfel, 2006)

$$W = \mu\left[\frac{1}{2}(I_1-3)+\frac{1}{20n}\left(I_1^2-9\right)+\frac{11}{1050n}\left(I_1^3-27\right)+....\right] \qquad 1.5$$

In this model, the first strain invariant $I_1$ is associated with the stretch in a chain by Equation 1.6 (Holzapfel, 2006).

$$\sqrt{I_1} = \sqrt{3}\lambda \qquad 1.6$$

**Yeoh (1993)**

The Yeoh hyperelastic material model (sometimes called the reduced polynomial model) describes the incompressible nonlinear isotropic deformation of solids such as rubber. The strain energy density function is shown in Equation 1.7 (Yeoh, 1993).

$$W = \sum_{i=1}^{N} C_i (I_1 - 3)^i \qquad 1.7$$

The shear modulus is calculated using $2C_1 = \mu$ (Holzapfel, 2006)

### *1.2.6.2 Anisotropy*

Material models can be composed of an isotropic matrix which incorporates one or more families of fibres, to give anisotropic mechanical properties. Such models can be extremely useful when modelling soft tissues such as skin because they can mimic the natural composition of the tissue. Tissues such as muscles, ligaments, tendons, arteries, and skin all consist of a material containing a matrix of fibres, thus allowing for large deformations and anisotropic properties. Depending upon the function of the tissue, the matrix orientation, network and strength of the fibres vary. Such material models can be manipulated to represent the mechanical response of many biological tissues.

The simplest form of anisotropy is transverse isotropy, where a single fibre family is orientated along one axis. As a whole, the mechanical response is orthogonal but when perpendicular to the direction of the fibres, the mechanical response is isotropic. Transversely isotropic models are useful for describing the mechanical behaviour of soft tissues such as ligaments, tendons and muscle because such tissues have a preferred fibre direction *in vivo* (Weiss, Maker and Govindjee, 1996). Additionally by incorporating multiple fibre families, it is possible to allow for a more complex anisotropic mechanical response, hence removing the isotropic behaviour of the preferred axis.

The research community has developed a range of constitutive laws which have been specifically designed to model the anisotropic behaviour of biological tissues. In an early study by Lanir in 1979 (Lanir, 1979), a model of collagenous tissues was developed, with the assumption that the mechanical response was largely influenced by the collagen and elastin fibres. Before load application, it was described that the elastin fibres were pre-stretched, providing the initial stress – strain response, and the collagen fibres were slack, giving rise to exponential stress at higher levels of strain. The fibre matrix within the model was in a non uniform distribution hence anisotropic behaviour was observed. An alterative approach which does not use a fibre matrix was developed by Fung *et al*. (Fung, Fronek and Patitucci, 1976), where an orthotropic constitutive model for a thin membrane was presented. The model connects the three components of stress in the plane of the membrane, with the three components of strain in the membrane, in the x, y and z directions. This orthotropic model can be reduced to a two dimensional strain energy function for skin and has shown to give good agreement with experimental data (Fung, 1993). Recently, new models have been established, and enhancements to existing theories, have given way to a range of constitutive laws which can account for anisotropy (Bischoff, Arruda and Grosh, 2002; Cacho et al., 2007; Kroon and Holzapfel, 2008).

### *1.2.6.3 Viscoelasticity*

Viscoelastic materials can be modelled using an arrangement of springs and dashpots which represent the linear elastic and viscous properties respectively. These can be orientated to allow for varying viscoelastic behaviours. In 1867, James Clark Maxwell established the Maxwell model using this method, where a purely elastic spring was connected in series to a purely viscous dashpot (Holzapfel, 2006). This model allowed the material to have a two fold strain behaviour, where the elastic response occurs simultaneously and relaxes if the stress is removed. Secondly a viscous component grows with time. William Thomas and Woldemar Voigt established the Kelvin – Voigt material model of viscoelasticity (Holzapfel, 2006). In this model an elastic spring and a viscous damper were connected

in parallel and upon constant load application, the material deforms at a decreased rate approaching towards a steady state, and upon stress release the material gradually recoils. With the addition of an elastic spring in parallel with the Maxwell model, a different viscoelastic material can be characterised, called the standard linear solid model (Holzapfel, 2006). This model allows for the material to instantaneously deform to some level of elastic strain, thereafter it will continue to deform until a steady state is reached.

### 1.2.7 Finite element modelling of skin tissue and inverse analysis

Finite element modelling is a commonly used engineering technique which models a material or structure under an applied stress. Such models can occasionally remove the need for lengthy tests on new designs prior to manufacture. Inverse analysis is an approach used to compare an experimental measurement with a computational model to check and increase accuracy. Thus by systematically optimising the parameters and boundaries within a FEM it is possible to create a close correlation with an experimental measurement and hence to identify the material parameters. This technique has significant implications when modelling the mechanical behaviours of complex materials such as skin. This can be useful as it not only produces models which accurately detail the mechanical behaviour of a material, but the parameters can act as an additional way of comparing the complex characteristics of biological tissues. Thus, many have used finite element modelling on a theoretical level to represent the mechanical characteristics of skin, or used finite element modelling coupled with inverse analysis to further quantify the behaviours using the extracted material parameters.

Some authors have used FEMs of human skin and inverse analysis to optimise material parameters matched to experimental measurements and obtained a close agreement using linear elastic, isotropic constitutive models (Delalleau et al., 2006; Delalleau et al., 2008a; Pailler-Mattei, Bec and Zahouani, 2008). Such models were correlated against indentation and

extensometry tests on human skin *in vivo*. However, due to the simplistic linear elastic model, the computed observations did not always provide a good fit with experimental measurements post inverse analysis. Additionally, the influence of the underlying tissue layers were largely ignored within the FEMs and it was noted that these layers may play a significant role in the mechanical characteristics of skin during indentation (Pailler-Mattei et al., 2008). A study by Tran *et al*. in 2007 again used indentation methods to characterise the mechanical properties of human skin *in vivo*, using a multilayer FEM, incorporating the epidermis, dermis, hypodermis and underlying tissues. The deflection of the skin layers and tissues were imaged using MRI. The neo-Hookean parameters for all layers were then optimised to produce a best fit with experimental data. It was noted that the neo-Hookean model sufficiently described the mechanical characteristics of the three skin layers, but as only one indenter geometry was used, no validation of the extracted properties took place. Additionally, as larger indentation depths were examined, it may have been possible that at increased depth, the influence of the underlying tissues may have had a greater influence on the measurements. Thus the results may not be truly representative of the biomechanical properties of skin alone.

A study by Hendriks *et al*. in 2004 (Hendriks et al., 2004) imaged the deformation of human skin *in vivo* using OCT and ultrasound techniques, upon the application of suction. The pressure and deflection measurements were used to establish a single layer FEM of human skin and the Mooney material model was used. The model showed a good approximation for the stress - strain response of the tissue. In a later study by Hendriks *et al*. in 2006 (Hendriks et al., 2006), a two layered FEM of human skin, again under suction was established using the neo-Hookean constitutive model. Although the model worked well for some subjects, it was observed that the finite element software at that time was not able to allow for large deformations when using a two layer composite material to represent skin. Both investigations used suction cups of 1mm, 2mm and 6mm in diameter to characterise the material properties of skin *in vivo*. However, for both single and two layer FEM, different material parameters for each suction cup

diameter, relative to each volunteer were identified by the inverse analysis. This implies that the extracted material parameters for the neo-Hookean and Mooney model were not the definitive parameter set for each volunteer, as they do not describe the skin's response when using all three suction cups.
*Ex vivo* measurements have also been used as a basis for inverse FEM. In two studies by Shergold *et al*. in 2006 the Ogden and M-R material models were used to detail the mechanical characteristics of pig skin under uniaxial tension and compression (Shergold, Fleck and Radford, 2006b). Additionally, the Ogden material model was successfully used to represent *ex vivo* skin puncture using a flat bottomed punch (Shergold, Fleck and King, 2006a). It was shown that the Ogden material model could appropriately describe the stress - strain response of pig skin during uni-axial tension at high levels of strain hardening, much more adequately than the M-R model. In a recent study by Lapeer *et al*. in 2010 (Lapeer, Gasson and Karri, 2010), a series of tensile tests were performed on *ex vivo* human skin tissue. The stress - strain response of the tissue was matched with the Ogden material model, along with the general and reduced polynomial models, which are both derivatives of the Yeoh material model. Due to instabilities within the FEMs, only the reduced polynomial model was extensively tested, and was concluded to give a good agreement with experimental measurements.

An important characteristic of skin is that it wrinkles under compression and when the skin begins to lose its elasticity. As a result, some have developed theoretical models of wrinkling behaviour. In a study by Evans in 2009, a constitutive model based the Ogden model of hyperelasticity was developed which allowed for membrane wrinkling, similar to that found during in plane compression of skin. Skin wrinkling has also been simulated using a multilayered models (Thalmann et al., 2002) some of which have implemented different constitutive laws for each skin layer, where a strong agreement between computational and experimental data was noted (Flynn and McCormack, 2010). Additionally, modelling the creep response of the subcutaneous tissue has also been explored and validated against experimental measurements (Wu et al., 2006a). Moreover, viscoelastic components have been used to model scar contraction (Flynn and

McCormack, 2008b) and have been incorporated within simulations which detail other mechanical characteristics of soft tissues such as anisotropy. Thus creating a material model with both viscoelastic and anisotropic behaviour (Taylor et al., 2009).

Finite element analysis alone has numerous implications for modelling the mechanical behaviour of skin as it shows how manipulating certain material parameters or boundary conditions can affect the overall mechanical response of the simulated tissue. For example, in a study by Flynn and McCormack in 2010, it was shown that by altering the collagen fibre density or the moisture content of the SC within the model, skin wrinkles can vary in depth (Flynn and McCormack, 2010). Additionally, when correlated with experimental observations, it is possible to extract a set of material parameters from an appropriate constitutive model which can predict and describe the mechanical characteristics of complex soft tissues such as skin.

## 1.3 Discussion

The reviewed literature has highlighted the diversity of microneedle designs and applications currently studied. However, there are several areas which have not at present been extensively investigated. A key area is the effectiveness and reproducibility of microneedle puncture within skin. This requires a greater understanding of the mechanical characteristics of human skin *in vivo*. If the deflection of skin under low loads comparable to microneedle application were to be modelled, it could lead the way to manufacturing microneedle arrays based on experimental and model data which could potentially allow for uniform skin puncture across all needles within the array. Furthermore, many studies have applied a range of microneedle designs to *ex vivo* human and animal tissue, as well as *in vivo* human skin. However there appears to be large discrepancies within the measurements obtained. Whilst there has been some investigation into the absorption differences between *ex vivo* human and animal skins (Schmook, Meingassner and Billich, 2001), little recognition has been given to the

variations between the mechanical properties of *in vivo* and *ex vivo* skin with regard to microneedle penetration. One study which highlighted the importance of research towards understanding the mechanical characteristics of *in vivo* skin puncture by microneedles was conducted by Coulman *et al*. in 2011, where OCT was used to image the penetration mechanics of microneedles within human skin *in vivo*. While the testing of microneedle designs within *ex vivo* skin and animal models does serve an important purpose, the differences in the mechanical properties between *ex vivo* and *in vivo* tissues should be acknowledged and potentially accommodated for when conducting such studies.

The mechanical characteristics of skin are very complex and as a result many have used inverse analysis techniques to develop validated FEMs correlated against experimental observations. Such techniques could be used to accurately model small deformations *in vivo* comparable to microneedle administration. Whilst some studies have attempted to model microneedle application and insertion into skin (Roxhed et al., 2007; Kong and Wu, 2009; Kong et al., 2011) and silicone rubber (Aoyagi et al., 2008) using finite element techniques, all assumed the material properties of skin and silicone rubber from previous studies, and their findings were not validated against experimental measurements. Moreover, the FEMs of microneedle application to skin did not always take into account the subcutaneous tissues which contribute to skin deformation during load application.

Some have established multilayered FEMs of human skin *in vivo* using inverse techniques, but inaccuracies still remain within the resulting simulation. Additionally, the influence of the underlying tissues is largely ignored. There has been little attempt to link these models with the development of new and intuitive microneedle designs. One recent study which developed multilayer FEMs of skin with an ultimate aim to further understand microneedle penetration, was an investigation by Crichton *et al* (Crichton et al., 2011). This study used nanoindentation and inverse finite element methods using *ex vivo* murine ear skin to characterise the mechanical properties of the separated skin layers for the SC, epidermis and dermis. Although the inverse

techniques gave a strong agreement between experiment and model observations, the tested skin was again animal *ex vivo* tissue and the influence of the underlying layers were ignored. Additionally, the model provided measurements relating to each skin layer, rather than the entire skin tissue.

The majority of studies conducted into microneedle puncture have aimed to quantify the penetration capabilities of a single microneedle rather than the array as a whole. It is quite possible that array geometry could be just as, if not more, important for skin penetration. To allow microneedle devices to be used as an effective tool for drug delivery, it is important that the majority of the microneedles within the array penetrate to a sufficient depth. It has been noted that for flat arrays, the microneedles within the centre of the array penetrate superficially compared to those at the periphery (Coulman et al., 2011). Therefore, with the development of accurate and validated *in vivo* models of human skin deformation at loads comparable to microneedle application, it would be possible to develop curved arrays which follow the deformation of skin upon load application. Such a device could apply an equally distributed load onto each microneedle, possibly allowing for uniform and repeatable penetration.

This study therefore aims to address the current gaps in research regarding microneedle design and to allow for a better understanding of the mechanical properties of skin *in vivo* and *ex vivo*. Sections 1.4 & 5 will detail the aims and objective of this research, followed by a thesis summary.

## 1.4 Aims of the study

**Aim 1:** To quantify the mechanical properties of human skin *in vivo* under small levels of deformation which are comparable to microneedle application

**Aim 2:** Assess the different mechanical characteristics of human and murine *ex vivo* skin to suggest whether such tissues serve as an appropriate model for assessing microneedle puncture.

**Aim 3:** Develop microneedle array designs which can be applied to human skin *in vivo,* that potentially allow for uniform microneedle puncture across all the needles within the array.

**Aim 4:** Use the new microneedle design to preliminarily investigate whether repeatable observations can be made when applied to *ex vivo* skin, compared with analysis made using human skin *in vivo*.

# 1.5 Objectives of the study

To achieve these aims the following objectives were met:

**Objective 1: Experimentally examine the mechanical properties of skin**
Indentation measurements were obtained on human skin *in vivo* at small loads comparable to microneedle application. Furthering this, murine and human *ex vivo* skin was tested in tension, along three load axes to obtain anisotropic mechanical measurements.

**Objective 2: Develop FEMs of skin**
Using appropriate constitutive laws, two sets of FEMs were developed. Firstly, a multilayer FEM was established, which incorporated the epidermis, dermis and hypodermis. Secondly, an anisotropic model was developed to represent human and murine skin in tension

**Objective 3: Inverse analysis to further describe the mechanical properties of skin**
The material parameters within both sets of FEMs were matched with experimental observations using inverse analysis, where appropriate optimisation algorithms were chosen for each problem. The resulting parameters were used to further describe the mechanical properties of the examined tissues and create predicative models of skin deformation. Additionally, by comparing measurements of two single microneedles of varying geometries applied to the skin *in vivo* prior to penetration, with the predicative multilayer FEM, further validation of the inverse methods were achieved.

**Objective 4: Use the *in vivo* model of skin to develop a more rational microneedle array design**
By applying a pressure load comparable to microneedle array application to the multilayer model of human skin *in vivo*, the deformation shape of the skins surface was used to create a curved in plane array of microneedles. A

flat array was also designed to act as a control. Microneedle arrays were then fabricated from stainless steel sheets using wire cutting technologies. Furthermore, the FEM of a single microneedle applied to skin provided information regarding skin deformation, prior to microneedle puncture.

**Objective 5: Use the models and preliminary experiments to hypothesise whether *in vivo* measurements of skin penetration by microneedles can be replicated *ex vivo***

The curved and flat arrays were preliminarily tested in human skin *in vivo* using a methylene blue dye to determine whether the new design created uniform skin penetration across all microneedles compared to the flat arrays. Additionally, the curved and flat arrays were applied to *ex vivo* murine and human skin to demonstrate whether the measurements could potentially be repeatable in *ex vivo* tissues. This served as a possible validation of the comparisons made between the mechanical properties of human and murine skin previously examined.

# 1.6. Thesis summary

Table 1.2 shows the thesis summary for all experimental Chapters 2-5. Following which the conclusions and further work will be presented in Chapters 6 and 7.

Table 1.2: Thesis summary.

| **Chapter** | **Objective of Chapter** | **Skin examined** | |
|---|---|---|---|
| | | ***in vivo*** | ***ex vivo*** |
| **2** | Experimental observations | Indentation measurements on human skin at low loads to replicate microneedle application. | Uni-axial tensile tests on human and murine skin taken along three load axes. |
| **3** | Develop FEMs of skin | Following the dimensions of the *in vivo* test, a multilayered FEM of human skin was established, incorporating the epidermis, dermis and hypodermis. | Following the dimensions of the *ex vivo* test, an anisotropic model of human and murine skin in tension using fibre families to create anisotropic behaviour, was developed. |
| **4** | Inverse analysis to further describe the mechanical properties of skin | An optimisation loop was developed to extract the best set of material parameters which described the mechanical properties of human skin during indentation. | An optimisation loop was developed to extract the best set of material parameters which described the anisotropic mechanical properties of human and murine skin in tension. |
| **5** | Optimising microneedle array design | The model was further validated against *in vivo* measurements of a single microneedle applied to skin. Models of human skin deformation were used to design a curved array which followed the curvature of the skin. New curved and flat in plane microneedle array design was manufactured and preliminarily tested on human skin to assess skin puncture | Curved and flat in plane microneedle array designs were preliminarily tested in *ex vivo* human and murine skin to determine whether *in vivo* measurements could be replicated *ex vivo*. |

# CHAPTER 2

# MEASURING THE MECHANICAL PROPERTIES OF SKIN *IN VIVO* AND *EX VIVO*

## 2.1 Introduction

The mechanical behaviour of skin is very complex exhibiting nonlinear, anisotropic and viscoelastic properties. There are many applications, including the development of transdermal delivery devices, where an understanding of the mechanical characteristics of human and animal skin, *ex vivo* and *in vivo,* are required. Therefore this Chapter aims to address this problem by developing experiments to examine these characteristics.

When testing the penetration efficiency of microneedle designs or analysing the diffusion of therapeutic compounds delivered via microneedle arrays, such devices have been applied on human skin *in vivo* and *ex vivo.* However *ex vivo* human skin samples and ethical approval for clinical *in vivo* tests can be difficult to obtain, and when coupled with the increased risk of infection associated with handling human tissue, many favour the use of rodents such as mice to provide tissue samples and animal models. However, there are questions regarding the appropriateness of such replacement tissues and whether they can be used to truly represent the human *in vivo* equivalent. Furthermore, few have compared the differences in the mechanical properties of tissues such as skin when tested *in vivo* and *ex vivo* and along different planes.

This Chapter will detail experimental protocols that have been developed to characterise the mechanical properties of human skin *in vivo*, in addition to a series of analyses examining the mechanical behaviour of *ex vivo* human and murine tissues. *In vivo* measurements were made perpendicularly to the skin's surface using indentation measurements, as the approach analysed the characteristics of human skin in a manner which was comparable to microneedle application. Secondly, *ex vivo* assessments were made on human and murine skin samples in tension, and anisotropic properties were examined by altering the orientation of the load axis. Chapters 3 and 4 present the inverse finite element methods used to further examine the variations noted within these investigations.

## 2.2 Aims of the study

1. Establish a repeatable method of analysing human skin *in vivo* using indentation tests at small loads to assess tissue deformation, at forces which replicate those used during microneedle application.
2. Develop a uni-axial tensile testing method which could examine the mechanical characteristics of human and murine skin *ex vivo* along three load axes, to extract anisotropic measurements.
3. Quantify the Young's Modulus of human skin *in vivo* and the stiffness of murine and human skin *ex vivo*.

## 2.3 Measuring the mechanical properties of human skin *in vivo*

Indentation tests were used to assess the mechanical properties of human skin *in vivo* using two indenter geometries, to further explore the mechanical behaviour at applied loads of up to approximately 0.1N.

### 2.3.1 Experimental set up

To perform indentation tests, a servohydraulic testing machine (Losenhausen Maschinenbau, Dusseldorf) with an MTS FlexTest GT controller (MTS, Eden Prairie, Minnesota, USA), shown in Figure 2.1, was used to measure displacement. This was connected to a 5N load cell (Interface Force Measurements, Crowthorne, UK) with an accuracy of 0.5%. The system was displacement controlled but a limit was implemented so that when the load reached 0.1N, the test was terminated and the indenter returned to the original position. The two indenters, with varying geometries were attached to the 5N load cell. These included a spherical and a flat-bottomed cylindrical indenter with diameters of 1.5875mm and 0.5mm respectively, both manufactured from stainless steel.

*Figure 2.1: Servohydraulic testing machine and 5N load cell used to apply prescribed displacement to each indenter.*

### 2.3.2 Experimental protocol

The chosen skin site was the volar aspect of the right forearm, where the application point was measured at a distance of 35mm away from the centre of the forearm crease. This site is shown in Figure 2.2. During measurement, the arm was held still and at 90° by using two straps either side of the marked area of skin to prevent body movements. The experimental set up as described in Section 2.3.1 was used to apply a load of up to 0.1N to the skin site, where the reaction force on each indenter and the relative indentation depth was recorded. Five indentation cycles at a speed of 10mm/sec were performed on the forearm site for both of the indenter geometries, with a rest period of 30 seconds, to discount the viscoelastic behaviour of skin from the results. Each cycle was recorded by a control computer.

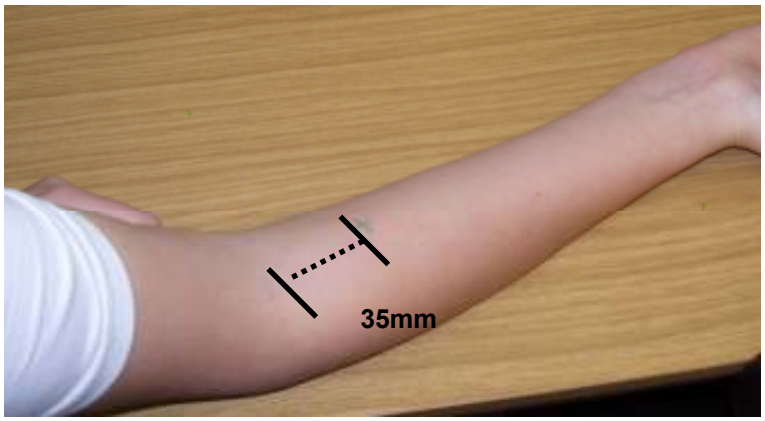


*Figure 2.2: Image of the test site on the volar aspect of the forearm indicating the location where the indenter was applied.*

### 2.3.3 Volunteer information

Studies using human volunteers were approved by the Cardiff University School of Engineering Ethics Committee (see Appendix E for information sheet). Following written consent from seven Caucasian volunteers within the student population at Cardiff University, the series of indentation tests were performed on the chosen skin site. Details of the human participants are presented in Table 2.1. The skin of all volunteers was checked to be free from scarring and imperfections.

Table 2.1: Age and sex of subjects used for *in vivo* skin indentation tests.

| ***Subject Number*** | ***1*** | ***2*** | ***3*** | ***4*** | ***5*** | ***6*** | ***7*** |
|---|---|---|---|---|---|---|---|
| ***Age (years)*** | 24 | 26 | 25 | 24 | 22 | 26 | 22 |
| ***Sex (M/F)*** | F | F | F | F | M | M | M |

## 2.3.4 Data analysis

The reaction force and relative indentation depth recorded for both indenter geometries, during the five indentation cycles, were documented for each volunteer. As the measurement proceeded to be recorded some time prior to the indenter contact with the skin, a common zero point was stipulated for all indention cycles using both indenters. This point was taken to be a load of 0.001N, which was the point where the gradient of the curve began to increase. There was also little noise on the measurements, so this small load could be used. The average measurement of the five indentation cycles for both indenters were recorded and filtered through a Butterworth low pass filter at a frequency of 0.1Hz, to reduce the fluctuations due to noise and body movements which occurred during the test. Results section 2.4.1 shows example plots of the unfiltered 5 indentation cycles and the noise at low loads for the indentation tests. This produced two plots comparing relative indentation depth to indentation force for both indenters, across all seven volunteers. The following observations were made

1. Influence of using two indenter geometries.
2. Comparisons between volunteers
3. Variations with other studies

Previous studies have used indentation measurements of human skin *in vivo* to calculate the Young's Modulus of the material. Although skin is a nonlinear material, hence does not conform to Hooke's law, researchers have still extracted the reduced Young's Modulus of skin at very low strain levels to

reduce the effects of exponential stiffening (Pailler-Mattéi and Zahouani, 2006; Pailler-Mattei et al., 2008; Zahouani et al., 2008). Equation 2.1 shows the reduced Young's Modulus, $E_R$, calculation where $K_N$ refers to stiffness of the skin which was equated as the gradient of the load - displacement curve, assuming that loading and unloading follow the same path. This is shown in Figure 2.3. The influence of the alteration to the indenter contact area on the skin as the indentation depth increases, is described using parameter $\sqrt{A}$, which is the projected area of the indentation at a given contact depth. This can be calculated for the spherical indenter by $A=\pi a^2$, where $a = \sqrt{\delta} r$ so that $\delta$ = indenter displacement, and flat bottomed cylindrical indenter is equated by $A=\pi r^2$, which is irrespective of indentation depth. Parameter $r$ is the radius of the indenter or the penetration depth for the spherical indenter. All symbols are detailed in the Nomenclature on page xi.

$$E_R = \frac{\sqrt{\pi}}{2}\frac{K_N}{\sqrt{A}} \qquad 2.1$$

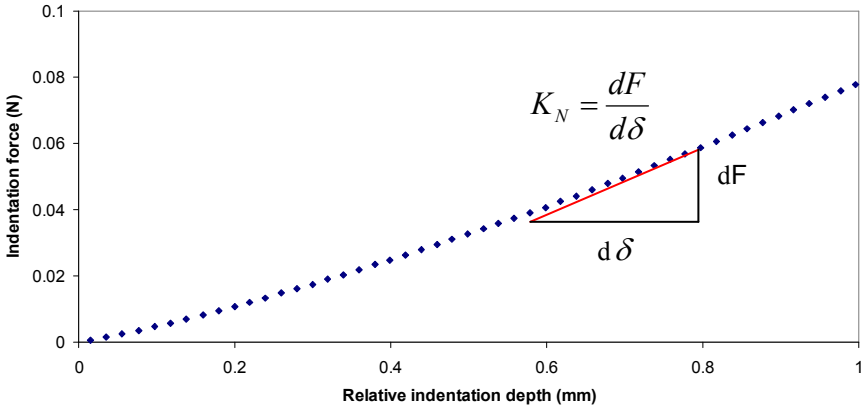


*Figure 2.3: Measurement of material stiffness value between 0.6 and 0.8 relative indentation depth extracted from load – displacement curve.*

Using Equation 2.2, the $E_R$ can be related to the Young's Modulus of skin, where $E_i$, $\nu_i$, $E_s$ and $\nu_s$ are the Young's Modulus and Poisson's ratio of the steel indenter and the *in vivo* skin respectively (Pailler-Mattéi and Zahouani, 2006; Pailler-Mattei et al., 2008; Zahouani et al., 2008).

$$\frac{1}{E_r} = \frac{1-\nu_s^2}{E_s} + \frac{1-\nu_i^2}{E_i} \qquad 2.2$$

As $E_i >> E_s$, Equation 2.2 can be reduced to Equation 2.3 to calculate the Young's Modulus of skin by removing the last term, where the Poisson's ratio of skin was assumed to be 0.4 (Maibach, Agache and Humbert, 2004).

$$E_s = \left(1-\nu_s^2\right)E_r \qquad 2.3$$

When considering the Young's Modulus value for human skin *in vivo,* only small levels of deformation were considered because skin exhibits nonlinear behaviour. Hence stiffness measurements were taken at increments to detail the change in Young's Modulus and stiffness upon increased indentation depth. Average measurements were then compared with published studies.

# 2.4 Results

In this section, data from *in vivo* indentation measurements performed on seven volunteers are presented. General characteristics are detailed by examining the load – displacement curves, followed by comparative Young's Modulus data with other published studies.

## 2.4.1 Load – displacement curves

Measurements comparing the reaction force to the relative indentation depth for the flat bottomed cylindrical and spherical indenter, for all seven volunteers are presented. Figure 2.4 shows an example graph of the raw load-displacement data prior to filtering for one of the indentation cycles at load of up to 0.3mm, to illustrate the noise present for all recordings. The application of the cylindrical indenter to the skin of volunteer 2 was selected for this graph, however all raw data showed a similar relationship. This plot shows very few fluctuations in the measurements; hence the noise from the system was

minimal. This was important as the loads measured during the experiments were extremely low.

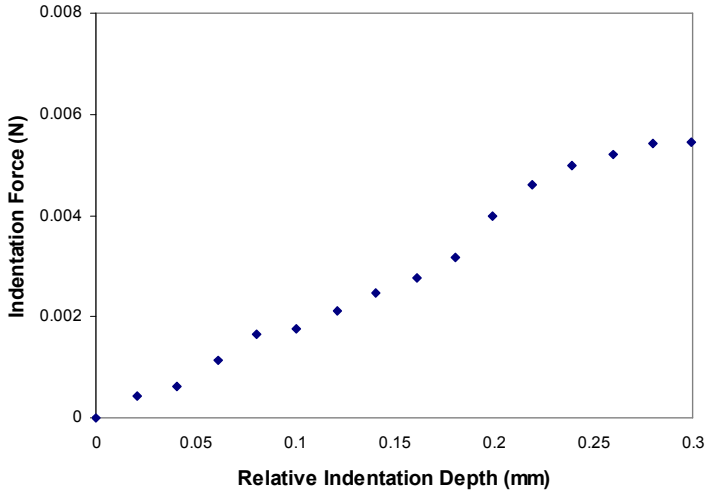


*Figure 2.4: Graph of raw data for one indentation cycle using the cylindrical indenter applied to the forearm of volunteer 2.*

Figure 2.5 shows the variation between the five indentation cycles for the application of the cylindrical and spherical indenters to the skin of volunteer 2. This graph illustrates that there was little variation between the five cycles, hence it was appropriate to take an average of the five. Additionally, it further suggests that the viscoelastic properties of the skin have not been reflected in these measurements.

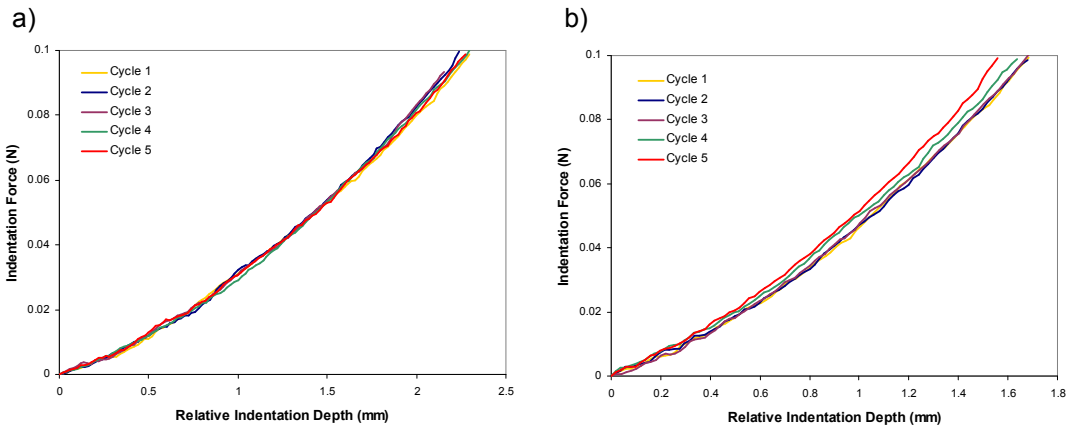


*Figure 2.5: Example graphs from volunteer 2, illustrating the spread across the five indentation cycles for the a) cylindrical and b) spherical indenters.*

Figure 2.6 illustrates the average load – displacement curves across all seven volunteers, comparing both indenter geometries. Additionally, the data spread is represented by the upper and lower standard deviation (SD) cross and square points respectively.

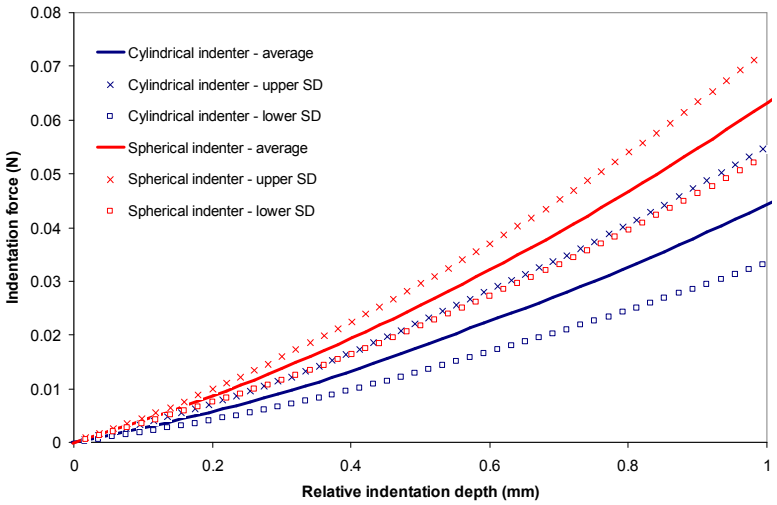


*Figure 2.6: Plot showing the mean relative indentation depth against indentation force for the cylindrical and spherical indenters, comparing all volunteers (N=7).*

Figure 2.7 shows the load – displacement curves for all volunteers, examining both indenter geometries at low levels of deformation comparable to microneedle application.

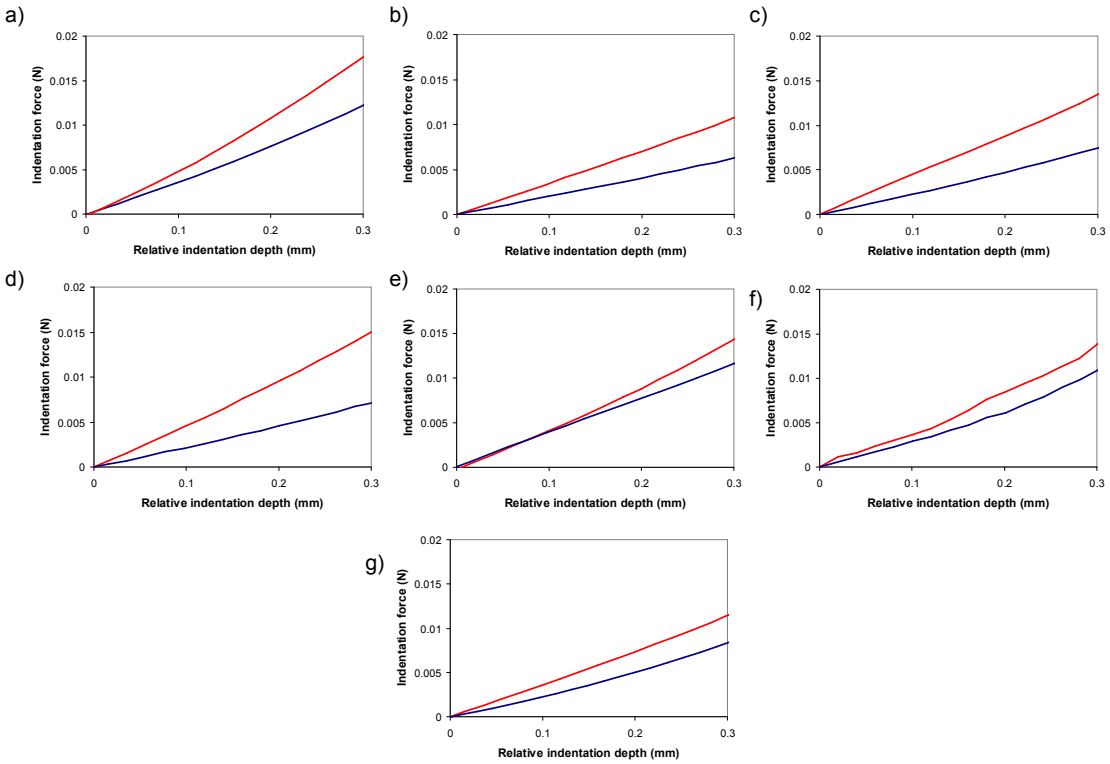


*Figure 2.7: Plots illustrating the relative indentation depth against indentation force for the two indenters applied to human skin in vivo at small levels of deformation. The blue and red lines show measurements from the cylindrical and spherical indenters respectively (Graphs a-g represent volunteers 1-7).*

Figure 2.8 illustrates the load – displacement curves for all seven volunteers, comparing the application of both indenter geometries to *in vivo* skin. These plots show that volunteer 1 has the stiffest skin as a greater load was induced upon the application of both indenters, compared to the other volunteers.

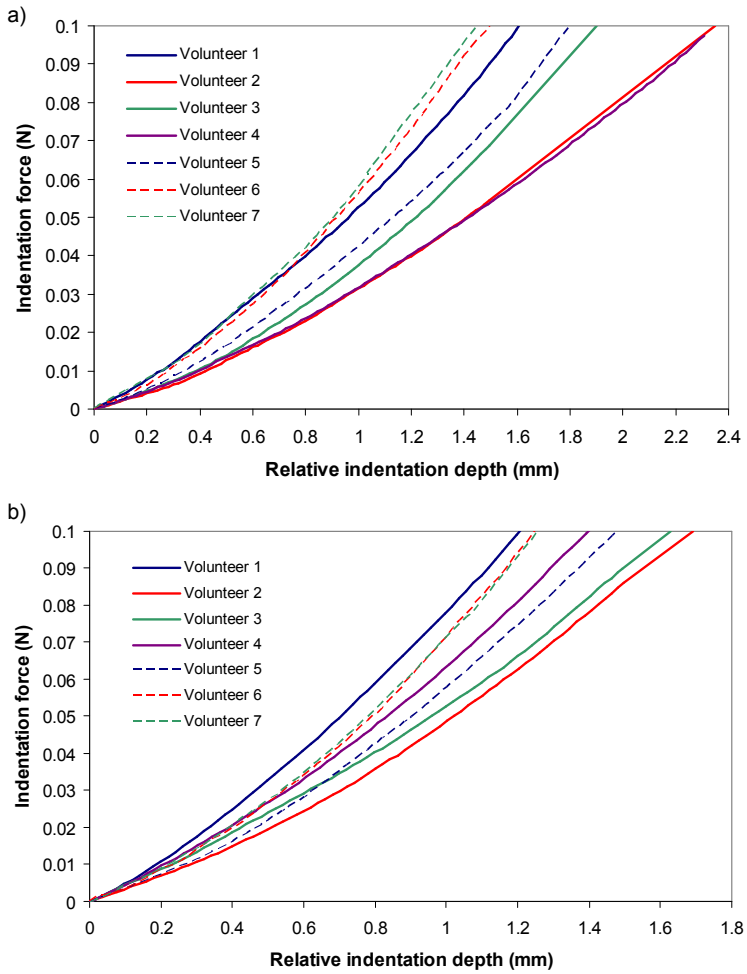


*Figure 2.8: Graphs illustrating relative indentation depth against indentation force for all seven subjects, comparing the application of a) the cylindrical and b) the spherical indenter to in vivo skin. The solid and dashed lines refer to female and male volunteers respectively.*

## 2.4.2. Young's Modulus of skin

Skin displays nonlinear stress - strain characteristics, therefore does not abide by Hooke's Law, but the Young's Modulus data collected in this study at low levels of deformation can be compared with other investigations and used to detail the variations between volunteers. It should be noted that the unloading and loading path taken during indentation measurements were assumed to be identical for all stiffness calculations.

### 2.4.2.1 *Comparison between volunteers*

Figure 2.9 shows the stiffness values, $K_N$, upon indentation loading across the seven volunteers, comparing both indenter geometries. The plots show the $K_N$ calculated at increments of 0.1mm at relative indentation depths up to 1mm, illustrating the change in stiffness during increased load application.

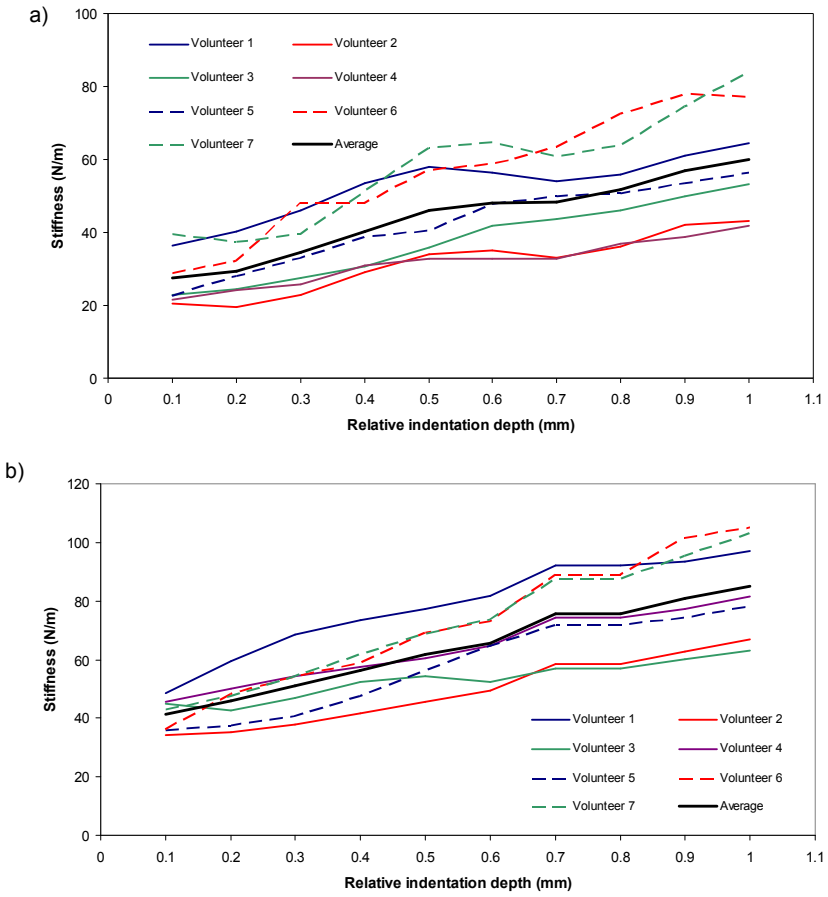


*Figure 2.9: Plots showing the stiffness of skin, $K_N$, compared to relative indentation depth for all seven volunteers, for a) the cylindrical and b) the spherical indenter. The solid and dashed lines refer to female and male volunteers respectively.*

Figure 2.10 illustrates the Young's Modulus calculated for skin, $E_s$, against relative indentation depth, for all seven volunteers, comparing both indenter geometries. There was a correlation between the $E_s$ values for the cylindrical and spherical indenters at 0.1mm relative indentation depth, as both are within the range of 30-70kPa. At this stage, the contact areas for both indenters correlate closely at 0.1963mm² and 0.2493mm² for the cylindrical and spherical indenter respectively.

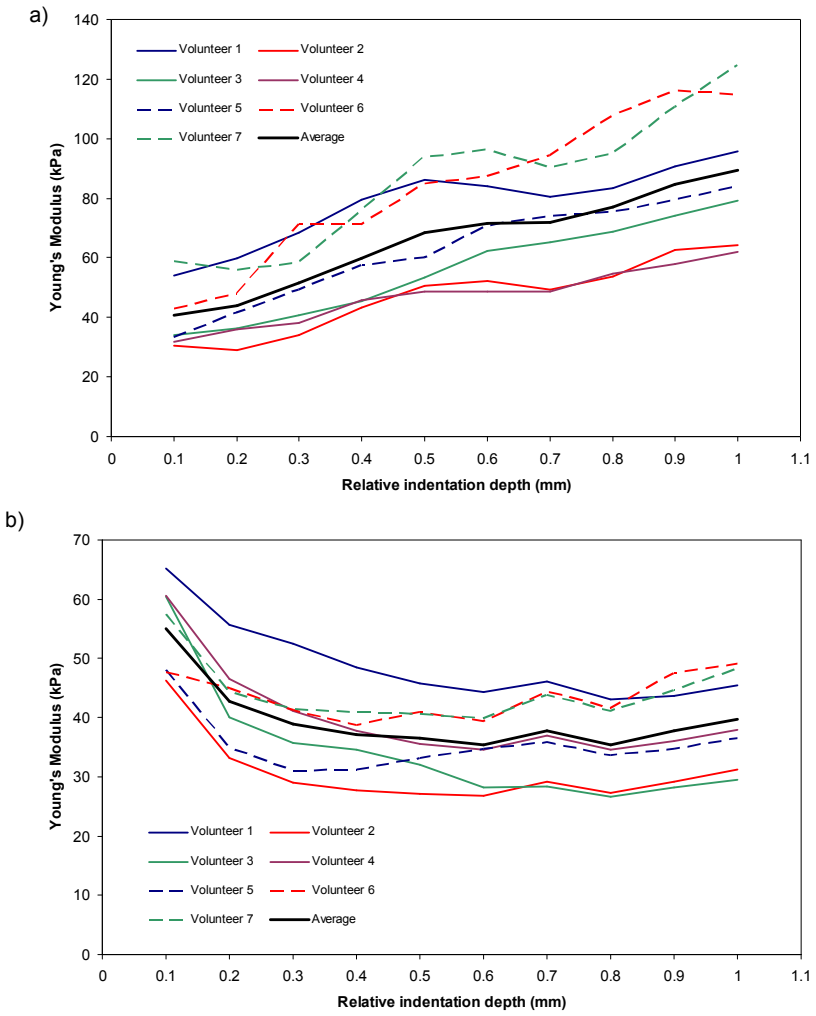


*Figure 2.10: Plots showing the apparent Young's Modulus of skin, $E_S$, compared to relative indentation depth for all seven volunteers, for a) the cylindrical and b) the spherical indenter. The solid and dashed lines refer to female and male volunteers respectively.*

Figure 2.11 shows the average Young's Modulus, $E_s$, and standard deviation values across all seven subjects, comparing the cylindrical and spherical indenters at indentation depth increments of 0.1mm. The cylindrical indenter has measured a higher average Young's Modulus and spread of data for *in vivo* skin compared to the spherical indenter, but at low levels of deformation, the average values show some correlation.

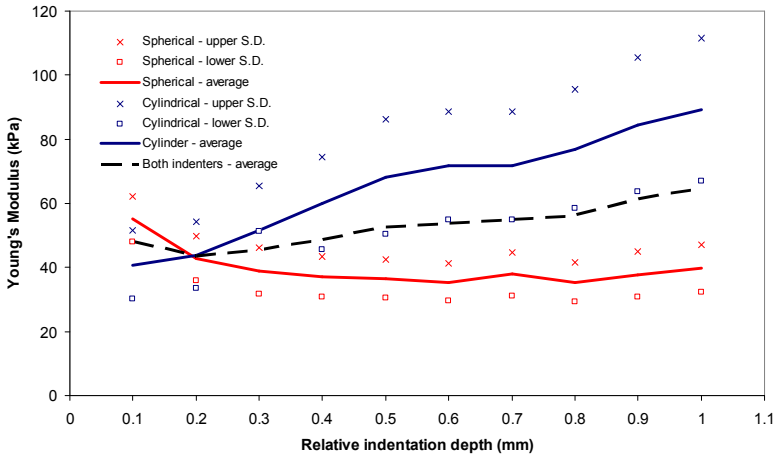


*Figure 2.11: Plot showing average apparent Young's modulus for the tested skin, $E_S$, and the standard deviation values, comparing measurement using the cylindrical and spherical indenters to an average of both.*

Table 2.2 shows the average Young's Modulus, reduced Young's Modulus and stiffness values for *in vivo* skin, relative to each indenter for all volunteers. These average parameters were calculated using the $E_S$, $E_R$ and $K_N$ obtained at increments of 0.1mm indentation depth between 0-1mm.

Table 2.2: Average Young's Modulus, reduced Young's Modulus and stiffness values for all volunteers.

| ***Volunteer*** | ***Spherical indenter*** | | | ***Cylindrical indenter*** | | |
|---|---|---|---|---|---|---|
| | **Average Young's Modulus, $E_S$, (kPa)** | **Average reduced Young's Modulus, $E_R$ (kPa)** | **Average stiffness, $K_N$ (N/m)** | **Average Young's Modulus, $E_S$, (kPa)** | **Average reduced Young's Modulus, $E_R$ (kPa)** | **Average stiffness, $K_N$ (N/m)** |
| ***1*** | 49.03 | 58.36 | 78.43 | 78.26 | 93.17 | 52.56 |
| ***2*** | 30.69 | 36.54 | 49.14 | 46.92 | 55.88 | 31.53 |
| ***3*** | 34.36 | 40.91 | 53.06 | 55.96 | 66.62 | 37.59 |
| ***4*** | 40.18 | 47.83 | 64.04 | 47.31 | 56.33 | 31.78 |
| ***5*** | 35.42 | 42.16 | 57.94 | 62.60 | 74.52 | 42.04 |
| ***6*** | 43.56 | 51.86 | 72.46 | 83.90 | 99.88 | 56.35 |
| ***7*** | 44.25 | 52.68 | 72.34 | 86.10 | 102.50 | 58.29 |
| ***Standard Deviation*** | **10.19** | **7.12** | **5.98** | **13.37** | **18.56** | **15.58** |
| **Average** | **39.64** | **47.19** | **63.92** | **65.86** | **78.41** | **44.31** |

### 2.4.2.2 Comparison with previously published studies

Table 2.3 compares the average parameters shown in Table 2.2 for the reduced Young's Modulus, Young's Modulus and stiffness of skin, with previous investigations which aimed to extract the same parameters for *in vivo* human skin using experimental data. This table shows that there was a wide range of values obtained, which appears to be largely related to the testing method.

Table 2.3: Average Young's Modulus and stiffness values for human skin from current study, compared to published studies conducted *in vivo* on human skin.

| ***Experimental method*** | ***Indenter Details*** | ***Young's Modulus $E_S$ (kPa)*** | ***Reduced Young's Modulus, $E_R$ (kPa)*** | ***Stiffness $K_N$ (N/m)*** | ***Reference*** |
|---|---|---|---|---|---|
| ***Indentation*** | ***Spherical (Ø = 1.5875mm)*** | ***39.64*** | ***47.19*** | ***63.92*** | ***Current study*** |
| | ***Cylinder (Ø = 0.5mm)*** | ***65.86*** | ***78.41*** | ***44.31*** | ***Current study*** |
| | Spherical (Ø = 6.35mm) | | 9.5 | | (Pailler-Mattéi and Zahouani, 2006) |
| | | | 7-8 | 25 | (Pailler-Mattei et al., 2007) |
| | Conical Indenter | | 12.5 | 24 | (Pailler-Mattei et al., 2008) |
| | | 1.53 | | | (Bader and Bowker, 1983) |
| | Spherical (Ø = 6.35mm) | | 8.3 | 42 | (Zahouani et al., 2009) |
| ***Suction*** | | 129 | | | (Diridollou et al., 2000) |
| | | 56 | | | (Hendriks et al., 2003) |
| ***Tension*** | | 4600-20000 | | | (Manschot and Brakkee, 1986) |
| ***Torsion*** | | 420-850 | | | (Agache et al., 1980) |
| ***Wave propagation*** | | 24.9-101.2 | | | (Liang and Boppart, 2010) |

Table 2.4 compares the Young's Modulus and reduced Young's Modulus calculated for the current study, with data obtained from *ex vivo* measurements. Values from *ex vivo* samples are significantly higher than those from the presented *in vivo* study.

Table 2.4: A Comparison between average *in vivo* measurements for reduced Young's modulus and Young's modulus from the presented study with published *ex vivo* data from human and animal donors.

| ***In vivo / Ex vivo*** | ***Skin layer*** | ***Young's Modulus $E_S$ (kPa)*** | ***Reduced Young's Modulus $E_R$ (kPa)*** | ***Skin details*** | ***Reference*** |
|---|---|---|---|---|---|
| ***In vivo*** | ***All*** | ***39.64*** | ***47.19*** | ***Human*** | ***Current study – Spherical indenter*** |
| | | ***65.86*** | ***78.41*** | ***Human*** | ***Current study – Cylindrical indenter*** |
| ***Ex vivo*** | SC | | 50000 | Porcine (dry) | (Yuan and Verma, 2006) |
| | | | 200000 | Porcine (hydrated) | |
| | | | 500000 | human | (Pailler-Mattei et al., 2007) |
| | | 1400 | | murine | (Crichton et al., 2011) |
| | Dermis | 1293 | | murine | |
| | Epidermis | 16130 | | murine | |

# 2.5 Discussion

This study applied indentation measurements, using two geometrically different indenters, to characterise the mechanical properties of human skin *in vivo*, at the volar aspect of the forearm. The raw data showed little noise, which was important as such low loads were measured and a starting point for all load-displacement curves was stipulated at 0.001N (Figure 2.4). The measurements were repeated five times using both indenters, across all subjects and an average reading was then presented and repeatability was apparent as all seven subjects and an example of which is shown in Figure 2.5. Additionally similar load – displacement curves for skin indentation was noted, resulting in corresponding standard deviation values for both the spherical and cylindrical indenters, was shown in Figure 2.6. Moreover, Figure 2.6 shows the load – displacement curves for both indentation measurements taken on all subjects, illustrating that the spherical indenter applied a higher load on the skin compared to the smaller cylindrical indenter for all. This was to be expected as a greater surface area was in contact with the skin when applying the spherical indenter.

Analysing the mechanical characteristics of skin using indentation measurements has provided a method of testing the skin which was comparable to microneedle application, and has provided repeatable measurements across a range of volunteers. However it should be noted that there were limitations to this method. As the measurements were taken *in vivo,* the response of the underlying hypodermis and tissues cannot be removed. Consequently inverse analysis needed to consider this contribution. Further validation of the displacement measurements could have been obtained by using imaging techniques such as OCT (Lim et al., 2008; Liang and Boppart, 2010), MRI (Tran et al., 2007) and ultrasound (Hendriks et al., 2006; Delalleau et al., 2008b), in addition to characterising skin layer thicknesses, which could have also been used within the inverse calculations in Chapter 4.

All skin sites were measured and marked on each volunteer, but as the site chosen was relatively close to a bony area, some recordings may have been more affected by the influence of the underlying bone. A method of reducing the influence of the underlying tissues on the results is to only model small deformations as such measurements would be principally related to the mechanical response of the upper skin layers.

Whilst the skin of all volunteers was checked for scarring and imperfections, variations within the skin's anatomy may have impacted the data. Moreover, as the data was taken *in vivo*, the influence of body movements during indentation could have affected the final measurements. However as the arm was constrained and the indentation test was applied at relatively high speed, the influence of such fluctuations were limited, and any remaining anomalies were filtered using a Butterworth filter. Additionally, even though the skin site chosen was relatively flat, there is a slight curvature on the volar aspect of the forearm, and as a result, the indenter may have initially touched the skin at an angle, consequently influencing the initial recordings. Whilst every effort was made to maintain experimental consistency between volunteers, some variability may have arisen but these appear to be limited as few anomalies were found within the measurements obtained.

The data obtained allowed for basic interpretation, prior to inverse analysis. Figure 2.7 illustrates the relative indentation depth against indentation force measurements for each volunteer, comparing both indenter geometries at low levels of deformation (maximum of 0.3mm). The volunteer's skin which induced the highest load upon the application of both indenters to skin, was subject 1, and volunteer 2 induced the lowest load, shown in Figure 2.8. Thus, suggesting volunteer 1 had the stiffest skin and volunteer 2 had the softest. Although the measurements did show slight variability between the mechanical properties of skin from all volunteers, the general behaviour appears to be similar from Figure 2.7. All volunteers show an almost linear load – displacement response for the tested skin, which was most likely due to the low maximum load implemented during testing. Consequently exponential stiffening may not be apparent at the tested levels of deformation. However, a slightly more nonlinear response was noted when applying the cylindrical indenter to the skin when compared with the larger spherical indenter, which may be related to the differences in the indenter geometries. This could imply that different microneedle geometries may induce different load – displacement characteristics.

The observations noted from the load – displacement curves of skin indentation also correlate with the stiffness values calculated with increasing indentation depths, shown in Figure 2.9. Both indenters show greater stiffness upon increased relative indentation depths of both indenters. Again, volunteer 1 shows increased skin stiffness compared to other subjects, and volunteer 2 illustrates lower stiffness, upon the application of both indenters. The stiffness measurements for the cylindrical and spherical indenters for all seven volunteers do appear to show a correlation, as those volunteers detailing the highest stiffness for the spherical indenter, are also shown for the cylindrical indenter. This again implies the approach used gives repeatable results as similar observations were noted when applying both indenter geometries. However, Figure 2.9 indicates that volunteers 6 and 7 had higher skin stiffness measurements upon increasing indentation depth, which was a conclusion not observed when analysing the load – displacement data alone.

The plot also demonstrates that volunteer 5 had the closest match with the average skin stiffness values, calculated across all seven volunteers.

Many studies have used indentation measurements to calculate the Young's Modulus of skin. As the skin is a nonlinear material this representation may not be appropriate. However such measurements allow for a comparison between this current study and published investigations, as well as helping to further detail the inter-individual differences in the mechanical properties of human skin. Figure 2.10 a) shows an increase in Young's Modulus with heightened relative indentation depth. This relationship is not apparent for the spherical indenter, which exhibited an initial lowering in Young's Modulus with increasing indentation depth. This may be because the adhesive properties of skin were ignored within this analysis and the contact area increases (Pailler-Mattéi and Zahouani, 2006), or because the skin is a complex nonlinear, anisotropic, stratified tissue and the estimated Young's Modulus values cannot accurately represent this behaviour. However, the general relationship between the mechanical properties of skin, previously noted from all seven volunteers remains unchanged when compared with the stiffness and load – displacement values. This suggests that the Young's Modulus calculations obtained can be used as a simplistic means of comparing the skin properties of volunteers. It was also possible that the variations noted in the Young's Modulus between indenters and indentation depths may be because different indenter geometries, at different depths, may be measuring the mechanical properties of individual skin layers, rather than the skin as a whole tissue.

The average Young's Modulus values for skin, comparing the measurements taken from the cylindrical and spherical indenters are shown in Figure 2.11. This plot also illustrates the average Young's Modulus value for both indenters, which show an almost linear relationship, which is not related to indentation depth. This could suggest that each indenter may be analysing different layers of the skin, which average out to give a consistent mechanical response. However, it should be noted that as both indenters were testing the same material, it would be expected that both should give similar results for

the Young's Modulus, therefore it is possible that this method of analysis is not appropriate for skin.

Table 2.2 shows the average Young's Modulus, reduced Young's Modulus and stiffness of skin for each volunteer. There appears to be little variation between subjects, but again subjects 1, 6 and 7 had the stiffest skin, where as subject 2 appears to have the softest. It does show that there is little variation between subjects with few anomalies as shown by the standard deviation calculations, implying the methods of testing were reliable.

Table 2.3 compares the average Young's Modulus, reduced Young's Modulus and stiffness values, across all indentation depths and volunteers for the cylindrical and spherical indenters, to other *in vivo* measurements of the mechanical properties of skin. It is clear from this table that there were large differences between this current study and previous studies. For the reduced Young's modulus and stiffness calculations obtained from this study, there was a 7-11 times and a 2-3 times increase respectively, compared to previously published investigations. This may be because the stiffness was calculated at increments and the loading and unloading cycles were assumed to be identical for all measurements within this study. It should be noted that those studies which used indentation to measure the skins' properties, applied larger indenters to the forearm skin. Hence, this may have resulted in the variations between the presented and published studies. When analysing the Young's Modulus of skin, the values obtained for this investigation were much more similar to those measured in suction experiments and wave propagation analysis. Those experiments which show a higher Young's Modulus calculation occurred when the skin was tested in plane using torsion and tensile tests. The wide range of values retrieved from previous studies imply that calculating the Young's Modulus may not be an appropriate method of analysing the mechanical behaviour of complex soft solids such as skin, or simply that the mechanical properties of skin does vary considerably between volunteers and testing methods. However, this study does indicate that there was little variability between the seven subjects tested.

Table 2.4 compares the Young's Modulus and reduced Young's Modulus values obtained from *ex vivo* indentation measurements on human and animal skin, compared to those found in the current study. For each separate layer, the Young's Modulus of *ex vivo* murine skin was calculated to be between 20-250 times higher than that calculated within this *in vivo* investigation. This margin was even larger when comparing *ex vivo* human SC tissue to *in vivo* skin, which was 100,000 times higher for *ex vivo* analysis. These variations were most likely due to the lack of underlying tissue present during *ex vivo* measurements. Although the considerably higher Young's modulus values obtained from *ex vivo* samples imply an increased stiffness, it may be possible that when considering microneedle puncture, a lower stiffness would be less desirable as the skin may deform around the needle, rather then penetrating the tissue.

In conclusion, this study has presented a repeatable and robust method of testing human skin *in vivo* using indentation measurements, which have allowed for further interpretation. The Young's Modulus values have facilitated further comparisons between subjects and other studies, but it is difficult to make solid conclusions from these values as the constitutive equations involved did not account for the skins multilayer, anisotropic and nonlinear properties. Additionally, when comparing *in vivo* measurements, from this study to other published data, large variations were noted depending upon the method of testing. Also, *in vivo* and *ex vivo* indentation measurements again show significant differences between the two skin tissues. This implies that different observations would be found when applying microneedle devices to *ex vivo* tissue, apposed to *in vivo* skin. Consequently, such variations should be accounted for when assessing microneedle puncture *ex vivo.* Further analysis should acknowledge the nonlinear behaviour of skin, in addition to considering the effects of all skin layers on the over all mechanical properties of human *in vivo* skin during indentation.

# 2.6 Measuring the mechanical properties of human and murine skin *ex vivo*

Tensile tests were chosen to examine the mechanical properties of human and murine skin *ex vivo*. This allowed for anisotropic measurements to be acquired as the orientation of the load axis could be altered, thus indicating the differences in the mechanical characteristics along different trajectories. This had particular significance as the dermis consists of a matrix of collagen and elastin fibres which influence the anisotropic nature of skin.

## 2.6.1 Skin specimen selection

In total, 8 human and 14 murine skin samples were tested from 2 and 8 donors respectively. Two large human skin samples were obtained after mastectomy surgery with informed consent and the appropriate ethical approval, and 8 mice were obtained post sacrifice. Both human donors were Caucasian females, aged 68 and 56 years. There was no age, weight or gender details for the murine donors, however all were adult mice. All skin samples were checked to be free from damage, scarring, moles, disease or other imperfections which could affect the mechanical properties. Table 2.5 shows a summary of the donor details.

Table 2.5: A summary of the donors used to create the skin specimens.

| | ***Donor number*** | ***Age (years)*** | ***Prior storage arrangements*** | ***Number of specimens collected*** |
|---|---|---|---|---|
| ***Human*** | 1 | 68 | Extracted on 18/6/2010 – frozen on day of collection | *4* |
| | 2 | 56 | Extracted on 20/4/2010 – frozen on day of collection | *4* |
| ***Mouse*** | 1 | unknown | All mice were frozen whole on the day of sacrifice | *2* |
| | 2 | | | *2* |
| | 3 | | | *2* |
| | 4 | | | *1* |
| | 5 | | | *2* |
| | 6 | | | *2* |
| | 7 | | | *2* |
| | 8 | | | *1* |

All samples were frozen on the day of sacrifice, in the case of murine skin, or the day of surgery, in the case of human skin. As the dermis is the layer that provides most of the mechanical support during in plane tension, the hypodermis was subsequently removed from all skin samples. It was however decided that the epidermis should not be removed as the separation methods such as heat, ionic and mechanical can also destroy or damage the dermis. The epidermis may also contribute significantly to the stiffness of the skin.

## 2.6.2 Specimen preparation

For human skin donors the sample was thoroughly defrosted, and using a razor blade, the layer of fat was carefully removed ensuring that the dermis was not damaged during the separation. Each sample was then laid flat dermis side down onto a piece of aluminium foil to prevent the skin from curling or drying. Using a template, four circular samples of human skin 31mm in diameter were cut in a parallel line across the rectangular samples for donors 1 and 2, which were numbered from 1 to 4. All human skin work was conducted in an isolated cabinet within a containment 2 facility. As the mice were frozen whole, the entire animal was defrosted and then the hair was removed using hair removal cream (Veet®, Slough, UK). The area of skin on the back between the head and the tail extending to the legs was then removed, shown in Figure 2.12. Using a razor blade, the dermis was carefully peeled away from the underlying tissue, again ensuring that the dermis was not damaged. The skin sample was then laid dermis side down, onto a sheet of aluminium foil to keep the skin flat and taut. Two samples, 31mm in diameter, were removed along the midline, labelled upper back (UB) and lower back (LB) as shown in Figure 2.10. For murine donors 4 and 8, only one specimen could be removed for testing due to scarring, therefore this was taken from the site located on the UB.

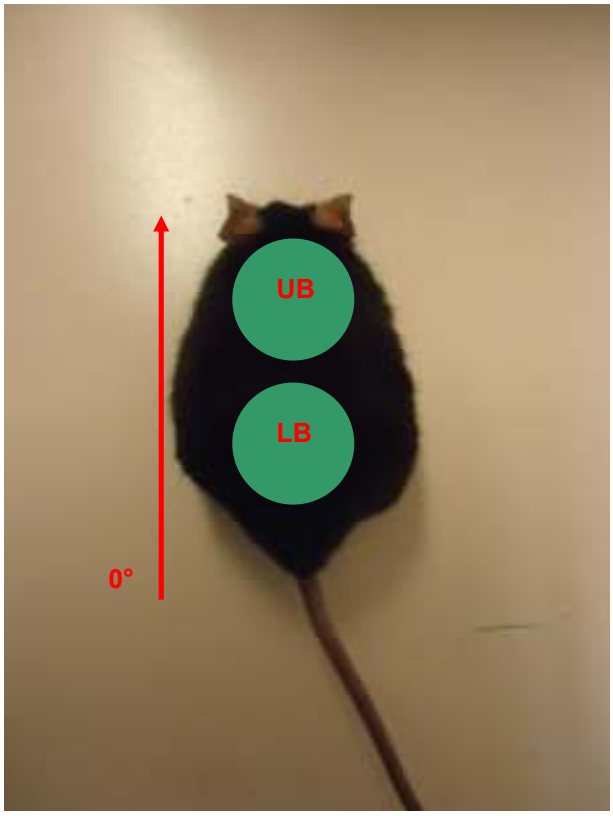


*Figure 2.12: Murine skin sites where the UB and LB samples are indicated by a green circle and the 0° axis is shown in red.*

To test anisotropy it was important to determine a common global coordinate system for each donor. The human skin samples were received without record of their orientation, hence an arbitrary axis was defined which was common for all specimens, taken from the same human donor. A single piece of skin was used to prepare the four specimens, making it possible to compare the properties of the four skin samples from each donor. As all mice were frozen whole, a common coordinate system for all murine skin samples from all donors was specified. This was taken to be along the spine of the animal pointing in the cranial direction as shown in Figure 2.12. Figure 2.13 details the orientation of the axes chosen for loading during the tensile tests, common for all specimens from all donors.

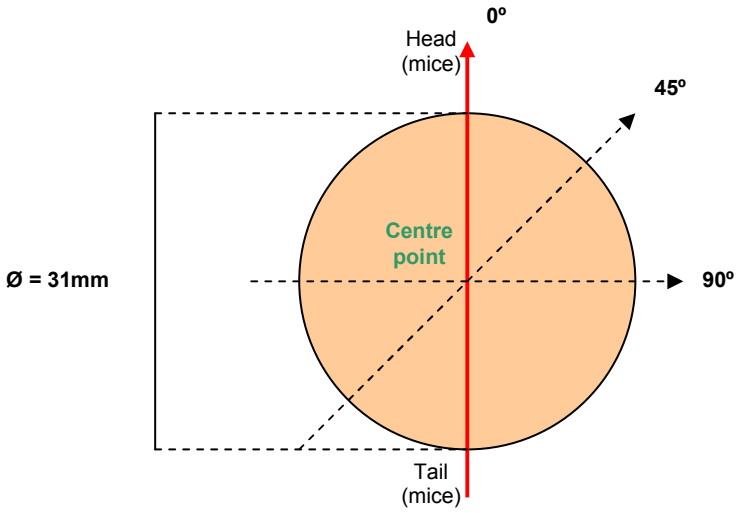


*Figure 2.13: Diagram to show the dimensions of the human and mouse skin specimens with load axis orientation (epidermis side up).*

After the specimens were collected, the 0º, 45° and 90° axes were clearly marked on each sample which was then re-frozen. Due to the time taken to prepare each sample, it was difficult to extract a sample and test within the same day, so all samples were prepared and frozen ready for testing at a later date. It was assumed that the refreezing process had little impact on the mechanical properties of the tissue (Moon et al., 2005). This approach maintained the experimental consistency between all human and murine samples.

## 2.6.3 Experimental setup

### *2.6.3.1 Tensile testing machine*

A bespoke Zwick® tensile test machine (Zwick® Testing Machines LTD, Herefordshire, UK), which had a total height low enough to be positioned within a laminar flow hood, was used to carry out the tensile tests. Figure 2.14 shows the testing machine set up used throughout the study. A load cell which could measure up to a maximum of 5N was chosen as it allowed for sensitive measurements within an accuracy level of 0.4%. The system and load cell were calibrated *in situ* by the manufacturer.

*Figure 2.14: Image of Zwick® testing machine used to apply tensile loads to human and murine ex vivo skin samples.*

Using the software package testXpert® II (Zwick® Testing Machines Ltd, Herefordshire, UK), the specification for the test was detailed, including the testing limits. Once the test had been performed the program outputted the relevant data, ready for analysis

### *2.6.3.2 Grips used for tensile tests*

It is notoriously difficult to clamp soft tissue samples within a standard grip. Therefore purpose built grips, that could not only hold the skin whilst performing the test but could also affix to the tensile machine, were developed. Additionally clamps that can apply a constant pressure as the thickness changes during tensile loading were needed, therefore spring clips were used with the addition of flat 2x15mm jaw faces as shown in Figure 2.15.

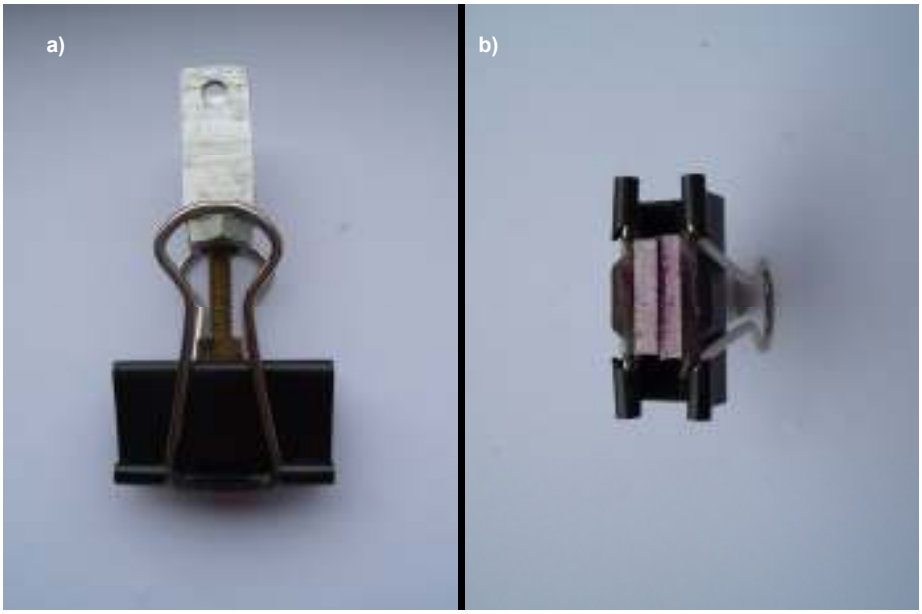


*Figure 2.15: Image of the grips used to grasp the skin specimen during the tensile tests where a) shows the grips in detail and b) illustrates how the inner jaws were adapted.*

To ensure the grips were strong enough to hold a skin sample in place, latex rubber was firstly clamped within the grips. Tension was then applied to the rubber using the grips and any slippage of the material within the clamps was noted. It could be seen from this test that no slippage or damage to the material occurred, implying the grips were strong enough to hold a thin material such as murine skin, whilst applying a tensile load

#### *2.6.3.3 Precautions taken whilst handling human tissue*

All tests on human skin were performed in Level II containment conditions to minimise any risk of infection.

### 2.6.4 Experimental protocol

The skin was thoroughly defrosted prior to examination and two specimens were tested simultaneously in one session. Whilst one sample was tested, the other was kept hydrated in physiological saline solution. The tested specimen, dermis side down, was laid across two overlapping pieces of foil where the split between the two pieces was perpendicular to the loading axis.

This prevented the skin from curling, reduced the drying rate and reduced deformation of the specimen making it possible to accurately place the grips. The grips were firstly attached to the specimen before connected to the testing machine as it was easier to accurately position the grips. Both grips were affixed in line with the desired load axis at 7.5mm either side of the central point (Figure 2.13), with the aid of a template. Both grips with the skin sample clamped between them were then attached to the Zwick® testing machine and the foil was peeled away from the sample.

The displacement was manually adjusted to bring the initial load to zero before testing. All tensile tests were carried out at a speed of 25mm/min with an upper force limit of 2N and a maximum extension of 30mm. After each tensile test was performed, the grip separation was returned to the start position. The samples were preconditioned by cyclically loading five times, with a rest period of 30 seconds between cycles, which was sufficient for the load – displacement curves to reach a steady state. When the first of the two specimens had been tested along one of the three load axes, the tested sample was placed in the PBS solution, whilst the other specimen was examined. This ensured that both were treated identically, whereby each sample was rehydrated after each test. Additionally, by maintaining the skin in the PBS solution for a similar amount of time, the swelling effects on the tissue was consistent for every sample. Specimens were tested using the same protocol in the 0, 45 and 90° directions, with a maximum load of 2N to ensure that no permanent deformation occurred.

### 2.6.5 Data analysis

During the initial stages of testing, all specimens were in no tension; consequently all measurements taken at this point have no relevance. As a result, a common starting point was specified, which was taken to be a load of 0.01N for all tensile tests, as this was the point where the gradient of the curve began to increase, suggesting the skin was in tension. This value was identical for both human and murine skin to ensure that the results could be

directly compared and as the cut off load was low, the influence of the variations in failure loads of both human and murine skin was small. Additionally all measurements were taken from the final cyclic load applied to the specimen, as the skin was assumed to be fully preconditioned at this stage, based on preliminary tests.

The following behaviours were observed:

1. The preconditioning behaviour
2. Nonlinear and anisotropic properties
3. Linear stiffness and length of phase 1

Figure 2.16 shows the typical J shaped force – displacement curve for *ex vivo* skin tissue under applied tension. Different donors, samples and load axes orientations were compared. The red line shown on Figure 2.16 highlights the gradient of the final linear phase of the load – displacement curve, which is described as the linear stiffness. The green arrow refers to the length of phase 1 characterised by high, almost linear, extension at low loads. Both basic characteristics can be used to analyse the tensile properties of the skin sample. The length of phase 1 was taken as the point from zero to where the linear portion begins to turn nonlinear, and the start of phase 3 was defined as the point at which the nonlinear phase turned linear.

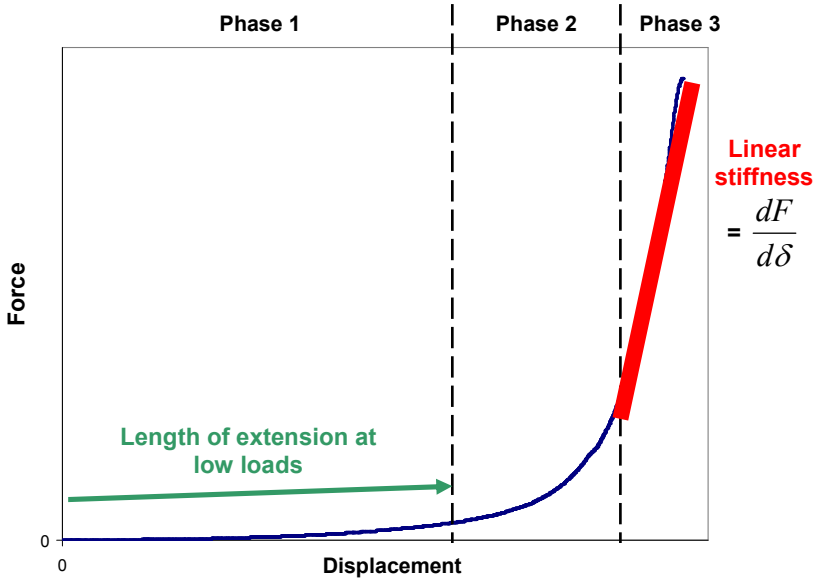


*Figure 2.16: Analysis of the tensile properties of human and murine ex vivo skin tissue.*

## 2.6.6 Histological examination

When describing the mechanical behaviours of a tissue, it is important to consider anatomical characteristics as this may provide further details useful for analysis. This includes factors such as the thickness of the tissue and its constituent layers, collagen density and microscopic imperfections. Therefore after tensile testing, a selection of human and murine *ex vivo* skin was preserved for histological examination.

Skin samples were selected for histological analysis from three murine and both human donors after tensile testing. Table 2.6 shows details regarding the skin samples chosen.

Table 2.6: Murine and human *ex vivo* skin samples used in histology examination post testing.

| ***Mouse / Human*** | ***Donor number*** | ***Location*** |
|---|---|---|
| ***Mouse*** | 5 | LB |
| | 6 | LB |
| | 7 | LB |
| ***Human*** | 1 | Sample number 4 |
| | 2 | Sample number 4 |

One skin sample was taken along the 0º load axis in the centre of the tissue, which measured less than 4mm², from each sample listed in Table 2.6. All were placed in formaldehyde solution for at least two months to preserve the tissue. After this period, all traces of formaldehyde were subsequently removed by rinsing the samples through an ethanol in water gradient, to extract any water still present within the tissue. This was achieved by immersing the skin samples in the following solutions:

1. 30% ethanol in distilled water (2 hours)
2. 50% ethanol in distilled water (2 hours)
3. 70% ethanol in distilled water (4 hours)
4. 95% ethanol in distilled water (3 hours)

5. 100% ethanol (2 hours)
6. Xylene (<1 hour)
7. Parafin (<1 hour)

Following dehydration, all specimens were solidified within paraffin wax, making it possible to externally embed the samples. All skin sections were placed within a mould along with the paraffin wax and orientated so that the transverse section could be analysed. This substance then hardened and stored below -2ºC to prevent the paraffin wax from softening.

Using a microtome, samples were sliced into 10μm transverse sections and mounted onto glass slides. The skin was then rehydrated and stained to distinguish the tissue structure. To achieve this, the samples required rehydration in an ethanol and water gradient by immersing the sections in the following solutions

1. Xylene (2 minutes, 3 times)
2. 100% ethanol (2 minutes, 2 times)
3. 90% ethanol in distilled water (2 minutes, 2 times)
4. 70% ethanol in distilled water (2 minutes, 2 times)
5. 50% ethanol in distilled water (2 minutes, 2 times)
6. 30% ethanol in distilled water (2 minutes, 2 times)
7. deionised water (2 minutes, 2 times)

A haematoxylin and eosin staining agent was applied to distinguish the SC from the epidermal and dermal tissue by submerging the section into the following solutions

1. tap water (4-5 dips)
2. haematoxylin (2 minutes)
3. tap water (4-5 dips)
4. alcohol / acid (1 dip)
5. tap water (4-5 dips)
6. Eosin (1 dip)
7. rinse in tap water (1 minute)
8. tap water (10 minutes)

Images were taken using a microscope (Olympus BX50, Essex, UK) and a graticule was used to provide a scale bar

# 2.7. Results

Principal observations relating to the mechanical characteristics of *ex vivo* human and murine skin will be shown, in addition to histological examination of a selection of skin samples.

## 2.7.1 Preconditioning

As discussed previously, skin is subjected to preconditioning where the stress-strain relationship alters throughout a series of cyclic loads until reaching a steady state. Figure 2.17 shows an example of the load – displacement curves, comparing all five tensile load cycles, for skin from murine donor 1 (LB) and from human donor 2 (sample 1), both measured along the 0º axis. The influence of preconditioning can be seen clearly across both example skin samples, as a steady state is reached after five cycles. (Note that measurements shown in both plots were not been taken from a small load of 0.01N, as with all other data. See Section 2.6.5)

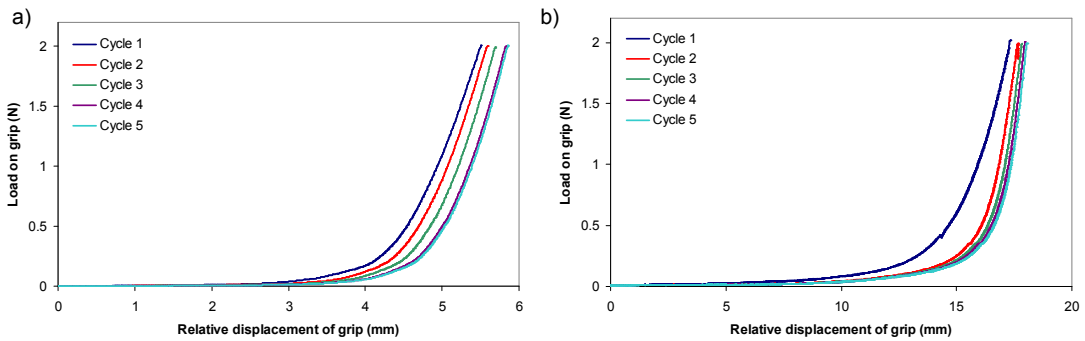


*Figure 2.17: Example plots illustrating the load – displacement curves upon loading across all five tensile cycles for a) murine skin sample taken from donor 1 (UB) and b) human skin sample extracted from donor 2 (sample 1), along the 0º axes.*

## 2.7.2 Load-displacement curves

Figures 2.18 and 2.19 show the load - displacement data obtained from tensile measurements for each murine and human skin sample respectively, at 0º, 45º and 90º degrees. Both demonstrate the level of anisotropic and nonlinear mechanical behaviour expressed within all tested murine and human skin samples under tensile load. All illustrate the same J shaped load-displacement curve, but the amount of anisotropy appears to be a characteristic related to each donor, and potentially the load axis orientation. The key variation between human and murine skin appears to be the amount of extension experienced at low loads, hence the length of phase 1.

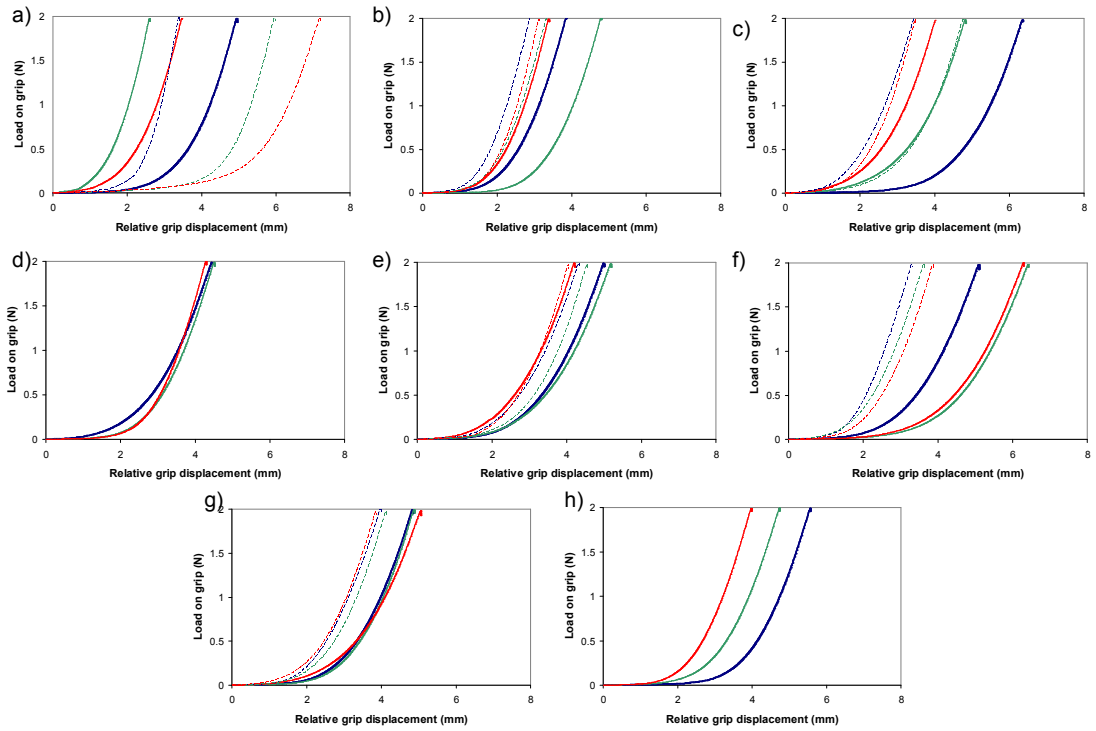


*Figure 2.18: Plots illustrating the tensile load on the grip against relative grip displacement when loaded at an orientation of 0º, 45º and 90º, shown in blue, green and red respectively, for all murine donors. (Samples taken from the UB are shown by a solid line, and those from the LB by the dashed line, graphs a-h represent donors 1-8).*

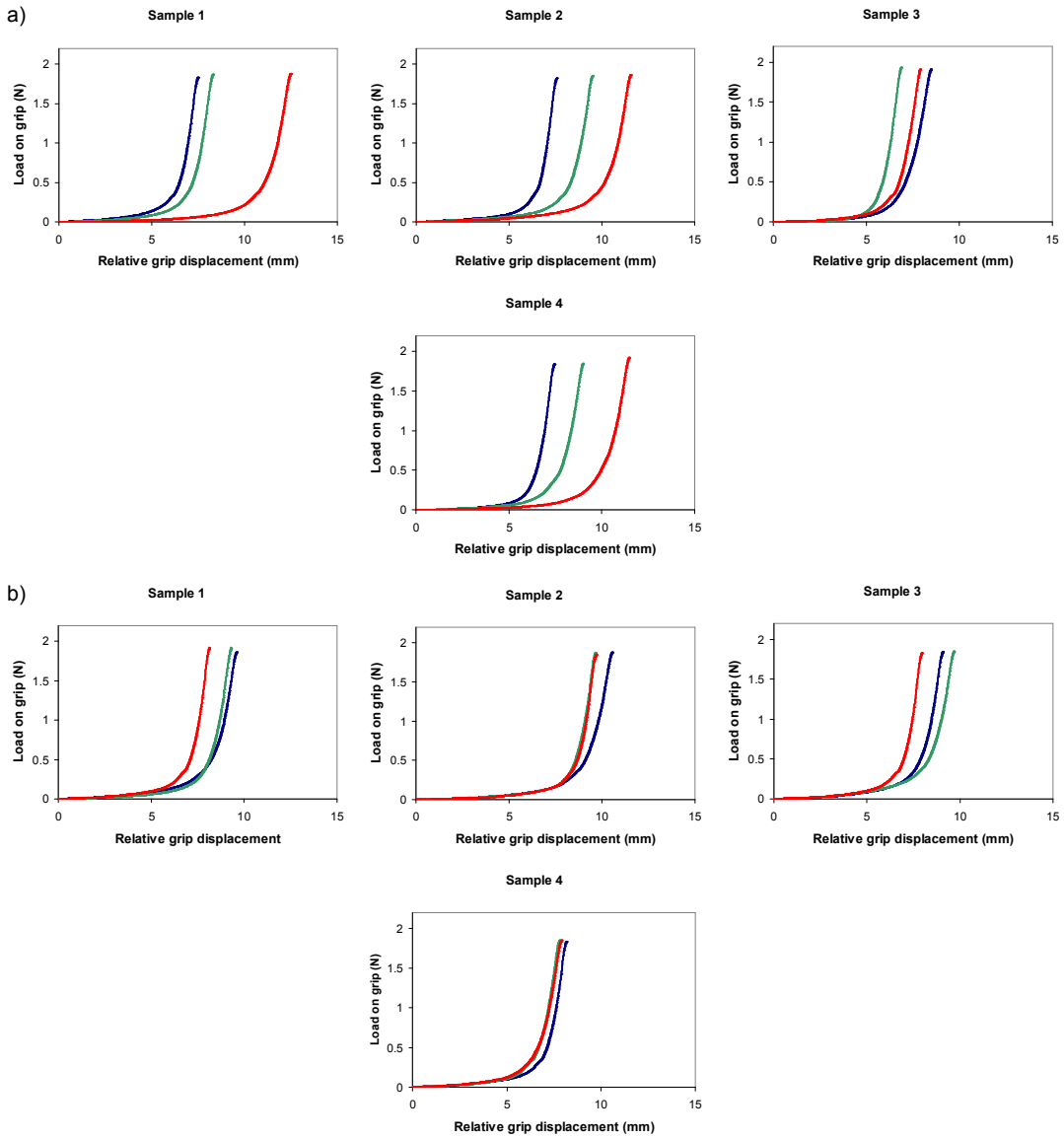


*Figure 2.19: Plots illustrating the tensile load on the grip against relative grip displacement when loaded at an orientation of 0º, 45º and 90º, shown in blue, green and red respectively, for all human donors. Skin sample location is indicated at the top of each plot (a) and b) represents donors 1 and 2 respectively).*

Figure 2.20 represents the average load on the grip against relative grip displacement for skin taken from murine donors 1 to 3 and 5 to 7, comparing UB to LB. Figure 2.21 illustrates the average measurements comparing skin taken from human donors 1 and 2, as the orientation of the skin samples relative to the donor was not known.

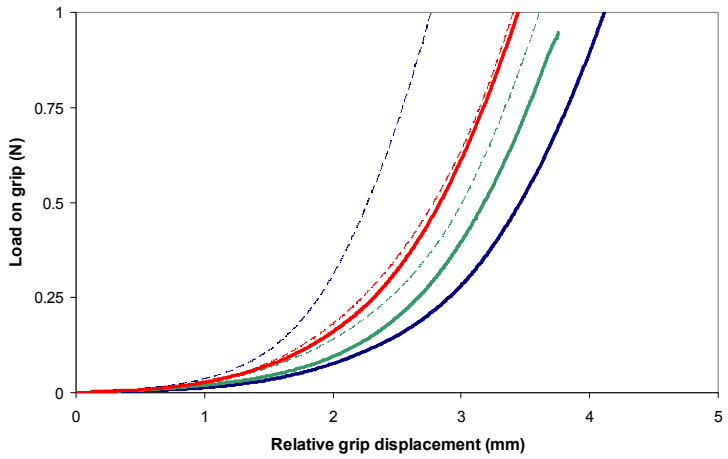


*Figure 2.20: Plots illustrating the average tensile load against relative grip displacement at 0º, 45º and 90º, shown in blue, green and red respectively for murine skin samples taken from the UB (solid line) and LB (dashed line).*

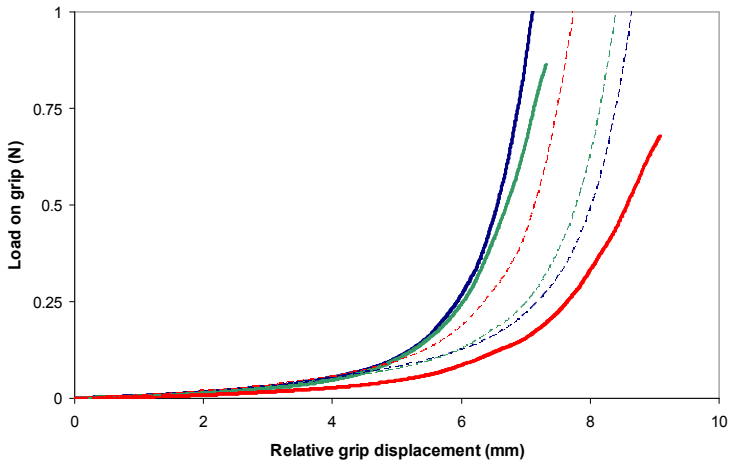


*Figure 2.21: Plots illustrating the average tensile load against relative grip displacement at 0º, 45º and 90º, shown in blue, green and red respectively for human skin samples taken from donor 1 (solid line) and donor 2 (dashed line).*

## 2.7.3 Linear stiffness

Figure 2.22 and 2.23 present the linear stiffness values for all tensile tests along the three load axes, performed on murine and human skin respectively. The data indicates that human skin has a slightly higher linear stiffness of 1.178N/mm compared to murine skin which was 1.063N/mm.

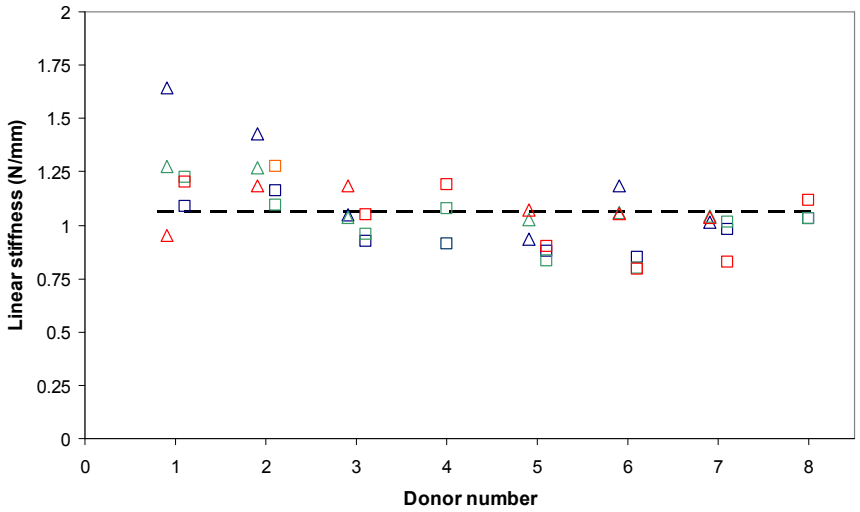


*Figure 2.22: Plot to show the linear stiffness against each donor number for murine skin when loaded at 0º, 45º and 90º, shown in blue, green and red respectively. The triangle and square markers represent the LB and UB skin regions respectively and the dashed black line shows to the average.*

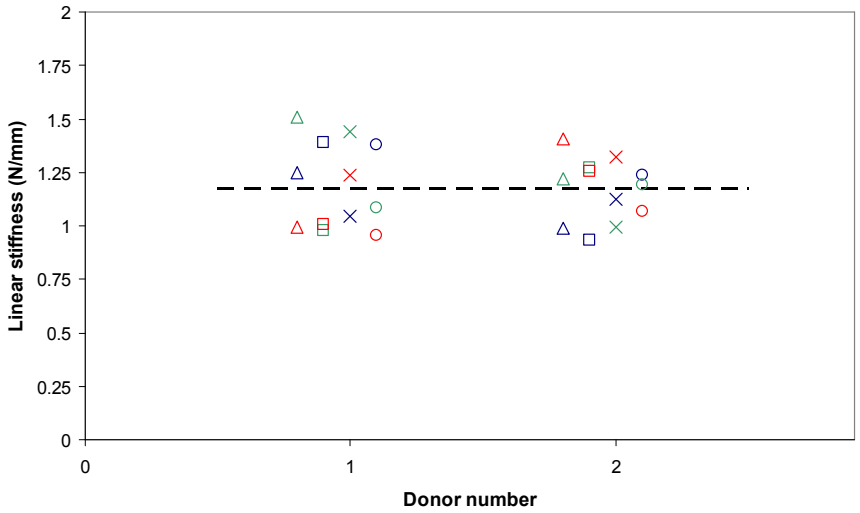


*Figure 2.23: Plot to show the linear stiffness against each donor number for human skin when loaded at 0º, 45º and 90º, shown in blue, green and red respectively. The triangle, square, cross and circle markers represent skin samples 1, 2, 3 and 4 respectively and the hashed black line is the average.*

## 2.7.4 Length of extension at low loads

From the load displacement curves, it is apparent that the main difference between human and murine skin was the level of extension at low load. Figure 2.24 illustrates the average and standard deviation for the length of extension at low tensile loads, comparing murine to human skin. The average

length of phase 1 was calculated at 5.10mm and 1.61mm for human and murine skin samples respectively. This plot shows that human skin samples underwent a statistically different higher duration of phase 1 in tension ($p<0.05$), compared with murine tissue.

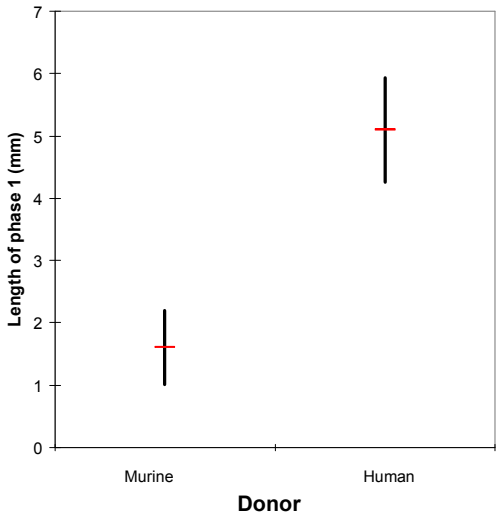


*Figure 2.24: Average and standard deviation length extension at low loads, shown in red and black respectively, comparing murine to human skin.*

## 2.7.5 Histological examination

Figure 2.25 and 2.26 shows a section of skin tissue taken from human donors 1 and 2 respectively, illustrating the SC, the viable epidermis and dermis, which is a mass of connective tissue.

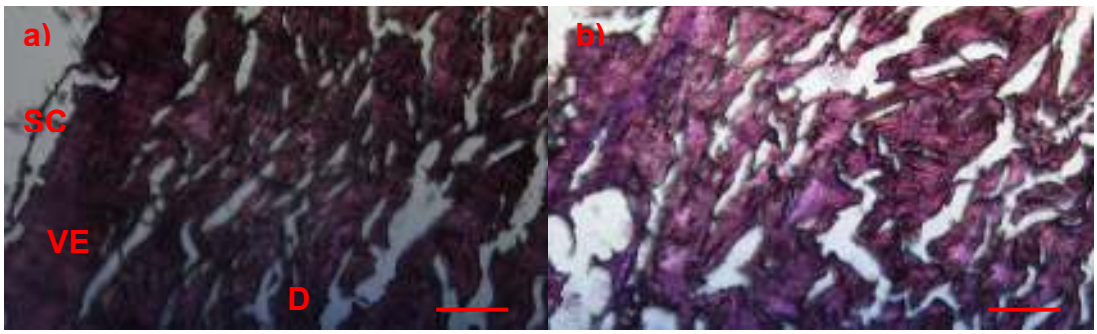


*Figure 2.25: Skin section stained with haematoxylin and eosin from human donor 1, sample 4 showing a) the upper skin layers b) the dermal fibres, the scale refers to 10μm. (SC= stratum corneum, VE = Viable epidermis, D = dermis).*

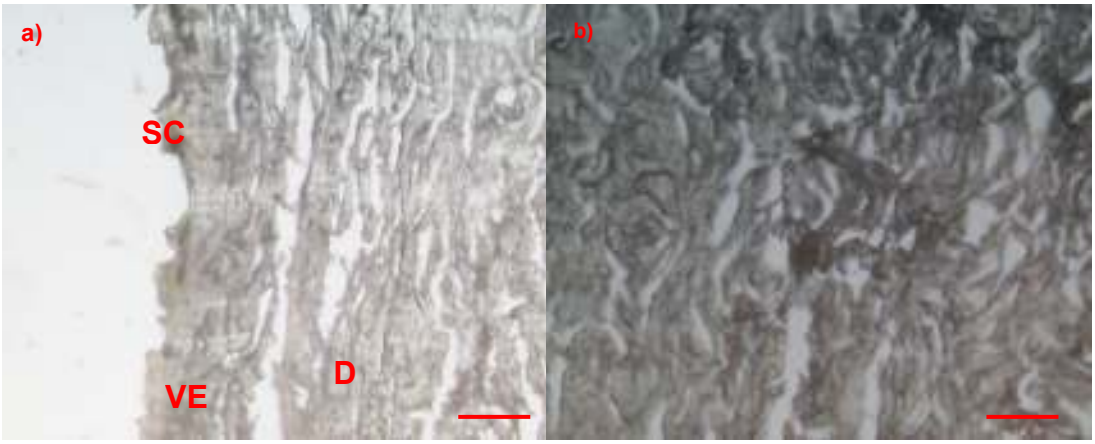


*Figure 2.26: Unstained skin section from human donor 2, sample 4 showing a) the upper skin layers b) the dermal fibres, where the scale refers to 10μm. (SC= stratum corneum, VE = Viable epidermis, D = dermis).*

Figure 2.27 shows stained skin sections from murine donors 5, 6 and 7, taken along the LB of all animals. Comparing sections taken from murine and human donors, there is a considerably larger volume of dermal tissue within human skin. Additionally, the skin thickness of murine skin is significantly less when compared to human skin, but the measurement between murine donors remains relatively consistent, shown in Table 2.7. Moreover, the skin and layer thickness fluctuates for all sections, implying the measurement is not constant throughout the tested samples.

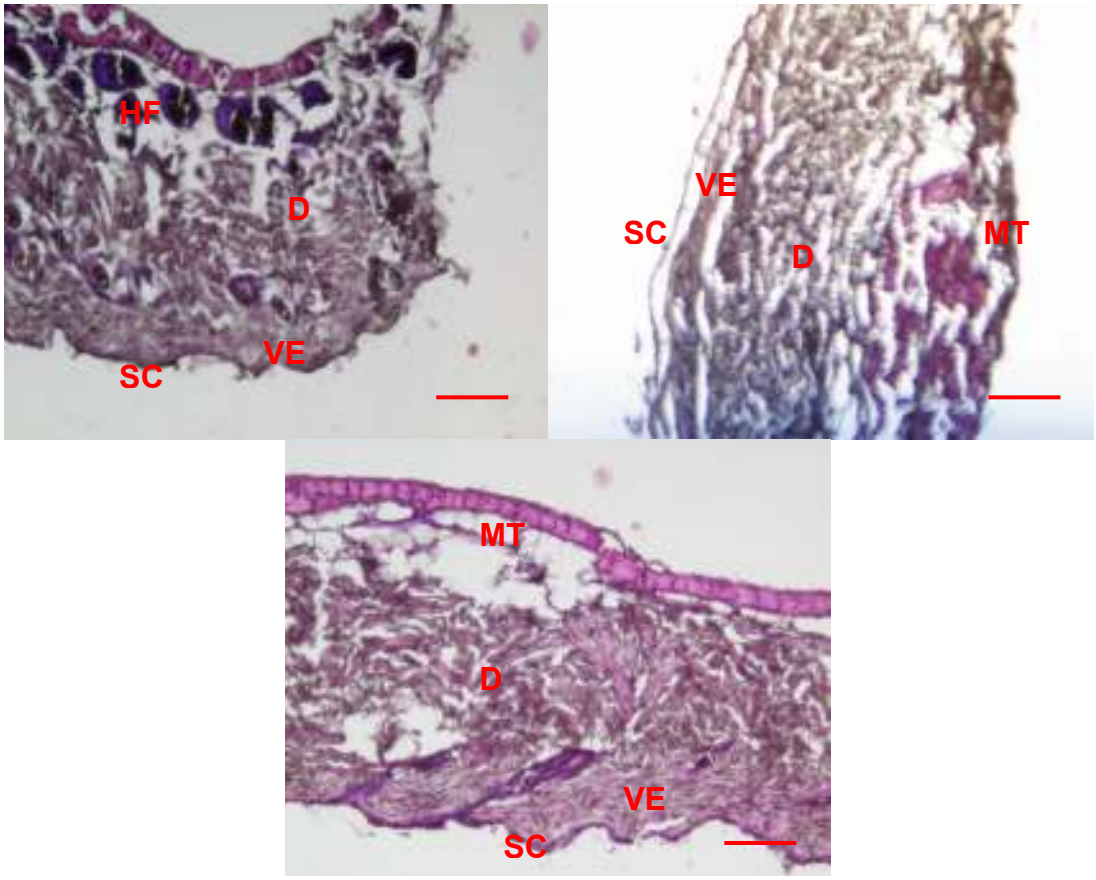


*Figure 2.27 Skin sections stained with haematoxylin and eosin from murine donors a) 5, b) 6 and c) 7, taken from the LB, where the scale refers to 10μm. (SC= stratum corneum, VE = Viable epidermis, D = dermis, MT = muscle tissue, HF = hair follicle).*

Table 2.7 shows the average skin thickness measurements taken from histological examination, illustrating that human skin is significantly thicker than murine, with average measurements of 1.86mm and 0.453mm respectively.

Table 2.7: Average skin thickness measurements taken from histology examination.

| ***Human / Murine*** | ***Donor Number*** | ***Location/ number*** | ***Average epidermis thickness (μm)*** | ***Average dermis thickness (mm)*** | ***Average skin thickness (mm)*** | ***% of total thickness dermal tissue*** |
|---|---|---|---|---|---|---|
| ***Human*** | 1 | 4 | 14 | 1.696 | 1.71 | 99.2 |
| | 2 | 4 | 13 | 1.977 | 1.99 | 99.3 |
| ***Murine*** | 5 | LB | 10 | 0.322 | 0.472 | 68.2 |
| | 6 | LB | 6 | 0.244 | 0.461 | 52.9 |
| | 7 | LB | 10 | 0.222 | 0.428 | 51.9 |

## 2.8 Discussion

This study applied tensile loads to *ex vivo* samples of human and murine skin, to characterise the anisotropic mechanical properties and the variations between both tissues. After which, histological examination took place on the loaded skin, to detect any anatomical differences which could account for the observed variations. The tensile tests performed were shown to work well, with no sample slippage observed during increased load application. Additionally, it was noted that the grips could be accurately placed for all experiments as the foil backing kept the skin sample flat and undeformed. As only five cycles at a maximum force of 2N were applied, minimal damage was incurred by the samples, moreover the short testing duration reduced sample dehydration. Whilst every effort was made to maintain testing consistency between samples, slight variations in experimental protocol and timing could have affected the results. However, the general mechanical behaviour of all skin tissues from murine and human donors, hence the variations and comparisons between tissues, appears to have been maintained throughout.

Figure 2.17 shows example plots comparing relative grip displacement against load for one human and one murine skin sample, orientated at 0º. Both plots show how the load - displacement relationship altered during the cyclic loads, where a steady state was reached after 4 cycles. Human and murine skin samples, had become fully preconditioned after 4 cycles, consequently it was appropriate to take all measurements from the final fifth cycle. It may have also been beneficial to measure the unloading behaviour of all samples during the cyclic loads to further examine the viscoelastic characteristics of the skin tissues. This could have allowed for additional analysis and comparison with other related studies which have also evaluated this behaviour.

All load-displacement curves show that both human and murine skin exhibit a nonlinear, J shaped response during tensile loading, as shown in Figures 2.18 and 2.19 Furthermore, the extent of anisotropic behaviour appears to be a

characteristic related to the donor, rather than a variation between human and murine skin. For example, murine donors 1, 3 and 6 and human donor 1 show a higher level of anisotropy, as the load – displacement curves for all samples along the three load axis orientations, were spread over a wider range. The analyses of the anisotropic characteristics could have been potentially furthered, by the inclusion of bi-axial experiments. However the Zwick® testing machine only accommodated for uni-axial loading, but when the skin samples were examined along the load axes, an estimation of the biaxial properties can be made. The number of donors selected for the tensile analysis was relatively small for both human and murine skin, therefore it is difficult to conclude whether the inter-individual differences noted within the level of anisotropic and nonlinear behaviour are related to age and anatomical variations. Consequently, to extensively examine correlations corresponding to donor age and skin structure, a larger population would need to be tested.

The main difference between human and murine skin was related to the level of extension at the maximum load of 2N. Human skin shows considerably more extension at maximum load when compared to murine skin, with values almost six times greater for some experiments. The higher level of extension at maximum load for human skin appears to be characterised by a greater duration of extension at low loads, consequently an increased length of phase 1. This difference was also observed in Figures 2.20 and 2.21, which plots the average load – displacement curves for all skin samples along the three load axes, for murine and human skin respectively. Again, the average duration of phase 1 experienced during tensile loading, was considerably greater for all human skin tissue. This is reiterated within Figure 2.24, which compares the initial length of extension at low load across all tensile tests, comparing murine to human skin. This plot indicates the length of phase 1 for human skin samples is on average around 3 times higher than that of murine skin, with a relatively similar spread of values for both donor types illustrated by the standard deviations. This resulted in a p value of $<0.05$, hence a significant difference between the length of phase 1 was observed between human and murine skin during tensile loading when performing a statistical t-test. This great variation between human and murine skin may be due to

differences in the network of collagen and elastin fibres between the two tissue groups. Consequently, it is possible that human skin contains considerably more fibres which are more crimped before load application. Thus upon the application of a tensile load, the fibres undergo a substantially longer period of un-crimping prior to the fibres coming under direct load.

The behaviour of the examined *ex vivo* skin during phase 3 (a stage of almost linear stiffening) is detailed in Figures 2.22 and 2.23. When considering murine against human skin, there is only a slight difference between the average linear stiffness variable with a value of 1.178N/mm and 1.063N/mm for human and murine skin respectively. As this phase represents the dermal fibres coming under direct load (Brown, 1973), it is possible that the properties of the dermal fibres within murine and human skin are not dissimilar. Hence the key variation between human and murine *ex vivo* skin tissue in applied tension, is the length of phase 1, hence the amount of extension experienced at low loads. Hence, the crimp of the fibres could be the main difference between human and murine skin as this characteristic may allow for greater extension at low loads, rather than the properties of the fibres themselves

Figures 2.20 and 2.21 illustrate that human skin donor 2 exhibited less anisotropic behaviour and a slightly greater duration of phase 1, when compared to donor 1. However, there is little difference between the linear stiffness values calculated for Figure 2.23. Any directional variation between human donors 1 and 2 is difficult to quantify as the skin orientation relative to the body was not known. On the contrary, there is some coherence between sample location and skin properties for murine skin. Figure 2.20 shows an increased stiffness for donors 2, 3, 5, 6 and 7, for the LB compared to UB, for the linear stiffness calculations. Additionally, Figure 2.20 shows a close agreement between the average tensile properties of the tested skin at load orientation of 45º and 90º. This observation is most likely related to the Langer's lines on the murine donor, resulting in correlations between donors.

Few studies have compared the anisotropic mechanical properties of human and murine *ex vivo* skin tissue using uni-axial tensile tests. However, several

have analysed human and animal skin samples independently. When examining the tensile properties of pig (Shergold et al., 2006b; Corr et al., 2009; Kang and Wu, 2011), cow (Ventre, Mollica and Netti, 2009), rabbit (Lanir and Fung, 1974), mouse (Del Prete et al., 2004) and human (Ridge and Wright, 1965; Brown, 1973; Stark, 1977; Dunn, Silver and Swann, 1985; Lapeer et al., 2010) skin, researchers have also found that tissues from all donor exhibit nonlinear mechanical properties, which produced a J-shaped load – displacement curve. In a study by Corr *et al.* in 2009, porcine skin was loaded in tension and the length of strain experienced at low load and the linear stiffness was calculated for scarred and unscarred tissue. The average duration of phase 1 was 6.5mm and 4.5mm for unscarred samples taken along and perpendicularly to the spine, respectively. This correlates with the measurements obtained for human skin within this study (average length of phase 1 was 5.1mm for human skin) suggesting porcine and human skin could share similar mechanical characteristics. However, this presented study also calculated the linear stiffness of the tissues, and the average value of 1.178N/mm found in this study was considerably lower than for those found within the investigation by Corrs *et al* for all samples. This is most likely due to the higher loads endured by the porcine skin (max. load of 180N), hence the later stage of stiffening may have been represented within their calculations.

This investigation has illustrated that both human and murine *ex vivo* skin exhibits anisotropic properties and are subject to preconditioning. These findings are in correspondence with observations made by Stark *et al.* in 1977, who noted the significant directional variations within the mechanical properties of the tested human skin, a conclusion also shown in rabbit (Lanir and Fung, 1974) and pig (Corr et al., 2009) skins. Moreover, preconditioning examination on murine (Tatlidede et al., 2009) and human (Lapeer et al., 2010) skin have been shown to give measurements which are in agreement with this study, illustrating that the stress-strain relationship alters continuously until a steady state is reached after approximately three cyclic loads.

Imaging techniques have also been used to characterise the strain distribution on the surface of the skin during the application of a load. In a study by Mahmud *et al*. in 2010, DIC was used to measure the deformation of human *in vivo* skin during in plane tension. If this technique were to be used *in situ* with this presented study, the deformation of the skin tissue during loading may have been mapped, providing further measurements which could be implemented within the inverse calculations in Chapter 4. Additionally, this data could have served as a further validation for the displacement measurements obtained and prove that the sample was not subject to slippages throughout the tests. It may also have provided information regarding the anisotropic properties of the tissue as the strain distribution may have been varied across the sample whilst under tension. However, due to the regulations stipulated for testing *ex vivo* human tissues, it was not possible to use the DIC equipment within the containment lab.

Histological examinations of the excised tissue shown in Figures 2.25 – 2.27, illustrate the anatomical differences between the chosen samples. Skin tissues taken from human donors had a considerably larger volume of dermal fibres, which give the skin a greater thickness (Table 2.7). The viable epidermis is only slightly thicker for human skin (difference of 4.8μm), attributing the majority of the thickness to the dermal layer. As the stretch and un-crimping of dermal fibrils is predominantly responsible for the in plane mechanical properties of skin (Brown, 1973), this anatomical variation between human and murine skin may be the key explanation as to why human skin can endure greater deformations at the same load. Moreover, human skin samples do not only show an increased thickness of dermal tissue, the dermal fibres themselves appear thicker, again possibly explaining why human skin has a greater extensibility.

The irregular matrix of fibres shown for all human and murine skin samples, are in agreement with two separate studies by Brown in 1973 and Dunn *et al*. in 1985, suggesting the skin had returned to an unstressed state as fibres were not aligned. The dermal layer for some samples had a much more loosely connected matrix of fibres, such as human donor 1 and murine donor

7, which could have potentially impacted the mechanical properties of the tissue. It is unclear however, if the disruption to this layer is indicative of the original anatomical structure, or as a result of the mechanical loads and / or the sectioning process. Sections also demonstrate that skin and layer thickness measurements varied throughout all five human and murine samples, even though the sections themselves were relatively small compared to the total tested area. Human skin samples housed less extra structures such as residual hypodermal tissue and hair ducts, where as murine skin, in particular donor 5, encapsulate additional structures such as a layer of underlying muscle tissue and hair follicles. The abundance of hair follicles present within murine skin may have reduced tensile strength of the tissue due to the micro-perforations caused by the hair ducts. Also, as the dermal layer is significantly thinner, these additional structures and layers may have affected the skins' reaction to an applied load.

In conclusion, this initial analysis has indicated some basic observations relating to the mechanical properties of the tested skins. It also suggests that there were great differences between the mechanical properties of tissues extracted from the two species groups (human and murine), which were likely due to the dermal fibres within the tissues, implying that murine skin may not be an appropriate model for human skin *ex vivo* for microneedle penetration tests. Additionally, due to the complex anisotropic mechanical nature of the tissue, additional examination was required. Consequently, further analysis was needed to account for the anisotropic nature and the complex nonlinear relationship *ex vivo* human and murine skin has shown to exhibit.

## 2.9 Conclusions

This Chapter aimed to establish approaches which could accurately measure the mechanical properties of human skin *in vivo* using indentation methods, and the anisotropic characteristics of human and murine skin *ex vivo* during uni-axial tensile loading. The experimental methods gave a high level of

repeatability for the majority of *in vivo* and *ex vivo* measurements, further demonstrated by the consistency of the correlations observed.

*In vivo* indentation measurements illustrated that volunteers 1, 6 and 7 had the stiffest skin by examining the reduced Young's modulus, Young's modulus and stiffness values. Such measurements imply that the mechanical properties of skin vary considerably from volunteer to volunteer. Analysis against published studies which have also calculated the Young's Modulus, reduced Young's Modulus and stiffness of *in vivo* skin, showed large discrepancies between most investigations, where the current study was shown to correlate best with *in vivo* suction experiments. This implies that the method of testing does give considerably different results hence approaches should be selected with care. However the range of variables calculated for each volunteer show agreement between all seven subjects, implying a high level of repeatability within the methods used. Thus further analysis beyond this Chapter can take place.

The *ex vivo* uni-axial tensile measurements performed on human and murine skin samples showed that human skin has the ability to endure much higher levels of strain at the same loads. This was characterised by a greater duration of extension at low loads (the length of phase 1) for human skin. Histological examination illustrated that human skin consists of a greater volume of dermal tissue hence increasing the material thickness, fibre length and width, potentially contributing the differences in the mechanical properties of human and murine skin. The differences between the mechanical properties and anatomy of human and murine skin noted within this investigation, further emphases the importance of selecting appropriate tissues so that these variations will not affect the outcome of a conducted study. This has particular significance for microneedle puncture tests, as studies have performed analysis on *ex vivo* murine tissue as a way of replicating puncture *in vivo* .

These basic analyses, imply further quantification is required to fully understand the complex biomechanical properties of the skin tested within

these studies. Both *in vivo* and *ex vivo* measurements show that the mechanical properties of both tissue types vary between donor and volunteer. Consequently, Chapters 3 and 4 presents the inverse finite element methods used to supplement these findings. The results were then used to design and analyse a new microneedle device which aims to facilitate uniform puncture of all microneedles within the array.

# CHAPTER 3

# FINITE ELEMENT MODELLING THE MECHANICAL PROPERTIES OF SKIN AS A MULTILAYER AND AS AN ANISOTROPIC MATERIAL

## 3.1 Introduction

As discussed in Chapter 1, finite element modelling is a technique used to develop computational models of a material or design that can be stressed or analysed to obtain specific data. However complex simulations can take longer to solve, but simplified models can be less accurate. Therefore it is important that all Finite element models (FEMs) are assessed to ensure that the analysis has the correct level of complexity for the desired outcome. This Chapter aims to address the development of appropriate models of human skin indentation and skin under tension. This will produce two sets of FEMs which will be used for inverse analysis in Chapter 4. Suitable models must be established, as when using inverse finite element methods, the FEM is solved between 1000 and 2000 times, thus to reduce solution time the model must solve quickly with a high level of accuracy.

As two indenters of varying geometries were used during the *in vivo* tests (Chapter 2), it was possible to establish a stratified model of human skin, incorporating the epidermis, dermis and hypodermis. This was possible because the two readings from both indenters could validate the model further,

increasing accuracy and allowing for additional parameters to be added. Additionally, as the human and murine skin samples were loaded along three load axes, it was possible to obtain anisotropic measurements. Thus the resultant finite element analysis could model the skin specimens as anisotropic materials.

## 3.2 Aims of the study

The investigation aims to achieve the following:

1. Develop a FEM of human skin indentation at small deformations incorporating the epidermis, dermis and hypodermis skin layers.
2. Establish an anisotropic model of human and murine skin in tension along three load axes that incorporates fibres which represent the dermal fibrils, allowing for anisotropic behaviour.
3. Both models must have a high level of accuracy but still maintain the ability to solve in a short period of time.

## 3.3 Development process

All 3D FEMs were pre-processed in Preview (Version 1.1.4), which was designed specifically for use with FEBio (Version 1.3) and post processed in Postview (Version 1.3.1., Musculoskeletal Research Laboratories, University of Utah, http://mrl.sci.utah.edu). FEBio is a nonlinear finite element solver explicitly developed for biomechanical problems. It provides a wide range of constitutive models, several of which are appropriate for modelling skin, which were discussed in Chapter 1. Preview accommodates for simple geometries and meshes, but has the capacity to import models from other software packages. However for the purposes of these studies the simple meshes and geometries provided were sufficient.

The development of both FEMs followed five steps to reach the final model which was used for inverse analysis. Figure 3.1 shows a flow diagram

indicating the process carried out for the development of a multilayer FEM of human skin indentation and the anisotropic model of human and murine skin in tension.

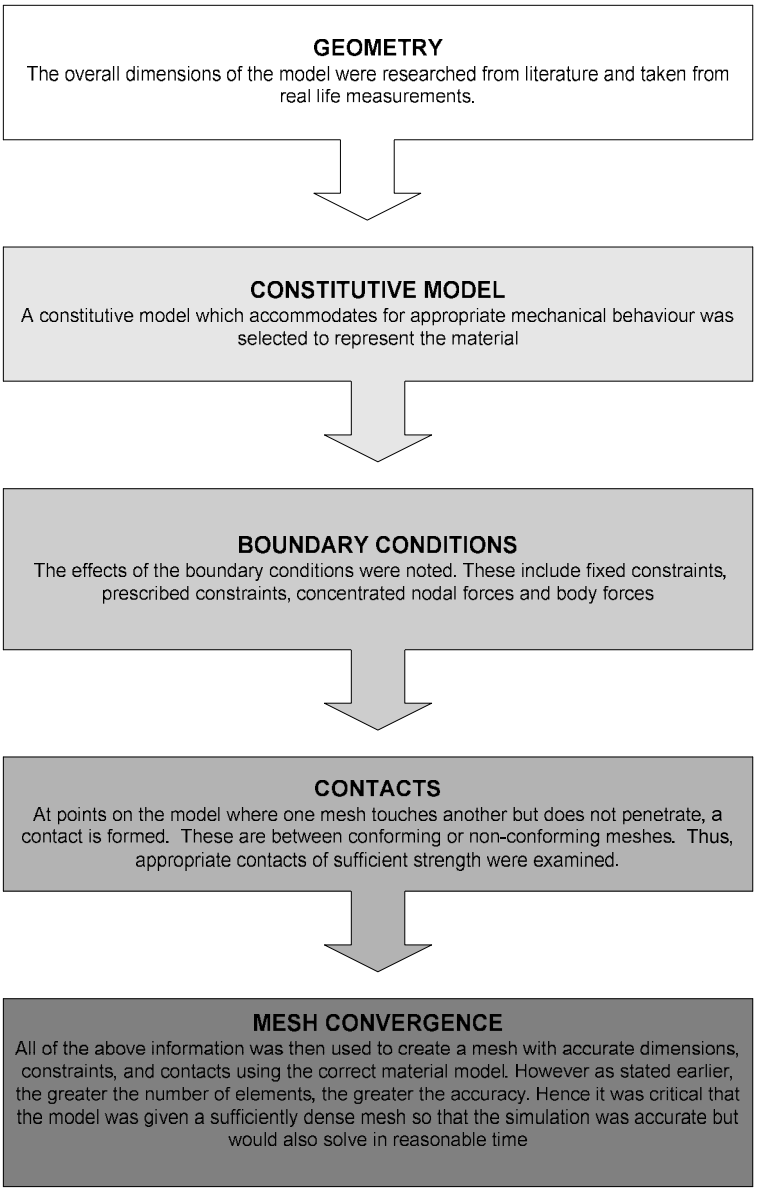


*Figure 3.1: Flow chart used when developing both the multilayer and anisotropic model of skin.*

# 3.4 Development of a multilayer FEM of human skin indentation

This section presents the method used to establish a multilayer FEM of human skin, incorporating the epidermis, dermis and hypodermis, under the application of small deformations allowing for a comparison with microneedle application.

## 3.4.1 Dimensions

To simplify the model, several assumptions were made regarding the dimensions of human skin. The epidermis was determined to be 0.07mm thick, a value obtained from OCT imaging of the forearm (Gambichler et al., 2006) and the dermis thickness was established at 0.84mm, an average value taken from ultrasound measurements in males and female healthy volunteers again at the forearm (Moore et al., 2003). The hypodermis thickness was 3mm, which is double the depth of previous models (Flynn and McCormack, 2008a), therefore at maximum displacement and low tissue stiffness, the stress at the base of the hypodermis was minimal. Hence when compression was applied, the constraints along the base were less influential on the resultant FEM

Both the flat bottomed cylindrical and spherical indenters were geometrically identical to the *in vivo* indenters. Hence, the cylindrical and spherical indenters had diameters of 0.5mm and 1.5875mm respectively.

## 3.4.2 Constitutive model

There are several nonlinear constitutive models provided by FEBio that could be used to describe soft tissues such as skin, two of which will be considered in this study. The M-R and Ogden models (Chapter 1) can withstand large strains and account for nonlinearities within the mechanical properties of the

material. The slightly compressible Ogden and M-R strain energy density functions are shown in Equations 3.1 and 3.2, where $C_1$, $C_2$, $\alpha$ and $\mu$ are material constants and J is the Jacobian of the deformation (volume ratio)

$$W = \sum_{i=1}^{n} \frac{\mu}{\alpha^2}\left(\lambda_1 + \lambda_2 + \lambda_3 - 3\right) + U(J) \qquad 3.1$$

$$W = C_1\left(I_1 - 3\right) + C_2\left(I_2 - 3\right) + \frac{1}{2}K\left(\ln J\right)^2 \qquad 3.2$$

As several volunteers were used to test the mechanical characteristics of human skin, and each possesses unique biomechanical properties, the chosen constitutive model was required to provide a wide range of stress-strain relationships.

To test the two constitutive models, a simple cube of geometry 1x1x1mm, with a 10x10x10 element mesh was established in Preview. The cube was constrained along the base in the x, y and z planes and a compressive strain of 20% (comparable to the strain applied *in vivo*) was applied to the face opposite to the constrained base, shown in red on Figure 3.2. Both the M-R and Ogden models were then given a set of input parameters and the resultant stress-strain relationships were recorded. Table 3.1 shows the input parameters used for each model. Starting values were obtained from the literature (Shergold et al., 2006b) each consecutive set of parameters was approximately 50%, 100% and 150% increase and 50 % decrease on the initial set of values. For the M-R model, $C_1$ was assumed to be 0.

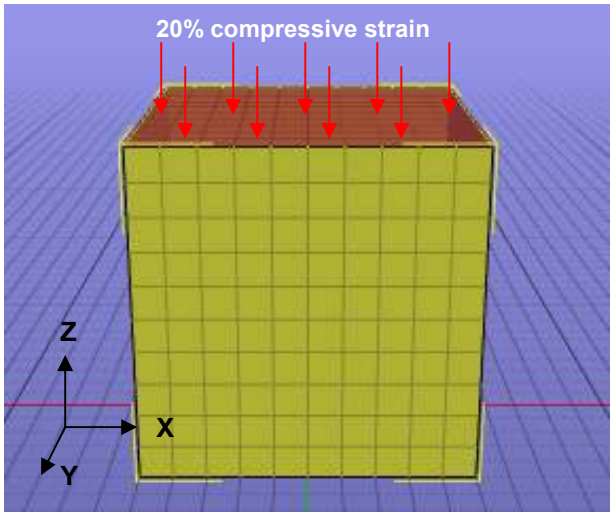


*Figure 3.2: Diagram showing the FEM used to determine an appropriate constitutive model.*

Table 3.1: M-R and Ogden parameters used to find the most appropriate material model.

| ***Parameter set*** | ***Description*** | ***Ogden*** | | ***M-R*** |
|---|---|---|---|---|
| | | $\mu$ ***(MPa)*** | $\alpha$ | $C_1$ |
| ***1*** | Initial parameter set taken from Shergold *et al.* | 0.11 | 9 | 0.3 |
| ***2*** | 50% increase | 0.17 | 14 | 0.45 |
| ***3*** | 100 % increase | 0.22 | 18 | 0.6 |
| ***4*** | 150% increase | 0.28 | 23 | 0.75 |
| ***5*** | 50% decrease | 0.07 | 6 | 0.2 |

Figure 3.3 shows the maximum stress compared to maximum strain curves for the Ogden and M-R models in the z plane, using the parameters displayed in Table 3.1. Figure 3.3 illustrates that the Ogden material model can depict a wide range of nonlinear stress –strain relationships, when altering the input parameters by the same percentage increase and decrease, when compared with the M-R model. For example, parameter set 5 gives an almost linear stress-strain relationship; however this curve becomes more nonlinear through to parameter set 1. Hence the Ogden material model was chosen as it gives almost linear and nonlinear stress-strain curves, with small input parameter changes.

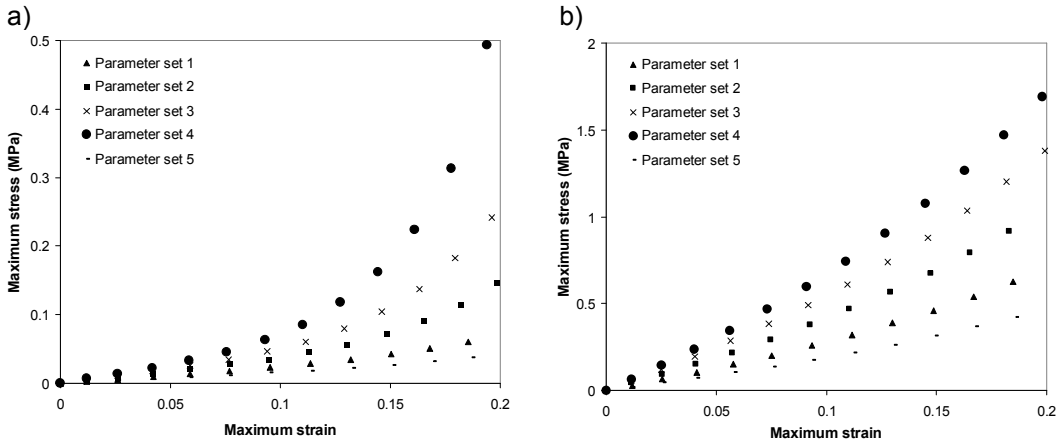


*Figure 3.3: Plots to show the stress-strain response of a) the Ogden and b) the M-R material model using the input parameters shown in Table 3.1.*

When modelling both metal indenters, the stiffness of the material was several orders of magnitude higher than the skin, therefore it was possible to model them as rigid bodies.

### 3.4.3 Boundary Conditions

Due to axial-symmetry it was possible to only use a section of the geometry. This approach was advantageous as it reduces the number of elements, hence decreasing the time taken for the model to solve. However it was necessary to ensure the boundary conditions implemented did not affect the measurements obtained.

Three models were constructed for this investigation, an entire model, a half and a quarter model, shown in Figure 3.4. The orange material was skin, which was assigned Ogden properties, and the yellow spherical object was the indenter, which was assumed to be a rigid body. The sliding contact between indenter and skin, and the mechanical properties of both objects were identical for all three models. The rigid body indenter was prescribed a displacement of 0.1mm in the z negative direction

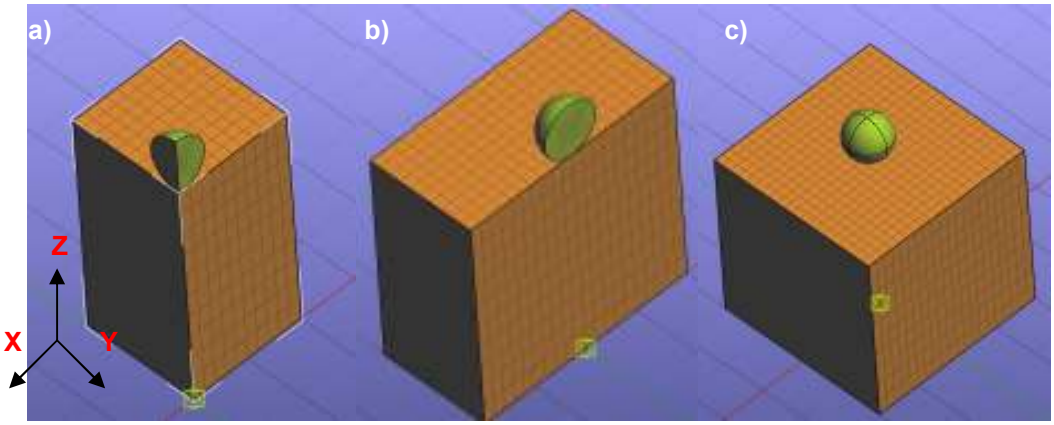


*Figure 3.4: Images of the three models, a) quarter, b) half and c) whole model, used to examine the effect of the boundary conditions.*

For the quarter model, constraints were placed along the quarter slices in the perpendicular direction (x and y planes for left and right faces respectively) and in the y direction for the slice on the half portion model, preventing any deformation in these directions (Figure 3.4). A diagram of the constraints for the quarter and full model is shown in Figure 3.5. The half model had the constraints as shown in Figure 3.5 a) along the x plane and as shown in Figure 3.5 b) in the y direction.

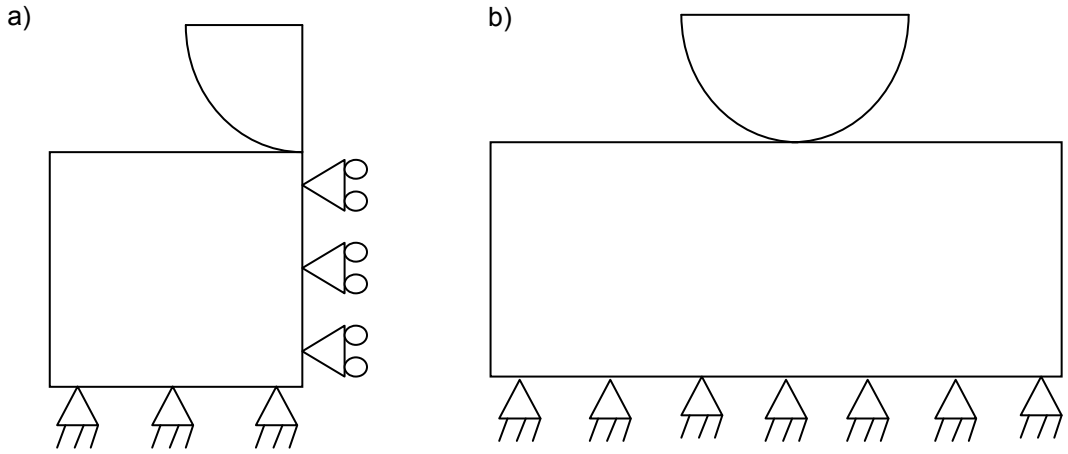


*Figure 3.5: Diagram of constraints used for a) the quarter and b) the full model*

The reaction force on the rigid body indenter was then compared with the indenter displacement for all three models. For the half and quarter dimension models, the load on the indenter was multiplied by 2 and 4 respectively to scale up the measurements to represent a whole model.

Figure 3.6 shows the resultant plots indicating the load on the rigid body indenter, compared to the indenter displacement for the quarter, half and whole portion models. This plot illustrates that all three models gave very similar load-displacement results, indicating that a quarter and half model can be used in place of the complete model. As the quarter was constructed of less elements, this model was used for the final analysis.

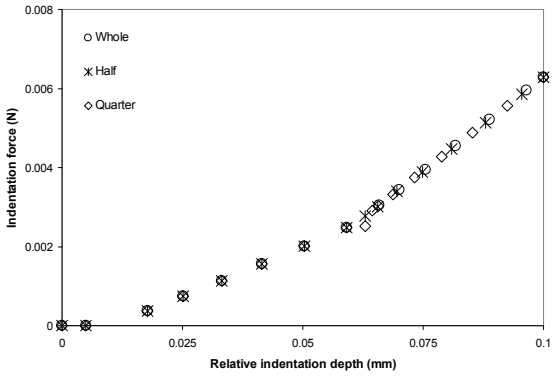


*Figure 3.6: Plot comparing relative indentation depth against indentation force for the quarter, half and whole models shown in Figure 3.4.*

### 3.4.4 Contacts

Each layer was modelled as a separate geometry, so that during inverse analysis, the material properties could be assigned to each layer individually. Additionally, the epidermis required a finer mesh compared to the underlying layers because the indenter was in direct contact with the epidermal surface. Hence this was possible by modelling each layer as a separate geometry. Due to this, contacts were required between the epidermis and dermis and between the dermis and hypodermis, in addition to a contact between the indenter and the skins' surface. It was desirable that the skin reacted as an entire structure, ensuring that the skin layers did not slide over one another or become displaced. Hence the most appropriate form of contact was a tied interface which joined the two meshes from the two geometries. On the contrary, the applied contact between indenter and skin was described as a sliding interface because it allowed the indenter to slide over the skin during compression. A frictional coefficient of 1.2 was applied between skin and

indenter (Kwiatkowska et al., 2009), however it should be noted that no variations in the analysis were observed if this value was modified, most likely because the indenter only displaced in the z plane.

As the contact stiffness was related to material properties of the mesh, all contacts were given a stiffness which was approximately the same as the Bulk Modulus of the stiffer of the two materials. This ensured that the meshes did not penetrate whilst the model was solving. Nonetheless, it is important to note that if the penalty was too high or too low, the model would not converge efficiently, however this approximation was shown to work well for all contact strengths

### 3.4.5 Mesh convergence

In finite element analysis, when dealing with a relatively simple mesh, a finer mesh increases accuracy, however an increased number of elements results in a slower solution time. Therefore mesh convergence tests were conducted. To achieve this, the lowest number of elements which were considered reasonable for the FEM were analysed then compared with further models with an increased number of elements. Once the analysis converged to a satisfactory level (i.e. the FEM gave the same response as the previous less finely meshed model), the FEM had reached an adequate mesh quality. However as both FEMs were used for inverse analysis within Chapter 4, it was critical that the model solved within reasonable time (< 90 seconds).

For this evaluation, certain assumptions were made for both models. These are as follows:

- Geometries described in Section 3.4.1 were used, where only one quarter of the model was analysed.
- Tied interfaces were employed between each skin layer and a sliding contact with a coefficient of friction of 1.2 was applied between indenter and the skins surface.

- All skin layers for all models were given the same Ogden material coefficients of α=4 and μ=0.8MPa.
- The spherical indenter was modelled as a rigid body shell and the cylindrical indenter was assumed to be a rigid body constructed of solid elements. All skin layers were represented by solid elements.
- The mesh density of both indenters remained constant throughout all tests.
- A finer mesh was employed where the indenter tip touched the skin's surface as this was an area of increased strain.

Table 3.2 shows the proposed mesh densities used for an FEM of human skin indentation by a spherical and a cylindrical indenter. Convergence test 1 utilised models with the least number of elements which was considered to be reasonable, successive convergence tests (tests 2 and 3) analysed models with a finer mesh.

Table 3.2: Number of elements in each skin layer for both FEMs for all three convergence tests.

| ***Number of elements within each skin layer*** | ***Convergence test 1*** | | ***Convergence test 2*** | | ***Convergence test 3*** | |
|---|---|---|---|---|---|---|
| | **Cylindrical** | **Spherical** | **Cylindrical** | **Spherical** | **Cylindrical** | **Spherical** |
| ***Epidermis*** | 1040 | 1040 | 2280 | 2280 | 4000 | 4000 |
| ***Dermis*** | 1100 | 2250 | 2970 | 4960 | 6200 | 12900 |
| ***Hypodermis*** | 500 | 1125 | 1800 | 3200 | 4000 | 4000 |
| ***Total*** | 2640 | 4415 | 7050 | 10440 | 14200 | 20900 |

Figure 3.7 show the FEMs post processing within FEBio, which were developed for the skin indentation using a cylindrical and spherical indenter

respectively, from convergence test 1. A finer mesh was implemented near the indenter tip in the skin and the different meshes used for each skin layer

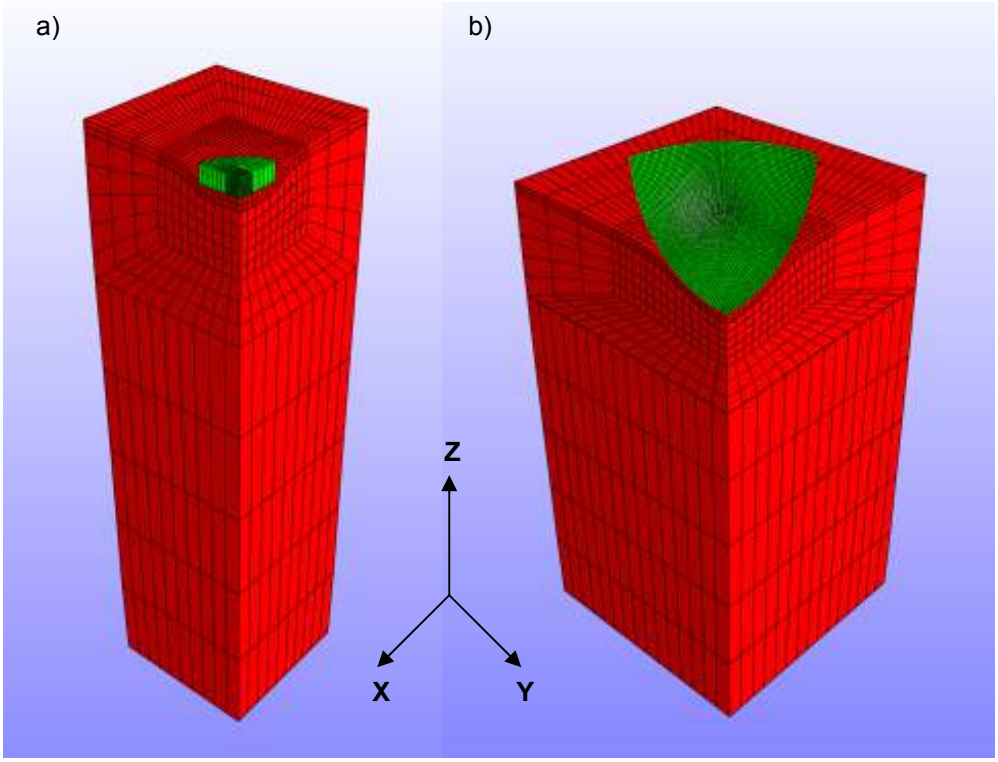


*Figure 3.7: Post processed FEMs for a) the cylindrical and b) the spherical indenter, using meshes from convergence test 1.*

Plots shown in Figure 3.8 compare relative indentation depth against the reaction force on the rigid body indenter for both the spherical and cylindrical indenter, for all three mesh convergence tests. There was no difference between the three convergence tests for both models, therefore it was appropriate to use the mesh derived for convergence test 1. This will produce accurate results but with a coarser mesh. It should be noted however that if larger deformations were modelled it may be necessary to use a finer mesh. Hence for the purposes of this investigation, where a relative indentation depth of up to 0.3mm was modelled, a coarse mesh was considered appropriate.

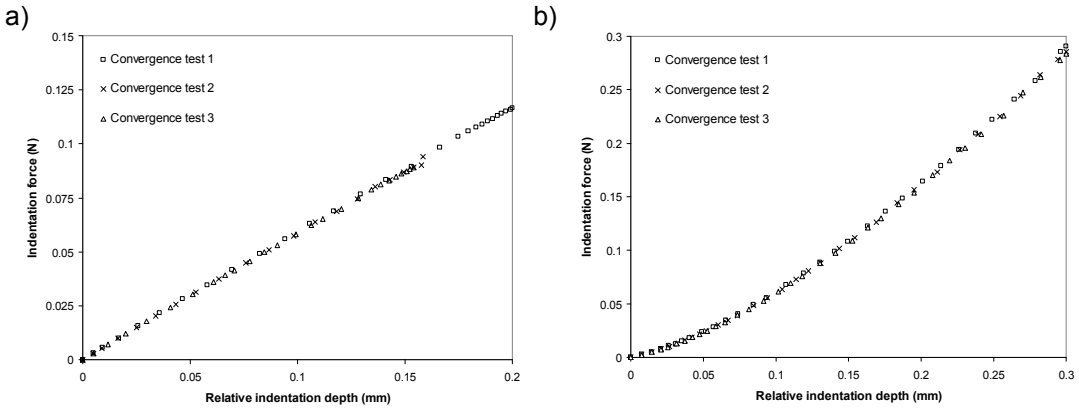


*Figure 3.8: Plots comparing relative indentation depth to the reaction force on the cylindrical (a) and spherical (b) indenter for all three convergence tests.*

# 3.5 Resulting multilayer FEM of human skin

Table 3.3: shows a summary of the chosen parameters for both stratified FEM of skin indentation using a spherical and cylindrical indenter (detailed in Chapter 3.4).

Table 3.3 summary of FEM parameters for cylindrical and spherical indenter applied to skin

| | ***Cylindrical indenter applied to skin*** | ***Spherical indenter applied to skin*** |
|---|---|---|
| ***GEOMETRY*** | | |
| Epidermis thickness (mm) | 0.07 | 0.07 |
| Dermis thickness (mm) | 0.84 | 0.84 |
| Hypodermis thickness (mm) | 3 | 3 |
| Width and length of skin - x and y dimensions (mm) | 1 x 1 | 2 x 2 |
| Indenter dimensions | Diameter of 0.5mm, height of 0.1mm | Diameter of 1.5875mm |
| ***CONSTITUTIVE MODEL*** | | |
| Skin | Ogden model of hyperelasticity | Ogden model of hyperelasticity |
| Indenter | Rigid body | Rigid body |
| ***BOUNDARY CONDITIONS (assuming quarter model)*** | | |
| Constraint at base | x, y and z planes | x, y and z planes |
| Constraint along slices | x and y planes | x and y planes |
| ***CONTACTS*** | | |
| Between skin and indenter | Sliding interface with a frictional contact of 1.2 | Sliding interface with a frictional contact of 1.2 |
| Between epidermis and dermis | Tied interface | Tied interface |
| Between hypodermis and dermis | Tied interface | Tied interface |
| ***MESH DENSITY*** | | |
| Epidermis | 1040 | 1040 |
| Dermis | 1100 | 2250 |
| Hypodermis | 500 | 1125 |

Figure 3.9 shows images of both models, post processing. The convergence time was 42 and 115 seconds for the modelled cylindrical and spherical indenter respectively, which was small enough to use for inverse analysis.

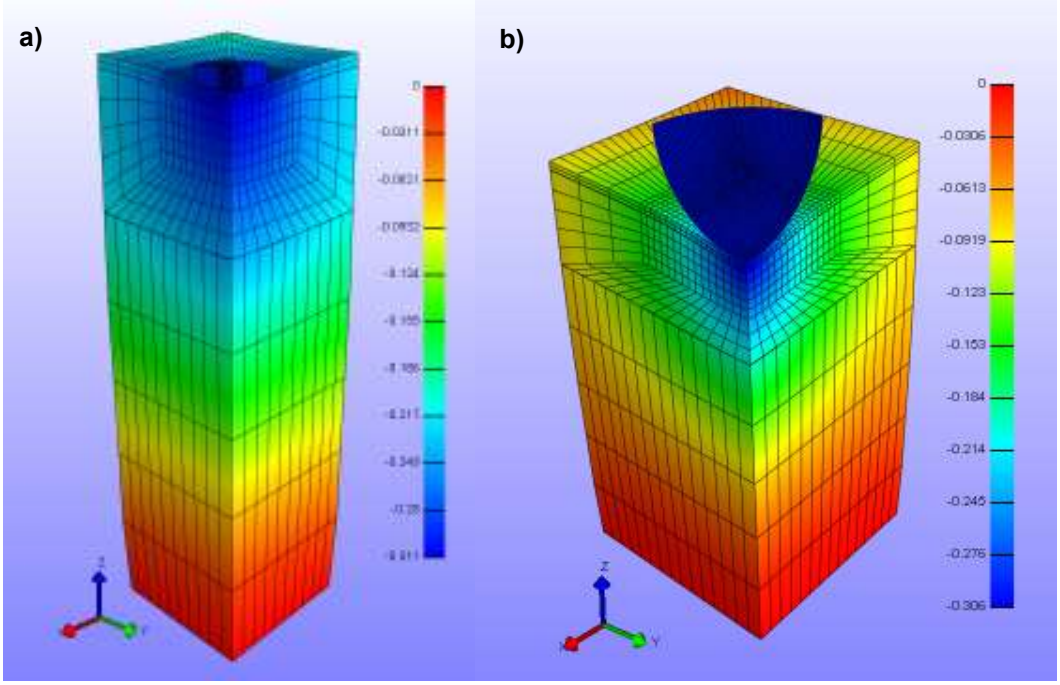


*Figure 3.9: Images showing both FEMs of a) cylindrical and b) spherical indenter applied to skin, the scale refers to the displacement in the z direction.*

# 3.6 Development of an anisotropic FEM of human and murine skin under tension

This section follows the method outlined in Figure 3.1 used to develop an anisotropic model of human and murine skin in tension. This model was used for inverse analysis and correlated with *ex vivo* measurements obtained in Chapter 2, to produce a validated anisotropic FEM of human and murine skin in tension.

## 3.6.1 Dimensions

Both FEMs followed the dimensions of the skin samples described in Section 2.4.2, where a 31mm diameter disc of skin was removed and tested. Skin thickness measurements were taken from histological examination, which were averaged at 1.86mm and 0.453mm for human and murine skin respectively. As specified in Chapter 2, the grips were placed 7.5mm either side of the central point of the skin specimen as presented in Figure 3.10, where the area of the grips which held the skin measured 30mm².

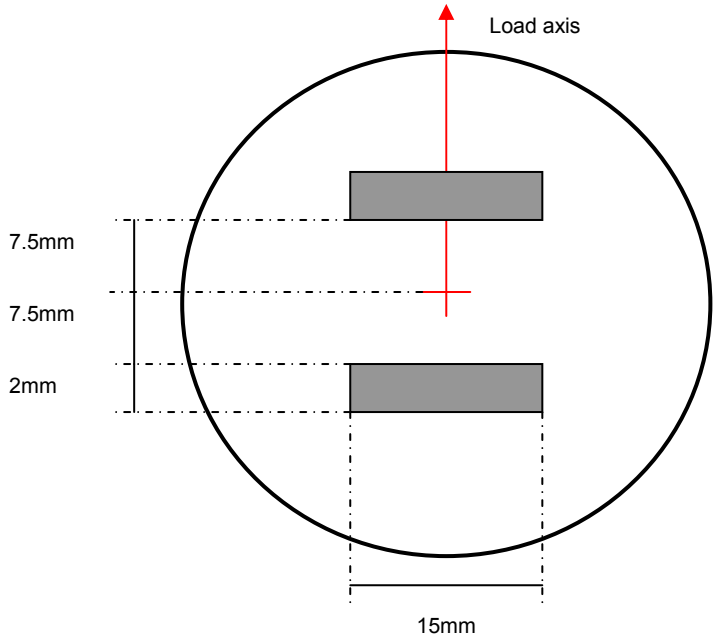


*Figure 3.10: Diagram indicating the model dimensions in the x – y plane for both murine and human skin models.*

### 3.6.2 Constitutive model

A transversely isotropic constitutive model developed by Weiss *et al,* in 1996, which incorporated fibres within an isotropic matrix, was implemented for each fibre family to represent human and murine skin. This model was the only transversely isotropic model available within the finite element software FEBio. Upon preliminary tests, it was shown to converge well and give a highly nonlinear stress-strain curve, which was extremely important when modelling skin in tension. To increase anisotropy, multiple fibre families were implemented within the material. This allowed manipulation of the properties of each fibre family, giving more control over the stress-strain relationship of the material. This was important as the model was correlated with the *ex vivo* measurements obtained along three planes at 0º, 45º and 90º degrees (Chapter 4).

The fibres which were embedded within the isotropic matrix had several defined properties which can be adapted to modify the mechanical characteristics of the material. The elastic response of the tissue was determined from the resistance of the fibre family and the isotropic matrix to an applied force. It was assumed that the uncoupled strain energy function can be written as Equation 3.3

$$W = F_1(I_1, I_2) + F_2(\lambda) + \frac{K}{2}\left[\ln(J)\right]^2 \qquad 3.3$$

Where $I_1$ and $I_2$ were the first and second invariant of the deviatoric version of the right Cauchy Green deformation tensor $C$, $\lambda$ is the deviatoric part of the stretch along the fibre direction and $J$ is the Jacobian of the deformation (volume ratio). $F_1$ refers to the material response of the isotropic matrix, while $F_2$ represents the contribution of the fibre family.

Equation 3.4 shows the strain energy density function derived for the incompressible V-W model (Veronda and Westmann, 1970) which was used describe the isotropic matrix, where $C_1$ and $C_2$ are material constants.

$$W = C_1\left[e^{(C_2(I_1-3))} - 1\right] - \frac{C_1 C_2}{2}(I_2 - 3) \qquad 3.4$$

The V-W model is similar to the M-R model, which has been commonly used to describe biological tissues, however it allows for a much higher level of exponential stiffening with increased strain. This was important when representing skin when high levels of strain were applied (see Chapter 1).

### *3.6.2.1 Fibre Properties*

The strain energy of the fibre family was defined as follows:

$$\text{when } \lambda \le 1 \quad \lambda\frac{\partial F_2}{\partial \lambda} = 0 \qquad 3.5$$

$$\text{when } 1 < \lambda < \lambda_m \quad \lambda\frac{\partial F_2}{\partial \lambda} = C_3\left(e^{C_4(\lambda-1)} - 1\right) \qquad 3.6$$

$$\text{when } \lambda \ge \lambda_m \quad \lambda\frac{\partial F_2}{\partial \lambda} = C_5 + C_6\lambda \qquad 3.7$$

Where the coefficients were defined by:

$\lambda_m$ = fibre stretch for straightened fibres

$C_3$ = scales the exponential stresses

$C_4$ = the rate of un-crimping

$C_5$ = modulus of the straightened fibres

$C_6$ = determined from the requirement that the stress is continuous at $\lambda_m$

The modulus of the straightened fibres can be assumed to be in the same order of magnitude as a function of the scaled exponential stresses, the fibre stretch of the straightened fibres and the rate of un-crimping. Hence Equation 3.8 was used to estimate this parameter, thus reducing the total number of coefficients, decreasing computation time and producing a smooth curve.

$$C_5 = C_3 C_4 \lambda \left( e^{C_4(\lambda - 1)} \right) \qquad 3.8$$

### *3.6.2.2. Fibre Orientation*

The orientation of the embedded fibres can be defined in three ways:

- *Local:* This fixes the direction of the fibres along a defined mesh edge
- *Spherical:* The orientation is determined by a point in space, where the spherical fibre distribution is centred around this particular point
- *Vector:* The fibre direction is specified by a vector

A vector coordinate system was used to describe the orientation of the dermal fibres as this was most representative of how the fibres were aligned in the skin, and allowed for more control over the positioning of the fibres. All points and vectors are defined using the x, y, z coordinate system, however only the x and y coordinates were considered as the z axis lay perpendicularly to the direction at which the load was applied. By manipulating $\lambda_{m,}$ $C_3$, $C_4$, the fibre orientation and the V-W constants, the stress strain relationship of the material was manipulated. Furthermore, when multiple fibre families were implemented within the skin material, there was more control over the anisotropic behaviour.

Due to the relatively large number of coefficients for each fibre family, a sensible number of fibre families needed to be implemented within the FEMs. Too many parameters could result in an increased computational time, however too few could decrease the potential variations of stress – strain relationships possible. Therefore a simple test was derived to examine the level of anisotropy noted in a strip of material with 2, 3 and 4 families of fibres.

Figure 3.11 shows the simplified FEM used for this investigation. The rectangular object is the strip of transversely isotropic material with, in this case, 2 fibre families shown in yellow and orange. The material is constrained along the red edge in the x, y and z directions. The pink object is a rigid body which was given a prescribed displacement of 10mm in the positive x plane.

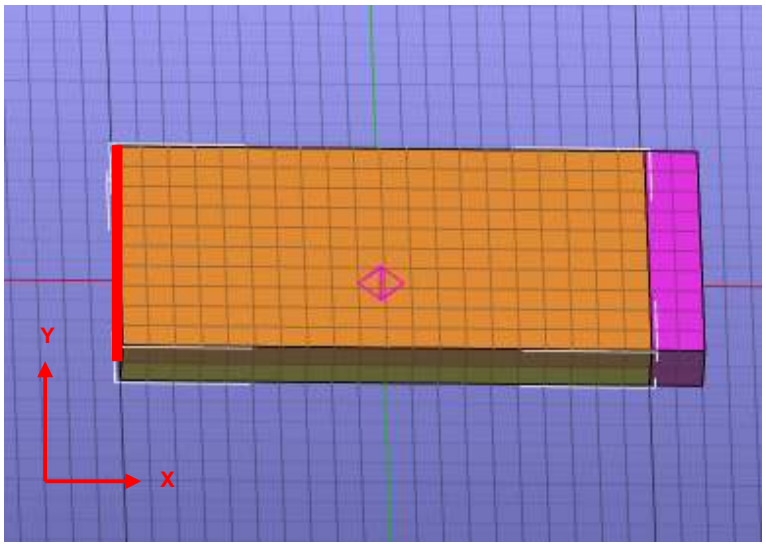


*Figure 3.11: Image of FEM used to investigate the appropriate number of fibre families.*

The vector of the fibre orientation was altered for each fibre family so that the applied load was orientated at 0º, 45º and 90º clockwise, explained in Figure 3.12. Each fibre family was given different values for parameters $C_3$, $C_4$ and $\lambda_m$. The fibres were orientated in a manner so that no two fibre families lay perpendicularly, for example family 1 at 0º and family 2 at 180º. Table 3.4 shows a summary of the parameters used, where it was assumed that V-W coefficients remained consistent at $C_1$ = 0.001MPa and $C_2$= 3MPa for all tests and $C_5$ was calculated from Equation 3.8.

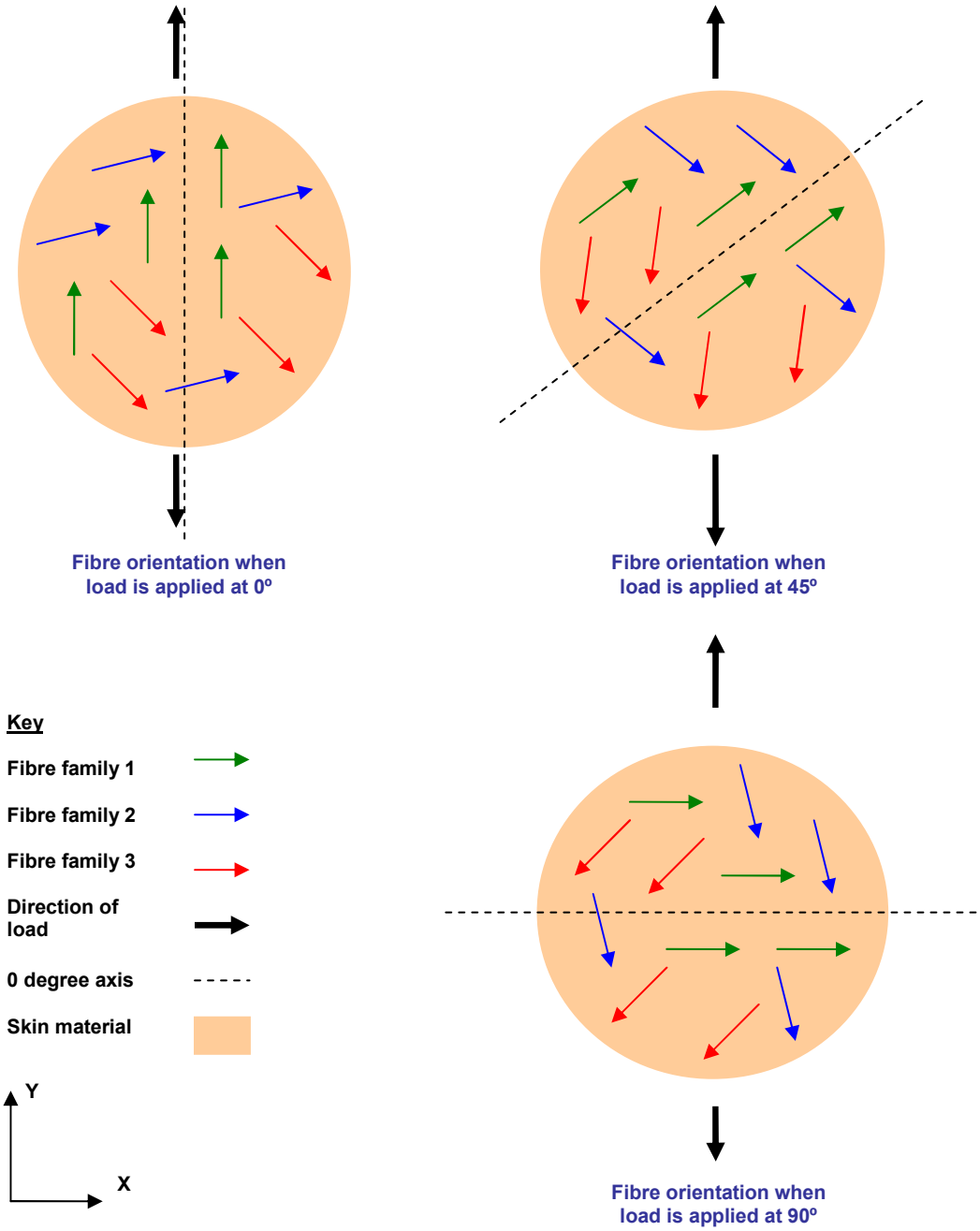


*Figure 3.12: Image illustrating the fibre family orientations when the load axis was at 0º, 45º and 90º, for three fibre families.*

Table 3.4: Parameters used for each fibre family.

| ***Fibre family number*** | ***1*** | ***2*** | ***3*** | ***4*** |
|---|---|---|---|---|
| $C_3$ | 0.01 | 0.012 | 0.015 | 0.016 |
| $C_4$ | 30 | 25 | 20 | 15 |
| $\lambda$ | 1.2 | 1.4 | 1.6 | 1.8 |
| ***Fibre orientation when load axis at 0º (º)*** | 0 | 90 | 45 | 135 |
| ***Fibre orientation when load axis at 45º (º)*** | 315 | 45 | 0 | 90 |
| ***Fibre orientation when load axis at 90º (º)*** | 270 | 0 | 315 | 45 |
| ***Model incorporating 2 fibre families includes the following -*** | ☒ | ☒ | | |
| ***Model incorporating 3 fibre families includes the following -*** | ☒ | ☒ | ☒ | |
| ***Model incorporating 4 fibre families includes the following -*** | ☒ | ☒ | ☒ | ☒ |

Figure 3.13 shows plots comparing relative grip displacement to load on the grip for all three FEMs incorporating 2, 3 and 4 fibre families within an isotropic V-W matrix. There was little variation in the level of anisotropy for all three models, using the specified input parameters. Hence it was decided that three fibre families would be modelled, as the skin samples were loaded along three load axes. The decision was taken to limit to three fibre families to constrain the time taken to perform inverse calculations.

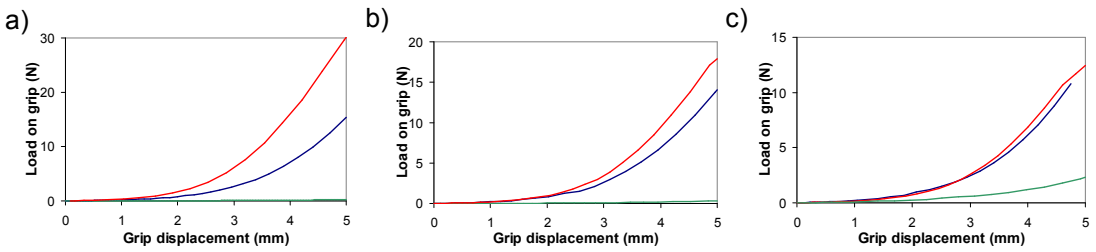


*Figure 3.13: Plots comparing grip displacement to load on grip for FEM with a) two, b) three and c) four fibre families loaded at 0º, 45º and 90º indicated by the blue, green and red lines respectively.*

### 3.6.3 Boundary conditions

Due to axis symmetry of the model, it was possible to only use a section of the geometry. As discussed previously, this is advantageous as it allows the simulation to solve quicker as there are a reduced number of elements.

Three models were constructed for this investigation, an entire model, a half and a quarter model. All dimensions were taken from Section 3.6.1, where a murine skin sample was modelled. For the purposes of this investigation the skin was assumed to be an Ogden material where $\mu$ = 10 and $\alpha$ = 0.01 for all three simulations. A tied interface was employed between the rigid body grips and the skins surface where a prescribed displacement was applied in the positive x direction, causing the skin to stretch. All contact penalties and mesh densities were kept consistent.

Figure 3.14 shows an image of the pre-processed full model, where the moving grip is shown in orange, the stationary grip in blue and the disc of skin in purple. For all models, a constraint was implemented in the z direction to stop the skin from folding during the simulation. The load on the moving grips and the relative grip displacement were documented. Figure 3.15 show a diagram of the half and quarter model constraints.

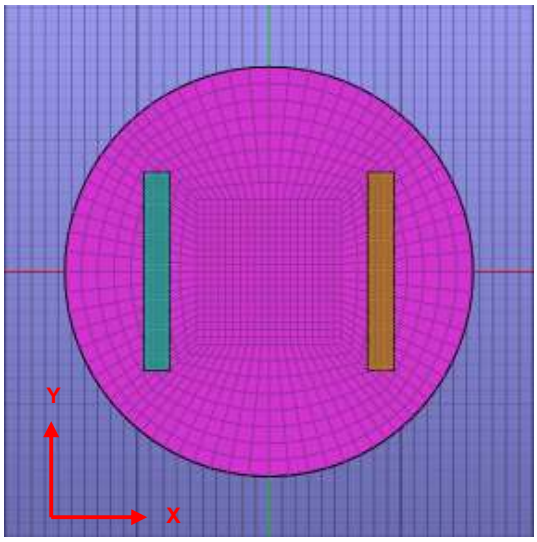


*Figure 3.14: Image showing full portion FEM of skin (purple), stationary grip (blue) and moving grip (orange).*

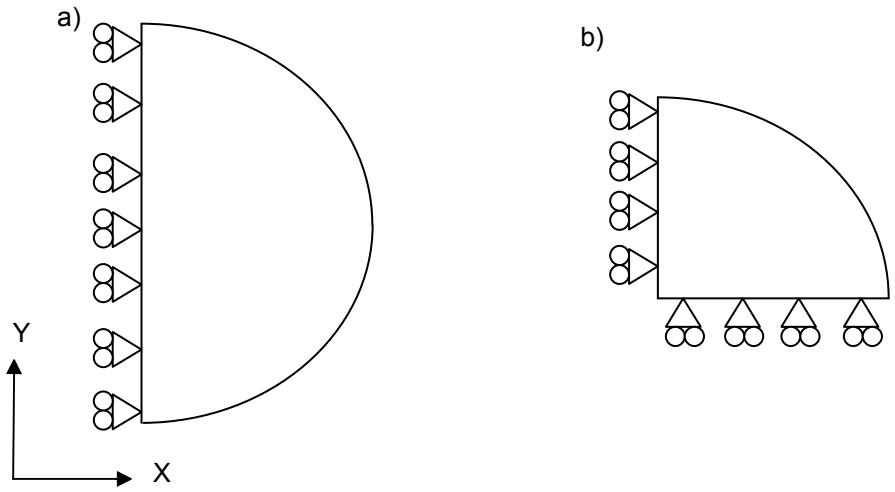


*Figure 3.15: Diagram showing the constraints implemented on a) the half and b) the quarter FEM of skin.*

Figure 3.16 illustrates the plots comparing load on moving grip to the grip displacement for all three models. In the quarter and half models the grip displacement was multiplied by 2 and the load on the grip was multiplied by 2 for the quarter model as only half the grip was modelled. This was so that the measurements were comparable with a full scale model.

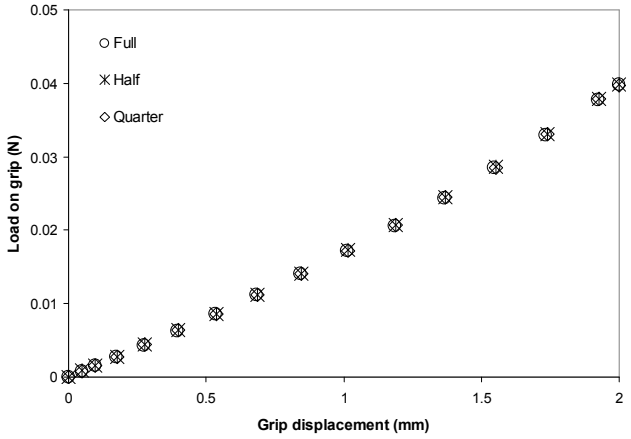


*Figure 3.16: Plot comparing load on grip with grip displacement for the full, half and quarter portion models.*

Figure 3.16 shows that all three models produce identical load – displacement relationships, therefore it is appropriate to use the quarter portion model to reduce computational time.

### 3.6.4 Contacts

The contacts were used between the skin and grips and a prescribed displacement was applied to the rigid body grips causing the skin to stretch. The grips were required during inverse analysis to determine the tensional load applied to the skin. It was extremely important that the contacts were of adequate strength to prevent the skin mesh becoming detached from the grip. Hence the effects of skin and grip meshes were tested.

To examine the effects of altering the mesh on the grip to skin contacts, two mesh shapes were examined. Figure 3.17 shows both meshes, firstly a non-conforming mesh between the skin and grip was reviewed followed by a conforming mesh. For both FEMs the skin material is shown in yellow and the grips are indicated in orange.

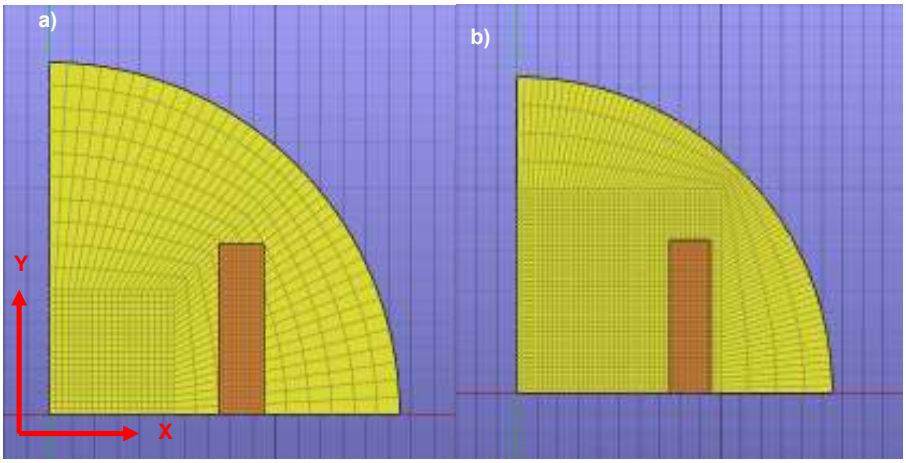


*Figure 3.17: Images showing the meshes tested for the a) non-conforming and b) conforming mesh between the skin and grip.*

A prescribed displacement in the positive x direction was then executed. Figures 3.18 and 3.19 show the mesh deformation at the grip-to-skin contact for the non-conforming and conforming meshes respectively.

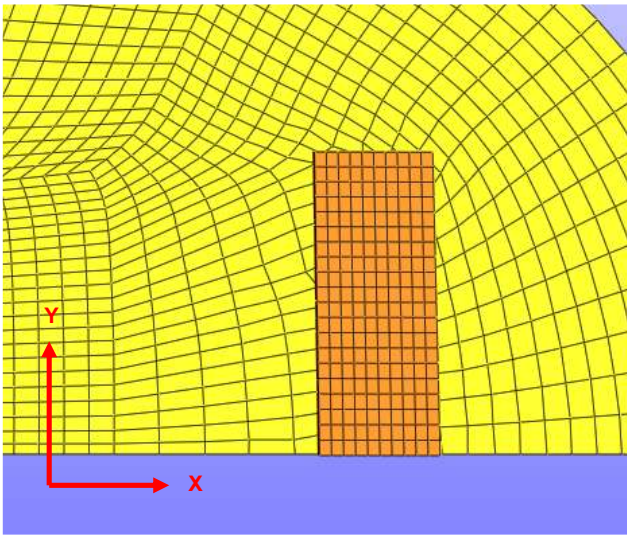


*Figure 3.18: Image of non-conforming mesh between grip and skin at a displacement of 5mm in the x direction.*

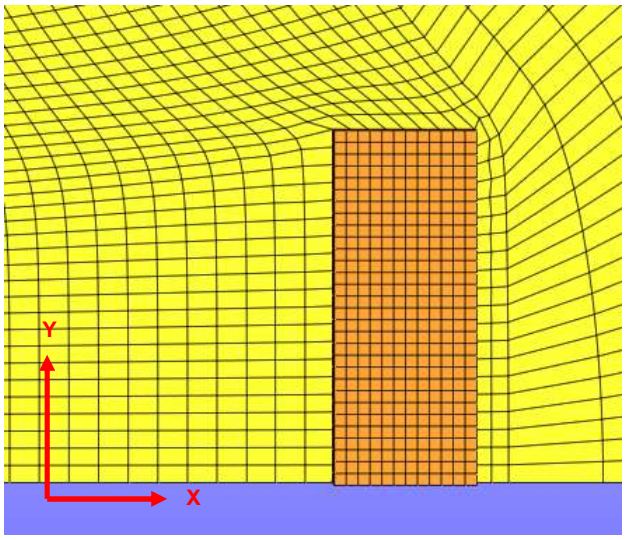


*Figure 3.19: Image of conforming mesh between grip and skin at a displacement of 5mm in the x direction.*

Figure 3.18 illustrates that there appears to be a large amount of mesh deformation on the skin mesh at a maximum displacement of 5mm when a non-conforming mesh was used. However less mesh contortion was noted

when a conforming grip to skin mesh was implemented. This was further exemplified by Figure 3.20 which indicates the contoured plot of both the non-conforming and conforming meshes, showing the stress in the x direction at maximum grip displacement. Both indicate a stress concentration at the edge of the grip, which was to be expected as the force at this point was uneven because the skin around this area was unstressed, resulting in an area of high stress. Figure 3.20 a) shows a less uniform stress distribution along the grip to skin contact line when compared to Figure 3.20 b), demonstrating deformities in the non-conforming grip to skin mesh. This uneven stress distribution is evidence that the mesh may not be in full contact with the grip, hence at high x displacements the skin becomes misaligned with the rigid body grip.

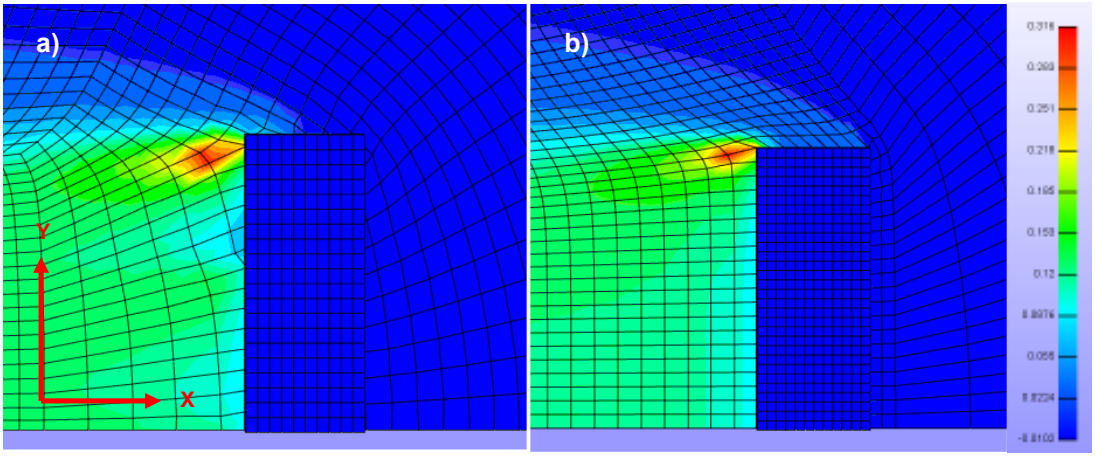


*Figure 3.20: Contoured plots showing stress in the x direction at maximum displacement for the a) non-conforming and the b) conforming grip to skin meshes (scale on the right indicates the stress in MPa).*

Therefore a conforming mesh between the skin and grip was used. Furthermore, the contact was given a stiffness of at least 10 times the bulk modulus of the skin material. Using contacts for this problem was not ideal, however with a high contact penalty and conforming mesh, the contacts were shown to work well, hence could be used within inverse analysis.

### 3.6.5 Mesh convergence

Mesh convergence tests aim to determine the lowest number of elements which is reasonable for the FEM. This is achieved by comparing with models that possesses an increased number of elements so that once the analysis converges to a satisfactory level, hence indicating that the FEM has reached an appropriate mesh density.

For this evaluation, assumptions were made for both models. These were as follows:

- Geometries described in Section 3.6.1 for the murine skin sample were used, where only one quarter of the model was analysed.
- A conforming mesh between the skin and grip was implemented and contact strength of 10000 was applied
- For simplicity, the skin was modelled as an Ogden material with coefficients of $\alpha=10$ and $\mu=0.01$MPa and the grips were assumed to be rigid bodies.
- The mesh density of the grips remained constant for all tests .
- The grips were given a displacement of 5mm in the positive x direction. However the model was a quarter, therefore the actual displacement when scaled to a full scale model was 10mm. This was an estimated average strain taken from the experimental data obtained in Chapter 2.

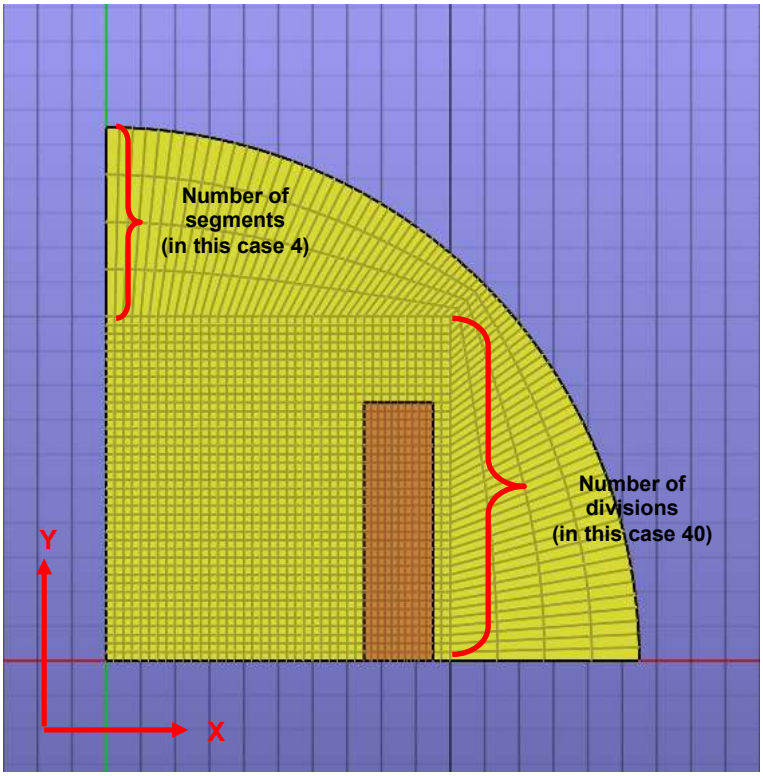


*Figure 3.21: Illustration of the parameters used to create the meshes for the convergence tests.*

Figure 3.21 illustrates the parameters used to create the meshes and Table 3.5 presents the proposed densities for all convergence tests. Convergence test 1 shows the model with the smallest number of elements which is considered to be reasonable. Successive convergence tests (tests 2, 3 and 4) analyse models with a denser mesh. The model must accommodate for three fibre families, therefore there were three layers of elements in the z plane.

Table 3.5: Description of the skin meshes for all three convergence tests.

| ***Mesh convergence test number*** | ***Divisions*** | ***Segments*** | ***Total number of elements*** |
|---|---|---|---|
| ***1*** | 20 | 4 | 1680 |
| ***2*** | 40 | 4 | 5766 |
| ***3*** | 60 | 4 | 12240 |
| ***4*** | 80 | 4 | 21120 |

The plot in Figure 3.22 compares the grip displacement to the grip load for all four convergence tests. There was a slight deviation between the mesh used

for convergence test 1 and the successive meshes 2, 3 and 4, therefore at high levels of strain it would be inappropriate to use this mesh density. Hence the mesh used for convergence test 2 was employed as the final mesh for the FEM of human and murine skin in tension, producing accurate results but with a coarser mesh.

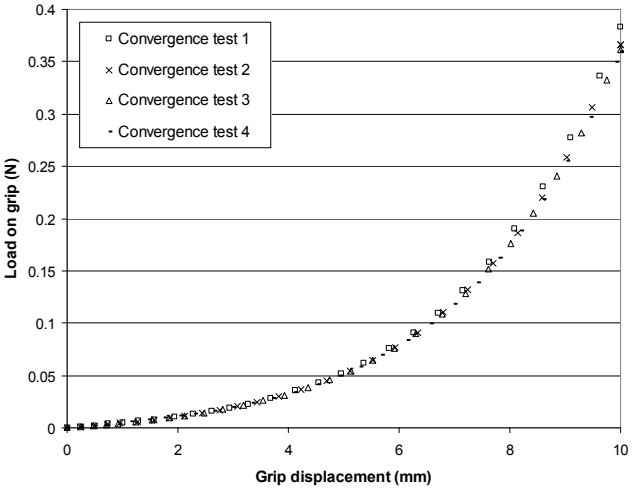


*Figure 3.22: Plot comparing grip displacement to load on grip for all four mesh convergence tests.*

# 3.7 Resulting FEM of human and murine skin in tension

Section 3.6 described the process used to develop an anisotropic FEM of human and murine skin in tension. Table 3.6 shows a summary of the chosen parameters, for both anisotropic models of human and murine skin in tension.

Table 3.6: Summary of the FEM parameters for the human and mouse skin models in tension.

| | ***Mouse skin in tension*** | ***Human skin in tension*** |
|---|---|---|
| ***GEOMETRY*** | | |
| Skin thickness (epidermis + dermis) (mm) | 0.453 | 1.86 |
| Area of grip in contact with skin ($mm^2$) | 15 | 15 |
| ***CONSITITUTIVE MODEL*** | | |
| Skin for all fibre families | Transversely isotropic V – W | Transversely Isotropic V - W |
| Grips | Rigid body | Rigid body |
| ***BOUNDARY CONDITIONS (assuming quarter model)*** | | |
| Constraints along slices | x and y planes | x and y planes |
| Surface of skin | z direction | z direction |
| ***CONTACTS*** | | |
| Between skin and grips | Tied interface | Tied interface |
| ***MESH DENSITY*** | | |
| Skin | 5760 | 5760 |
| Per grip | 360 | 360 |

Figure 3.23 shows post processed images of the FEM used to represent human skin in tension in the x-z and x-y plane, where the scale refers to the displacement in the x plane. The grips indicated in Figure 3.22 a) show that the thickness of the skin becomes distorted at high displacements because the grips do not move closer together as the material thins. However as the

majority of the force was in the x plane, when implementing inverse calculations, the grip displacement was correlated against the load on the grip in the x direction. Therefore the relative load in the z plane would have minimal affect on the parameters. Observations were similar for the FEM of murine skin in tension detailed in Figure 3.23. As both models have an identical number of elements and surfaces, both models took 48 seconds to converge, which was small enough to be used for inverse analysis.

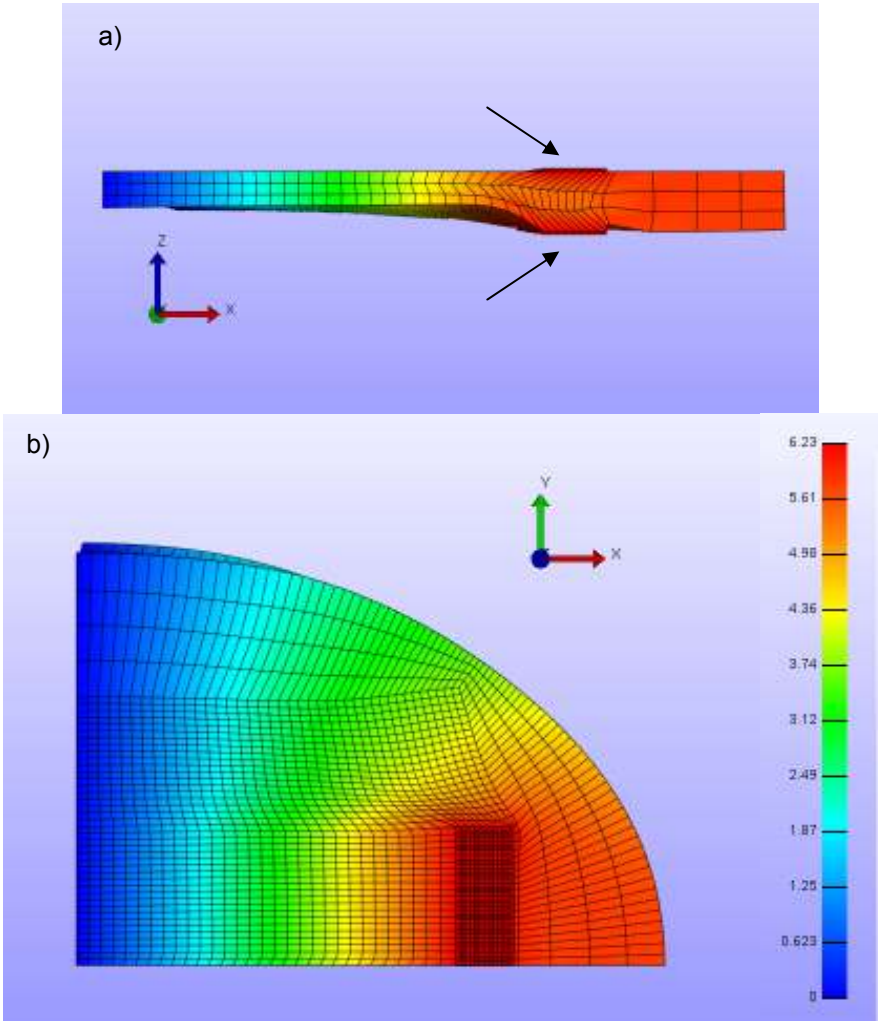


*Figure 3.23: Images of the FEM of human skin in tension in a) the x-z plane and b) the x-y plane, where the right hand scale denoted the displacement in the x direction and the grips are indicated on by an arrow.*

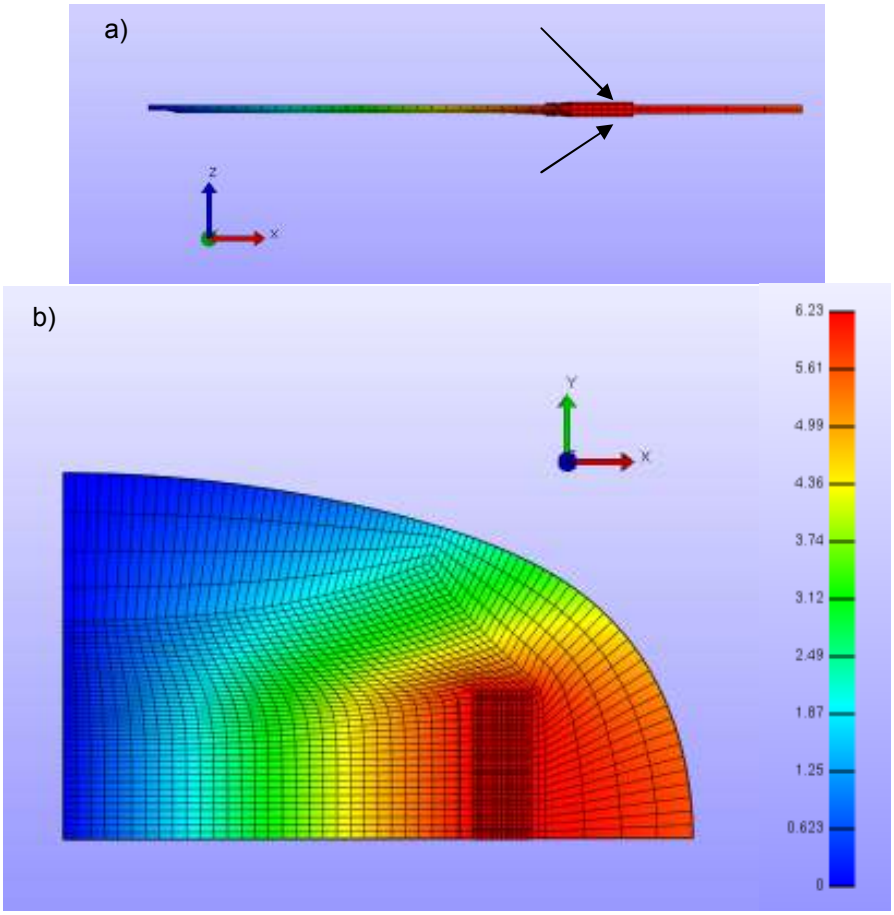


*Figure 3.24: Images of the FEM of murine skin in tension in a) the x-z plane and b) the x-y plane, where the right hand scale denoted the displacement in the x direction and the grips are indicated on by an arrow.*

## 3.8 Discussion

The key aim of this study was to develop two sets of FEMs which enabled a high level of accuracy, using appropriate constitutive models, whilst maintaining the ability to solve in a relatively short period of time. The finite element software, FEBio, was chosen for all FEMs as accommodated for numerous constitutive models which could be used to represent skin.

Firstly, appropriate geometries were specified for both the modelled skin tissue, in addition to the grip and indenters used during experimentation. Skin layer thicknesses were assumed from literature for the FEM of skin indentation (sections 3.4-3.5), whereas total skin thickness measurements

were taken from histological examination detailed in Chapter 2 for the models of human and murine *ex vivo* skin in tension (sections 3.6-3.7). The assumptions made for the model of skin indentation may affect the optimal material coefficients extracted, as the load was applied perpendicularly through the skin material. To increase model accuracy, OCT, MRI and ultrasound imagery could have been used to visualise the thicknesses of the skin layers, and validate skin deformation measurements. However, the model is still applicable when used as a tool to model skin deformation at loads comparable to microneedle application, as appropriate skin layer thickness measurements were sourced from the literature.

To ensure the success of the inverse calculations shown in Chapter 4, it was crucial that appropriate constitutive models were selected to represent skin. The Ogden model of hyperelasticty was chosen to describe skin for the FEM of skin indentation, as a wider range of nonlinear stress-strain relationships were produced when compared with the M-R model. A transversely isotropic material was chosen to represent the three fibre families present within the modelled human and murine skin in tension. This model was shown to have anisotropic properties, comparable to those found for *ex vivo* skin in Chapter 2.

For all FEMs describing the skin during indentation and in applied tension, it was found that the number of elements could be reduced by constructing a quarter of the skin mesh and by using appropriate boundary conditions. This resulted in a decreased number of elements, hence a reduction in computing time. Furthermore, the total number of elements within all models could be optimised by conducting mesh convergence tests to establish the smallest mesh density which could still give accurate results.

For both sets of FEMs the contacts were of extreme importance as they separated or attached the skin material to either a grip which is applying the load or to an indenter which is compressing the skin. The strength of these contacts were manipulated and it was documented that by using a strength which was at least 10 times the Bulk Modulus values of the skin material, both meshes did not detach or penetrate. However, this should only be noted as

an estimation and all contacts should visually be checked after inverse analysis, to ensure that the model with the extracted parameters does still maintain non penetrating or detaching contacts.

When considering the model of skin indentation, it may have been beneficial to assume the skin was a single geometry, rather than three, to remove the contacts between each skin layer. However the model was still shown to converge with the contacts between each skin layer, so it was possible to use the FEM for inverse analysis. Additionally, by modelling the skin as three geometries, it was easier to assign properties to each layer during inverse analysis. When examining the deformation of the skin material in the x-z plane at high x displacements for models of human and murine skin in tension (Figures 3.23 and 3.24), it was remarked that the skin mesh became distorted around the grip. Although the grip to skin contact did not lose its integrity, this should be checked after inverse calculations. The model could have included a displacement for the grips in the z direction to discount this action, however as the Poisson's ratio of the material was not known, it was difficult to conclude an appropriate displacement. Moreover, the grips could have been removed and a nodal force applied to the skin, rather than applying a load with the grips. However, there was not an appropriate function within FEBio which recorded the load; hence a rigid body was required for this problem.

Previous studies which have used finite element analysis to represent skin have incorporated several constitutive models including linear elastic (Delalleau et al., 2006; Pailler-Mattei et al., 2008) and nonlinear models such as M-R (Hendriks et al., 2003; Hendriks et al., 2006), neo-Hookean and Ogden (Shergold et al., 2006b; Evans, 2009). In a study by Shergold and Fleck in 2006, it was observed that the Ogden material model was better equipped at describing the mechanical characteristics of skin when compared with the M-R model, which is in agreement with this presented study. Early research has generally ignored the multilayer architecture of skin, assuming that the material is a single layer in thickness (Delalleau et al., 2006; Delalleau et al., 2008b). However, some have begun to realise the importance of including a stratified aspect to their analysis, but more commonly the influence

of the underlying hypodermis is ignored (Hendriks et al., 2003; Hendriks et al., 2006). This study has found that when applying a load which acts through the thickness of the skin material, it is crucial to include this layer, as even at low indentation depths, the constraints underneath the skin can manipulate the mechanical characteristics of the tissue. This is an important observation for microneedle application, as this layer is largely ignored and could be important when considering skin puncture.

Several transversely isotropic and anisotropic models have been developed many of which have been discussed in Chapter 1. However, only a few have used such models to describe mechanical properties of skin (Bischoff, Arruda and Grosh, 2004). This study has shown that by incorporating families of fibres within an isotropic matrix, a wide range of anisotropic stress –strain relationships can be represented, allowing for inverse calculations within Chapter 4.

# 3.9 Conclusions

This Chapter has outlined a development process for establishing FEMs of skin during indentation and when under tension. Both sets of models have allowed for complex mechanical characteristics which have been relatively under explored at present. Due to the success of this study, Chapter 4 aims to use these models for inverse calculations, where the computational measurements were compared against *in vivo* and *ex vivo* data obtained in Chapter 2. Such models have been used to detail the mechanical response of *in vivo* skin tissue at loads comparable to microneedle application, in addition to facilitating in the comparison between the mechanical properties of *ex vivo* skin tissues.

# CHAPTER 4

# INVERSE ANALYSIS TO DESCRIBE THE MECHANICAL PROPERTIES OF SKIN

## 4.1 Introduction

Chapter 2 has described the development of a methodology for analysing the mechanical properties of human skin *in vivo* using indentation and a series of tensile tests examining the anisotropic properties of both human and murine *ex vivo* skin. Chapter 3 established a set of appropriate FEMs, one of which depicts the skin as a multilayered material incorporating the epidermis, dermis and hypodermis during indentation, the second represents the anisotropic characteristics of murine and human skin in tension. This Chapter aims to combine these two approaches using inverse analysis, a technique used to fit mathematical expressions, in this case the constitutive models used in the FEMs, to experimental data. This will not only provide validated FEMs of skin which can be used to optimise microneedle device design, but the resultant parameters themselves can be utilised to further describe the characteristics of the tissue.

This approach has been used in several studies to identify the material characteristics of biological tissues such as skin, but few have noted the multilayer structure or used anisotropic models to compare skin samples from human and murine donors. Within this Chapter, robust techniques were established to extract the material parameters from constitutive models which

gave the best agreement with the experimental data. Previous studies have explored a range of methods and algorithms with varying degrees of success, hence this Chapter aims to not only assess the outcomes of the inverse process in terms of the mechanical properties extracted, but also the methods used.

## 4.2 Aims of the study

The investigation aimed to achieve the following:

1. Develop extraction algorithms that could provide material model parameters which allow for a closeness of fit between all experimental measurements and sets of FEMs.
2. Analyse parameters to further describe the mechanical properties of skin.
3. Create FEMs of *in vivo* skin indentation and *ex vivo* skin in tension which replicate experimental measurements.

## 4.3 Parameter extraction process

All parameter extraction algorithms (see Appendix C and D) were programmed in Matlab (version 7.9.0529, Math Works, US), as it provided all the features required for the study. It was possible for the FEBio input to be recoded within the Matlab program developed for the parameter extraction, so that a separate output file was produced documenting the load and displacement of a selected rigid body. As stipulated in Chapter 3, both indenters for the multilayer skin model, and the grips for anisotropic model of skin in tension, were assumed to be rigid body objects, therefore it was possible to use this feature to produce load – displacement measurements for the model. Figure 4.1 shows a general flow diagram depicting the parameter extraction process.

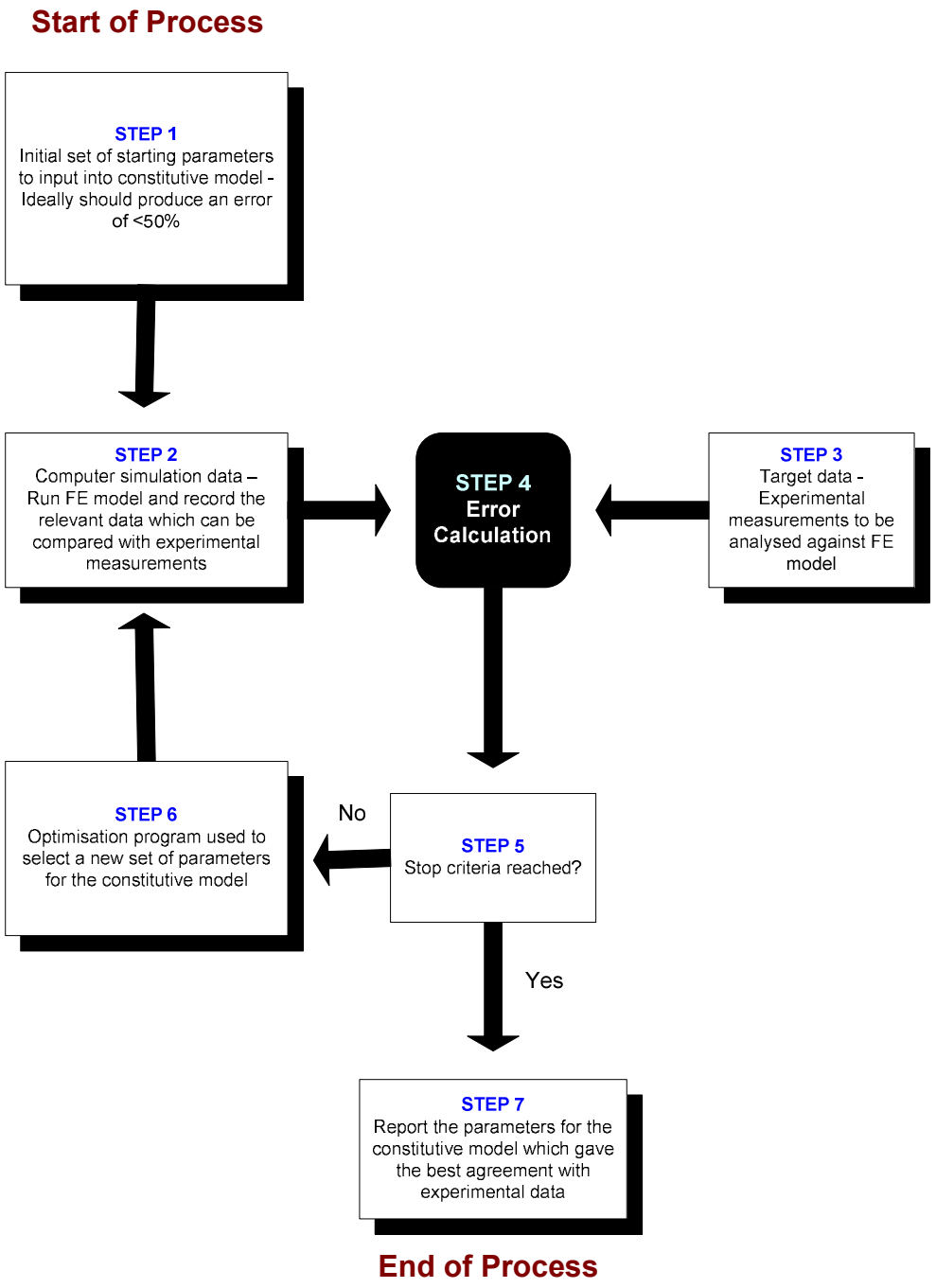


*Figure 4.1: Flow diagram showing the parameter extraction process.*

Chapters 2 and 3 describe the steps involved in the development of appropriate FEMs and the collection of experimental measurements (steps 2 & 3 from Figure 4.1), however it also important to highlight the other stipulations of the parameter extraction shown in Figure 4.1. A cost function

is required for the simulation which must be appropriately chosen. Additionally, it is critical that a relevant optimisation algorithm is used to select the next set of input parameters for the constitutive model. All optimisation functions have a stop criterion where no further iterations occur, this can be either when the change in the cost function value is low enough to assume a local minimum has been reached, or when a maximum number of iterations have occurred.

### 4.3.1. Cost function

For the optimisation algorithm to establish a new set of input parameters, the agreement between the experimental readings and computational data required quantification. Thus the choice of the cost function was crucial for this comparison. The root mean squared error ($R^2$) shown in Equation 4.1 was chosen for the calculation, as it always equates to a positive integer and converges towards zero. The $R^2$ value measures the variability between the two sets of measurements, where when the value is closer to zero, there is less difference between the two data sets. Within this equation, $f_i^{EXP}$ was the target data, which was the experimental measurements, and $f_i^{FEM}$ was the computational data, which are the FEM results.

$$R^2 = \frac{\sum_i^n \left( f_i^{EXP} - f_i^{FEM} \right)^2}{\sum_{i=1}^n \left( f_i^{EXP} \right)^2 - \left[ \sum_{i=1}^n \left( f_i^{EXP} \right) \right]^2 / n} \qquad 4.1$$

As seen in Figure 4.1, this value is then fed to the optimisation algorithm which aims to reduce the $R^2$ until it is as close as possible to zero.

### 4.3.2. Optimisation algorithms

Optimisation refers to obtaining the best element from a set of available alternatives. In simple terms, this implies solving problems to minimise or maximise a function (the $R^2$ between computational and experimental data),

by systematically choosing values (the parameters for the constitutive model) from within a defined set. Such problems tend to have several local minima, which the algorithm aims to seek out. However it should be noted that it is incredibly challenging to obtain a global minimum within the number of iterations specified, so generally only a local minimum is extracted. Therefore it is important to select starting parameters for the optimisation algorithm that produce relatively close data to the experimental observations to obtain the best solution set possible (Step 1, Figure 4.1). As each optimisation algorithm extracts end values using different methods within varying boundaries, it is important that an appropriate method is used for the problem.

Researchers have used several optimisation algorithms within inverse finite element calculation to extract information on the mechanical properties of biological tissues such as skin, some of which are a function accommodated by Matlab, whereas others have been specially coded. One such method uses a stochastic technique, where random parameter sets within a boundary are implemented within the FEM. After a suggested number of iterations the program terminates and outputs the parameter set which produced the lowest error (local minima) (Evans and Holt, 2009; Ghaemi, Behdinan and Spence, 2009). This is advantageous as it explores a wider variety of inputs, hence a more global minimium is achieved. This works well for models were the input parameters do not rely heavily on one another. Hence this method would not be appropriate for those FEMs which are sensitive to extreme changes in the input material coefficients, as they may have difficulty converging when using parameters which are vastly different from the initial set.

Another commonly used method is the Simplex algorithm (Arora, 2004) which is a function available within Matlab (Namani and Simha, 2009). As the program uses downhill optimisation, it is crucial that the starting set of parameters produce an outcome which is within a close range of the desired output. Other approaches include using Kalman's Filters (Delalleau et al., 2008a), which is a statistical method that uses measurements taken over time and produces an output which tends towards the true value, and constrained nonlinear programming (Liu, VanLandingham and Ovaert, 2009).

The optimisation program chosen was required to be appropriate for each problem, therefore each was assessed for the individual extraction process.

## 4.4 Extracting the mechanical properties of human skin *in vivo* using a multilayer FEM

Two sets of *in vivo* skin indentation measurements were taken on human volunteers, using two geometrically different indenters. These experimental observations were then modelled using finite element analysis, where the skin was given stratified properties by incorporating the epidermis, dermis and hypodermis. Consequently for this problem, six parameters required optimisation, which were $\mu$ and $\alpha$ for all three skin layers. These were as follows:

- $\mu_E$ (Pa) and $\alpha_E$ - parameters for the epidermis
- $\mu_D$ (Pa) and $\alpha_D$ - parameters for the dermis
- $\mu_H$ (Pa) and $\alpha_H$ - parameters for the hypodermis

As two FEMs were used in the parameter extraction process, the cost function which was to be minimised by the optimisation algorithm, was the average root mean squared error of both, termed $R_{ave}^2$.

### 4.4.1 Parameter extraction algorithm

As discussed previously, all FEBio files were written as text documents which were then processed within the FEBio solver. This allowed for alterations to the file prior to processing. Therefore, the new material parameters suggested by the optimisation program could be added, in addition to the inclusion of an output section which logged the load on the rigid body indenter along with the relative displacement. This data was then compared with the experimental measurements. All extraction algorithms were written in Matlab

(see Appendix C) and Figure 4.2 shows a flow diagram of the program developed to solve this problem, covering steps 1-5 in Figure 4.1.

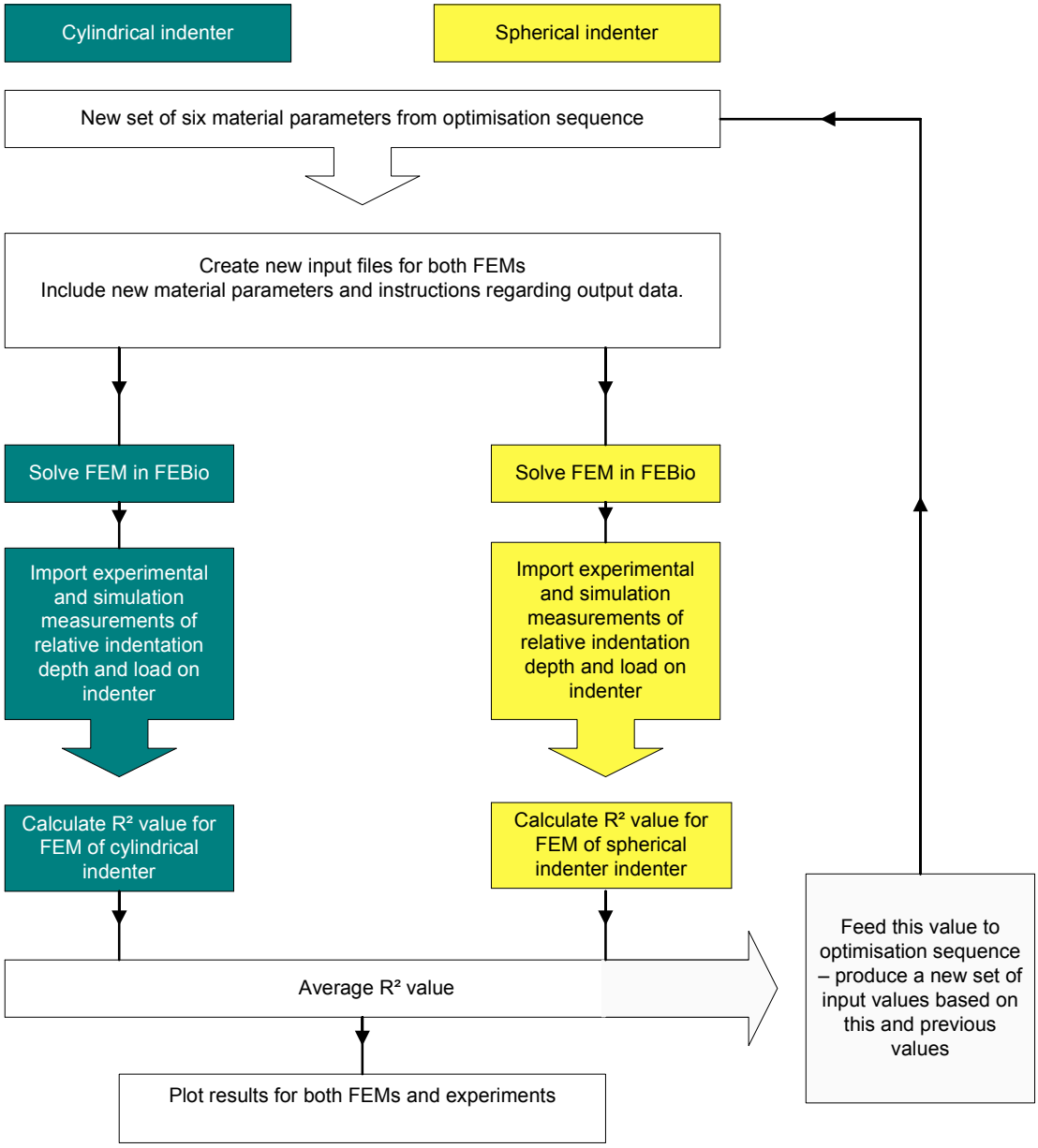


*Figure 4.2: Flow diagram showing the algorithm developed to compile and run the FEBio files, and compare the simulation results to the experimental indentation measurements for the multilayer FEMs of human skin indentation in vivo.*

Multiple parameters were optimised within this problem, hence a wrapper function was required. This program also delegated the tasks so that the operations were performed in the correct order shown in Figure 4.1.

### 4.4.2 Optimisation algorithm

There was little information regarding a possible set of starting parameters, and the three skin layers were independent of one another hence the variables were less sensitive to extensive change. Therefore a stochastic optimisation program was chosen as it searched a wider pool of potential parameters for the constitutive equations.

The program took the initial set of starting parameters and set bounds which were initially 30% either side of the initial parameter set, subsequently 20 random sets of parameters within these bounds were then implemented within both FEMs. The 20 sets were then plotted in a hierarchical order with the parameters which produced the lowest $R^2_{ave}$ value positioned at the top. New sets of coefficients were then inputted into the FEMs and if a parameter set produced an $R^2_{ave}$ value which was lower than any of those within the sorted 20, this was then placed within the hierarchy. Thus moving the bounds between which the parameters could be sourced. When the simulation was complete, the top 20 sets of parameters which gave the lowest calculated $R^2_{ave}$ were outputted.

With this approach, the stop criterion was set to the total number of iterations rather than a minimum as with the Simplex algorithm, hence this point was estimated appropriately. This was achieved as after 1000 iterations, the variation in the top twenty parameter sets was small enough (<5% difference) to conclude that a local minimum had been sourced.

### 4.4.3 FEM considerations

Chapter 3 described the development process used to establish stratified FEMs of human skin indentation. However it was noted that extreme variations in the inputted material parameters for the constitutive models, could affect the accuracy or convergence ability of the model. Therefore, when selecting a set of input variables for the constitutive model, variations

75% either side of this initial set were tested to check that the model could still converge. Also, the number of retries for both FEMs was stipulated at 50, in case the model could not converge well with the inputted parameter set. Moreover, all contacts were visually checked after the parameter extraction had taken place with the optimal material parameters to ensure that no penetration was occurring between the layers and the skin to indenter contact.

The assumption was made that for all initial sets of starting parameters that the values for $\alpha_E$ and $\mu_E$ would provide a stiffer and more linear mechanical response when compared to the two underlying layers. This was due to the influence of the stiff SC (Papir et al., 1975). Consequently the starting coefficients for $\alpha_H$ and $\mu_H$ would allow for a much more nonlinear behaviour and a reduced stiffness.

### 4.4.4 Data analysis

After parameter extraction two sets of outputs were analysed, these include:

- Closeness of fit between experiment and model measurements
- Optimal material parameters obtained
- Variations between volunteers

## 4.5 Results

The parameter set for the constitutive model which gave the lowest $R^2_{ave}$, the top 20 parameter sets which gave the lowest $R^2_{ave}$ and the lowest $R^2_{ave}$ were examined for the purposes of this study. This allowed for comparisons between subjects and provided clues as to how efficient the optimisation algorithm had been. Furthermore, principal observations taken from the experimental measurements shown in Chapter 2 were analysed against the model data to further test the effectiveness of the optimisation algorithm.

### 4.5.1 Closeness of fit with experimental data

Table 4.1 shows the lowest calculated $R^2_{ave}$ value for each subject and the $R^2$ value for both FEMs using two geometrically different indenters applied to skin, termed $R^2_{cyl}$ and $R^2_{sph}$ for the cylindrical and spherical indenter respectively.

Table 4.1: Root mean squared errors for all volunteers comparing FEMs of cylindrical and spherical indenter applied to skin.

| ***Volunteer Number*** | ***Root mean squared error for model of cylindrical indenter*** $R^2_{cyl}$ | ***Root mean squared error for model of spherical indenter*** $R^2_{sph}$ | ***Average root mean squared error*** $R^2_{ave}$ |
|---|---|---|---|
| ***1*** | 0.0345 | 0.0088 | 0.0217 |
| ***2*** | 0.0131 | 0.000643 | 0.00687 |
| ***3*** | 0.0136 | 0.0133 | 0.01345 |
| ***4*** | 0.000152 | 0.0019 | 0.00103 |
| ***5*** | 0.07408 | 0.0237 | 0.0488 |
| ***6*** | 0.0022 | 0.0129 | 0.00755 |
| ***7*** | 0.0513 | 0.0267 | 0.039 |

Figure 4.3 shows plots for all seven volunteers indicating relative indentation depth against indentation force for both indenter geometries, comparing *in vivo* measurements to optimised FEM data. It can be seen that a closer relationship between model and experiment was observed at a lower $R^2_{ave}$.

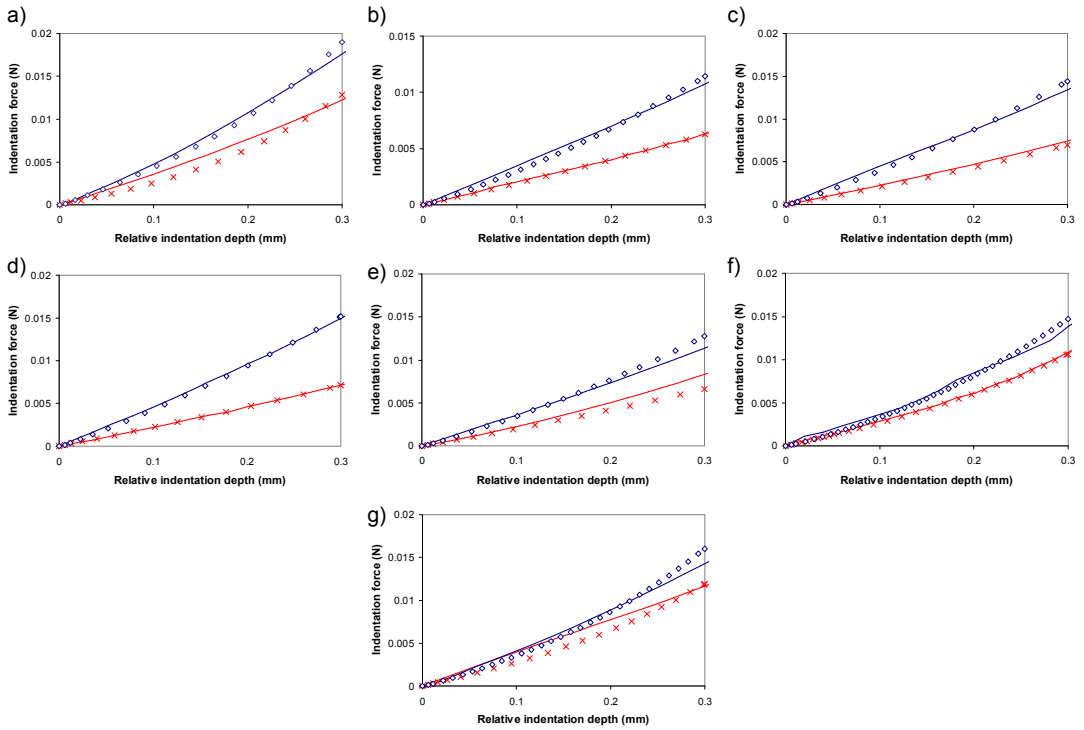


*Figure 4.3: Plots comparing FEM data from the cylindrical and spherical indenters applied to skin (shown by the cross and diamond markers respectively) to the experimental measurements (illustrated by the solid red and blue lines respectively). Graphs a-g represents volunteers 1-7.*

## 4.5.2. Optimal material parameters

Table 4.2 shows the optimised Ogden coefficients comparing each subject which calculated to give the lowest $R^2_{ave}$, for each skin layer after 1000 iterations.

Table 4.2: Individual Ogden material coefficients for the three major layers of human skin.

| ***Subject Number*** | ***Age (years)*** | ***Sex (M/F)*** | ***Epidermis*** | | ***Dermis*** | | ***Hypodermis*** | |
|---|---|---|---|---|---|---|---|---|
| | | | ***μ (MPa)*** | ***α*** | ***μ (MPa)*** | ***α*** | ***μ (MPa)*** | ***α*** |
| ***1*** | 24 | F | 5.18 | 1.65 | 0.0207 | 2.70 | 0.0105 | 29.8 |
| ***2*** | 26 | F | 2.92 | 6.35 | 0.0152 | 3.29 | 0.0094 | 3.43 |
| ***3*** | 25 | F | 5.86 | 2.74 | 0.0264 | 4.41 | 0.0085 | 6.88 |
| ***4*** | 24 | F | 7.48 | 2.42 | 0.0205 | 3.19 | 0.0094 | 4.03 |
| ***5*** | 22 | M | 3.95 | 3.17 | 0.0205 | 3.30 | 0.0089 | 5.30 |
| ***6*** | 26 | M | 1.21 | 2.47 | 0.0309 | 2.53 | 0.0128 | 20.4 |
| ***7*** | 22 | M | 2.10 | 2.07 | 0.0244 | 3.59 | 0.0132 | 25.3 |
| ***Average*** | | | 4.10 | 2.98 | 0.0226 | 3.29 | 0.0104 | 13.6 |
| ***Standard Deviation*** | | | 2.05 | 1.45 | 0.00468 | 0.572 | 0.00175 | 10.4 |

Figure 4.4 shows the stress compared to the stretch for the average parameters shown in Table 4.2 calculated for all three skin layers. Figure 4.5 presents how the properties of these three layers compare to other models of human skin (Dunn et al., 1985; Shergold et al., 2006b; Evans and Holt, 2009), two of which used the Ogden model of hyperelasticity with extracted μ values of 0.11Mpa and 10Pa and α coefficients of 9 and 26 respectively.

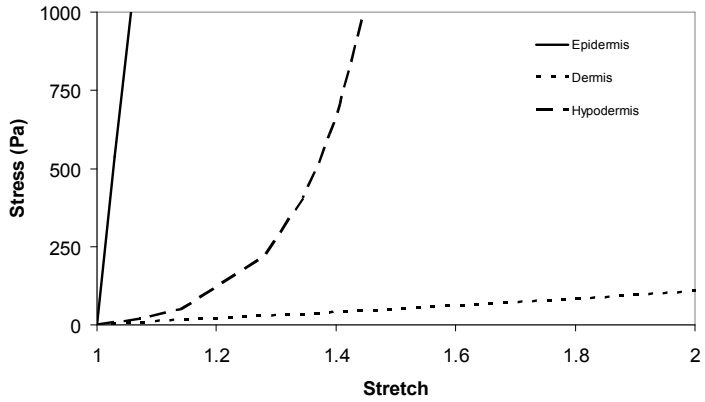


*Figure 4.4: Plot relating stress to stretch for the average Ogden material coefficients for each skin layer.*

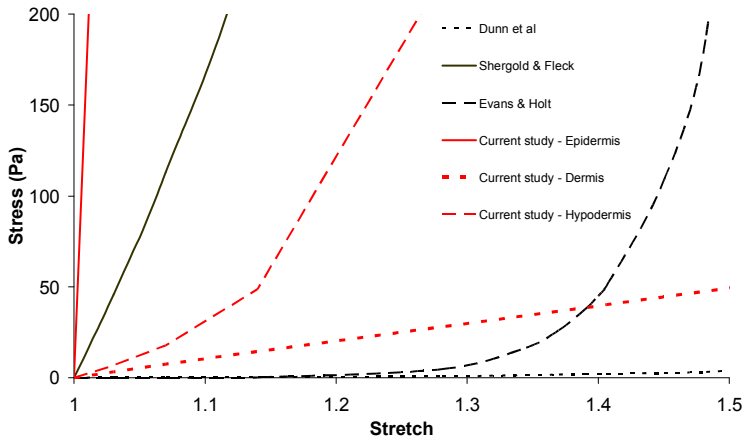


*Figure 4.5: Plot relating stress to stretch for the average Ogden material coefficients for each skin layer and three other comparative studies.*

### 4.5.3. Variations between subjects

When comparing the mechanical properties of *in vivo* skin from all seven volunteers it was possible to analyse the six parameters for all three skin layers to account for any correlations. Figure 4.6 shows the distribution of the $\alpha$ and $\mu$ coefficients which gave the lowest $R^2_{ave}$ analysed for all subjects, for epidermis, dermis and hypodermis respectively.

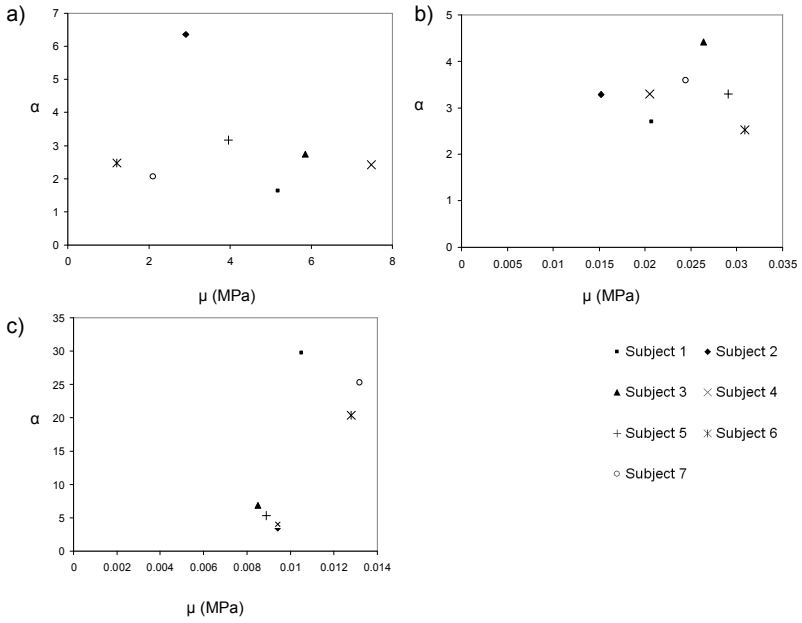


*Figure 4.6: Plot showing $\mu$ and $\alpha$ coefficients obtained after parameter extraction which gave the lowest $R^2_{ave}$ for all subjects for the a) epidermis, b) dermis and c) hypodermis.*

Figure 4.7 show the stress – stretch plots for each volunteer using each optimal Ogden parameter set extracted for each skin layer, compared to the average Ogden parameters for all subjects. This again shows the variations between the extracted Ogden coefficients for the hypodermal skin layer across all seven volunteers, compared to the epidermis and dermis, with volunteers 1, 6 and 7 having the greatest level of exponential stiffening within this layer.

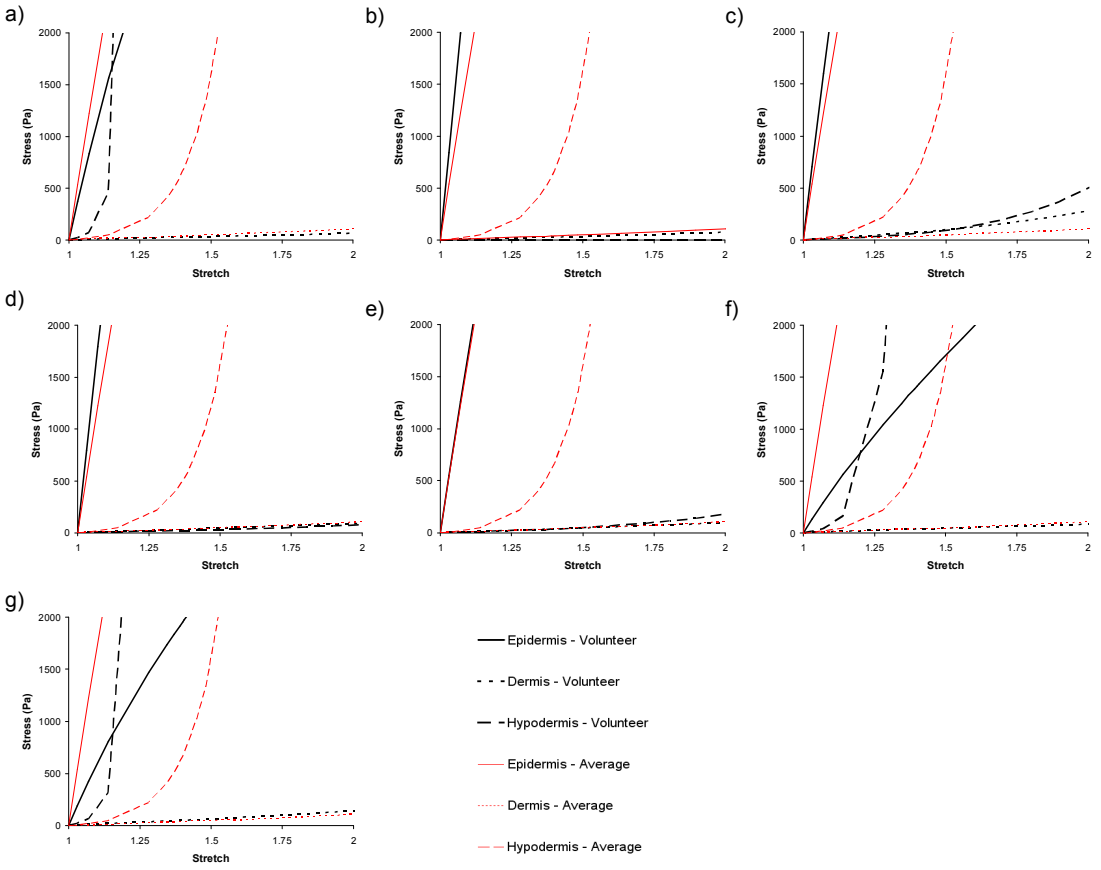


*Figure 4.7: Plots for each volunteer comparing the stress – stretch response of each skin layer using the optimal Ogden material parameters extracted, compared to the average Ogden material parameters, relative to each skin layer (volunteers 1-7 represented by a)- g)).*

If a parameter has less effect on the mechanical behaviour of the model, it could be hypothesised that a high range of values for that parameter will be present within the top 20 parameter sets, as a similar $R^2_{ave}$ was calculated using such values for that particular material coefficient. Figure 4.8 illustrates the range of top 20 values which gave the lowest $R^2_{ave}$ for each volunteers, relative to all six parameters.

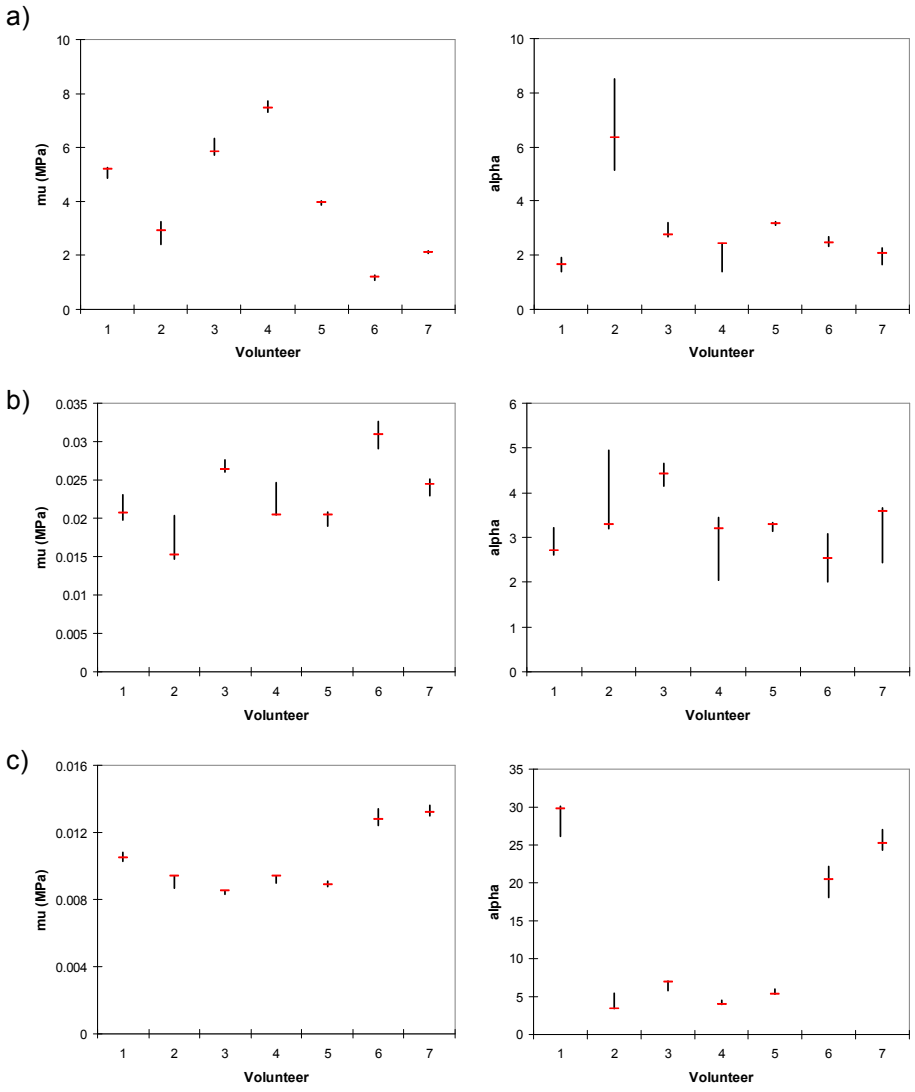


*Figure 4.8: Plots illustrating the range of values, for each subject, within the top 20 hierarchy for material coefficients μ and α for the a) epidermis, b) dermis and c) hypodermis. (The optimal coefficient which gave the lowest $R^2_{ave}$ is shown by the red hash.).*

# 4.6. Discussion

The principal aim of this study was to develop a parameter extraction algorithm which could select a single set of Ogden material coefficients that correlate with experimental observations for the three skin layers, from the stratified FEM. The Ogden coefficients were then used to develop a validated model of human skin, and as a tool to compare the difference between subjects. Moreover, the FEM of human skin could replicate small levels of deformation comparable to microneedle application, to aid in the optimisation of microneedle array design.

The degree of correspondence between simulation curves and *in vivo* data varied between human volunteers with $R^2_{ave}$ values ranging from 0.00105 to 0.0488 (Table 4.1), implying a model accuracy of between 99.9% and 95.1%. This relationship is further illustrated in Figure 4.3, where the best fit between experiment and model was shown by less deviation between both measurements. The Ogden material model was shown to allow for a large range in mechanical behaviours, possibly allowing for the strong agreement between model and experiment.

Figure 4.4 compares the stress to stretch relationship for the average Ogden material coefficients for each skin layer, documented in Table 4.2. As predicted, the average material coefficients for the epidermis give rise to a significantly stiffer and more linear mechanical behaviour than the underlying dermal and hypodermal layers. This response is characterised by the comparatively low $\alpha_E$ and the high $\mu_E$ average parameters. On the contrary, the average values for the dermis give rise to an almost linear stress – stretch relationship which experiences very low amounts of stress at increased stretch. This is most likely due to the low average $\alpha_D$ and $\mu_D$ calculated for this skin layer, across all subjects. However, the stress – stretch behaviour of the average hypodermis parameters allow for highly nonlinear behaviour, with exponential stiffening upon the application of strain, which is a result of the high average $\alpha_H$ coefficient. The optimal shear stiffness variables, μ, for each skin layer shown in Table 4.2 can be evaluated against the Young's Modulus values calculated in Chapter 2. The average $E_S$ values for the cylindrical and spherical indenters were 39.6kPa and 65.86kPa respectively, across all seven tested volunteers. The average shear modulus values for the dermal and hypodermal layers were within the same order of magnitude, at 22.6kPa and 10.4kPa, as the average $E_S$ variables. As a result, this suggests a correlation between the basic experimental analyses and the inverse finite element methods. However, it should be noted that altering the Ogden values could give rise to a similar mechanical response for the skin material as a whole because only local minimum was obtained. Hence increased stiffness in one layer may be compensating for a lower stiffness in another. Nonetheless,

results indicate that inverse finite element methods may be a useful tool to predict the behaviour of skin that is subjected to small strains.

Figure 4.5 shows how the average Ogden coefficients extracted for each skin layer compared to a selection of studies which have also explored the possibility of modelling the mechanical properties of skin using inverse techniques. Shergold *et al*. used penetration data for human skin to establish a model also using the Ogden strain energy density function. In their investigation the skin was assumed to be a single layer, and when examined against the average parameters obtained within this study, they appear to show a relative stress – stretch response which correlates well with the average material coefficients for the epidermal and hypodermal layer. More recently the Ogden model has been used to describe the properties of skin during in plane tension (Evans and Holt, 2009). A significantly higher nonlinear mechanical response was noted within this model, due to a high α value of 26, the shape of which follows that of the stress- stretch behaviour of the hypodermis, with the key variation relating to the level of stretch experienced prior to exponential stiffening. Finally, using an early model by Dunn *et al.* to detail the mechanical characteristics of skin; a resemblance to the average extracted dermal Ogden coefficients found within this study was shown. It should be noted however, due to the anisotropic nature of skin tissue, the mechanical properties vary considerably in different planes. Therefore it is unsurprising that the stress – stretch responses are different for each separate study, and for those obtained during this investigation. Additionally, the variations within the testing methodology and the *ex vivo* nature of some of the investigations used within this comparison, may have resulted in the documented discrepancies. What is apparent is that each skin layer produces a wide range of stress – stretch responses, which appear to average out across the whole spectrum of the three comparative studies by Dunn *et al*., Shergold *et al*. and Evans *et al*.

Using the optimal material coefficients for each skin layer, it was possible to further compare the mechanical characteristics of skin, relative to each subject, more so than through *in vivo* measurements alone. Figure 4.6 shows

the distribution of the $\alpha$ and $\mu$ values for each subject, relative to each skin layer. A wide distribution of $\alpha$ coefficients were extracted for the epidermis, however, there appears to be less difference between the $\mu$ values, suggesting the nonlinearity of this layer is generally uniform throughout. The distribution of the $\alpha$ and $\mu$ values for the dermis however are less spread, implying similarities in the mechanical characteristics of this layer between all subjects. This observation was further exemplified by the standard deviation values obtained in Table 4.2 for the dermal layers. Finally, there is a close relationship between $\mu$ and $\alpha$ values for the hypodermis when comparing 4 out of the seven volunteers where as subjects 1, 6 and 7 have an increased $\alpha$ value. This shows a correlation with the experimental analysis illustrated in Chapter 2, where volunteers 1, 6 and 7 were found to have the stiffest skin. As all volunteers tested within this study were within an age range of 22-26 years, the variations within the mechanical characteristics obtained cannot be truly attributed to age.

These observations were further noted within Figure 4.7, which illustrates the comparison between the stress – stretch response of each skin layer compared to the average parameters, for all seven subjects. As discussed previously, there is little variation between the mechanical properties of the dermis across all seven subjects, this is reflected in the agreement between all stress – stretch plots for the dermal skin layer. Volunteers 2-5 show a similar mechanical response for the optimal Ogden material coefficients for the epidermis, with volunteers 1, 6 and 7 illustrating slightly less stiffness within this skin layer. This is most likely due to the lower $\mu_E$ value extracted for those subjects. Although a wide range of $\mu$ values for the epidermis were extracted across the volunteers, there was still a high level of conformity across the stress- stretch plots for each subjects, suggesting that different Ogden coefficients can result in a similar stress – stretch behaviour. These graphs further reinforce the differences noted between each subject regarding the mechanical characteristics of the hypodermis. Volunteers 2- 5 all illustrate low stiffness within this tissue, not dissimilar to that found within the dermal layer. On the contrary, volunteers 1, 6 and 7 all show high levels of exponential stiffening at increased strain within the hypodermis, due to the

high $\alpha_H$ parameters extracted, again in agreement with experimental analyses as these volunteers were found to have stiffer skin. This is particularly interesting for volunteers 6 and 7 as both models illustrate comparatively less stiffness within the epidermis, hence the increased exponential stiffening within the hypodermis may be compensating for this characteristic, whilst still producing a stiffer response when compared to skin models representing volunteers 2-5.

These findings further reinforce the importance of including the hypodermis within FEMs of skin indentation and the level of conformity noted across all subjects regarding the mechanical characteristics of the dermis. Additionally, the results show a level of correspondence with experimental data as the volunteers shown to have the stiffest skin from experimental analysis also have higher levels of exponential stiffening within the hypodermis, from the optimal Ogden material parameters.

The stochastic optimisation program outputted the top 20 parameter sets which calculated to give the lowest $R^2_{ave}$. By examining this range, it may be possible to determine the influence of that material parameter on the model as a whole. Those with a wider range could be considered to be less influential as a similar $R^2_{ave}$ value was calculated regardless of any noted variations. This hypothesis does follow the general observations noted within Figures 4.8, as the properties of the dermal layer appear to be uniform throughout all seven volunteers, possibly implying that the manipulation of the epidermal and hypodermal layers contribute to the majority of variations noted between each subject. This is emphasised by the wider range of $\alpha$ and $\mu$ coefficients for this skin layer when compared to the hypodermis and epidermis. As a general rule, the range of the top 20 $\alpha$ values are higher than the $\mu$ values for all three skin layers across all volunteers, although subjects 3 and 5 have the least variability compared with volunteer 2 which has the greatest variability across all top 20 coefficients. Although these observations cannot be directly proved, they do serve as a further potential explanation for the trends found. Importantly, the hypothesis also allow for the same general conclusions noted previously.

The lower model accuracy values, shown in Table 4.1, may be due to limitations within the model and/or experimental procedures discussed in Chapters 2 and 3. Factors which may have affected the optimal parameters that were extracted relate to skin layer thickness measurements and the constraint placed along the base of the hypodermal tissue within the FEMs. To increase the accuracy of the optimal material parameters obtained, *in vivo* imaging techniques such as OCT or MRI could be used to measure skin layer thicknesses relative to each subject and to validate deformation measurements. The inclusion of an additional indenter geometry, which could possibly have been larger in size to help characterise the deeper layers, may also have allowed for the addition of muscle tissue to the model thus reducing the effect of the base constraint. However, as only small deformations were measured, the modelled skin tissue thickness may have been sufficient to reduce the influence of the base constraint on the hypodermal layer. As discussed previously, the trends noted within the experimental data can also be observed with the extracted material parameters, suggesting the approaches used in this study have worked well.

A 2006 study by Delalleau *et al*. also used *in vivo* indentation and inverse analysis to characterise the mechanical properties of human skin. However, the skin was assumed to be a single layer of linear elastic material and therefore experimental and computational results did not correlate well for some subjects. This may to be due, in part, to the simplicity of the model compared to the stratified skin tissue. This presented study considered skin to be a multilayer composite but inaccuracies were still noted between experimental and FEM measurements. It may therefore be necessary to account for other aspects such as viscoelasticity and anisotropy within future FEMs. In a subsequent study by Tran *et al*. in 2007, *in vivo* indentation of the forearm was coupled with nonlinear finite element analysis. This investigation modelled the skin as a stratified tissue along with underlying muscles and validated the modelled skin deformation using MRI images. Although the principles of this published study are comparable to this work, the magnitudes of the modelled deformations are significantly larger and therefore cannot be

extrapolated to this study, where micron scale skin deformations have been examined.

In conclusion, this investigation has extracted a single set of Ogden material parameters relative to each volunteer for human skin incorporating the three major skin layers, which provide a good agreement with experimental measurements. When compared against other skin models, the average optimal parameters extracted show a range of stress – stretch relationships, which average out across the spectrum of the three comparative studies. The optimal material parameters extracted also emphases the variations between volunteers and show a strong agreement with experimental analyses, particularly for the extracted parameters for the hypodermal skin layer. Finally, the inverse analysis used has allowed for the establishment of stratified FEMs which can detail the deformation of skin upon load application comparable to microneedle application, allowing for further interpretation in Chapter 5.

# 4.7. Extracting the mechanical properties of human and murine *ex vivo* skin using an anisotropic FEM

Chapters 2 and 3 collected data relating to the mechanical properties of *ex vivo* human and murine skin in tension and established a set of FEMs representing these measurements. The skin model incorporated three fibre families embedded within an isotropic V-W matrix to represent the dermal fibres and to allow for anisotropic behaviours. As a result, a large number of parameters required optimisation, all of which are shown in Table 4.3.

Table 4.3: Summary of parameters used in constitutive model of human and murine skin

| ***Symbol*** | ***Description*** | ***Units*** |
|---|---|---|
| ***ISOTROPIC MATRIX*** | | |
| $C_1$ | V-W coefficient | Pa |
| $C_2$ | V-W Coefficient | Pa |
| ***FIBRE FAMILY 1*** | | |
| $C_{3,1}$ | Scales exponential stresses | Pa |
| $C_{4,1}$ | Rate of un-crimping | - |
| $\lambda_1$ | Fibre stretch of straightened fibres | - |
| $a_1$ | Angle of fibre vector relative to 0º axis (converted to a vector within parameter extraction algorithm) | º |
| ***FIBRE FAMILY 2*** | | |
| $C_{3,2}$ | Scales exponential stresses | Pa |
| $C_{4,2}$ | Rate of un-crimping | - |
| $\lambda_2$ | Fibre stretch of straightened fibres | - |
| $a_2$ | Angle of fibre vector relative to 0º axis (converted to a vector within parameter extraction algorithm) | º |
| ***FIBRE FAMILY 3*** | | |
| $C_{3,3}$ | Scales exponential stresses | Pa |
| $C_{4,3}$ | Rate of un-crimping | - |
| $\lambda_3$ | Fibre stretch of straightened fibres | - |
| $a_3$ | Angle of fibre vector relative to 0º axis (converted to a vector within parameter extraction algorithm) | º |

In total 14 parameters were implemented within the FEM hence were used for inverse analysis, where $C_5$ and $C_6$ for all three fibre families were assumed using the 14 coefficients. By manipulating the fibre orientation for all three families, it was possible to change the direction of the load axis. This made it possible to analyse the mechanical characteristics of the skin material when the load axes were orientated at 0º, 45º and 90º. Hence the cost function, which was to be minimised by the optimisation algorithm, was the average root mean squared error of the three, termed $R^2_{ave}$.

### 4.7.1 Parameter extraction algorithm

All FEBio files were written as text files, which were then processed within the FEBio solver. This allowed for alterations to the file to take place prior to processing, hence the new material parameters for all fibre families and an output section which logged the load on the rigid body grip along with the relative grip displacement, could be added. This data was crucial as it provided the output which was to be compared with the experimental measurements. Figure 4.9 shows a flow chart showing the parameter extraction process which was written in Matlab (see Appendix D), for steps 1-5 indicated in Figure 4.1. A wrapper function was used as multiple parameters required optimisation. This also delegated the tasks so that the operation was performed in the correct order, indicated in Figure 4.1.

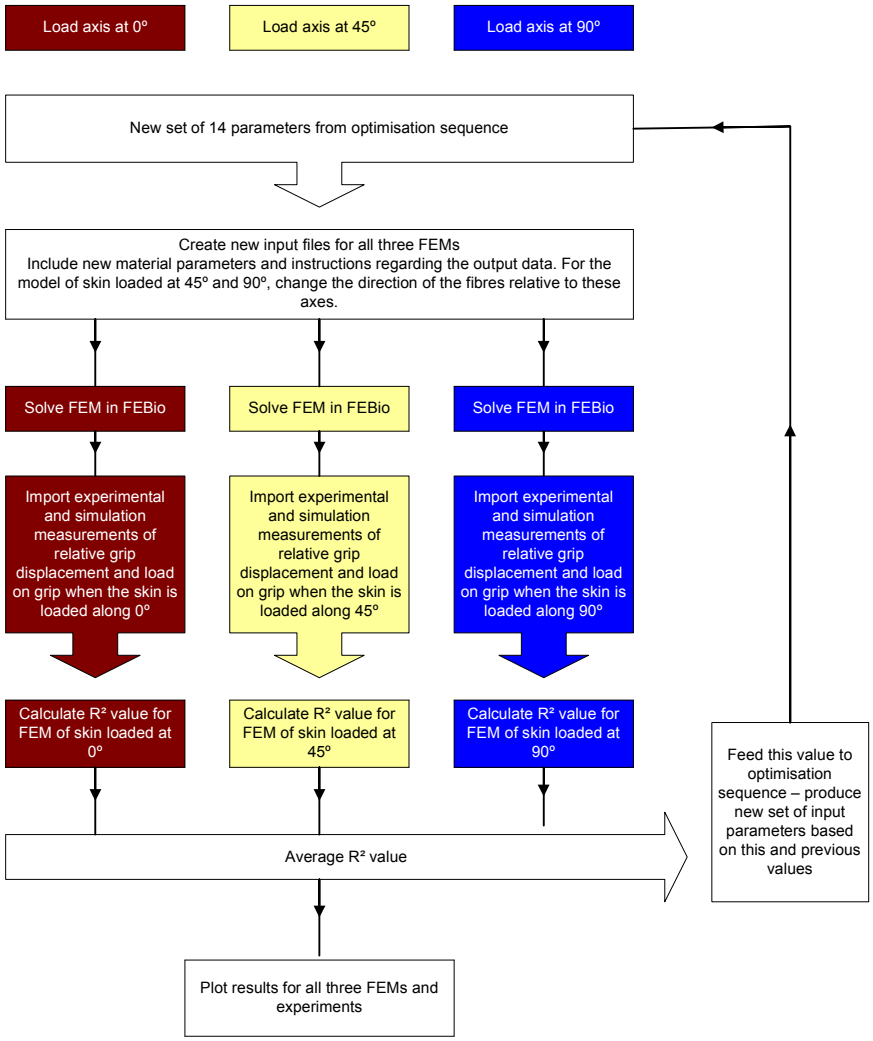


*Figure 4.9: Flow diagram showing the algorithm developed to compile and run the FEBio files, then compare the simulation results to the experimental measurements for the anisotropic models of human and murine skin in tension.*

## 4.7.2. Optimisation algorithm

For this problem a large number of coefficients needed to be optimised, so a suitable optimisation algorithm was required. It was noted that the 14 input parameters were sensitive to extreme alterations to the coefficients, resulting in vast changes to the mechanical response of the material. Also, the parameters themselves were not independent of one another, hence extreme variations in one parameter affected others, subsequently making convergence for the FEMs difficult. Stochastic optimisation was inappropriate

as it trialled values from a wide pool, hence the Simplex algorithm (Arora, 2004) was used to optimise this problem. The Simplex algorithm is a function in Matlab (fminsearch), where the maximum number of iterations can be stipulated. A test was performed where the total number of iterations was set to 1000, 1500 and 2000. When comparing the $R^2_{ave}$ value at 1000 and 1500 iterations, a variation between the two errors remained, implying that a local minimum had not yet been reached. However when comparing the $R^2_{ave}$ value at 1500 and 2000 iterations, no variation was noted, suggesting that it would be appropriate to specify a maximum number of iterations at 1500. After reaching this maximum, the fminsearch function outputted the set of 14 material coefficients that calculated to give the lowest $R^2_{ave}$ value.

### 4.7.3. FEM considerations

Chapter 3 detailed the development of a set of anisotropic FEM of human and murine skin in tension. Even though the Simplex algorithm generally prevents extreme variation within the parameter sets, the convergence ability of the model could be influenced by small changes in the input coefficients. Therefore the maximum number of retries for each step within all FEMs was set to 50, in case the model could not converge well for a particular parameter set.

Initial sets of parameters were chosen depending on the load - displacement data obtained from the *ex vivo* measurements. All fibre directions for the three fibre families were initially orientated at 2º, 120º and 240º, relative to the 0° axis.

### 4.7.4. Data analysis

After parameter extraction, the following outputs were assessed:

- Closeness of fit between experiment and model measurements
- Optimal material parameters obtained
- General differences between human and murine skin *ex vivo* tissue

# 4.8. Results

Two main outputs were recorded during inverse analysis, these were the correlation between experimental and model data post parameter extraction, characterised by the root mean square error calculations, and the parameter set which gave the lowest $R^2_{ave}$ for each skin sample. As discussed previously, this allows comparisons between groups and gives clues as to how efficient the optimisation algorithm was.

## 4.8.1 Closeness of fit with experimental data

After parameter extraction, the optimisation algorithm outputted the coefficients set which gave the lowest calculated $R^2_{ave}$ value during the process. Table 4.4 shows the $R^2$ values for each load axis direction of 0°, 45° and 90°, termed $R^2_0$, $R^2_{45}$ and $R^2_{90}$ respectively, and the average of all three calculations $R^2_{ave}$ for each human and murine skin sample. The average and standard deviation calculations for each $R^2_0$, $R^2_{45}$, $R^2_{90}$ and $R^2_{ave}$ values comparing human and murine skin groups are also shown. The experimental and computational measurements on average correlate slightly better for murine skin, implying the model can be used as a better representation of murine skin. All details regarding the location and selection of the skin samples and the donors are described in Chapter 2.

Table 4.4: The lowest $R^2_{ave}$ for all human and murine skin samples comparing experimental to computational measurements using inverse analysis.

| | ***Donor number*** | ***Location or number*** | ***Root mean squared error when load axis orientated at 0°, $R^2_0$*** | ***Root mean squared error when load axis orientated at 45°, $R^2_{45}$*** | ***Root mean squared error when load axis orientated at 90, $R^2_{90}$*** | ***Average root mean squared error, $R^2_{ave}$*** |
|---|---|---|---|---|---|---|
| ***Mouse*** | 1 | UB | 0.0037 | 0.0104 | 0.0151 | 0.0097 |
| | | LB | 0.0079 | 0.0011 | 0.0119 | 0.0070 |
| | 2 | UB | 0.0025 | 0.0114 | 0.0079 | 0.0073 |
| | | LB | 0.0012 | 0.0049 | 0.0054 | 0.0038 |
| | 3 | UB | 0.0092 | 0.0022 | 0.0051 | 0.0055 |
| | | LB | 0.0162 | 0.00094 | 0.0044 | 0.0072 |
| | 4 | UB | 0.0186 | 0.0087 | 0.0085 | 0.0119 |
| | 5 | UB | 0.0104 | 0.0019 | 0.0042 | 0.0055 |
| | | LB | 0.0133 | 0.0021 | 0.0031 | 0.0062 |
| | 6 | UB | 0.0067 | 0.0090 | 0.0070 | 0.0075 |
| | | LB | 0.0116 | 0.0156 | 0.0062 | 0.0112 |
| | 7 | UB | 0.0064 | 0.0076 | 0.0202 | 0.0114 |
| | | LB | 0.0051 | 0.0116 | 0.0202 | 0.0123 |
| | 8 | UB | 0.0061 | 0.0041 | 0.0074 | 0.0053 |
| | ***Average*** | | ***0.0085*** | ***0.0065*** | ***0.0090*** | ***0.0080*** |
| | ***Standard deviation*** | | ***0.0049*** | ***0.0045*** | ***0.0055*** | ***0.0027*** |
| ***Human*** | 1 | 1 | 0.0046 | 0.0059 | 0.00484 | 0.018 |
| | | 2 | 0.0086 | 0.0116 | 0.0102 | 0.0101 |
| | | 3 | 0.0065 | 0.0135 | 0.0036 | 0.0078 |
| | | 4 | 0.0084 | 0.0081 | 0.0143 | 0.0103 |
| | 2 | 1 | 0.0029 | 0.0144 | 0.0021 | 0.0065 |
| | | 2 | 0.0055 | 0.0302 | 0.0131 | 0.0163 |
| | | 3 | 0.0068 | 0.0029 | 0.0024 | 0.0041 |
| | | 4 | 0.0062 | 0.0028 | 0.0083 | 0.0058 |
| | ***Average*** | | ***0.0062*** | ***0.0112*** | ***0.0128*** | ***0.0099*** |
| | ***Standard deviation*** | | ***0.0018*** | ***0.0083*** | ***0.0142*** | ***0.0047*** |

Figure 4.10 and 4.11 shows the plots for all murine and human skin samples during the application of tension along three load axes, comparing experimental to computational analysis. The parameter set used for the constitutive model which calculated to give the lowest $R^2_{ave}$ value.

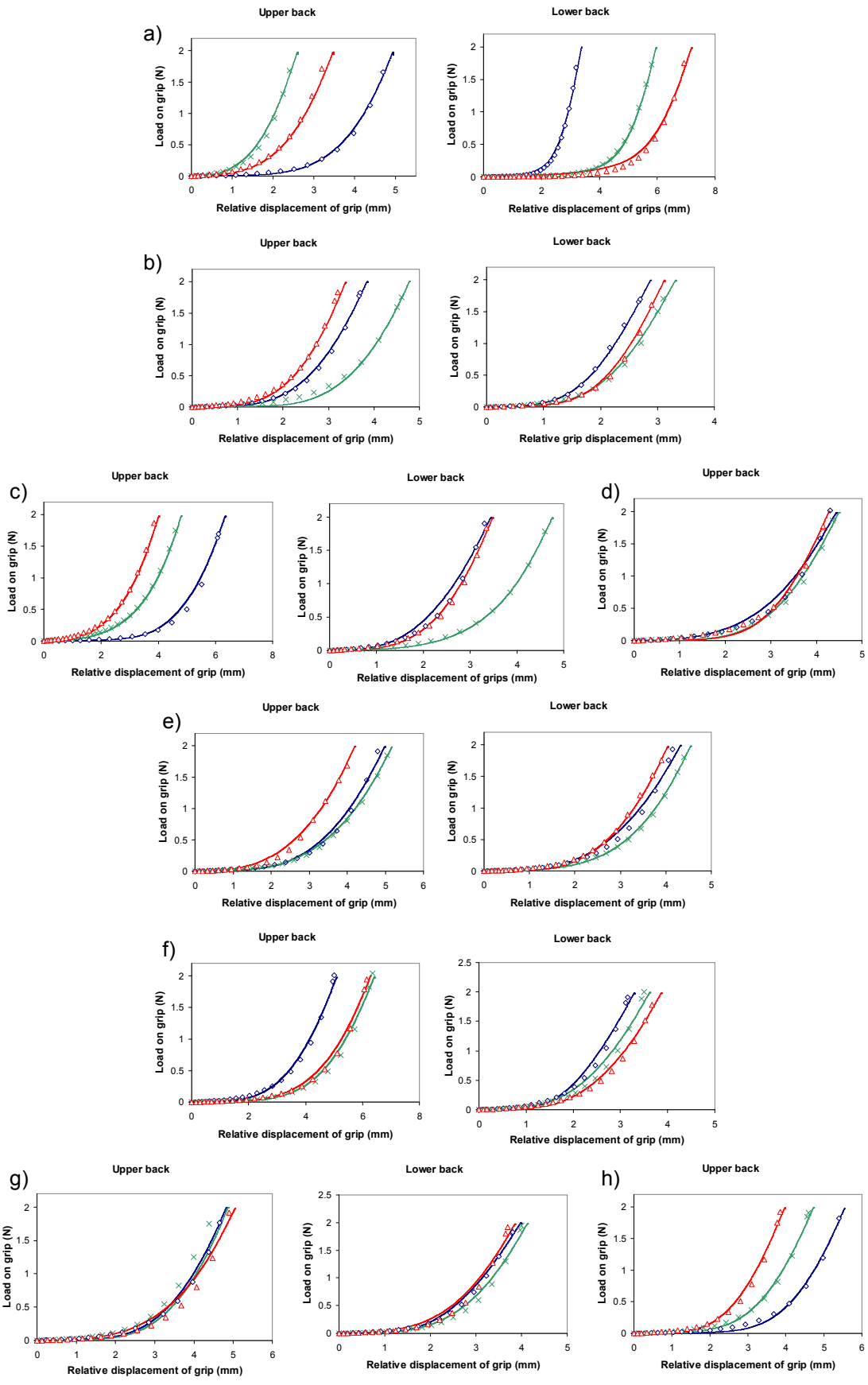


*Figure 4.10: Load – displacement curves for murine skin samples from donors 1 to 8 (a) –g) respectively) comparing experimental to FEM measurements using optimal material coefficients. Location is indicated at the top. Points and solid line indicate the FEM and experimental measurements respectively. Blue, green and red indicate measurements taken at 0°, 45° and 90 respectively*

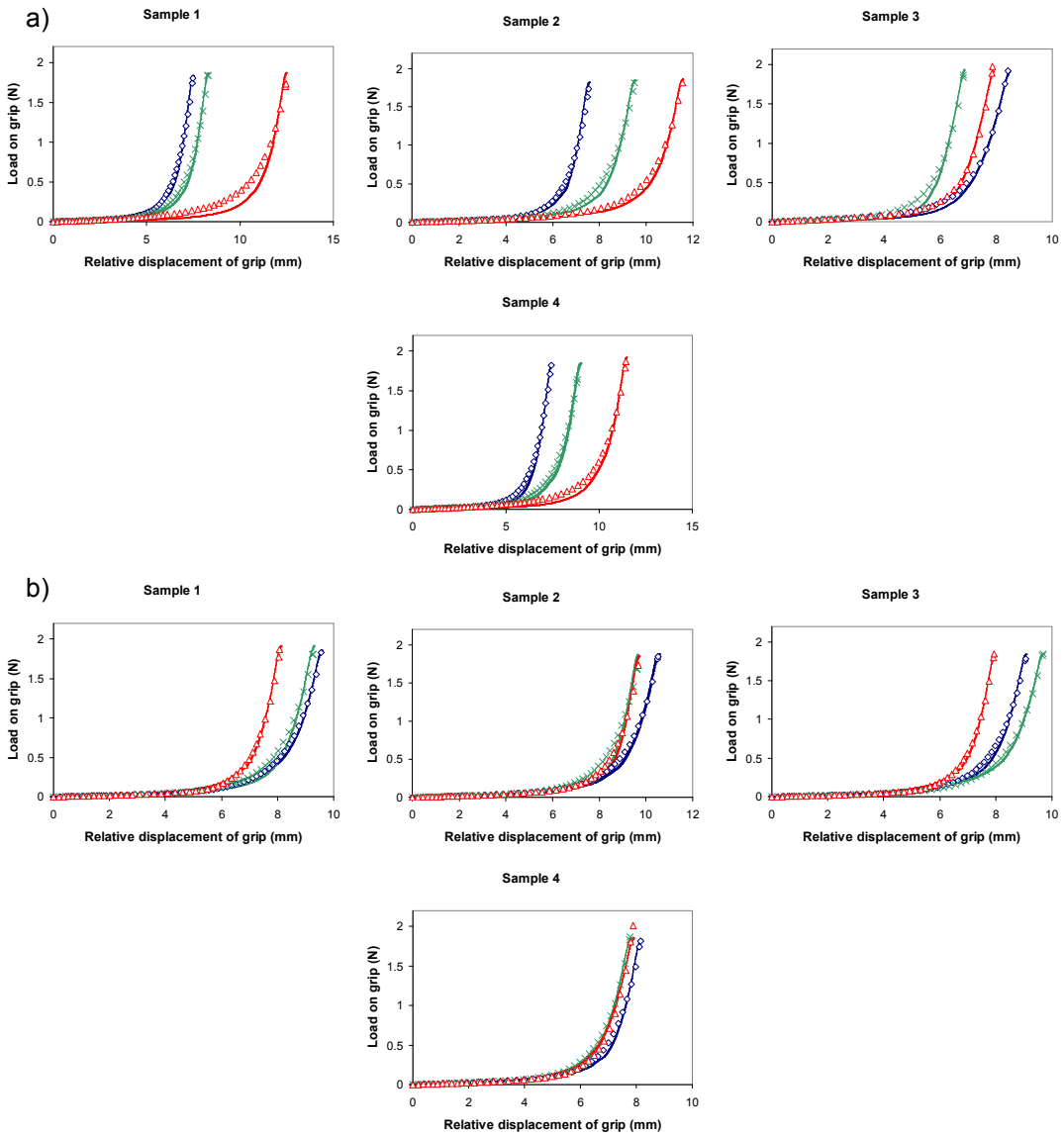


*Figure 4.11: Load – displacement curves for human skin samples from donors 1 and 2 (a) and b) respectively) comparing experimental to FEM measurements using optimal material coefficients. Location is indicated at the top. Points and solid line indicate the FEM and experimental measurements respectively. Blue, green and red indicate measurements taken at 0°, 45° and 90 respectively.*

.

Figure 4.12 illustrates the closeness of fit between model and experiment for a selection of human and murine skin samples (donor and location details are shown above each plot) at low load. Plots in Figures 4.10 and 4.11 show a high level of agreement between model and experimental data over the complete loading cycle. However this relationship is not translated to the initial stages of extension at low loads, depicted in the plots below.

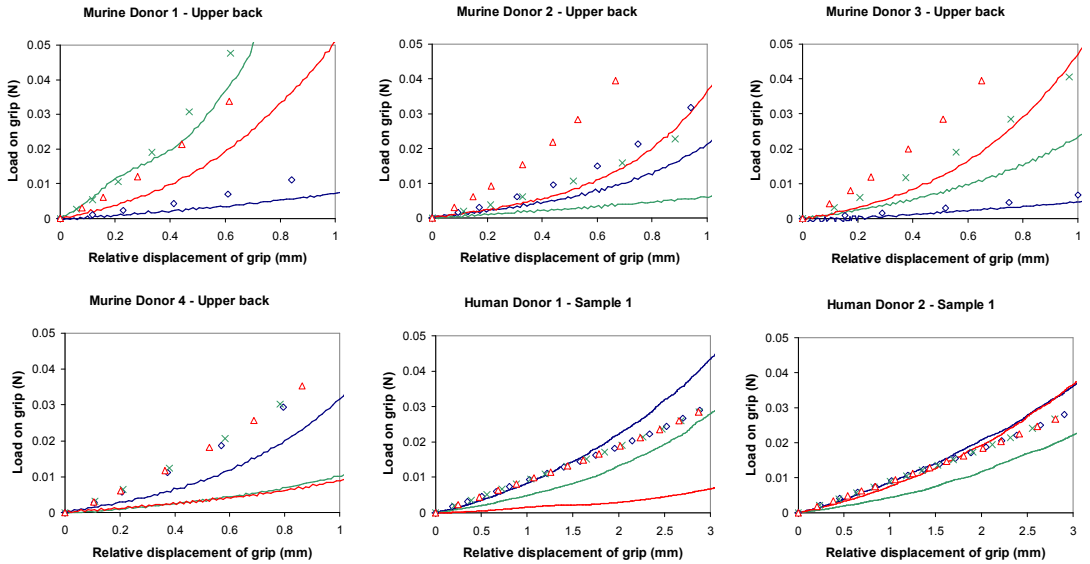


*Figure 4.12: Load – displacement curves comparing experimental to FEM measurements using the optimal extracted material coefficients, at low loads. Sample location and donor details are indicated at the top of each plot. Data shown in the solid blue, green and red lines indicate the experimental measurements taken at 0°, 45° and 90° respectively and points illustrated by the diamond, cross and triangle markers indicate the FEM measurements orientated at 0°, 45° and 90 respectively.*

## 4.8.2 Optimal material parameters

Tables 4.5 and 4.6 detail the parameters for the anisotropic material model extracted for murine and human skin respectively, which gave the lowest $R^2_{ave}$.

Table 4.5: Values for optimal material coefficients for anisotropic models of murine skin, post parameter extraction, correlated against *ex vivo* tensile tests.

| ***Donor number*** | ***Sample location*** | ***V-W coefficients for isotropic matrix*** | | ***Fibre family number*** | $C_3$ ***(MPa)*** | $C_4$ | $\lambda_m$ | $\alpha$ (º) |
|---|---|---|---|---|---|---|---|---|
| | | $C_1$ ***(MPa)*** | $C_2$ ***(MPa)*** | | | | | |
| ***1*** | UB | 0.000316 | 10.9 | 1 | 0.00630 | 23.5 | 1.69 | 1.97 |
| | | | | 2 | 0.00630 | 35.2 | 1.81 | 127 |
| | | | | 3 | 0.00560 | 25.4 | 1.06 | 213 |
| | LB | 0.000629 | 2.15 | 1 | 0.0000609 | 22.3 | 2.99 | 2.00 |
| | | | | 2 | 0.0000735 | 35.7 | 3.86 | 112 |
| | | | | 3 | 0.0000876 | 62.7 | 1.93 | 251 |
| ***2*** | UB | 0.000250 | 10.5 | 1 | 0.00620 | 24.2 | 2.04 | 2.25 |
| | | | | 2 | 0.00640 | 17.9 | 2.35 | 150 |
| | | | | 3 | 0.00750 | 39.6 | 1.87 | 236 |
| | LB | 0.000385 | 12.5 | 1 | 0.00240 | 31.5 | 1.47 | 2.09 |
| | | | | 2 | 0.00400 | 25.9 | 2.56 | 137 |
| | | | | 3 | 0.00200 | 40.6 | 1.12 | 275 |
| ***3*** | UB | 0.000288 | 9.12 | 1 | 0.00618 | 10.4 | 2.31 | 2.16 |
| | | | | 2 | 0.00923 | 15.0 | 2.04 | 140 |
| | | | | 3 | 0.0128 | 19.0 | 2.67 | 195 |
| | LB | 0.000311 | 9.66 | 1 | 0.00646 | 21.7 | 2.65 | 2.03 |
| | | | | 2 | 0.00929 | 24.6 | 2.44 | 168 |
| | | | | 3 | 0.00606 | 42.0 | 2.54 | 235 |
| ***4*** | UB | 0.000290 | 14.7 | 1 | 0.00653 | 15.5 | 1.82 | 1.87 |
| | | | | 2 | 0.00911 | 12.5 | 1.76 | 134 |
| | | | | 3 | 0.00131 | 18.1 | 2.05 | 241 |
| ***5*** | UB | 0.000180 | 11.7 | 1 | 0.00300 | 24.4 | 1.18 | 1.93 |
| | | | | 2 | 0.00300 | 20.3 | 1.19 | 117 |
| | | | | 3 | 0.00300 | 18.7 | 1.46 | 247 |
| | LB | 0.000103 | 12.0 | 1 | 0.00520 | 21.8 | 1.19 | 2.06 |
| | | | | 2 | 0.00520 | 20.8 | 1.35 | 115 |
| | | | | 3 | 0.00510 | 18.6 | 1.37 | 277 |
| ***6*** | UB | 0.000226 | 8.38 | 1 | 0.00290 | 13.2 | 2.15 | 2.38 |
| | | | | 2 | 0.00320 | 16.2 | 2.19 | 107 |
| | | | | 3 | 0.00320 | 16.9 | 1.61 | 257 |
| | LB | 0.000216 | 9.91 | 1 | 0.00630 | 21.3 | 2.06 | 2.00 |
| | | | | 2 | 0.00620 | 27.6 | 2.05 | 118 |
| | | | | 3 | 0.00620 | 32.0 | 1.52 | 244 |
| ***7*** | UB | 0.000256 | 11.2 | 1 | 0.00290 | 16.9 | 1.94 | 1.89 |
| | | | | 2 | 0.00310 | 19.4 | 1.91 | 118 |
| | | | | 3 | 0.00300 | 17.0 | 1.41 | 257 |
| | LB | 0.000192 | 9.47 | 1 | 0.00300 | 25.0 | 1.53 | 2.00 |
| | | | | 2 | 0.00310 | 28.0 | 1.45 | 115 |
| | | | | 3 | 0.00310 | 27.1 | 1.15 | 247 |
| ***8*** | UB | 0.000251 | 10.0 | 1 | 0.00310 | 23.3 | 2.09 | 2.06 |
| | | | | 2 | 0.00310 | 19.9 | 2.08 | 124 |
| | | | | 3 | 0.00310 | 29.0 | 1.56 | 226 |

Table 4.6: Values for optimal material coefficients for anisotropic models of human skin, post parameter extraction, correlated against *ex vivo* tensile tests.

| ***Donor number*** | ***Sample location*** | ***V-W coefficients for isotropic matrix*** | | ***Fibre family number*** | $C_3$ ***(MPa)*** | $C_4$ | $\lambda_M$ | $a$ (º) |
|---|---|---|---|---|---|---|---|---|
| | | $C_1$ ***(MPa)*** | $C_2$ ***(MPa)*** | | | | | |
| ***1*** | 1 | 0.00124 | 0.959 | 1 | 1.28E-7 | 18.5 | 4.91 | 1.92 |
| | | | | 2 | 1.3E-7 | 34.8 | 6.95 | 132 |
| | | | | 3 | 1.9E-7 | 50.06 | 9.23 | 241 |
| | 2 | 0.00119 | 1.01 | 1 | 1.32E-7 | 20.9 | 5.11 | 2.09 |
| | | | | 2 | 1.51E-7 | 33.3 | 7.11 | 118 |
| | | | | 3 | 1.78E-7 | 41.3 | 10.1 | 247 |
| | 3 | 0.00142 | 1.37 | 1 | 1.26E-7 | 31.5 | 2.01 | 1.98 |
| | | | | 2 | 1.71E-7 | 41.5 | 5.02 | 128 |
| | | | | 3 | 14.5E-7 | 39.0 | 6.29 | 240 |
| | 4 | 0.00124 | 1.02 | 1 | 1.27E-7 | 21.0 | 2.07 | 2.12 |
| | | | | 2 | 1.72E-7 | 34.9 | 5.12 | 119 |
| | | | | 3 | 1.52E-7 | 48.9 | 6.98 | 242 |
| ***2*** | 1 | 0.0012 | 0.969 | 1 | 1.34E-7 | 31.6 | 2.06 | 2.06 |
| | | | | 2 | 1.79E-7 | 35.4 | 5.43 | 116 |
| | | | | 3 | 1.54E-7 | 20.0 | 7.26 | 242 |
| | 2 | 0.00119 | 0.999 | 1 | 1.31E-7 | 25.5 | 2.04 | 2.03 |
| | | | | 2 | 1.71E-7 | 31.8 | 5.10 | 118 |
| | | | | 3 | 1.52E-7 | 20.3 | 7.12 | 242 |
| | 3 | 0.00121 | 0.997 | 1 | 1.33E-7 | 32.0 | 2.03 | 2.04 |
| | | | | 2 | 1.73E-7 | 32.7 | 5.15 | 116 |
| | | | | 3 | 1.52E-7 | 41.9 | 7.145 | 236 |
| | 4 | 0.0012 | 1.23 | 1 | 1.32E-7 | 32.0 | 1.99 | 1.93 |
| | | | | 2 | 1.72E-7 | 35.5 | 4.91 | 130 |
| | | | | 3 | 1.46E-7 | 42.9 | 6.88 | 241 |

### 4.8.3. Variations between the mechanical properties of human and murine *ex vivo* skin

Table 4.7 show the average and standard deviation value for the material parameters detailed in Tables 4.5 and 4.6, comparing human and murine skin models

Table 4.7: Average and standard deviation values for the all optimum material parameters for human and murine skin.

| | ***Human / Murine*** | ***V-W coefficients for isotropic matrix*** | | ***Fibre family number*** | $C_3$ ***(MPa)*** | $C_4$ | $\lambda_M$ | $\alpha$ (º) |
|---|---|---|---|---|---|---|---|---|
| | | $C_1$ ***(MPa)*** | $C_2$ ***(MPa)*** | | | | | |
| ***Average*** | Human | 0.00124 | 1.07 | 1 | 1.30E-07 | 26.6 | 2.78 | 2.02 |
| | | | | 2 | 1.65E-07 | 35 | 5.6 | 122 |
| | | | | 3 | 1.59E-07 | 38 | 7.74 | 241 |
| | Murine | 0.000278 | 10.2 | 1 | 0.00432 | 21.1 | 1.94 | 2.05 |
| | | | | 2 | 0.00469 | 22.8 | 2.07 | 127 |
| | | | | 3 | 0.00528 | 29.0 | 1.67 | 243 |
| ***Standard Deviation*** | Human | 8.21E-5 | 0.138 | 1 | 2.73E-9 | 5.44 | 1.29 | 0.715 |
| | | | | 2 | 1.53E-8 | 2.76 | 0.838 | 43.1 |
| | | | | 3 | 1.51E-8 | 10.9 | 1.21 | 85.3 |
| | Murine | 0.000118 | 2.71 | 1 | 0.00200 | 5.23 | 0.496 | 0.132 |
| | | | | 2 | 0.00290 | 6.79 | 0.628 | 16.3 |
| | | | | 3 | 0.00365 | 12.8 | 0.479 | 21.2 |

To determine whether there was a statistical significant difference between the optimal parameters extracted for human and murine skin, a t test was conducted. Table 4.8 shows the results, relative to each parameter (see Table 4.3 for details regarding each parameter), indicating whether there was a significant difference ($p<0.05$) between the extracted parameters for human and murine skin.

Table 4.8: Significant differences between optimal material coefficients for human and murine skin.

| *Description* | *Parameter* | *Significant difference between human and murine skin coefficients* |
|---|---|---|
| ***Coefficient for V-W matrix*** | $C_1$ | No |
| | $C_2$ | Yes |
| ***Coefficients for fibre family 1*** | $C_{3,1}$ | Yes |
| | $C_{4,1}$ | No |
| | $\lambda_1$ | Yes |
| | $a_1$ | No |
| ***Coefficients for fibre family 2*** | $C_{3,2}$ | Yes |
| | $C_{4,2}$ | No |
| | $\lambda_2$ | No |
| | $a_2$ | No |
| ***Coefficients for fibre family 3*** | $C_{3,3}$ | Yes |
| | $C_{4,3}$ | No |
| | $\lambda_3$ | Yes |
| | $a_3$ | No |

Figure 4.13 compares the properties of the average coefficient shown in Table 4.7 relative to each fibre family extracted for both murine and human skin. This plot only shows the contribution of the particular fibre family orientated in the direction of load application, not including the influence of the isotropic V-W matrix.

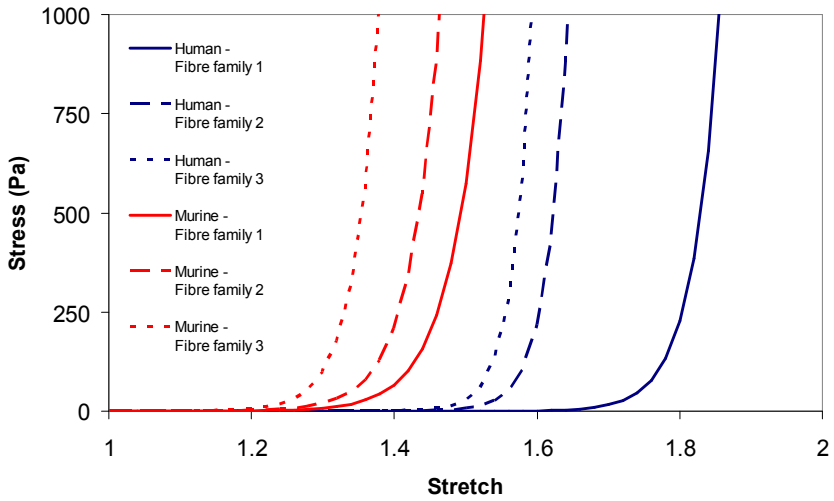


*Figure 4.13: Plot showing the stress to stretch relationship for the average coefficients obtained for all fibre three fibre families, comparing human to murine skin.*

## 4.9 Discussion

This study reports on the success of an anisotropic material model which incorporated three fibre families to describe the properties of skin under large levels of deformation, when correlated against experimental observations. Additionally, the model has served as a comparative tool for analysing the variations between skin from human and murine donors and to hypothesise whether murine skin is a suitable model for human tissue when performing mechanical tests and microneedle penetration tests.

As discussed in Chapter 2, murine skin samples display a much shorter period of extension at low loads compared to human skin. This is the main difference between the mechanical characteristics of human and murine skin in applied tension when inspecting the *ex vivo* measurements alone. As a result, the inverse analysis process required the capacity to extract a single set of material parameters for each skin sample, in order to represent the wide range of mechanical characteristics. The model described in Chapter 3 used three families of fibres embedded within an isotropic material matrix to represent anisotropic behaviour. The three fibre families had coefficients relating directly to the fibres and by manipulating these parameters, the fibre family orientation and material constants within the isotropic matrix, it was shown that a wide range of nonlinear anisotropic relationships could be represented. This material was adapted from an existing transversely isotropic model, currently implemented in finite element software therefore produced a computationally efficient and easy to use anisotropic material.

The use of inverse finite element modelling allowed for a single set of material coefficients to be extracted which closely matched with tensile test data evaluated along three load axes. The lowest $R^2_{ave}$ values calculated for each material parameter set which was extracted using the Simplex algorithm, indicated a strong agreement between experiment and model for the majority of the skin samples. The lowest $R^2_{ave}$ was found to be 0.0038, illustrating an 99.6% accuracy between experimental and model data across all three load

axes using one parameter set, and the highest was 0.0163, showing a 98.4% accuracy (Table 4.4). Figures 4.10 and 4.11 demonstrate the closeness of fit between experiment and model comparing load on grip to relative grip displacement for all three load axes, for murine and human skin samples respectively. The model adequately details long periods of extension at low loads, which is a prominent characteristic for human skin tissue in tension. Importantly, the model has the capacity to describe a wide range of anisotropic behaviours with just one set of material parameters, in particular murine 1 (UB), shown in Figure 4.10 a) where the load-displacement response at 0° is almost double that shown at 45°. On the contrary, the model can also specify almost isotropic behaviour as seen for skin samples taken from murine donors 4 and 7, illustrated in Figures 4.10 d) and g).

Discrepancies between experiment and model data in Figures 4.10 and 4.11, appear to be attributed to phase 2 of the load – displacement curves. This is the point at which the material begins to exponentially stiffen, signifying a potential incompetency within the developed model. For samples 1 and 3, taken from human donor 1 at 90° and 45° respectively, and for sample 2 extracted from donor 2 tested at 45° (Figure 4.11). Figure 4.12 indicates the poor agreement between model and experiment at low loads of up to 0.05N, for an example selection of four murine and two human skin tissues. For murine skin tensile measurements, the relationship between all three load axes is closer matched between experiment and model. Whereas for the selected human skin the computational data, gives a very similar load – displacement relationships for all three load axes. This may be because higher levels of extension at low loads are experienced for the tensile tests performed on human skin, producing a corresponding relationship across all three load axes. The general pattern from Figure 4.12 implies that the model on occasion has difficulties simulating high levels of extension at low loads, when analysing this section only, as it cannot compute low loads with increasing strain. Due to the nature of the parameter extraction algorithm, which measures the variation between model and experiment across the entirety of the load-displacement curve, it is quite possible that if only this initial portion had been analysed within the inverse FE calculations separately,

a closer fit between experiment and model would have been obtained during this phase. However, the model can predict the general nonlinear, anisotropic load-displacement relationship of the analysed skin tissue in applied tension, as illustrated in Figures 4.10 and 4.11.

The extracted optimal material coefficients that best describe the mechanical response of each human and murine skin tissue, shown in Tables 4.5 and 4.6 respectively, can provide data to further quantify the skins mechanical properties. As the fibre families contribute to the anisotropic nature of the material, it is possible to deduce the extent of non homogenous behaviour. Hence those with more isotropic characteristics may have less variation between the optimal parameters obtained for each fibre family. The skin sample with the least level of anisotropy was that obtained from the UB of murine donor 7. The optimal coefficients obtained post extraction show little variation in the parameters for all three fibre families when compared with the murine donor 1 from the LB, which was shown to have the highest anisotropic behaviour and a greater range of coefficients for each fibre family. However, as only local minimum was extracted during optimisation, other parameter sets may have yielded similar correlations between experiment and model. Consequently when analysing the individual parameters alone it may be difficult to detect small variations between the mechanical characteristics.

As detailed in Chapter 2, the key difference between human and murine skin is attributed to the length of phase 1. Human skin has been shown to undergo a much larger amount of strain at low loads during this initial load application. Table 4.7 shows the average material coefficients comparing human and murine skins, where there appear to be large variations in some of the coefficients calculated. T tests were conducted on each of the 14 parameters to determine whether there was a significant difference ($p<0.05$) between those extracted for murine and human skin. Table 4.8 shows that there was a significant difference between coefficient $C_2$ for the V-W, the scale factor for the exponential stresses $C_3$ and, for two out of the three fibre families, the fibre stretch $\lambda$, between human and murine skin. Suggesting that these coefficients are most related to the initial stages of load application as

this is the key difference between human and murine skin. There is however little contrast between the rate of un-crimping and fibre orientation angles when comparing murine and human skin, which could imply these coefficients either have less effect on the material behaviour or that they are uniform between human and murine skins. Consequently, it is difficult to deduce inter sample variations such as level of anisotropy by observing the material parameters extracted alone. However it is possible to identify large discrepancies within the modelled skin such as the difference in some material coefficients between human and murine skin, and the amount of strain experienced prior to exponential stiffening.

Figure 4.13 shows the stress–stretch curves for the average material coefficients for all three fibre families comparing human to murine skin. Although the influence of the isotropic matrix is neglected, the variations between human and murine fibre families are still significant. Those detailed for human skin allow a greater period of low stress at increasing strain, during the initial stages of load application. There is some correlation between the average fibre properties for human and murine skin as fibre family 1, which is usually orientated at around 0°, allows for a longer phase 1 compared to the other two fibre families.

Despite the closeness of fit between computational and experimental measurements, it should be noted however that several limitations were associated with both factors. Only three load axes were detailed, hence it may have been advantageous to collect uni-axial data relating to an additional load axis. Additionally, biaxial tests could have predicted the mechanical response of the tissue using the extracted material coefficients. Whilst every effort was made to reduce the occurrence of tissue degradation, it was still possible that some deterioration may have occurred between tensile tests, thus altering the mechanical properties of the tissue. The model assumed the skin to be nonlinear and anisotropic due to the three fibre families, but the viscoelastic time dependent properties were neglected. Also, the distribution of the fibre families within the model was not representative of the actual matrix pattern observed within tissue samples, which appears to adopt a more

irregular fibre distribution which changes its alignment upon load application (Brown, 1973). Although the Simplex algorithm has been shown to work well for this problem, it should be noted that it only accommodates for the extraction of material coefficients from a local minimum, as downhill optimisation was implemented. However, due to the sensitivity of the model to extreme material parameter changes, it was not possible to use any other method. Skin thickness measurements were kept constant for all murine and human skin which equated to be 0.435mm and 1.86mm respectively from histological measurements. Although the load was applied in plane with the skin, the alteration of these measurements would result in different mechanical behaviours of the modelled material. Consequently, the parameters obtained assume that the skin thicknesses are constant throughout the sample and that there were fibres throughout the entirely of the skin.

Whilst no other study to our knowledge has used the transversely isotropic model of hyperelasticity developed by Weiss *et al* in 1996 to implement three fibre families which describes the behaviour of skin in applied tension, several studies have modelled the in plane mechanical properties of human and animal *ex vivo* and *in vivo* skin using a range of constitutive equations. Some have used isotropic hyperelastic models coupled with finite element analysis, such as the Ogden (Evans and Holt, 2009; Lapeer et al., 2010) and Yeoh (Lapeer et al., 2010) materials, in addition to linear elastic models (Delalleau et al., 2008b), to describe the skin's response to applied in plane tension and compression. In a study by Lapeer *et al*. in 2010, tensile tests performed at 0° and 90° on *ex vivo* human skin samples were matched with the Ogden, general polynomial and reduced polynomial isotropic hyperelastic models and when fitted with the experimental measurements only the reduced polynomial could be implemented due to instabilities within the other two models. Despite the successes detailed within the original study in 1970, the V-W hyperelastic model used within this study to detail the mechanical properties of the isotropic matrix, has been relatively under applied for the modelling of skin tissue. Whilst such investigations have shown how hyperelastic models can be used to describe the mechanical response of human and animal skin in

applied tension, such models can only detail the response in one direction, resulting in isotropic properties. Two anisotropic hyperelastic models developed by Bischoff *et al* in 2004 and Tong and Fung in 1976 have been predominantly used to describe skin using a matrix of fibres or by implementing material parameters relating to the x, y and z planes. There is little information regarding the success when using the Bischoff model to detail skin, apart from Flynn and McCormack in 2008 where this model was used to describe the dermis during compression. A study which is closely related to this current investigation used the Tong and Fung orthogonal model which was subsequently matched with *in vivo* measurements of skin during multiaxial tests (Kvistedal and Nielsen, 2009), where a good relationship between model and experiment was shown. However due to the *in vivo* nature of testing, only small deformations were examined, furthermore an identical test performed on animals would have been extremely difficult to achieve.

In conclusion, by using the Weiss *et al* transversely isotropic hyperelastic model to detail three fibre families embedded within an isotropic V-W model matrix, it was possible to implement inverse finite element analysis to extract a single set of material parameters for each skin sample. The optimised models have proven to provide an excellent fit with experimental observations, when analysing the load-displacement relationship of the skin as a whole. The key variation between the mechanical characteristics of human and murine skin described by the *ex vivo* measurements, appear to be attributed to the initial phase of high extension at low loads, which is significantly longer for human skin. This characteristic is further reflected in the variation between the average extracted material coefficients for $C_2$, $C_3$ and $\lambda$ comparing murine to human skin. This is further demonstrated by a t test which confirmed a significant difference between both human and murine groups for the three parameters. Consequently, this study has shown the implications of modelling skin using three fibre families within constitutive models which are readily available within finite element software packages. It has also provided a method of comparison between the mechanical properties of human and murine skin, as a result this study has further indicated the great variations

between both tissues. Hence this study suggests care should be taken when using murine skin in place of human tissue for microneedle puncture tests, to compensate for the observed differences between the mechanical properties found within this study.

## 4.10 Conclusions

This Chapter has shown the feasibility of using extraction algorithms which output material coefficients for the FEMs detailed in Chapter 3, which give a good agreement between experiment and model data. The parameters extracted for the multilayer FEM of human skin showed a correlation between experiment and model, suggesting that the hypodermis is extremely influential on the overall mechanical properties of the tissue. Additionally, statistical significant differences were noted between 6 out of the 14 material parameters, when comparing the average coefficients obtained for human and murine skin. This implies that the model can predict the large variations between human and murine *ex vivo* tissue groups. The success of the inverse analysis has led to the formulation of predictive models of the skins tested in Chapter 2.

Further work will include the validation of the stratified model of human skin indentation using a separate experiment performed on one volunteer, where a single microneedle will be applied to skin and matched with a model using the extracted material parameters for that subject. Additionally, the success of the inverse methods detailed in this section have allowed for the establishment of seven stratified FEMs of human skin *in vivo* which can aid within the development of new microneedle designs, by modelling the deformation of the skin's surface upon the application of a load comparable to microneedle administration. The newly designed microneedle array can then be used to further quantify the variations between the mechanical properties of human skin *in vivo* and skin tissue from human and murine donors, by conducting microneedle penetration tests. Such findings can validate those observed within this Chapter.

# CHAPTER 5

# OPTIMISING MICRONEEDLE DEVICE DESIGN TO INCREASE SKIN PENETRATION EFFICIENCY

## 5.1 Introduction

Chapter 1 described the microneedle device design variations which have developed for transdermal drug delivery purposes. Several have considered the skin puncture of a single microneedle with various geometries (Khanna; Davis et al., 2004; Bal et al., 2010b; Donnelly et al., 2010; Gupta et al., 2011), while others have focused on the engineering techniques used to manufacture arrays from a range of biodegradable and non-biodegradable materials (Aoyagi et al., 2007; Ayittey et al., 2009; Han et al., 2009; Li et al., 2009; Lee et al., 2011). Although some studies have estimated the optimal number of microneedles within an array to predict maximum transdermal delivery (Al-Qallaf and Das, 2008), very few to date have investigated the effect of array shape on microneedle puncture. It has been suggested that upon array application, the individual needles within a device puncture to different depths whereby the needles within the centre penetrate more superficially (Coulman et al., 2011). An array shape which follows the curvature of skin upon the application of pressure may allow for equally distributed force on all microneedles within the array, causing uniform penetration and hence reproducing transdermal delivery. Additionally, using the validated multilayer FEM of skin developed through Chapters 2-4, the

application of a single microneedle to skin prior to penetration can be modelled.

This study therefore aimed to model microneedle application prior to penetration, as such an approach provided data relating to the micron scale deformation similar to the indentation measurements discussed in Chapter 2. This also served as a further validation for the FEMs and parameter extraction process. Again using the multilayered FEM, skin deformation at a pressure comparable to microneedle application was modelled. A series of curved microneedle arrays were designed which aimed to facilitate uniform skin puncture of all microneedles within the array. To enable scale-up, these arrays must also be manufactured simply and quickly. To test microneedle puncture, preliminary tests were performed on human skin *in vivo* and *ex vivo,* and murine skin *ex vivo* to hypothesise whether repeatable penetration can be obtained using all skin types.

## 5.2 Aims of the study

The investigation aimed to achieve the following:

1. *In vivo* load – displacement measurements of a single microneedle applied to skin were obtained and matched to the multilayer model data.
2. Using the multilayered FEMs of human skin indentation discussed through Chapters 2-4, models were established of skin under a pressure load comparable to that observed during microneedle array application. The deformation of the skin could then be measured to provide the new array dimensions.
3. Manufacture optimised designs
4. Preliminary measurements to determine the penetration efficiency of the bespoke microneedle designs in human and animal skin models

# 5.3. Methods

Methods are split between modelling the application of a single microneedle to *in vivo* skin and the development and preliminary testing of the bespoke microneedle array designs.

## 5.3.1 Modelling the application of a single microneedle to human skin *in vivo*

With the establishment of the validated multilayer FEMs of human skin indentation detailed through Chapters 2-4, it was possible to create a model to predict the mechanical response of skin upon the application of a single microneedle, prior to penetration. This served as a further validation of the multilayered FEMs previously developed and could also be used as a tool to anticipate the effects of microneedle geometry on skin puncture. This section will detail how the previous models have been adapted to simulate for this test and the experiments performed to collect *in vivo* measurements of microneedle administration to skin.

### *5.3.1.1 In vivo measurement of microneedle application to skin*

The experimental set up and protocol was identical to that described in Section 2.3, however instead of applying an indenter to the skin site, a single microneedle was applied. A servohydraulic testing machine (Losenhausen Maschinenbau, Dusseldorf) with an MTS FlexTest GT controller (MTS, Eden Prairie, Minnesota, USA), was used to measure the displacement. A 5N load cell (Interface Force Measurements, Crowthorne, UK) was attached to the testing machine, which provided an accuracy of 0.5% for all readings.

Two single microneedles, shown in Figure 5.1, were used for this study. One was a planar stainless steel microneedle with a total length of 700μm (Gill and Prausnitz, 2007) termed microneedle design A, and the second was a pyramidal needle manufactured from silicon with a length totalling 280μm (Wilke et al., 2005) called microneedle design B (Figure 5.1). Each

microneedle was mounted onto a screw which was then attached to the 5N load cell.

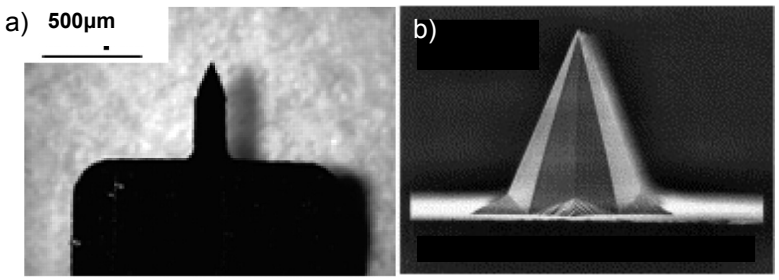


*Figure 5.1: Images showing a) microneedle design A (Figure reproduced from (Gill and Prausnitz, 2007) and b) microneedle design B (Figure reproduced from (Wilke et al., 2005) which were applied to skin.*

The skin site chosen for microneedle application was the same as that used for the indentation measurements described in Section 2.3. This area was 35mm away from the medial crease on the volar aspect of the forearm. To minimise body movement during the test, the forearm was constrained either side of the application site using two straps. Using the experimental set up described previously, a load of up to 0.15N was applied to the skin site using each microneedle, where the reaction force and the relative microneedle depth were recorded. Five application cycles were performed on the forearm site for both of the microneedles, with a rest period to allow any viscoelastic deformation to recover. Each cycle was recorded by the control computer. Volunteer 1, a 24 year old female, was selected for this investigation detailed in Section 2.3. After the indentation measurements were performed, a further two assessments were conducted using both single microneedles shown in Figure 5.1. The skin site was cleaned using an alcohol wipe before applying each microneedle, and both were sterilised prior to administration to the skin site. All analyses using human volunteers were approved by the Cardiff University School of Engineering Ethics Committee (see Appendix E for volunteer information sheet) and the skin of the volunteer was checked to be free from scarring and imperfections that may have affected the measurements.

### 5.3.1.2 *Finite element modelling of microneedle application to skin*

So that the model of microneedle application could also serve as a validation for the *in vivo* indentation model, the skin model of microneedle application was given identical geometry. Thus, the thickness of the epidermis, dermis and hypodermis and the boundary conditions detailed in Chapter 3, remained consistent. As administration prior to penetration was modelled, the maximum load on each individual microneedle did not exceed 0.01N, which was 0.09N lower than the lowest recorded force documented for skin puncture by a microneedle *in vivo* (Davis et al., 2004). Additionally, boundary conditions were implemented to prevent the microneedle penetrating the skin material.

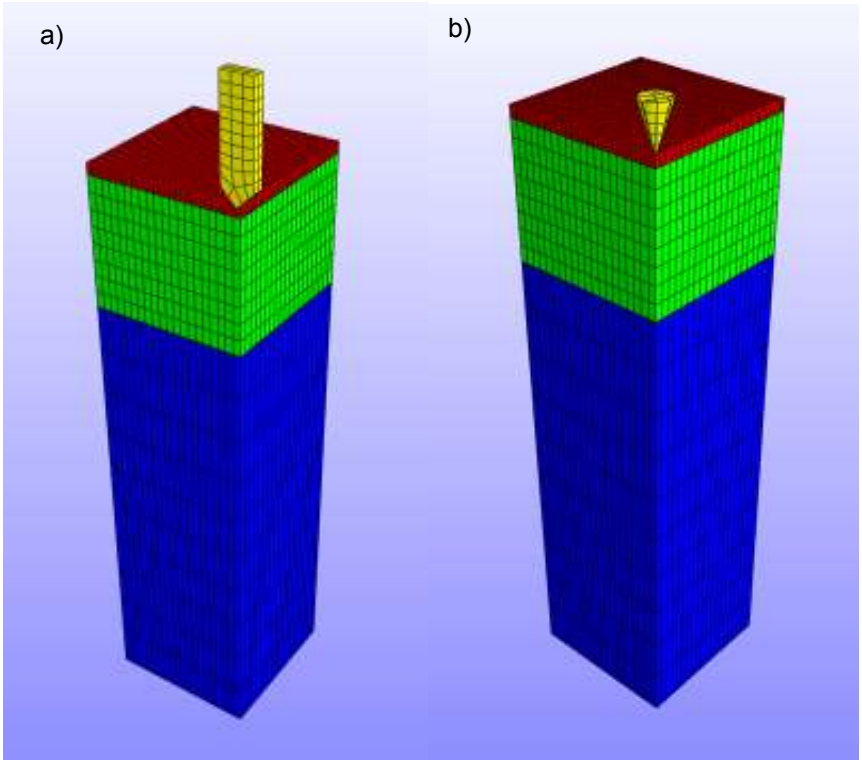


*Figure 5.2: Image showing the FEMs developed for the application of microneedle design a) A and b) B to the stratified model of human skin.*

Figure 5.2 a) and b) illustrate the multilayer FEMs established for the application of a single microneedle to skin with identical geometries to designs A and B, respectively. As both microneedles were manufactured from materials several orders of magnitude stiffer than skin, both were assumed to be rigid bodies. The material Ogden coefficients, $\mu$ and $\alpha$ for the epidermis, dermis and hypodermis, extracted for subject 1 (Chapter 4), were

implemented within both models of microneedle application. The relative microneedle depth and the load on each microneedle were then recorded and compared against the *in vivo* findings.

### 5.3.2. Development of optimal microneedle array designs to allow for uniform skin puncture

Using the multilayer FEMs of human skin *in vivo* developed through Chapters 2-4, it was therefore possible to (i) map the deformation of the skin under a load comparable to microneedle application and (ii) use this information to inform the design of a new microneedle device design

#### *5.3.2.1 Modelling skin deformation to inform microneedle array design*

A stratified FEM of human skin was developed, and by using the optimal Ogden material coefficients, shown in Table 4.2, it was possible to measure skin deformation for each individual. The hypodermis thickness was increased to 10mm as skin deformation was greater than previously modelled in this Chapter. This was because it reduced the overall effect of the constraint along the base of the hypodermis. It should be noted that this model may react differently to an applied load when compared to the simulations developed in Chapter 2-4, as one of the model criteria has been manipulated.

The stratified model was densely meshed and consisted of 5400 elements, which was more than the FEMs established in Chapter 3, and hence a mesh convergence test was not required. Due to the range of values obtained for the puncture of a single microneedle *in vivo*, it was difficult to obtain a definitive value, so a uniform load of 1N was applied to an area of 10x1mm. This force was chosen as it serves as a good approximation for the load applied to a microneedle array (Davis et al., 2004). However, it should be noted this is at the lower end of the values required for microneedle penetration observed by Davis *et al*. Although due to the stratified nature of

the model, at higher pressure loads the FEM could not converge as the skin layers were penetrating one another. Skin deformation was then measured for the 10mm wide pressure area to approximate array curvature for each of the 7 subjects. To achieve this, the displacement at the edge of the 10mm wide zone, shown by a red arrow in Figure 5.3, was subtracted from the total displacement in the y plane, shown by a white arrow. This measurement provided dimensions for a suitable array curvature.

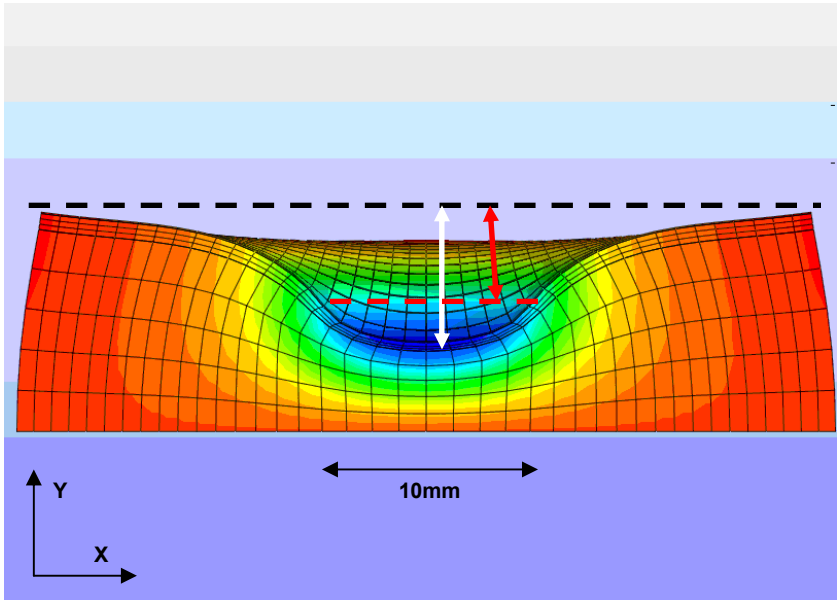


*Figure 5.3: Illustration showing how the array curvature was determined for each subject by subtracting the displacement at the edges of the 10mm (width white arrow) in y plane from the total displacement in the y plane.*

Table 5.1 shows skin deformation measurements for all 7 subjects and the subsequent suggested array curvature values. Array designs were then developed using the highest and lowest suggested curvature calculated, and an average of these two values.

Table 5.1: Microneedle array curvature suggestions using the stratified FEMs for all seven volunteers.

| ***Subject number*** | ***Total displacement (mm)*** | ***Displacement at the edge of the 10mm width (mm)*** | ***Suggested array radius (mm)*** |
|---|---|---|---|
| ***1*** | 2.95 | 2.00 | 0.95 |
| ***2*** | 6.24 | 3.52 | 2.72 |
| ***3*** | 5.24 | 2.94 | 2.30 |
| ***4*** | 5.24 | 3.49 | 1.74 |
| ***5*** | 5.87 | 3.25 | 2.62 |
| ***6*** | 3.75 | 2.18 | 1.57 |
| ***7*** | 3.22 | 1.86 | 1.36 |

### *5.3.2.2 Microneedle array designs*

Three microneedle arrays were developed using the information detailed in Table 5.1, with the addition of a fourth array design which incorporated no curvature to serve as a control. The lowest and highest suggested array radii where chosen and an average of the two provided the dimensions for the three new array designs. Individual microneedle geometries and the tip to tip distance between adjacent microneedles were kept consistent for all four designs. Figure 5.4 shows the dimensions implemented for each individual microneedle, where the height was measured along the centre of the needle to the array backing.

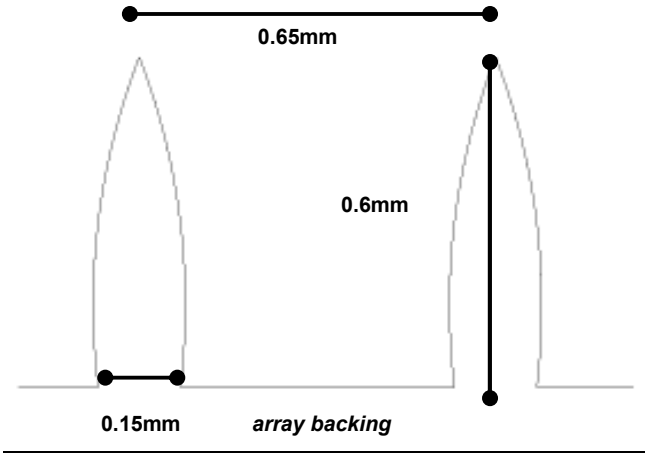


*Figure 5.4: Dimensions of individual microneedles, and the spacing between microneedles, used for all microneedle array designs*

As all arrays were manufactured from planar stainless steel sheets, each design only incorporated one row of microneedles. The total width and height of all array backings remained uniform throughout, allowing for 16 microneedles per array, numbered 1-16 from left to right. Figure 5.5 shows the dimensions of all four microneedle arrays.

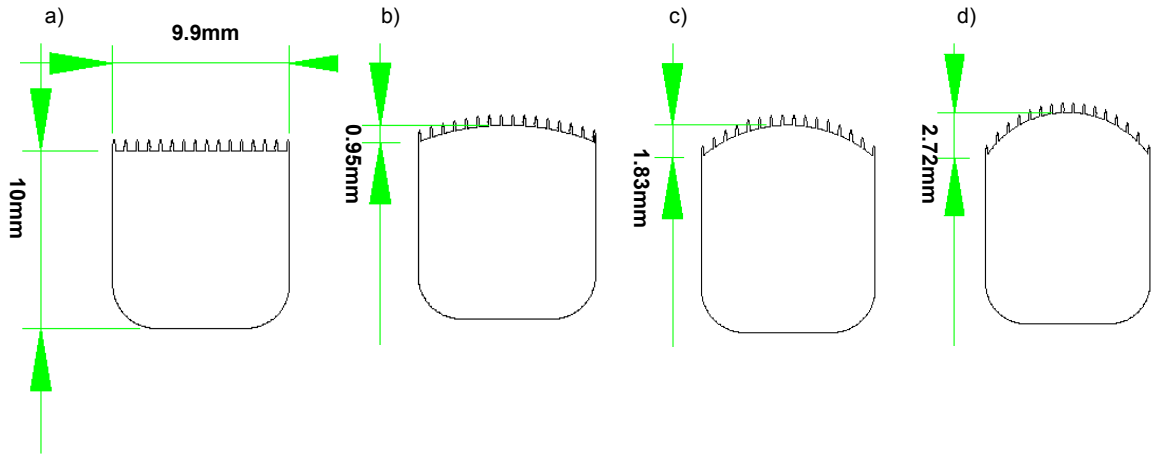


*Figure 5.5: Four array designs a) control array with no curvature and a curvature of b)0.95mm, c)1.83mm and d) 2.72mm*

### *5.3.2.3 Manufacture of microneedle arrays*

Microneedle devices were manufactured from 0.1mm thick cold rolled stainless steel sheets, type 302 (obtained from RS Components, Corby, UK, stock number: 518-801), a grade commonly used for surgical tools. All devices were manufactured in house at the Manufacturing Engineering Centre (MEC), within Cardiff University's School of Engineering.

To manufacture the arrays, ten stainless steel sheets were clamped together using a purpose built jig, allowing for ten microneedle profiles to be cut per attempt. During this process, it was critical that the sheets did not move during cutting, consequently the bespoke jig was able to hold the material in an adequate grip to allow for manufacture. All designs were developed in AutoCAD (Autodesk, San Rafael, USA), using the dimensions shown in Figure 5.4 and 5.5. The microneedle profiles were then cut using an AGIECUT Vertex wire EMD machine (Agie Charmilles LTD, Coventry, UK)

with a 50μm diameter wire. Post manufacture, the arrays were cleaned with ethanol to remove any residual material and cooling fluid used during the process.

#### *5.3.2.4 Testing microneedle penetration using ex vivo skin*

The newly developed microneedle arrays were applied to human and murine skin *ex vivo*, after which a methylene blue dye was applied to the site to detect skin puncture. The dye solution stained the microchannels created as the skin's surface was hydrophobic and methylene blue is aqueous, therefore the solution is easily removed (Haq et al., 2009). Surface swabbing cannot access underlying tissue, thus if the SC is broken, the underlying tissue will remain stained. Such preliminary experiments also provided a further comparison between human and murine skin, in terms of the mechanical properties of the both tissues, tested and modelled through Chapters 2-4. This consequently led to suggests as to whether murine skin is an appropriate model of human skin when assessing microneedle penetration.

A human skin sample frozen on the day of excision from a 41 year old female donor post mastectomy surgery was selected for the human skin penetration tests. The skin was obtained with full ethical approval and informed consent. Murine skin was excised from the spinal region of a single donor. Both samples were thoroughly defrosted and the hypodermis was removed with a scalpel prior to examination. All tests performed on human skin were conducted within a laminar flow hood in a containment II laboratory to prevent the spread of infection. Hair was also removed from the mouse with the use of hair removal cream (Veet®, Slough, UK). Both human and murine skin samples were pinned to a cork board which was covered in foil, as shown in Figure 5.6, to reduce the rate of dehydration. This also kept the skin flat and in tension throughout the test. This tension however could not be measured and subsequently compared with *in vivo* conditions

*Figure 5.6: Image of prepared murine skin sample was, prior to microneedle insertion tests.*

All microneedles used during testing were cleaned using 100% ethanol. The microneedle arrays were applied to the skin using a FH 20 Sauter force gauge (Sauter, Balingen, Germany) which measured the application load with an accuracy of 0.2% and a resolution beginning at 0.0001N. The decision was taken not to use a testing machine to apply the microneedles as this was not representative of clinical use, as in reality the array would be administered by hand. A single array of each design was attached to the force gauge using an adapter fabricated from three nuts which were fixed together, this then screwed onto the end of the force gauge. A slot was sawn through the nuts into which the microneedle sat and the surrounding area was filled with Blu-tack (Bostik Ltd, Leicester, UK) to prevent the microneedle becoming dislodged or misaligned. The force gauge with a microneedle array attached is shown in Figure 5.7.

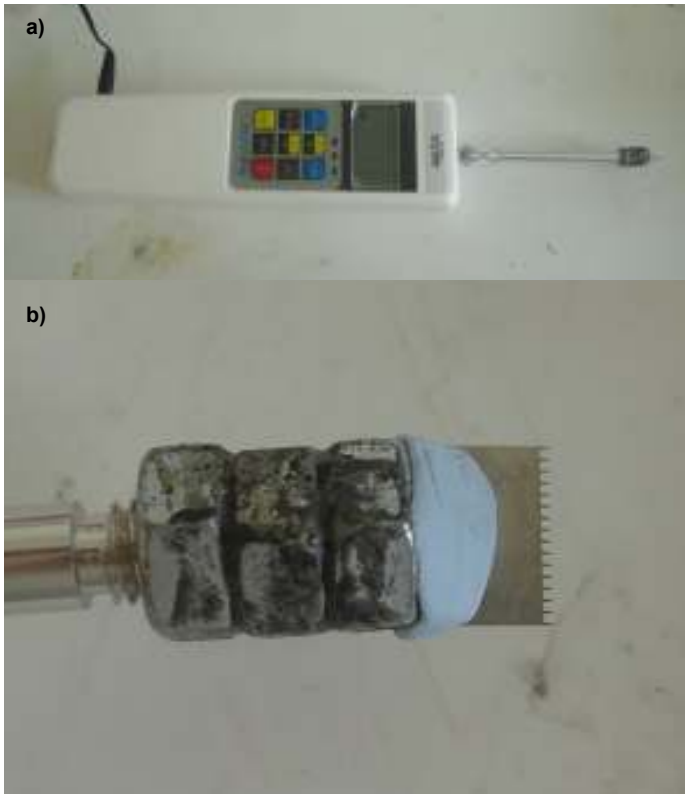


*Figure 5.7: Image showing a) the force gauge used to measure microneedle array application load and b) the adapted used to hold the array.*

All four arrays were applied to both human and murine skin samples at loads of between 1N - 5N, at increments of 1N. For each test, the microneedle arrays were applied to the skin site once, rather than cyclically loaded as with the single microneedle application to skin which was detailed previously in this Chapter. The desired and actual force readings taken from the force gauge are shown in Table 5.2 for experiments performed on the *ex vivo* human skin samples.

Table 5.2: Desired and actual force readings for each microneedle array applied to *ex vivo* human skin.

| | ***Desired force on microneedle (N)*** | ***Actual force reading on microneedle taken from force gauge (N)*** | | | |
|---|---|---|---|---|---|
| | | Flat microneedle array | 0.95mm curved microneedle array | 1.83mm curved microneedle array | 2.72mm curved microneedle array |
| *Human skin* | 1 | 1.11 | 1.00 | 1.20 | 1.03 |
| | 2 | 2.13 | 2.01 | 2.19 | 2.11 |
| | 3 | 3.18 | 3.08 | 2.98 | 3.23 |
| | 4 | 4.08 | 4.19 | 4.05 | 4.14 |
| | 5 | 5.10 | 5.19 | 5.04 | 5.23 |

A 2% methylene blue dye was applied to the microneedle treatment site for human skin and left for 30 minutes, after which the solution was removed from the skin's surface with ethanol and any microchannels created were stained blue.

A reduced concentration of 0.5% methylene blue was applied to the microneedle treatment site for the mouse skin sample, and removed instantly as the SC was significantly thinner and more permeable.

### *5.3.2.5 Testing microneedle penetration using in vivo skin*

A 36 year old male volunteer was selected to test all four microneedle devices *in vivo.* The volunteer selected for this test was not one of the subjects examined for the indentation tests described in Chapter 2-4. Ethical approval for all experiments using human volunteers was obtained from the School of Engineering Ethics Committee at Cardiff University prior to testing (see Appendix F for volunteer information sheet). In an identical manner to the indentation tests performed in Chapter 2, the skin on the volar aspect of the right forearm was selected as the treatment site. However a greater surface area was required to perform all measurements and so the skin from the medial crease to halfway down the forearm was used for microneedle application tests. The skin was checked for scarring, moles and imperfections that could affect the measurements, and the arm remained flexed at 90°. Prior to microneedle application, the area was cleaned using a pre-injection swab (Medlock Medical Ltd, Lancaster, UK) to prevent the risk of infection.

The arrays and 2% methylene blue solution were sterilised within an autoclave prior to application.

An identical experimental protocol was used for the ex *vivo* measurements, where the microneedles were applied to the skin site by hand and the force was measured using a FH 20 Sauter force gauge (Sauter, Balingen, Germany), with an accuracy of 0.2%. All microneedle arrays were applied to the skin once, and were not cyclically loaded onto the skin as with the single microneedle tests described previously in this Chapter. Table 5.3 shows the desired and actual microneedle application forces for each microneedle design.

Table 5.3: Desired and actual force readings for each microneedle array applied to *in vivo* skin.

| | ***Desired force on microneedle (N)*** | ***Actual force reading on microneedle taken from force gauge (N)*** | | | |
|---|---|---|---|---|---|
| | | Flat microneedle array | 0.95mm curved microneedle array | 1.83mm curved microneedle array | 2.72mm curved microneedle array |
| *Human skin* | 0.5 | 0.44 | 0.8 | 0.8 | - |
| | 1 | 1.37 | 1.48 | 1.38 | 1.42 |
| | 2 | 2.12 | 2.29 | 2.08 | 2.26 |
| | 3 | 3.44 | 3.10 | 3.03 | 3.44 |
| | 4 | 4.32 | 4.37 | 4.29 | 4.45 |
| | 5 | 5.35 | 5.12 | 4.52 | 5.08 |

Sterlised 2% methylene blue dye was applied to the treatment site where the for a contact time of 5 minutes. This was less than the *ex vivo* measurements in order to reduce the risk of excessive surface staining in the volunteer. The solution was removed from the skin's surface using a pre injection swab (Medlock Medical Ltd, Lancaster, UK). Microchannels created by the array were stained blue.

# 5.4 Results

## 5.4.1 Modelling the application of a single microneedle to human skin *in vivo*

Figure 5.8 illustrates the plots obtained for each microneedle design comparing relative microneedle depth, to the load application on each individual microneedle.

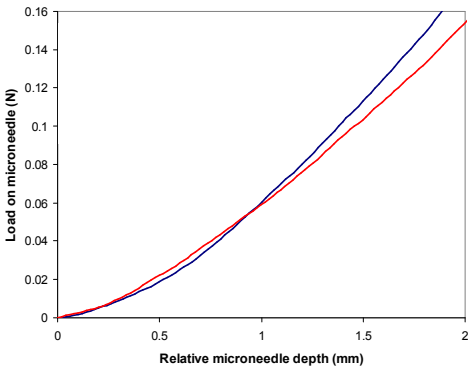


*Figure 5.8: Plot comparing relative microneedle depth to load on individual microneedle for designs A and B, illustrated by blue and red respectively.*

Figures 5.9 and 5.10 illustrate the FEMs describing the application of microneedle design A and B respectively to stratified skin tissue. Image a) shows the strain distribution and b) indicates the stress within the skin in the direction of microneedle application. Furthermore, it was noted that the skin mesh deformed around the tip of both microneedles, hence were not acting as though a nodal load had been applied.

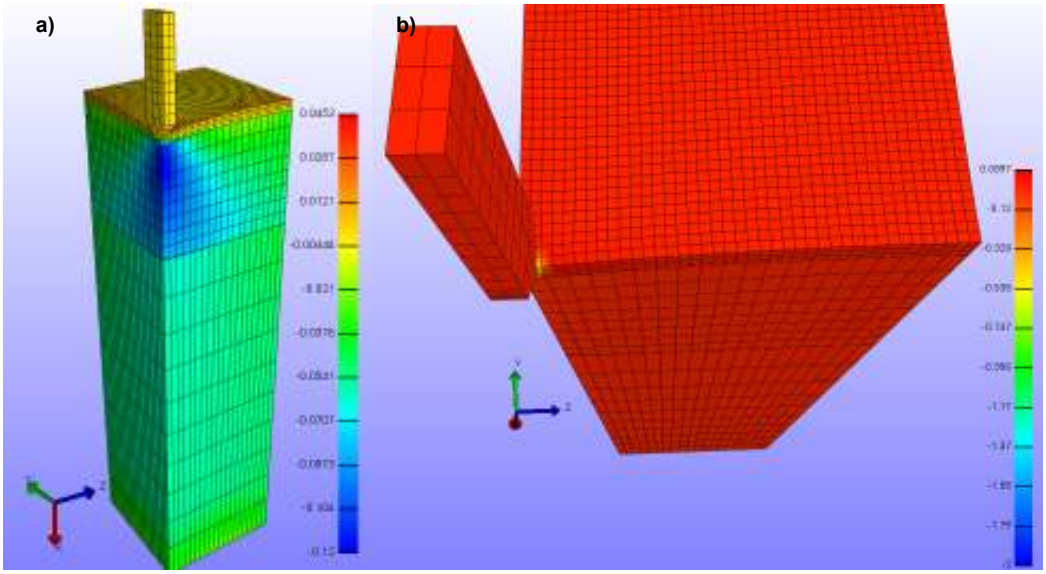


*Figure 5.9: Images showing FEM of microneedle design A applied to the stratified model of human skin indicating a) the strain distribution through the skin and b) the stress (MPa) in the direction of microneedle application.*

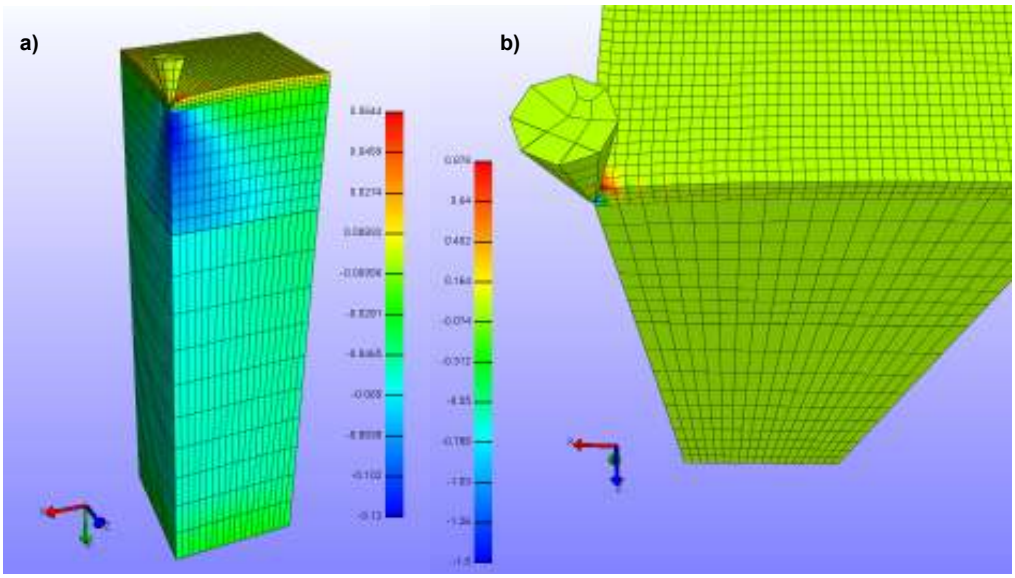


*Figure 5.10: Images showing FEM of microneedle design B applied to the stratified model human skin indicating a) the strain distribution through the skin and b) the stress (MPa) in the direction of microneedle application.*

Figure 5.11 shows both plots for microneedle application to the *in vivo* forearm skin of subject 1 for designs A and B, comparing experimental readings to FEM data using the Ogden material parameters collected for subject 1.

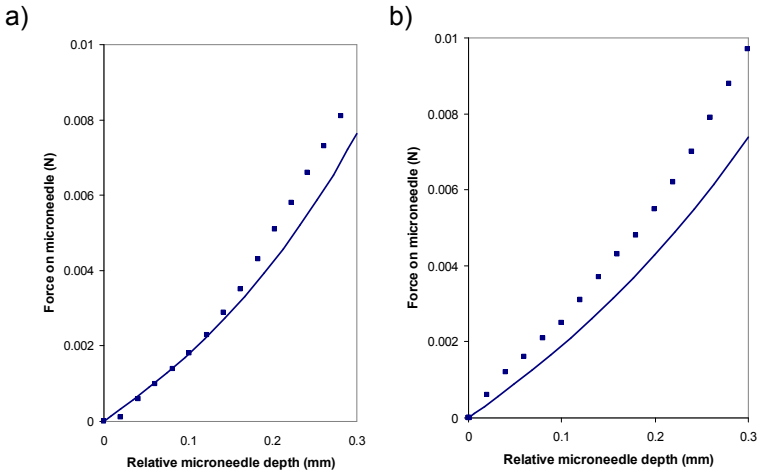


*Figure 5.11: Plots indicating measurements of relative indentation depth and force on microneedle for designs a) A and b) B, comparing in vivo (square markers) experiment to FEM data (solid line).*

## 5.4.2 Optimal microneedle designs

All stainless steel microneedle arrays were assessed to quantify the success of the manufacturing process. Figure 5.12 shows the resulting microneedle designs.

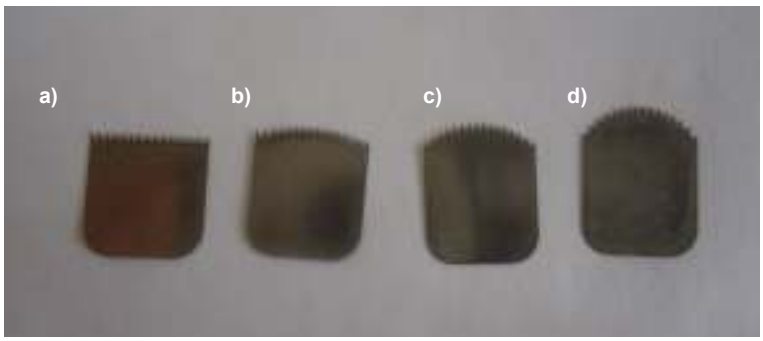


*Figure 5.12: Image showing the a) the flat microneedle array, b) the 0.95mm, c) the 1.83mm and c) the 2.72mm curved microneedle arrays.*

Table 5.4 shows microscopic images of several individual microneedles from each the four arrays. The summary illustrates the variations between different microneedles along the curvature and the quality of finish. The images show few burrs along the microneedle edge, indicating that no further action was required to remove any residual material. Additionally, the microneedles at the centre (microneedle number 8) lie almost flat against the array backing,

whereas those around the periphery of the curved array appear shorter due to the increased curvature of the array backing

Table 5.4: Summary of the microscopic images taken for microneedles 1, 4 and 8 along each microneedle array (red line = 200μm).

| **Array curvature (mm)** | **Number of microneedle within the array (imaged using a microscope )** | | |
|---|---|---|---|
| | **1 (edge)** | **4** | **8 (centre)** |
| **0** |  | *N/A* |  |
| **0.95** | 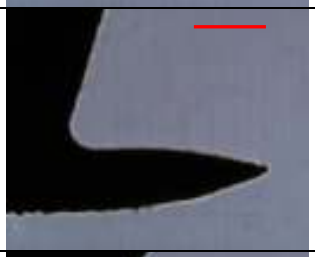 | 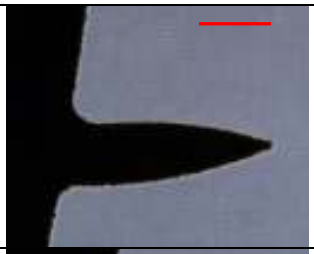 |  |
| **1.83** | 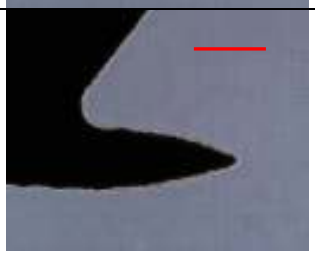 | 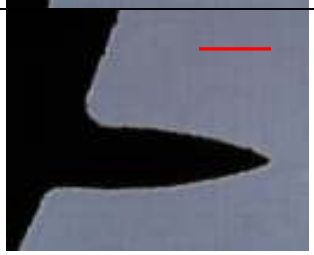 | 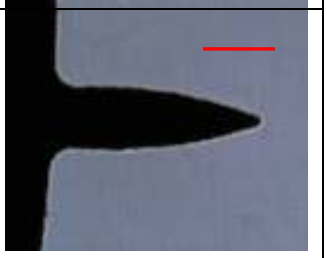 |
| **2.72** | 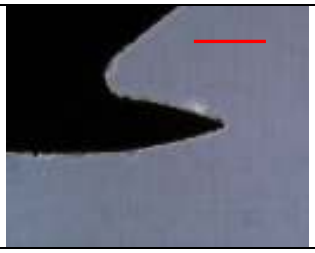 | 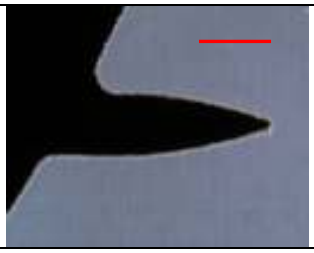 | 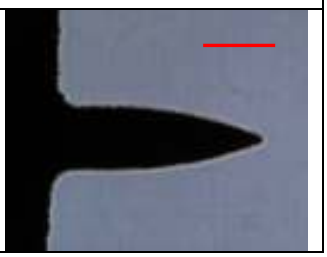 |

### 5.4.3 *Ex vivo* images of skin penetration by microneedles

Figure 5.13 shows the methylene blue staining post microneedle insertion into the human skin sample. The blue dots show disruption within the SC as the underlying epidermis or dermis has been stained, suggesting that the array has punctured the skin.

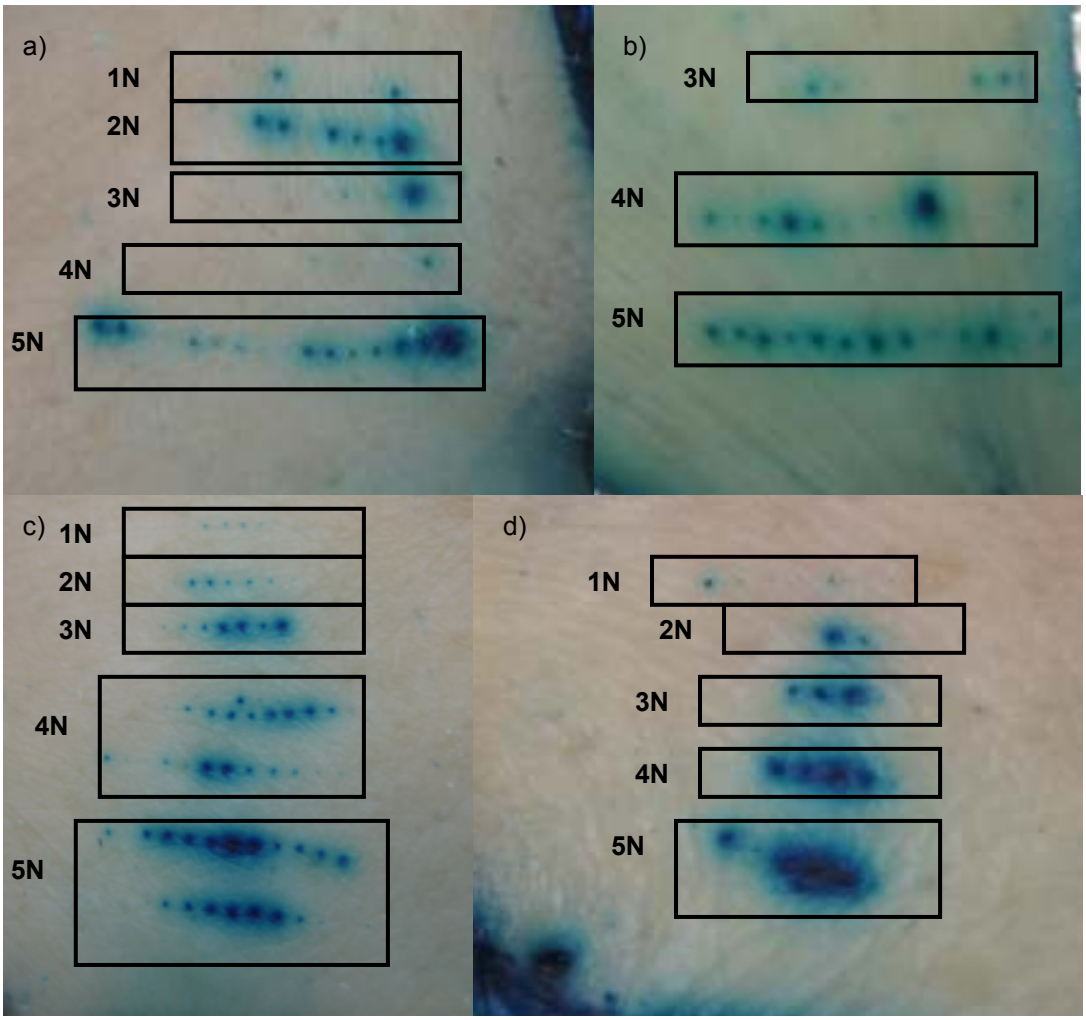


*Figure 5.13: Images showing microneedle array puncture in ex vivo human skin stained with methylene blue solution at 1-5N desired load application (indicated on each image) for a) the flat array, b) the 0.95mm, c) the 1.83mm and c) the 2.72mm curved arrays.*

When testing murine skin, using the same method but with a reduced concentration of methylene blue and reduced application time for the dye, microchannel staining was difficult to distinguish as the entire skin surface became stained. By increasing the application load to 10N, microchannel

staining was possible but only as a result of the increased channel diameter. Therefore, the results for this experiment were discounted as effective staining of microneedle puncture was not possible. However, as the previous results indicating puncture for human skin *ex vivo*, it suggests that mouse skin may also have been penetrated by the microneedle arrays as it is significantly thinner than human skin.

### 5.4.4 *In vivo* images of skin penetration by microneedles

Figure 5.14-5.17 shows the methylene blue staining post microneedle insertion into the human skin *in vivo* using the four array shapes. The blue dots show disruption in the SC. The red circle indicates the staining of a hair follicle.

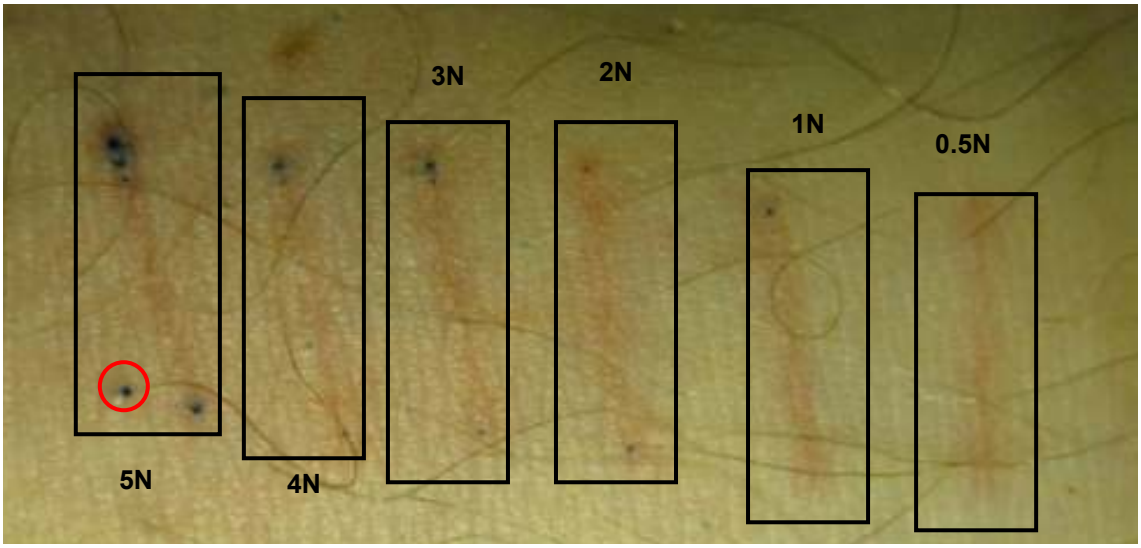


*Figure 5.14: Images showing microneedle array puncture into in vivo skin stained with methylene blue solution at 0.5-5N desired load application (indicated on each image) for the flat array, The red circle indicates the staining of a hair follicle.*

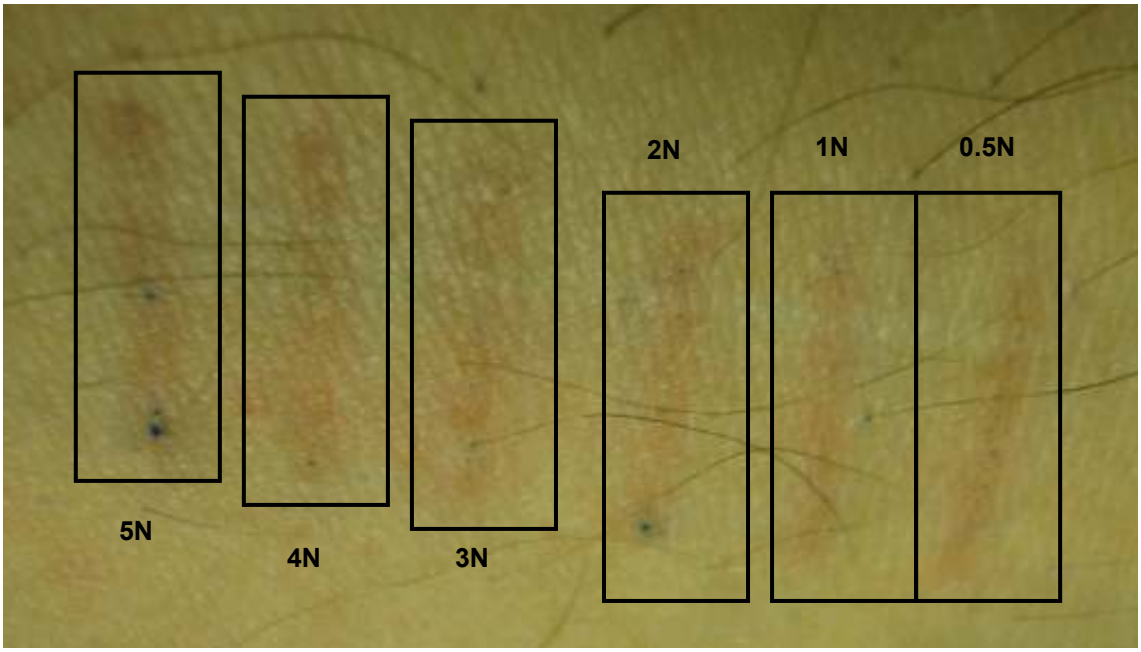


*Figure 5.15: Images showing microneedle array puncture into in vivo skin stained with methylene blue solution at 0.5-5N desired load application (indicated on each image) for the array with a curvature of 0.95mm.*

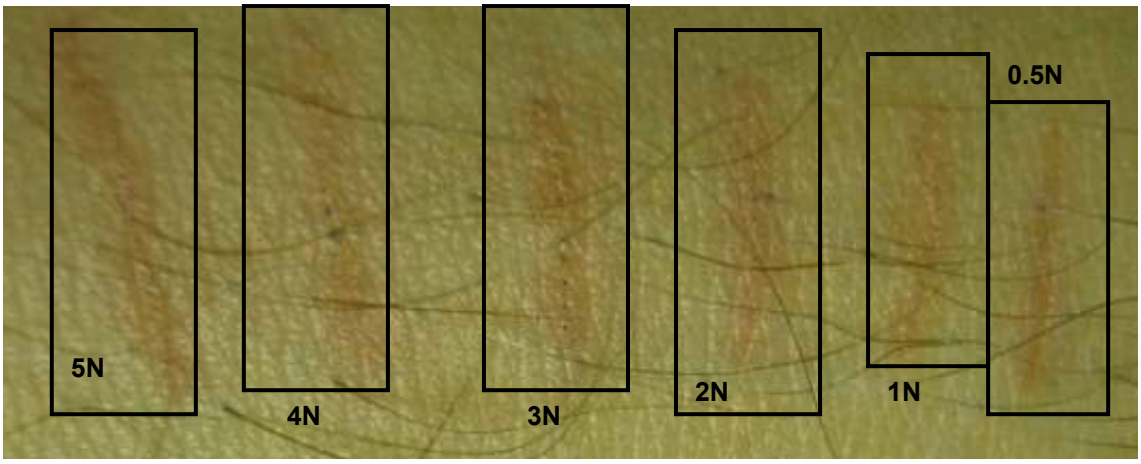


*Figure 5.16: Images showing microneedle array puncture into in vivo skin stained with methylene blue solution at 0.5-5N desired load application (indicated on each image) for the array with a curvature of 1.83mm.*

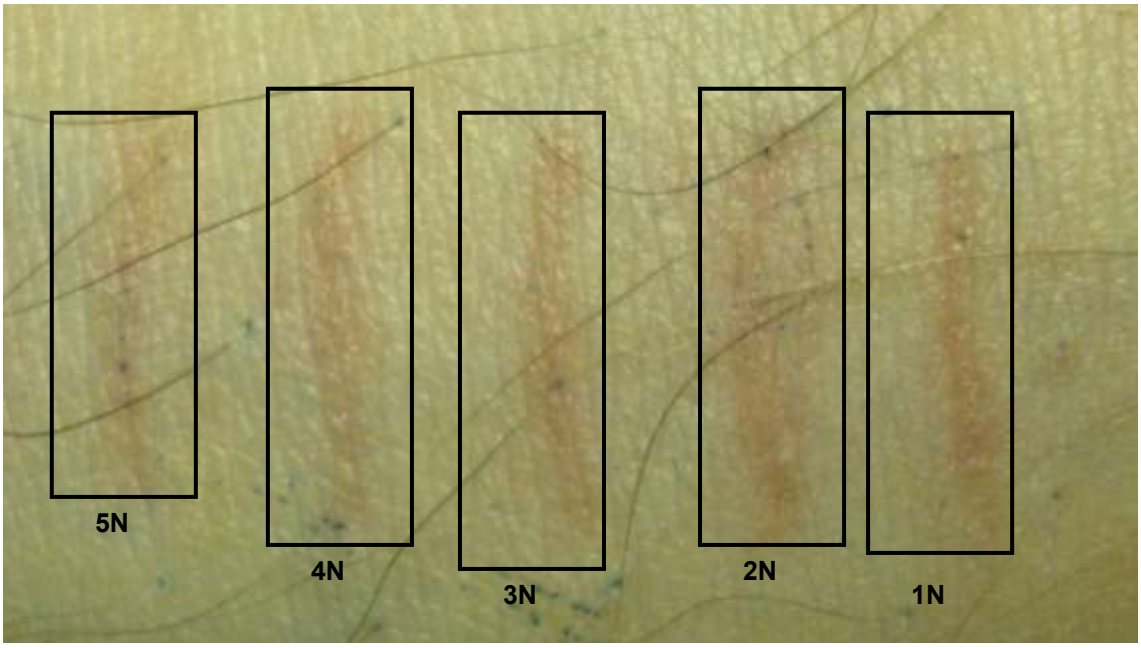


*Figure 5.17: Images showing microneedle array puncture into in vivo skin stained with methylene blue solution at 0.5-5N desired load application (indicated on each image) for the array with a curvature of 2.72mm.*

Figure 5.18 shows the skin site after microneedle application, clearly showing red marks were the arrays had been administered. The image also shows the large skin site tested which could have affected the measurements taken as some areas had a greater volume of fat beneath the skin than others. It was noted whilst applying the microneedle arrays to skin, that the skin deformed a considerable amount, as observed previously for the administration of a single microneedle to skin.

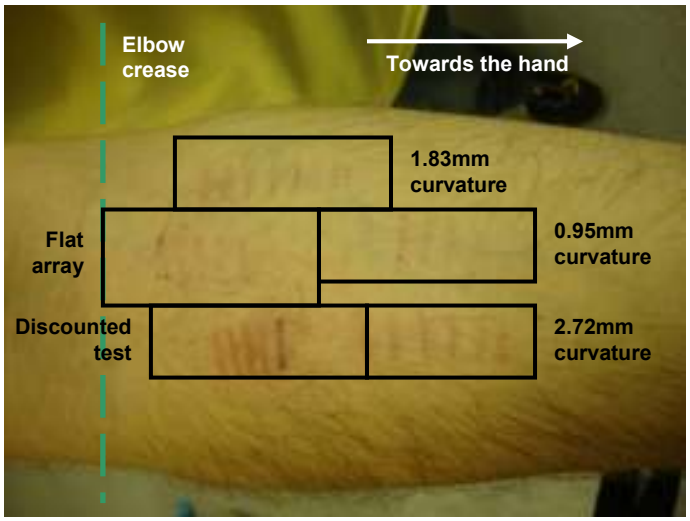


*Figure 5.18: Image showing the skin site after microneedle application and areas of skin treated by each microneedle array.*

## 5.5 Discussion

The *in vivo* measurements of a single microneedle applied to skin at low loads illustrated in Figure 5.3, show little difference between microneedle design A and B up to 1mm relative displacement, despite the differences in geometries for both microneedles. A maximum load of 0.15N was applied to both microneedles, which was only slightly higher than the lowest force required for *in vivo* skin puncture of an individual microneedle (Davis et al., 2004). Hence it was possible that the microneedles may not have penetrated, the skin during this study. Additionally, as there was no disruption to the load – displacement curve or a drop in load (it may be expected that the force on the microneedle would reduce when the skin barrier was broken) for either microneedle, it was difficult to determine the exact load at which skin puncture may have occurred (Davis et al., 2004). However it may suggest that if the skin had been penetrated at this low load, it may have done so through tearing, resulting in no sudden jump in the load – displacement curve for either microneedle. Further work could involve the inclusion of an additional measurement which could determine whether the skin barrier had been breached. These include measuring the electrical resistance of the skin as it

is penetrated by the microneedle, resulting in a drop in resistance (Davis et al., 2004). At maximum load, a relative microneedle depth of 2mm was reached, which was significantly greater than the individual length of each microneedle. This implies that the skin and subcutaneous tissues deform significantly prior to and / or during penetration. It is also possible, at maximum depth that the screw used to mount the microneedle onto the load cell, and the base of the microneedle itself, may have also contacted the skin's surface.

The stratified FEMs of human skin used to detail microneedle application *in vivo* for both microneedle geometries, did not account for skin puncture as only low application loads were simulated. As the boundary conditions of the model did not allow the microneedle to penetrate the stratified model, the very top of the skin appears deflect around the microneedle tip. This is more pronounced in Figure 5.5 a) which shows microneedle design B. Models of microneedle designs A and B show the deformation of each skin layer and the high levels of strain distribution through the hypodermis. Both models illustrate the great influence of the hypodermis during microneedle application as this layer shows significant levels of deformation at maximum microneedle displacement. This finding is in agreement with the *in vivo* measurements and models described in Chapters 2-4, which suggested that the mechanical contribution of the hypodermis should be considered when assessing microneedle application to skin. This observation implies that as, no hypodermis is present on *ex vivo* tissue, differences between *ex vivo* and *in vivo* penetration tests using microneedle devices may be noted. Further more, the strain distribution through each tissue appears to be varied, due to the differences in the mechanical properties of all three layers. High levels of stress were noted along the tissue surface at the site where the microneedle indents the skin upon contact. This is most likely due to the increased pressure at the microneedle tip, as it was apparent that the skin was deforming around the tip of the microneedle, rather than acting as though a nodal load had been applied. Microneedle design B shows a lower maximum stress when compared to design A, possibly due to the different interfacial areas of both microneedles, as it has been suggested that those with a smaller interfacial area, penetrate the skin with less force (Davis et al., 2004).

Figure 5.6 illustrates the comparison between experimental and computational measurements of microneedle designs A and B applied to human skin *in vivo.* A good agreement between experiment and model can be seen for designs A and B, serving as a validation for the material parameters for subject 1, obtained post extraction. The discrepancies between model and experimental data may be due to the assumptions within the FEM and experimental errors, which are magnified at the small loads that were measured. Also, the microneedle was cyclically applied to the skin site to loads of up to 0.15N, so it is possible that the microneedle may have damaged the skin site during this process. However, application forces of 0.01N were modelled so it is highly unlikely that either microneedle had punctured at that stage, so modelling microneedle application as opposed to penetration was the most appropriate.

Only one subject was assessed for this analysis, so it would have been extremely beneficial to increase the number of volunteers. However, as a preliminary study, the method has been shown to work well with predictable results and implications for future work. Additionally, by incorporating imaging techniques it may have been possible to record if there was a point of incision to determine whether model observations were paralleled with experimental recordings.

Several studies have investigated the penetration capabilities of individual microneedles. However, many of these cannot be compared with this current investigation as the application forces were not recorded. In a study by Davis *et al*. single microneedles with total heights of 720μm and varying tip radii were administered to the human hand *in vivo*. By measuring the electrical resistance of the skin and the load displacement curve for the microneedles applied to the skin, it was possible to estimate the load of insertion for the range of microneedle geometries. A linear relationship was shown between interfacial microneedle area and insertion force, where the insertion loads ranged from 0.1N to 3N. It should be noted however, that the palm of the hand was the chosen application site, hence it would be expected that higher insertion forces would be observed in the current study as the forearm has a higher volume of fat below the skin. Donnelly *et al.* in 2010 measured the

application force of an array containing 9 microneedles into neonatal porcine skin *ex vivo.* The study showed that at a load of 4.4N, the microneedles penetrated to half the total microneedle length. This value is again considerably higher than that applied to the microneedles used within this study, so it is unlikely either microneedle designs A and B had penetrated.

Attempts have been made to model the application and penetration of a single microneedle to skin. In a study by Aoyagi *et al*. in 2008, the stress within a rubber like material was analysed during microneedle insertion using a FEM. The observations in this published study agree with those found in this Chapter, where an increased stress was noted in the insertion material at the microneedle tip. Kong and Wu in 2009 modelled the insertion of the mosquito's fascicle into human skin using a multilayered FEM, and in 2011, Kong used a similar principle to model microneedle insertion to hypothesise the optimal microneedle geometry. Whilst both were shown to agree with experimental measurements from published studies, the material properties of the skin were assumed from literature and the model data was not fully validated against their own experimental measurements.

Again using the stratified FEM of human skin *in vivo,* developed through Chapters 2-4, it was possible to design array curvatures, rather than focusing on individual microneedle designs as discussed previously, based on deformation measurements from model data. Using wire cutting technologies, three curved microneedle arrays were manufactured using the approximated measurements of skin deformation, producing arrays with a highest, lowest and average curvature taken from model data. Additionally, a flat array was manufactured to act as control. All individual microneedle geometries and spacing were identical for all four arrays, so that the only variation between arrays was the radii of the device. The array designs were then tested in human skin *in vivo* and *ex vivo*, and in murine skin *ex vivo* at loads of between 0.5 and 5N to provide preliminary measurements. After microneedle treatment, a methylene blue staining was applied to the skin site to stain any resulting microneedle channels.

The suggested array curvatures shown in Table 5.1, show a large variation between the highest and lowest dimensions. These measurements are in agreement with the observations made in Chapters 2 and 4, where volunteer 1 was shown to have the stiffest skin, and volunteer 2 the softest. Hence a larger array curvature was suggested for volunteer 2 when compared with volunteer 1. The three radii of the curved arrays are spread over a wide range, implying that no single curvature would be most likely to allow for uniform penetration. This is most likely due to the large variations in the mechanical characteristics of the modelled skin. Due to the increased load applied to the skin within the FEMs, a greater thickness of hypodermal tissue was required. Hence the adapted model used within the study, was not entirely representative of that developed in Chapters 2-4, but the model worked well as an approximation. Additionally, the load applied to the skin models was slightly lower than some measurements obtained for microneedle insertion, so the suggested curvatures calculated may have been under estimated (Davis et al., 2004).

The microneedles themselves were 0.6mm in height, which is slightly shorter than microneedle design A, described previously in this Chapter. Each microneedle was 0.1mm in thickness, making the microneedles almost as wide as they were thick. Table 5.2 shows a summary of the microscopic images of several microneedles along each of the four array designs. All individual microneedles show little burring around the edges implying that the wire cutting technique worked well when producing the array profiles. As a result of the high finish quality, no further action was required to remove any remaining material from the cutting edges. The images also show that with increased curvature, the length of microneedle 1 (the needle at the periphery of the array), decreased in length. In a study by Gill *et al.* in 2007, stainless steel microneedles were manufactured by laser cutting technologies. It was noted in this study that three passes of the laser were required to cut the material. This was more so than the microneedles manufactured within this investigation, where only one pass of the wire was required to cut the microneedle profiles. It is also import to note that as ten stainless steel sheets were clamped at once, ten microneedle arrays could manufactured at once,

unlike the study by Gill *et al.* This implies that the approaches used presently are better equipped for the manufacture of planar stainless steel microneedles.

Figure 5.14 shows the application of all four microneedle array designs to human skin *ex vivo.* It was suggested that all four arrays punctured the skin at a desired load of 5N, as the methylene blue had stained the microchannels created. Little penetration was indicated at 1N for all arrays but beyond 2N, puncture was detected for some of the microneedles within the array. Figure 5.14 a) shows microchannel staining using the flat array, where the microneedles at the periphery were shown to penetrate to a greater depth, resulting in an increased staining within the microchannels. The array design with a curvature of 0.95N was shown to have the most uniform puncture across all microneedles within the array at an application load of 5N, as all perforations showed a more evenly distributed methylene blue staining. With increased curvature however, only the central microneedles were shown to penetrate, as indicated in Figures 5.14 c) and d) for array curvatures 1.83mm and 2.72mm respectively. As the skin was pinned to a cork board, the tension within the tissue may not have been consistent throughout the sample. This may have affected skin puncture when using the microneedle devices, as it has been suggested that microneedles are more likely to penetrate the skin if the tissue is in a greater degree of tension (Aoyagi et al., 2008).

These preliminary results show some repeatability but many factors have been neglected, thus a more robust testing methodology is required to form strong conclusions. Additional considerations such as assessing microneedle penetration using different donors of varying ages and different skin tensions would have determined the influence of such factors on microneedle penetration. It may also have been beneficial to use a mechanical testing machine to apply the arrays at varying loads and application speeds (Verbaan et al., 2008). With the inclusion of histological examination, microchannel depth could have been assessed to validate such findings. However these preliminary results have implies that the microneedle arrays do penetrate *ex vivo* human skin

When repeating the same experiment using murine skin *ex vivo*, it was observed that even with a lower concentration of methylene blue and a reduced application time of the dye (<10 seconds), the entirety of the untreated skin became stained. This made it impossible to distinguish the microchannels created. Observations were consistent when removing the hair via shaving, rather than with hair removal cream, as it was hypothesised that the formula within the hair removal cream may have been damaging the SC, thus increasing the diffusion of methylene blue. However, hair removal cream was used to remove the fur when performing the mechanical tests on *ex vivo* murine skin detailed in Chapter 2, and no / little damage to the SC was noted from histological examination. Figure 5.15 shows the staining of a hair follicle within human skin, indicated by a red circle. As mice have considerably more hair follicles than humans, it is possible that such structures may have increased the permeability of the SC to the methylene blue solution. When the microneedle application load was increased to 10N, the microchannels could be distinguished by methylene blue staining. This may be because the channels themselves may have been wider, so the methylene blue could sink into the microconduits at an increased rate before the solution was removed. As murine skin is significantly thinner than human skin, it would be sensible to hypothesise that the tissue would have been penetrated by the microneedles. However, due to the increased permeability of the SC, which is most likely due to the decreased thickness of the skin layer, this method of analysis was not appropriate.

Skin puncture was difficult to detect using methylene blue for the majority of preliminary tests performed on human skin *in vivo.* However, the flat array did show penetration at 5N for the peripheral microneedles (Figure 5.15), which is in agreement with *ex vivo* observations in human skin. The array with a curvature of 1.83mm was shown to have some penetration for the central microneedles at 3N and the microneedles at the edge of the 0.95mm curved array were also shown to puncture the skin at a load of 5N (Figures 5.16 and 5.16). Experimental observations showed that the skin deformed a large amount during microneedle array application, due to the soft tissues below. This offers a potential explanation as to why the microneedles did not

penetrate the skin as well as *ex vivo* measurements, because the soft tissue may have been distributing the load on the microneedle array over a wider area. This observation is in agreement with the indentation measurements described in Chapters 2-4, and with the application of a single microneedle applied to skin discussed previously within this Chapter. It should also be noted that the methylene blue solution was not left on human skin *in vivo* as long as the *ex vivo* skin sample to avoid permanent dying of the *in vivo* skin. This may have resulted in insufficient staining of the microchannels created by the array *in vivo.* Figure 5.19 shows the area of skin used during the test, where there are quite clearly areas of red where the microneedles had been applied. This suggests the arrays were administered at a high enough load to induce a response by the body. Therefore, even though the methylene blue staining did not detect many microneedle channels, it is possible that the microneedles may still have penetrated. In a study by Coulman et al. in 2011, it was observed that upon the application of a microneedle to human skin *in vivo*, the elastic properties of the skin may have caused the tissue to recoil quickly after the needle had been removed, which is an observation unlikely to be noted *ex vivo*. Hence it is possible that the microchannels may have closed enough to prevent the methylene blue from diffusing into the disruptions in the SC.

As with the *ex vivo* measurements discussed previously, analysis is based on preliminary results only, hence considerably more volunteers need to be assessed to validate any observations made during this study. Additionally it may be extremely beneficial to test microneedle penetration on different application sites on the body. The study could be developed to investigate the effect of insertion speed and different application loads on more volunteers and *ex vivo* skin samples, to allow for more conclusive data. Furthermore by applying the microneedle arrays using a testing machine which controls the load on the array, more repeatable application loads could be applied. Due to the shape of the arrays, it may have also been beneficial to monitor the angle of application for all arrays, however the study did replicate how the microneedles would be applied in clinical practise. This preliminary study has however shown that some microchannel staining can be

assessed *in vivo* and has also suggested that other methods may be more appropriate to assess microneedle penetration *in vivo.*

This preliminary study has also allowed for some comparison between microneedle penetration *in vivo* and *ex vivo* skin samples. The discounted test using murine *ex vivo* skin suggests that murine skin is not an appropriate substitute for human *ex vivo* skin due to the decreased SC thickness and increased permeability to applied substances. This observation is in agreement with the mechanical tests and subsequent inverse analysis performed on *ex vivo* samples of human and murine skin, which implied that both tissues have very different anatomical and mechanical properties. When comparing microneedle puncture tests performed on *ex vivo* and *in vivo* human skin, some observations were in agreement. It was concluded that for both *in vivo* and *ex vivo* tests that the flat array showed an increased microneedle puncture depth for those needles at the periphery of the array, indicated by a greater area of methylene blue staining. However, skin puncture by the microneedle arrays was either difficult to detect or not present for the preliminary *in vivo* analysis*,* most likely due to the high levels of skin deformation observed during array application. Therefore, substantial further work is required to assess the penetration of the microneedle devices in human skin *in vivo* and *ex vivo* to verify the measurements obtained and account for further factors which could potentially affect microneedle penetration

It has been shown that both *in vivo* and *ex vivo* testing have several advantages and disadvantages, future work could also focus on the development of an experimental set up which combines the two approaches. This could involve the use of an *ex vivo* skin sample on top of a substance which aims to mimic the mechanical properties of soft tissue below the skin. Using indentation measurement at higher loads than that applied in Chapter 2, it would be possible to further validate the experimental set up. Such an approach would allow for a higher exposure time to methylene blue at the treated skin site, whilst still using human skin. However, one important parameter to note is the amount of *in vivo* tension present within the skin, as

this also needs to be replicated *ex vivo.* But if the experimental set up were to validate against *in vivo* measurements, an estimate for the tension could be made. Moreover, Chapter 2 has shown that human skin can endure great periods of extension at low loads, prior to exponential stiffening, so it is quite possible that there may be a relatively large range of appropriate tensions for the skin, which would be comparable to *in vivo* circumstances.

All microneedle arrays were shown to penetrate *ex vivo* skin well at high loads (4-5N). The array which produced the most uniform skin puncture across all microneedles was the array with the smallest curvature of 0.95mm. Unfortunately it was difficult to determine whether this was the case *in vivo* as microchannel staining was not apparent for this array. However, the microneedle array with a curvature of 1.83mm showed some penetration at 3N for those within the centre, and as the flat array did illustrate penetration at higher loads for those microneedles around the periphery of the array, it could be suggested that the optimal array curvature potentially lies between flat and 1.83mm, which is in agreement with *ex vivo* measurements. However strong conclusions cannot be made regarding these observations due to the small number of skin samples and volunteers used within this study.

Numerous studies have also attempted to visualise microchannel formation post application to human and animal *in vivo* and *ex vivo* skin. Haq *et al.* used a similar experimental set up to visualise microperforations post microneedle application in human skin *in vivo* after 1, 4, 8 and 24 hours. The arrays used for the tests consisted of 36 silicon microneedles, which were identical to microneedle design B used previously in the Chapter, where each needle had a height of 280μm. A methylene blue solution was subsequently applied to the treated skin site and some microchannel staining was observed. However, as there was no information regarding the load applied to the microneedle array to induce puncture, the results obtained cannot be directly compared with this investigation.

A comparable microneedle array has been developed were individual microneedles are mounted onto a roller, which is then rolled across the skin.

A similar device which is currently used for cosmetic purposes is the Dermaroller® (AesthetiCare, Yorkshire, UK) (Badran et al., 2009; Zhou et al., 2010). Microneedle rollers have been shown to increase skin permeability in cadaver tissue when compared with flat arrays, at the same application forces (Park et al., 2010). It was suggested that this was due in part the lower number of microneedles in contact with the skin at any one time. In a study by Bond and Barry in 1987, the permeability of mouse and human *ex vivo* skin was analysed. It was noted that mouse skin is considerably more permeable than human skin, which is in correspondence with the findings from this study, as when the methylene blue dye was applied to *ex vivo* mouse skin, the solution was shown to rapidly stain and / or permeate the skin.

## 5.6 Conclusions

In conclusion, the application of a single microneedle applied to human skin *in vivo*, prior to penetration, serves as a good validation for the stratified model of human skin developed in Chapters 2-4. Additionally, measuring and modelling the application force and relative indentation depth of a microneedle has suggested that the subcutaneous tissues deform significantly during the administration of a single microneedle. This implies that *ex vivo* measurements of microneedle application may not be fully representative of *in vivo* data, as the subcutaneous tissue is usually striped from the sample. Furthermore, an agreement between model and experimental data was noted for both microneedle geometries, suggesting that both may act similarly when applied to human skin *in vivo.*

Using the validated multilayered FEMs of human skin for all seven subjects, it was possible to suggest array curvatures which could potentially increase the consistency of microneedle puncture of all those within the array. The manufacture of planar arrays from stainless steel sheets by wire cutting technologies allowed for ten microneedle profiles to be cut per pass, which is an improvement on previous methods (Gill and Prausnitz, 2007). It was shown that microneedle puncture into *ex vivo* murine skin was difficult to

detect due to the increased permeability of the tissue to the methylene blue dye, resulting in the entire tissue became stained. However, microneedle puncture into *ex vivo* human skin could be detected using this method, and it was shown that the flat array appeared to penetrate the skin to a greater depth for those microneedles at the periphery. When assessing microneedle penetration *in vivo* using an adapted experimental set up with a reduced exposure to the methylene blue solution, skin penetration was difficult to detect. As the measurements were only conducted on one volunteer and one donor, it is difficult to conclude significant results from such preliminary data. The study has instead shown the potential for further work but with the addition of significantly more volunteers and donors, the results presented could be validated.

One key observation noted when assessing microneedle puncture *in vivo* by applying either the arrays or single microneedles, is that the skin deforms significantly due to the subcutaneous fat and muscle present *in vivo.* Therefore further work beyond this thesis could include the development of a test rig which uses an *ex vivo* skin tissue, with the addition of a material below which has similar mechanical properties to fat and muscle, resulting in a substance which incorporates the benefits of *ex vivo* testing whilst still having similar mechanical properties to *in vivo* skin and the underlying tissues

# CHAPTER 6

# CONCLUSIONS

Microneedle arrays were developed as a means of promoting transdermal drug delivery via creating microperforations through the outer skin layer to increase drug diffusion. However, without effective skin puncture whilst using the device, the microneedle array is relatively useless. Hence, the aim of this Thesis was to further understand the mechanical properties of skin, to aid in the establishment of more rationally designed microneedle arrays which could allow for uniform and repeatable puncture across all microneedles into skin *in vivo.* As many use *ex vivo* human (Agache et al., 1980; Badran et al., 2009; Coulman et al., 2009; Ng et al., 2009; Gomaa et al., 2010; Khanna et al., 2010; Park et al., 2010) and murine (Gill and Prausnitz, 2007; Kendall et al., 2007; Crichton et al., 2010; Wei-Ze et al., 2010) skin for drug delivery and penetration tests using microneedles, a better understanding of the mechanical properties of human and murine skin both *in vivo* and *ex vivo* were required.

The mechanical characteristics of skin are extremely complex so mechanical testing alone was not appropriate for describing such behaviours. By using inverse finite element modelling coupled with mechanical testing, it was possible to establish validated models of skin *in vivo* and *ex vivo.* The optimal parameters extracted provided the basis for a comparison between human and murine *ex vivo* skin and a model describing the mechanical properties of human skin *in vivo* during indentation was used to measure the deformation of the skin under loads comparable with microneedle application. It was also shown that the FEMs of skin indentation could be validated by developing a

model of microneedle application, prior to penetration, which could be compared with *in vivo* findings. The *in vivo* skin deformation measurements provided the dimensions of curved microneedle arrays which followed the contours of the skin upon load application, aiming to allow for consistent microneedle puncture across all needles in the array. Once manufactured, the microneedle devices were applied to human skin *in vivo* and to *ex vivo* skin samples taken from human and murine donors, to assess whether repeatable skin puncture occurred across all three groups. These preliminary measurements provided information as to whether *ex vivo* skin samples can replicate the observations made during microneedle application performed on *in vivo* skin tissue.

The conclusions relating to the objectives outlined in Chapter 1 will be discussed individually.

***Objective 1: Experimentally examine the mechanical properties of skin***

To further understand the mechanical properties of skin, it was important that robust and repeatable methods of mechanically testing the tissues were derived. Chapter 2 focuses on this objective and the experimental observations were split between *in vivo* and *ex vivo*. *In vivo* measurements were taken using indentation tests, at loads comparable to microneedle application. A second series of experiments were taken using *ex vivo* samples from murine and human donors during tensile loading along three load axes to collect anisotropic measurements. Such an experiment provided the basis of a comparison between the mechanical properties from human and murine *ex vivo* skin to hypothesise whether murine skin is an appropriate model for human skin when examining the mechanical properties.

Both sets of experiments were shown to have a high level of repeatability. Indentation measurements on *in vivo* skin were performed on seven subjects using two small geometrically different indenters to further validate the measurements and FEMs. Tensile measurements were taken from a circular piece of skin tissue, where the underlying hypodermis had been removed, from 2 human and 8 murine donors. By altering the orientation of the load

axes, it was possible to characterise the anisotropic behaviour of the tissue. All tissue samples were shown to remain gripped resulting in no slippage during mechanical testing. Furthermore, due to the low maximum load of 2N, the tissue was not damaged during examination.

Basic analysis of the *in vivo* indentation measurement showed that by calculating the Young's Modulus of the tissue, it was possible to make comparisons between the volunteers' skin. Additionally, through analysing the load-displacement curves obtained from tensile tests performed on the *ex vivo* human and murine skin samples, it was noted that human skin endured much greater levels of deformation at low loads, characterised by a greater length of phase 1. From taking histological sections from a selection of *ex vivo* skin samples used in testing, it was possible to examine any anatomical variations which could potentially have led to the difference noted between the mechanical characteristics. The histology showed that the human skin was significantly thicker, with a greater volume of dermal tissue. Due to the network of collagen and elastin fibres, the dermis provides the majority of the mechanical support for skin during in plane tension. Hence it is most likely that this increased amount of dermal tissue within human skin allowed the sample to endure greater levels of extension at low loads, when compared with murine skin.

From these primitive observations it was shown that some conclusions could be made regarding the mechanical properties of the tested tissues. However, due to the complex mechanical properties of skin, such observations were primarily related to the comparison between samples and volunteers, rather than analysing the properties. As a result, inverse finite element modelling was chosen to further understand the properties of the tissue, as the constitutive models used to represent skin, were far more sophisticated than those methods used to examine the data from experimental tests alone. Also, as skin does not abide by Hooke's Law, calculating the Young's modulus and stiffness of the tissue is not representative of the complex properties of the skin.

When comparing average measurements taken from these studies, to published articles which have aimed to analyse similar observations, large variations were noted. It was also found that there were very different observations between the published articles themselves, particularly when comparing *in vivo* measurement taken using different approaches and when comparing *in vivo* indentation to *ex vivo*. This implies that the mechanical properties of skin should be quantified with care, consequently it should not be assumed that all tests, for example, indentation, suction, extension and torsion, will give comparable measurements. However for the aims of this study, the methods applied were appropriate for measuring the mechanical properties of skin *in vivo* using a method comparable to microneedle application, and as an approach for determining the variations between the mechanical characteristics of human and murine skin *ex vivo*. Additionally, it was shown that these findings illustrated that the variation in the mechanical properties of human and murine skin suggest that murine skin may not be an appropriate tissue to assess microneedle penetration.

***Objective 2: Develop FEMs of skin***

Following the success of experimental approaches and the measurements obtained, further analysis was possible. As stated previously, the evaluations taken from the experimental results alone were severely limited due to the simplistic nature of the constitutive models used, allowing only for a comparison between donors and volunteers. Hence, by modelling the skin using appropriate constitutive models, inverse analysis was used to extract the material parameters which best fit with the experiment. This not only allowed for another method of comparison between donors and subjects, but also lead to validated models of skin which were used in the design process for the new microneedle array. Chapter 3 described this second objective, which was to develop models which represented the mechanical tests, and could be used with inverse analysis calculations. To achieve this, the models were required to solve quickly by having a reduced number of elements, whilst maintaining a high level of accuracy.

All 3D models were developed for FEBio, which proved to be an excellent finite element modelling package specifically designed for modelling biomechanics and biomaterials. The software also incorporates an extensive range of constitutive models. The post processing software, PreView, allowed for simple meshes and geometries which were adequate for the study. All dimensions were taken from actual measurements where possible, but in the case of the model of skin indentation, layer thicknesses were assumed from the literature. As indentation measurements on human skin *in vivo* were taken using two geometrically different indenters, it was possible to add further variables to the model, as both could be used to as a comparison for the properties extracted during the inverse analysis. Hence, the skin was modelled incorporating the epidermis, dermis and hypodermis skin layers. Using the Ogden material model of hyperelasticity, the nonlinear characteristics of the skin tissue could be adequately represented, more so than through assuming linear elastic properties as with the Young's Modulus calculations. The tensile measurements performed on human and murine *ex vivo* skin, allowed for the characterisation of the anisotropic mechanical behaviour of the tissues. As a result, it was integral that the selected constitutive model had the ability to behave anisotropically, hence a model was developed where the skin was assumed to be an isotropic material matrix, incorporating three families of fibres, to create anisotropic properties. By conducting mesh convergence tests and reducing the size of the model to only a quarter of the original dimensions, it was possible to dramatically reduce the number of elements present. This was beneficial as the models were all to be implemented within inverse analysis, thus the models needed to solve quickly whilst maintaining a high level of accuracy.

Although the FEMs developed did allow for nonlinear, and in the case of the model used to represent *ex vivo* skin, anisotropic mechanical behaviour, the viscoelastic properties were ignored. However, for the purpose of using such models as a tool of optimising future microneedle device design and to aid in the comparison between the mechanical properties of human and murine skin, both sets for FEMs were of adequate complexity. Furthermore, with the addition of extra material parameters, an increase in convergence time would

have been likely, consequently increasing the time taken to execute inverse analysis. The constitutive models used were shown to behave in a similar manner to skin for both models of indentation and tension. The V-W model, which is rarely implemented was shown to give a highly nonlinear mechanical response when skin was modelled in tension. Additionally, the Ogden material model was illustrated to give almost linear and nonlinear mechanical properties for the FEM of skin indentation. However, further work could include development of both sets of FEMs to reduce the number of contacts present. For example, the FEM of skin indentation modelled the skin as three separate geometries for the epidermis, dermis and hypodermis. It may have been beneficial to model the skin as a single mesh and split the skin into the three layers by assigning different properties to the three sections.

***Objective 3: Inverse analysis to further describe the mechanical properties of skin***

Using the FEMs and experimental measurements, it was possible to implement inverse analysis to extract a single set of material parameters for the FEMs which gave the best agreement with experimental data. To achieve this, Matlab was used to create optimisation loops to systematically reduce the error between experiment and FEM, until the FEM acted as a good model for the experimental data. Different optimisation algorithms were chosen for the multilayer and anisotropic models of skin as both were shown to have different model sensitivities to input parameter alterations.

Post inverse analysis, all models were shown to have a good agreement with experimental data, implying the approach worked well. The anisotropic model of human and murine skin in tension was shown to have a higher correlation between model and experiment using a single parameter set, demonstrated by the lower $R^2_{ave}$ values. It was suggested that this may have been due to the increased number of parameters within the constitutive model.

The optimal material parameters extracted reinforced some of the observations made during the mechanical tests performed in Chapter 2, implying the method worked well for identifying general properties. The

parameters for the multilayered FEM of skin showed consistency between the Ogden coefficients extracted for the dermal layer, however significantly larger variations were related between the parameters obtained for the epidermal and hypodermal layers. This suggested that the differences between subjects were more due to these layers. This was apparent when comparing the coefficients for the hypodermis, as those with stiffer skin were shown to have similar properties for this layer upon inverse analysis. The optimal material coefficients for human and murine skin further reflected the great variations between the mechanical properties of the two groups, detailed by the tensile tests. It was found that there were significant differences ($p<0.05$) between the average $C_2$, $C_3$ and $\lambda$ values, comparing human to murine skin.

Despite the success of the study, it was also noted that the optimisation algorithms could converge to a local minimum, so the coefficients obtained were not necessarily a definitive set, hence further work could focus on testing the optimisation algorithms. Drastic changes to the initial set of starting parameters may have resulted in different optimal coefficients. Importantly, it is possible that the same $R^2_{ave}$ may have been calculated, but with different material coefficients. However, as the aims of this study were to develop a model which could represent skin and act as a comparative tool between donors and volunteers, the approach has been shown to work well. Subsequently, further validation of the multilayered FEM of skin indentation was achieved by using the model to predict the mechanical response of skin upon the application of a single microneedle applied to the skin of volunteer 1. Hence, by conducting a second experiment for the tensile tests performed on skin samples, possibly across a different load axis, validation of the model parameters could have also been found by using the model to predict the additional test. Furthermore, the anisotropic model of human and murine skin in tension gave a closer fit with experimental measurements. This may have been due to the increased number of parameters within this model.

***Objective 4: Use in vivo model of skin to develop a more rational microneedle array design***

The validated multilayer model of skin was used to develop a curved array of microneedles which could follow the deformation of the skin. By applying a pressure load of 1N, with an area identical to the array dimensions, the curvature of the skin was measured. From this, three curved microneedle arrays were designed incorporating the highest, lowest and average curvatures, in addition to a flat array which acted as a control. All individual microneedles were given the same geometry and needle to needle spacing so that a comparison between curvatures was possible. Array profiles were manufactured using wire erosion from stainless steel sheets, and the approach was shown to produce a high finish quality.

Upon the application of the device to *in vivo* and *ex vivo* human skin using preliminary tests, it was suggested that the majority of the microneedles penetrated the *ex vivo* skin at maximum load of 5N. However, microneedle penetration was not easily detected *in vivo* and hence it was difficult to determine whether the curved array had improved microneedle penetration consistency. By comparing *in vivo* to *ex vivo*, it was possible to hypothesise the approximate optimal array curvature. *In vivo* and *ex vivo* measurements using the flat array demonstrated that the microneedles at the periphery of the array appeared to penetrate to a greater depth. On the contrary, the average and highest array curvatures did show increased penetration for the central microneedles when applied to *in vivo* and *ex vivo* skin. However it was clear from these preliminary tests that significantly more donors and volunteers are required to validate any observations made during these tests.

***Objective 5: Use the models and preliminary experiments to hypothesise whether in vivo measurements of skin penetration can be replicated ex vivo***

With the manufacture of the curved microneedle arrays, it was possible to hypothesise whether repeatable measurements of microneedle insertion could be made when using *ex vivo* and *in vivo* tissues. The devices were also preliminarily tested to determine whether the new curved array could increase

the uniformity of skin puncture of all microneedles within the array, when compared to a flat array. Hence microneedle insertion experiments were performed on human skin *in vivo* and *ex vivo* and on murine skin *ex vivo,* to inform the findings previously discussed which compare the mechanical properties of *ex vivo* human and murine skin.

All four microneedle array designs were applied to each skin tissue at forces between 0.5-5N. Microchannels created by the needles were then stained using methylene blue. *Ex vivo* experiments performed on human skin suggested penetration for all four microneedle arrays at increased load, and it was indicated that the microneedles at the periphery of the flat array penetrated to a greater depth. This was demonstrated by increased staining within the microchannels. The arrays with a greater curvature (1.83mm and 2.72mm) were shown to only penetrate the central microneedles at maximum load, whereas the lowest microneedle curvature of 0.95mm was shown to have the most uniform puncture for all microneedles. When repeating the same experiment with a reduce methylene blue concentration and decreased exposure time, microchannel staining was not possible for *ex vivo* murine skin. This was most likely due to the increased permeability of the SC hence allowing the solution to defuse through the skin rapidly. This observation was reinforced by the histological examination shown in Chapter 2 of human and murine skin tissues, which demonstrate that murine skin was significantly thinner than human skin. It could be concluded that murine skin is not an appropriate substitute for human *ex vivo* skin due to these observations and the differences noted in the mechanical properties and skin thicknesses discussed previously.

Upon the application of all curved and flat microneedle arrays to human skin *in vivo,* skin puncture was difficult to detect within these preliminary studies. This could imply that either the microneedle arrays did not penetrate the skin sufficiently, or that the experimental procedure used could not identify any microchannels. Some staining was observed for the flat and 1.83mm curved arrays, for the peripheral and central microneedles respectively, implying the optimal array curvature could lie between these values. This does suggest

some repeatability between *in vivo* and *ex vivo* analysis, as *ex vivo* penetration tests suggested that the most effective array curvature which could allow for consistent puncture of all microneedles, was 0.95mm. But as only one volunteer and one donor was tested, it is difficult to confirm this observation. As a result, significantly more volunteers and donors need to be tested for future work.

The variations between *in vivo* and *ex vivo* could potentially be due to the influence of the subcutaneous fat which has been shown to be an important consideration when modelling skin indentation *in vivo.* Consequently, it was suggested that further work could focus on the development of a test set up which uses *ex vivo* skin and a substance to represent the underlying soft tissues, to mimic *in vivo* conditions. This study also showed that the array shape and application force does effect skin penetration both *in vivo* and *ex vivo*, thus further work could focus on assessing these parameters more extensively.

.

# CHAPTER 7

# FURTHER WORK

There are still numerous areas of further work which have the potential to reduce the limitations observed and develop the study further. Consequently, further work will be presented in the following categories.

***Number of donors and volunteers***

This thesis presented preliminary findings relating to a small number of volunteers and donors. Hence to reinforce the findings and identify additional trends, increasing the sample population would be extremely beneficial, particularly for the microneedle insertion measurements presented in Chapter 5. Additionally, it has been suggested that porcine skin potentially exhibits similar mechanical properties to human skin (Corr et al., 2009). Hence it maybe useful to include tensile tests performed on porcine skin to assess whether such tissues share the same mechanical characteristics expressed in human skin

***Skin indentation test body site***

As microneedle devices could potentially be applied to any skin site on the body, it may be beneficial to assess any variations in the mechanical properties of skin during indentation at several locations on the body.

***Validating the mechanical properties of skin***

When instigating inverse analysis, the addition of an extra experiment performed on each volunteer or skin sample could have been used as a further validation. The models could have then been used to predict the outcome for the additional experiment.

***Imaging techniques***

Several imaging techniques could have been used to quantify skin layer thickness measurements for the *in vivo* indentation tests, thus basing the FEM geometry on actual measurements. Several studies have used ultrasound (Hendriks et al., 2003), optimal coherence tomography (Hendriks et al., 2006) and magnetic resonance imaging (Tran et al., 2007) to quantify skin and layer deformation measurements during *in vivo* indentation. The measurements obtained may have served as additional parameters that could be used during inverse analysis. Both DIC and motion analysis techniques have been used to assess the strain distribution across *in vivo* skin during the application of in plane tension (Evans and Holt, 2009; Mahmud et al., 2010). If such an approach had been used whilst mechanically testing the *ex vivo* skin samples, the strain measurements obtained could be used as an additional set of parameters used during the optimisation process, thus increasing model accuracy. However, due to the regulations enforced whilst testing *ex vivo* human skin, it was not possible to use the DIC cameras in the laboratory.

***FEMs***

Additional parameters and observations could be applied to the FEMs to increase accuracy. As discussed above with the inclusion of imaging techniques, accurate measurements of the skin layer thicknesses could have been obtained. Also, the viscoelastic properties of skin were ignored for both models, so the inclusion of this characteristic may have resulted in a closer fit with experimental data

***Inverse analysis***

The inverse calculations were shown to produce a single set of material parameters which gave a strong agreement between experiment and model,

however the optimisation algorithms could only obtain local minima. Due to the complex mechanical properties of the skin tissue, the constitutive models used had numerous parameters and it is plausible that different material coefficients may have resulted in a similar mechanical response and $R^2_{ave}$ value. Additionally, implementing different initial coefficients into the inverse calculations may have altered the final material parameters obtained. Hence further work could include applying different starting parameters to determine whether similar end material coefficients were found. Additional work is required to fully understand the optimisation processes and develop new methods that could potentially provide a more global minimum, so that the material parameters extracted are those that truly do provide the best fit with experimental data.

***Assessment of microneedle insertion***

It was noted from the experimental measurements that murine skin was not an appropriate tissue to examine microneedle penetration. However it has been suggested previously that porcine skin may have similar properties to human skin, therefore a comparison between microneedle penetration into *ex vivo* human and porcine skin could be made.

As the microneedle penetration tests performed on human skin *in vivo* showed either very little penetration or inconclusive results as the microchannel staining was not possible , it may be beneficial to develop another approach to assess microneedle insertion *in vivo.* Published studies have used optical coherence tomography (Donnelly et al., 2010; Enfield et al., 2010; Coulman et al., 2011) to examine skin penetration by microneedle arrays *in vivo.* Such an approach could allow for individual microneedle penetration to be quantified, rather than estimates through microchannel staining. It is also important to highlight that only one volunteer and one donor was used for this preliminary study, hence further analysis on significantly more numbers may yield different results. Thus more volunteers and donors would need to be examined.

An approach which uses *ex vivo* tissue in a manner that includes the influence of the soft tissue below the skin *in vivo*, could allow for more appropriate method of analysis. Thus by applying a material to the underside of the *ex vivo* skin which has similar mechanical properties to human soft tissue *in vivo*, the skin sample would produce similar biomechanical properties to *in vivo* skin. Furthermore, the tension within the *ex vivo* skin, and the properties of the soft tissue could be validated against indentation measurements performed on human volunteers at greater loads to those applied to the skin in Chapter 2. This would incorporate the benefits of both *in vivo* and *ex vivo* analysis.

# REFERENCES

Agache P G, Monneur C, Leveque J L, and De Rigal J (1980) Mechanical properties and Young's Modulus of human skin in vivo. *Archives of Dermatological Research* 269: 221-232.

Al-Qallaf B, and Das D B (2008) Optimization of square microneedle arrays for increasing drug permeability in skin. *Chemical Engineering Science* 63: 2523-2535.

Al-Qallaf B, and Das D B (2009) Optimizing microneedle arrays to increase skin permeability for transdermal drug delivery. *Interdisciplinary Transport Phenomena: Fluid, Thermal, Biological, Materials, and Space Sciences* 1161: 83-94.

Alexander H, and Cook T H (1977) Accounting for natural tension in mechanical testing of human-skin. *Journal of Investigative Dermatology* 69: 310-314.

Andrews S N, Zarnitsyn V, Bondy B, and Prausnitz M R (2011) Optimization of microdermabrasion for controlled removal of stratum corneum. *International Journal of Pharmaceutics* 407: 95-104.

Aoyagi S, Izumi H, and Fukuda M (2008) Biodegradable polymer needle with various tip angles and consideration on insertion mechanism of mosquito's proboscis. *Sensors and Actuators A: Physical* 143: 20-28.

Aoyagi S, Izumi H, Isono Y, Fukuda M, and Ogawa H (2007) Laser fabrication of high aspect ratio thin holes on biodegradable polymer and its application to a microneedle. *Sensors and Actuators A: Physical* 139: 293-302.

Arora A, Prausnitz M R, and Mitragotri S (2008) Micro-scale devices for transdermal drug delivery. *International Journal of Pharmaceutics* 364: 227-236.

Arora J S (2004) *Introduction to Optimum Design*. Second ed. San Diego Elsevier Academic Press.

Arruda E M, and Boyce M C (1993) A 3-Dimensional constitutive model for the large stretch behaviour of rubber elastic-materials. *Journal of the Mechanics and Physics of Solids* 41: 389-412.

Ayittey P N, Walker J S, Rice J J, and de Tombe P P (2009) Glass microneedles for force measurements: a finite-element analysis model. *Pflugers Archiv-European Journal of Physiology* 457: 1415-1422.

Babiuk S, Baca-Estrada M, Babiuk L A, Ewen C, and Foldvari M (2000) Cutaneous vaccination: the skin as an immunologically active tissue and the challenge of antigen delivery. *Journal of Controlled Release* 66: 199-214.

Bader D L, and Bowker P (1983) Mechanical characteristics of skin and underlying tissues in vivo. *Biomaterials* 4: 305-308.

Badran M M, Kuntsche J, and Fahr A (2009) Skin penetration enhancement by a microneedle device (Dermaroller®) in vitro: Dependency on needle size and applied formulation. *European Journal of Pharmaceutical Sciences* 36: 511-523.

Bal S M, Caussin J, Pavel S, and Bouwstra J A (2008) In vivo assessment of safety of microneedle arrays in human skin. *European Journal of Pharmaceutical Sciences* 35: 193-202.

Bal S M, Ding Z, van Riet E, Jiskoot W, and Bouwstra J A (2010a) Advances in transcutaneous vaccine delivery: Do all ways lead to Rome? *Journal of Controlled Release* 148: 266-282.

Bal S M, Kruithof A C, Zwier R, Dietz E, Bouwstra J A, Lademann J, and Meinke M C (2010b) Influence of microneedle shape on the transport of a fluorescent dye into human skin in vivo. *Journal of Controlled Release* 147: 218-224.

Barry B W (2001) Novel mechanisms and devices to enable successful transdermal drug delivery. *European Journal of Pharmaceutical Sciences* 14: 101-114.

Birchall J C, Clemo R, Anstey A, and John D N (2011) Microneedles in clinical practice-An exploratory study into the opinions of healthcare professionals and the public. *Pharmaceutical Research* 28: 95-106.

Bischoff J E, Arruda E M, and Grosh K (2002) Finite element simulations of orthotropic hyperelasticity. *Finite Elements in Analysis and Design* 38: 983-998.

Bischoff J E, Arruda E M, and Grosh K (2004) A rheological network for the continuum anisotropic and viscoelastic behaviour of soft tissue. *Biomechanics and Modeling in Mechanobiology* 3: 56-65.

Brown I A (1973) Scanning electron-microscope study of effects of uniaxial tension on human skin. *British Journal of Dermatology* 89: 383-393.

Bystrova S, and Luttge R (2011) Micromolding for ceramic microneedle arrays. *Microelectronic Engineering* 88: 1681-1684.

Cacho F, Elbischger P J, Rodríguez J F, Doblaré M, and Holzapfel G A (2007) A constitutive model for fibrous tissues considering collagen fiber crimp. *International Journal of Non-Linear Mechanics* 42: 391-402.

Chen B, Wei J, and Iliescu C (2010) Sonophoretic enhanced microneedles array (SEMA)--Improving the efficiency of transdermal drug delivery. *Sensors and Actuators B: Chemical* 145: 54-60.

Chen H, Zhu H, Zheng J, Mou D, Wan J, Zhang J, Shi T et al. (2009) Iontophoresis-driven penetration of nanovesicles through microneedle-induced skin microchannels for enhancing transdermal delivery of insulin. *Journal of Controlled Release* 139: 63-72.

Chu L Y, and Prausnitz M R (2011) Separable arrowhead microneedles. *Journal of Controlled Release* 3: 242249.

Corr D T, Gallant-Behm C L, Shrive N G, and Hart D A (2009) Biomechanical behavior of scar tissue and uninjured skin in a porcine model. *Wound Repair and Regeneration* 17: 250-259.

Coulman S, Allender C, and Birchall J (2006) Microneedles and other physical methods for overcoming the stratum corneum barrier for cutaneous gene therapy. *Critical reviews in therapeutic drug carrier systems* 23: 1-54.

Coulman S A, Anstey A, Gateley C, Morrissey A, McLoughlin P, Allender C, and Birchall J C (2009) Microneedle mediated delivery of nanoparticles into human skin. *International Journal of Pharmaceutics* 366: 190-200.

Coulman S A, Birchall J C, Alex A, Pearton M, Hofer B, O'Mahony C, Drexler W et al. (2011) In Vivo, In situ imaging of microneedle insertion into the skin of human volunteers using optical coherence tomography. *Pharmaceutical Research* 28: 66-81.

Courtney T, Sacks M S, Stankus J, Guan J, and Wagner W R (2006) Design and analysis of tissue engineering scaffolds that mimic soft tissue mechanical anisotropy. *Biomaterials* 27: 3631-3638.

Crichton M L, Ansaldo A, Chen X, Prow T W, Fernando G J P, and Kendall M A F (2010) The effect of strain rate on the precision of penetration of short densely-packed microprojection array patches coated with vaccine. *Biomaterials* 31: 4562-4572.

Crichton M L, Donose B C, Chen X, Raphael A P, Huang H, and Kendall M A F (2011) The viscoelastic, hyperelastic and scale dependent behaviour of freshly excised individual skin layers. *Biomaterials* 32: 4670-4681.

Davis S P, Landis B J, Adams Z H, Allen M G, and Prausnitz M R (2004) Insertion of microneedles into skin: measurement and prediction of insertion force and needle fracture force. *Journal of Biomechanics* 37: 1155-1163.

Davis S P, Martanto W, Allen M G, and Prausnitz M R (2005) Hollow microneedles for insulin delivery to diabetic rats. *IEEE Transactions on Biomedical Engineering* 52: 909-915.

Del Prete Z, Antoniucci S, Hoffman A H, and Grigg P (2004) Viscoelastic properties of skin in Mov-13 and Tsk mice. *Journal of Biomechanics* 37: 1491-1497.

Delalleau A, Josse G, Lagarde J-M, Zahouani H, and Bergheau J-M (2006) Characterization of the mechanical properties of skin by inverse analysis combined with the indentation test. *Journal of Biomechanics* 39: 1603-1610.

Delalleau A, Josse G, Lagarde J M, Zahouani H, and Bergheau J M (2008a) Characterization of the mechanical properties of skin by inverse analysis combined with an extensometry test. *Wear* 264: 405-410.

Delalleau A, Josse G, Lagarde J M, Zahouani H, and Bergheau J M (2008b) A nonlinear elastic behavior to identify the mechanical parameters of human skin in vivo. *Skin Research and Technology* 14: 152-164.

Ding Z, Verbaan F J, Bivas-Benita M, Bungener L, Huckriede A, van den Berg D J, Kersten G et al. (2009) Microneedle arrays for the transcutaneous immunization of diphtheria and influenza in BALB/c mice. *Journal of Controlled Release* 136: 71-78.

Diridollou S, Patat F, Gens F, Vaillant L, Black D, Lagarde J M, Gall Y et al. (2000) In vivo model of mechanical properties of human skin under suction. *Skin Research and Technology* 6: 214-221.

Donnelly R F, Garland M J, Morrow D I J, Migalska K, Singh T R R, Majithiya R, and Woolfson A D (2010) Optical coherence tomography is a valuable tool in the study of the effects of microneedle geometry on skin penetration characteristics and in-skin dissolution. *Journal of Controlled Release* 147: 333-341.

Donnelly R F, Majithiya R, Singh T R R, Morrow D I J, Garland M J, Demir Y K, Migalska K et al. (2011) Design, optimization and characterisation of polymeric microneedle arrays prepared by a novel laser-based micromoulding technique. *Pharmaceutical Research (Dordrecht)* 28: 41-57.

Dunn M G, Silver F H, and Swann D A (1985) Mechanical analysis of hypertrophic scar tissue: structural basis for apparent increased rigidity. *Journal of Investigative Dermatology* 84: 9-13.

Enfield J, O'Connell M L, Lawlor K, Jonathan E, O'Mahony C, and Leahy M (2010) In-vivo dynamic characterization of microneedle skin penetration using optical coherence tomography. *Journal of Biomedical Optics* 15.

Eshel H, and Lanir Y (2001) Effects of strain level and proteoglycan depletion on preconditioning and viscoelastic responses of rat dorsal skin. *Annals of Biomedical Engineering* 29: 164-172.

Evans S L (2009) On the implementation of a wrinkling, hyperelastic membrane model for the skin and other materials. *Computer methods in biomechanics and biomedical engineering* 12: 319-332.

Evans S L, and Holt C A (2009) Measuring the mechanical properties of human skin in vivo using digital image correlation and finite element modeling. *Journal of Strain Analysis for Engineering Design* 44: 337-345.

Flynn C, and McCormack B A O (2008a) Finite element modelling of forearm skin wrinkling *Skin Research and Technology* 14: 261-269.

Flynn C, and McCormack B A O (2008b) A simplified model of scar contraction. *Journal of Biomechanics* 41: 1582-1589.

Flynn C, and McCormack B A O (2010) Simulating the wrinkling and aging of skin with a multi-layer finite element model. *Journal of Biomechanics* 43: 442-448.

Flynn C, Taberner A, and Nielsen P (2011) Measurement of the force-displacement response of in vivo human skin under a rich set of deformations. *Medical Engineering & Physics* In Press, Corrected Proof.

Fujimura T, Osanai O, Moriwaki S, Akazaki S, and Takema Y (2008) Development of a novel method to measure the elastic properties of skin including subcutaneous tissue: New age-related parameters and scope of application. *Skin Research and Technology* 14: 504-511.

Fung Y C (1993) *Biomechanics: Mechanical properties of living tissues* Second ed. Springer.

Fung Y C, Fronek K, and Patitucci P (1976) Pseudoelastic of arteries and the choice of its mathematical expression. *Journal of Physiology* 237: H620-H631.

Gambichler T, Matip R, Moussa G, Altmeyer P, and Hoffmann K (2006) In vivo data of epidermal thickness evaluated by optical coherence tomography: Effects of age, gender, skin type, and anatomic site. *Journal of Dermatological Science* 44: 145-152.

Gardeniers H J G E, Luttge R, Berenschot E J W, de Boer M J, Yeshurun S Y, Hefetez M, Oever R V et al. (2003) Silicon micromachined hollow microneedles for transdermal liquid transport. *Journal of Microelectromechanical Systems* 12: 855-863.

Geerligs M, Peters G W M, Ackermans P A J, Oomens C W J, and Baaijens F P T (2008) Linear viscoelastic behavior of subcutaneous adipose tissue. *Biorheology* 45: 677-688.

Geerligs M, Peters G W M, Ackermans P A J, Oomens C W J, and Baaijens F P T (2010) Does subcutaneous adipose tissue behave as an (anti-)thixotropic material? *Journal of Biomechanics* 43: 1153-1159.

Gerhard H, and Vogel M D (1981) Directional variations of mechanical parameters in rat skin depending on maturation and age. *The Journal of Investigative Dermatology* 76: 493-497.

Gerstel M S, and Place V A (1976) Drug delivery device United states.

Ghaemi H, Behdinan K, and Spence A D (2009) In vitro technique in estimation of passive mechanical properties of bovine heart: Part II. Constitutive relation and finite element analysis. *Medical Engineering & Physics* 31: 83-91.

Gill H S, and Prausnitz M R (2007) Coated microneedles for transdermal delivery. *Journal of Controlled Release* 117: 227-237.

Gill H S, and Prausnitz M R (2008) Pocketed microneedles for drug delivery to the skin. *Journal of Physics and Chemistry of Solids* 69: 1537-1541.

Gomaa Y A, Morrow D I J, Garland M J, Donnelly R F, El-Khordagui L K, and Meidan V M (2010) Effects of microneedle length, density, insertion time and multiple applications on human skin barrier function: Assessments by transepidermal water loss. *Toxicology in Vitro* 24: 1971-1978.

Gupta J, Gill H S, Andrews S N, and Prausnitz M R (2011) Kinetics of skin resealing after insertion of microneedles in human subjects. *Journal of Controlled Release* In Press, Corrected Proof.

Hafeli U O, Mokhtari A, and Liepmann D (2009) In vivo evaluation of microneedle-based miniature syringe for intradermal drug delivery. *Biomed Microdevices* 11: 943-950.

Han M, Kim D K, Kang S H, Yoon H-R, Kim B-Y, Lee S S, Kim K D et al. (2009) Improvement in antigen-delivery using fabrication of a grooves-embedded microneedle array. *Sensors and Actuators B: Chemical* 137: 274-280.

Haq M I, Smith E, John D N, Kalavala M, Edwards C, Anstey A, Morrissey A et al. (2009) Clinical administration of microneedles: skin puncture, pain and sensation. *Biomedical Microdevices* 11: 35-47.

Hendriks F M, Brokken D, Oomens C W J, and Baaijens F P T (2004) Influence of hydration and experimental length scale on the mechanical response of human skin in vivo using optical coherence tomography. *Skin Research and Technology* 10: 231-241.

Hendriks F M, Brokken D, Oomens C W J, Bader D L, and Baaijens F P T (2006) The relative contributions of different skin layers to the mechanical behavior of human skin in vivo using suction experiments. *Medical Engineering & Physics* 28: 259-266.

Hendriks F M, Brokken D, van Eemeren J T W M, Oomens C W J, Baaijens F P T, and Horsten J B A M (2003) A numerical-experimental method to characterize the non-linear mechanical behaviour of human skin. *Skin Research and Technology* 9: 274-283.

Henry S, McAllister D V, Allen M G, and Prausnitz M R (1998) Microfabricated microneedles: A novel approach to transdermal drug delivery. *Journal of Pharmaceutical Sciences* 87: 922-925.

Holzapfel G A (2006) *Nonlinear Solid Mechanics: A Continuum Approach for Engineering* John Wiley & Sons, LTD.

Hunsaker B D, and Perino L J (2001) Efficacy of intradermal vaccination. *Veterinary Immunology and Immunopathology* 79: 1-13.

Ito Y, Murano H, Hamasaki N, Fukushima K, and Takada K (2011) Incidence of low bioavailability of leuprolide acetate after percutaneous administration to rats by dissolving microneedles. *International Journal of Pharmaceutics* 407: 126-131.

Izumi H, Suzuki M, Aoyagi S, and Kanzaki T (2011) Realistic imitation of mosquito's proboscis: Electrochemically etched sharp and jagged needles and their cooperative inserting motion. *Sensors and Actuators a-Physical* 165: 115-123.

Jacquet E, Josse G, Khatyr F, and Garcin C (2008) A new experimental method for measuring skin's natural tension. *Skin Research and Technology* 14: 1-7.

Ji J, Tay F E H, Miao J, and Sun J [eds.] (2006) *Characterization of silicon isotropic etch by inductively coupled plamsa etcher for microneedle array fabrication* International MEMS Conference Journal of Physics: Conference Series.

Kalluri H, and Banga A K (2011) Formation and closure of microchannels in skin following microporation. *Pharmaceutical Research* 28: 82-94.

Kang G, and Wu X (2011) Ratchetting of porcine skin under uniaxial cyclic loading. *Journal of the Mechanical Behavior of Biomedical Materials* 4: 498-506.

Kaushik S, Hord A H, Denson D D, McAllister D V, Smitra S, Allen M G, and Prausnitz M R (2001) Lack of pain associated with microfabricated microneedles *The International Anesthesia Research Society* 92: 502-504.

Kendall M A F, Chong Y-F, and Cock A (2007) The mechanical properties of the skin epidermis in relation to targeted gene and drug delivery. *Biomaterials* 28: 4968-4977.

Khanna P Skin penetration and fracture strength testing of silicon dioxide microneedles. *Sensors and Actuators A: Physical* In Press, Accepted Manuscript.

Khanna P, Luongo K, Strom J A, and Bhansali S (2010) Sharpening of hollow silicon microneedles to reduce skin penetration force. *Journal of Micromechanics and Microengineering* 20.

Kim Y-C, Quan F-S, Compans R W, Kang S-M, and Prausnitz M R (2011) Stability kinetics of influenza vaccine coated onto microneedles during drying and storage. *Pharmaceutical Research (Dordrecht)* 28: 135-144.

Koehler M J, Vogal T, Elsner P, Konig K, Buckle R, and Kaatz M (2010) In vivo measurements of the human epidermal thickness in different localization by multiphoton laser tomography. *Skin Research and Technology* 16: 259-264.

Kong X Q, and Wu C W (2009) Measurement and Prediction of Insertion Force for the Mosquito Fascicle Penetrating into Human Skin. *Journal of Bionic Engineering* 6: 143-152.

Kong X Q, Zhou P, and Wu C W (2011) Numerical simulation of microneedles insertion into skin. *Computer methods in biomechanics and biomedical engineering*.

Koutroupi K S, and Barbenel J C (1990) Mechanical and failure behaviour of the stratum corneum. *Journal of Biomechanics* 23: 281-287.

Kroon M, and Holzapfel G A (2008) Estimation of the distributions of anisotropic, elastic properties and wall stresses of saccular cerebral aneurysms by inverse analysis. *Proceedings of the Royal Society A: Mathematical, Physical and Engineering Sciences* 464: 807-825.

Kvistedal Y A, and Nielsen P M F (2009) Estimating material parameters of human skin in vivo. *Biomechanics and Modeling in Mechanobiology* 8: 1-8.

Kwiatkowska M, Franklin S E, Hendriks C P, and Kwiatkowski K (2009) Friction and deformation behaviour of human skin. *Wear* 267: 1264-1273.

Lanir Y (1979) A structural theory for the homogeneous biaxial stress-strain relationships in flat collagenous tissues. *Journal of Biomechanics* 12: 423-436.

Lanir Y, and Fung Y C (1974) Two-dimensional mechanical properties of rabbit skin - II. experimental results. *Journal of Biomechanics* 7: 171-182.

Lapeer R J, Gasson P D, and Karri V (2010) Simulating plastic surgery: From human skin tensile tests, through hyperelastic finite element models to real-time haptics. *Progress in Biophysics and Molecular Biology* 103: 208-216.

Lee J W, Park J-H, and Prausnitz M R (2008) Dissolving microneedles for transdermal drug delivery. *Biomaterials* 29: 2113-2124.

Lee K, Lee C Y, and Jung H (2011) Dissolving microneedles for transdermal drug administration prepared by stepwise controlled drawing of maltose. *Biomaterials* 32: 3134-3140.

Li G, Badkar A, Nema S, Kolli C S, and Banga A K (2009) In vitro transdermal delivery of therapeutic antibodies using maltose microneedles. *Int J Pharm* 368: 109-115.

Liang X, and Boppart S A (2010) Biomechanical properties of in vivo human skin from dynamic optical coherence elastography. *IEEE Transactions on Biomedical Engineering* 57: 953-959.

Lim K H, Chew C M, Chen P C Y, Jeyapalina S, Ho H N, Rappel J K, and Lim B H (2008) New extensometer to measure in vivo uniaxial mechanical properties of human skin. *Journal of Biomechanics* 41: 931-936.

Lippmann J M, Geiger E J, and Pisano A P (2007) Polymer investment molding: Method for fabricating hollow, microscale parts. *Sensors and Actuators A: Physical* 134: 2-10.

Lippmann J M, and Pisano A P (2006) In-plane, hollow microneedles via polymer investment molding. In: *Micro electro mechanical systems, 2006. MEMS 2006 Istanbul 19th IEEE international conference on*.

Liu K, VanLandingham M R, and Ovaert T C (2009) Mechanical characterization of soft viscoelastic gels via indentation and optimization-based inverse finite element analysis. *Journal of the Mechanical Behavior of Biomedical Materials* 2: 355-363.

Lui Z, and Yeung K (2008) The preconditioning and stress relaxation of skin tissue. *Journal of Biomedical and Pharmaceutical Engineering* 2: 22-28.

Mahmud J, Holt C A, and Evans S L (2010) An innovative application of a small-scale motion analysis technique to quantify human skin deformation in vivo. *Journal of Biomechanics* 43: 1002-1006.

Maibach H I, Agache P G, and Humbert P (2004) *Measuring the Skin*. 1st ed. Springer.

Manschot J F M, and Brakkee A J M (1986) The measurement and modelling of the mechanical properties of human skin in vivo--I. The measurement. *Journal of Biomechanics* 19: 511-515.

Martanto W, Davis S P, Holiday N R, Wang J, Gill H S, and Prausnitz M R (2004) Transerdermal delivery of insulin using microneedles in vivo. *Pharmaceutical Research* 21: 947-952.

Matsumura H, Yoshizawa N, Watanabe K, and Vedder N B (2001) Preconditioning of the distal portion of a rat random-pattern skin flap. *British Journal of Plastic Surgery* 54: 58-61.

Matteucci M, Fanetti M, Gramatica F, Gavioli L, Tormen M, Grenci G, De Angelis F et al. (2009) Poly vinyl alcohol re-usable masters for microneedle replication *Microelectronics Engineering* 86: 752-756

McAllister D V, Wong P M, Davis S P, Park J H, Canatella P J, Allen M G, and Prausnitz M R [eds.] (2003) *Microfabricated needles for transerdmal drug delivery of macromolecules and nanoparticles: Fabrication methods and transport studies*. Proceedings of the National Academy of Sciences of the United States of AmericaNovember 25

McGrath M G, Vrdoljak A, O'Mahony C, Oliveira J C, Moore A C, and Crean A M (2011) Determination of parameters for successful spray coating of silicon microneedle arrays. *International Journal of Pharmaceutics* 415: 140-149.

Mikszta J A, Alarcon J B, Brittingham J M, Sutter D E, Pettis R J, and Harvey N G (2002) Improved genetic immunization via micromechanical disruption of skin-barrier function and targeted epidermal delivery. *Nature Medicine* 8: 415-419.

Miller-Young J E, Duncan N A, and Baroud G (2002) Material properties of the human calcaneal fat pad in compression: experiment and theory. *Journal of Biomechanics* 35: 1523-1531.

Miyano T, Tobinaga Y, Kanno T, Matsuzaki Y, Takeda H, Wakui M, and Hanada K (2005) Sugar micro needles a transdermic drug delivery system *Biomedical Microdevices* 7: 185-188.

Mofid Y, Josse G, Gahagnon S, Delalleau A, and Ossant F (2010) Mechanical skin thinning-to-thickening transition observed in vivo through 2D high frequency elastography. *Journal of Biomechanics* 43: 2954-2962.

Moon D K, Woo S L-Y, Takakura Y, Gabriel M T and Abramowitch S D (2006) The Effects of refreezing on the viscoelastic and tensile properties of ligaments. *Journal of Biomechanicals* 39: 1153-1157

Moore T L, Lunt M, McManus B, Anderson M E, and Herrick A L (2003) Seventeen-point dermal ultrasound scoring system - a reilable measure of skin thickness in patients with systemic sclerosis *Rheumatology* 42: 1559-1563.

Morrissey A, Wilke N, Coulman S, Pearton M, Anstey A, Gateley C, Allender C et al. (2005) Determination of mechanical properties of silicone and polymer microneedles In: *The 3rd European Medical and Biological Engineering Conference* Prague, Czech Republic November 20-25, 2005.

Mukerjee E V, Collins S D, Isseroff R R, and Smith R L (2004) Microneedle array for transdermal biological fluid extraction and in situ analysis. *Sensors and Actuators A: Physical* 114: 267-275.

Muñoz M J, Bea J A, Rodríguez J F, Ochoa I, Grasa J, Pérez del Palomar A, Zaragoza P et al. (2008) An experimental study of the mouse skin behaviour: Damage and inelastic aspects. *Journal of Biomechanics* 41: 93-99.

Namani R, and Simha N (2009) Inverse finite element analysis of indentation tests to determine hyperelastic parameters of soft-tissue layers *The Journal of Strain Analysis for Engineering Design* 44: 347-362.

Ng K W, Pearton M, Coulman S, Anstey A, Gateley C, Morrissey A, Allender C et al. (2009) Development of an ex vivo human skin model for intradermal vaccination: Tissue viability and Langerhans cell behaviour. *Vaccine* 27: 5948-5955.

Nickoloff B J, and Naidu Y (1994) Perturbation of epidermal barrier function correlates with initiation of cytokine cascade in human skin. *Journal of the American Academy of Dermatology* 30: 535-546.

Ogden R W (1972) Large deformation isotropic elasticity - on the correlation of theory and experiment for incompressible rubberlike solids. *Proceedings of the Royal Society A: Mathematical, Physical and Engineering Sciences* 326: 565-584.

Oxlund H, Manschot J, and Viidik A (1988) The role of elastin in the mechanical properties of skin. *Journal of Biomechanics* 21: 213-218.

Özyazgan I, Liman N, Dursun N, and Günes I (2002) The effects of ovariectomy on the mechanical properties of skin in rats. *Maturitas* 43: 65-74.

Pailler-Mattei C, Bec S, and Zahouani H (2008) In vivo measurements of the elastic mechanical properties of human skin by indentation tests. *Medical Engineering & Physics* 30: 599-606.

Pailler-Mattei C, Pavan S, Vargiolu R, Pirot F, Falson F, and Zahouani H (2007) Contribution of stratum corneum in determining bio-tribological properties of the human skin. *Wear* 263: 1038-1043.

Pailler-Mattéi C, and Zahouani H (2006) Analysis of adhesive behaviour of human skin in vivo by an indentation test. *Tribology International* 39: 12-21.

Papir Y S, Hsu K-H, and Wildnauer R H (1975) The mechanical properties of stratum corneum: I. The effect of water and ambient temperature on the tensile properties of newborn rat stratum corneum. *Biochimica et Biophysica Acta (BBA) - General Subjects* 399: 170-180.

Park J-H, Allen M, and Prausnitz M (2006) Polymer Microneedles for Controlled-Release Drug Delivery. *Pharmaceutical Research* 23: 1008-1019.

Park J-H, Allen M G, and Prausnitz M R (2005) Biodegradable polymer microneedles: Fabrication, mechanics and transdermal drug delivery. *Journal of Controlled Release* 104: 51-66.

Park J-H, Choi S-O, Kamath R, Yoon Y-K, Allen M G, and Prausnitz M R (2007) Polymer particle-based micromolding to fabricate novel microstructures *Biomedical Microdevices* 9: 223-234.

Park J H, Choi S O, Seo S, Bin Choy Y, and Prausnitz M R (2010) A microneedle roller for transdermal drug delivery. *European Journal of Pharmaceutics and Biopharmaceutics* 76: 282-289.

Parkinson J, Brass A, Canova G, and Brechet Y (1997) The mechanical properties of simulated collagen fibrils. *Journal of Biomechanics* 30: 549-554.

Pereira B P, Lucas P W, and Swee-Hin T (1997) Ranking the fracture toughness of thin mammalian soft tissues using the scissors cutting test. *Journal of Biomechanics* 30: 91-94.

Pereira J M, Mansour J M, and Davis B R (1991) Dynamic measurement of the viscoelastic properties of skin. *Journal of Biomechanics* 24: 157-162.

Quan F-S, Kim Y-C, Compans R W, Prausnitz M R, and Kang S-M (2010a) Dose sparing enabled by skin immunization with influenza virus-like particle vaccine using microneedles. *Journal of Controlled Release* 147: 326-332.

Quan F S, Kim Y C, Compans R W, Prausnitz M R, and Kang S M (2010b) Dose sparing enabled by skin immunization with influenza virus-like particle vaccine using microneedles. *Journal of Controlled Release* 147: 326-332.

Ridge M D, and Wright V (1965) Mechanical properties of skin: a bioengineering study of skin structure. *Journal of Applied Physiology* 21: 1602-1606.

Roxhed N, Gasser T C, Griss P, Holzapfel G A, and Stemme G (2007) Penetration-enhanced ultrasharp microneedles and prediction of skin interaction for efficient transdermal drug delivery *Journal of Microelectromechanical Systems* 16: 1429-1440.

Sanders J E, and Goldstein B S (2001) Collagen fibril diameters increase and fibril densities decrease in skin subjected to repetitive compressive and shear stresses. *Journal of Biomechanics* 34: 1581-1587.

Sanders R (1973) Torsional Elasticity of Human Skin in-Vivo. *Pflugers Archiv-European Journal of Physiology* 342: 255-260.

Scanlon V C, and Sanders T (1997) *Understanding Human Structure and Function*. First ed. F. A. Davis Company.

Schmook F P, Meingassner J G, and Billich A (2001) Comparison of human skin or epidermis models with human and animal skin in in-vitro percutaneous absorption. *International Journal of Pharmaceutics* 215: 51-56.

Shergold O A, Fleck N A, and King T S (2006a) The penetration of a soft solid by a liquid jet, with application to the administration of a needle-free injection. *Journal of Biomechanics* 39: 2593-2602.

Shergold O A, Fleck N A, and Radford D (2006b) The uniaxial stress versus strain response of pig skin and silicone rubber at low and high strain rates. *International Journal of Impact Engineering* 32: 1384-1402.

Shirkhansadeh M (2005) Microneedles coated with porous calcium phosphate ceramics: Effective vehicles for transdermal delivery of solid trehalose. *Journal of Materials Science: Materials in Medicine* 16: 37-45.

Silver F H, Siperko L M, and Seehra G P (2003) Review Mechanobiology of force transduction in dermal tissue. *Skin Research and Technology* 9: 3-23.

Song J-M, Kim Y-C, Barlow P G, Hossain M J, Park K-M, Donis R O, Prausnitz M R et al. (2010) Improved protection against avian influenza H5N1 virus by a single vaccination with virus-like particles in skin using microneedles. *Antiviral Research* 88: 244-247.

Stark H L (1977) Directional variations in the extensibility of human skin. *British Journal of Plastic Surgery* 30: 105-114.

Stoeber B, and Liepmann D (2005) Arrays of hollow out-of-plane microneedles for drug delivery. *Journal of Microelectromechanical Systems* 14: 472-479.

Tatlidede S, McCormack M C, Eberlin K R, Nguyen J T, Randolph M A, and Austen Jr W G (2009) A novel murine island skin flap for ischemic preconditioning. *Journal of Surgical Research* 154: 112-117.

Taylor Z A, Comas O, Cheng M, Passenger J, Hawkes D J, Atkinson D, and Ourselin S (2009) On modelling of anisotropic viscoelasticity for soft tissue simulation: Numerical solution and GPU execution. *Medical Image Analysis* 13: 234-244.

Thalmann N M, Kalra P, Leveque J L, Bazin R, Batisse D, and Querleux B (2002) A computational skin model: fold and wrinkle formation. *IEEE Transactions on Biomedical Engineering* 6: 317-323.

Tran H V, Charleux F, Rachik M, Ehrlacher A, and Tho M C H B (2007) *In vivo* characterisation of the mechanical properties of human skin derived from MRI and indentation techniques. *Computer methods in biomechanics and biomedical engineering* 10: 401-407.

Van Damme P, Oosterhuis-Kafeja F, Van der Wielen M, Almagor Y, Sharon O, and Levin Y (2009) Safety and efficacy of a novel microneedle device for dose sparing intradermal influenza vaccination in healthy adults. *Vaccine* 27: 454-459.

Ventre M, Mollica F, and Netti P A (2009) The effect of composition and microstructure on the viscoelastic properties of dermis. *Journal of Biomechanics* 42: 430-435.

Verbaan F J, Bal S M, van den Berg D J, Dijksman J A, van Hecke M, Verpoorten H, van den Berg A et al. (2008) Improved piercing of microneedle arrays in dermatomed human skin by an impact insertion method. *Journal of Controlled Release* 128: 80-88.

Veronda D R, and Westmann R A (1970) Mechanical characterization of skin--Finite deformations. *Journal of Biomechanics* 3: 111-122, IN119, 123-124.

Wan Abas W A B, and Barbenel J C (1982) Uniaxial tension test of human skin in vivo. *Journal of Biomedical Engineering* 4: 65-71.

Wei-Ze L, Mei-Rong H, Jian-Ping Z, Yong-Qiang Z, Bao-Hua H, Ting L, and Yong Z (2010) Super-short solid silicon microneedles for transdermal drug delivery applications. *International Journal of Pharmaceutics* 389: 122-129.

Weiss J A, Maker B N, and Govindjee S (1996) Finite element implementation of incompressible, transversely isotropic hyperelasticity. *Computer Methods in Applied Mechanical Engineering* 135: 107-135.

Wenger M P E, Bozec L, Horton M A, and Mesquida P (2007) Mechanical Properties of Collagen Fibrils. *Biophysical Journal* 93: 1255-1263.

Wildneuer R H, Bothwell J W, and Douglass A B (1971) Stratum Corneum Biomechanical Properties *The Journal of Investigative Dermatology* 56: 72-78.

Wilke N, Mulcahy A, Ye S R, and Morrissey A (2005) Process optimization and characterization of silicon microneedles fabricated by wet etch technology. *Microelectronics Journal* 36: 650-656.

Wu J Z, Cutlip R G, Welcome D, and Dong R G (2006a) Estimation of the viscous properties of skin and subcutaneous tissue in uniaxial stress relaxation tests. *Bio-Medical Materials and Engineering* 16: 53-66.

Wu K S, van Osdol W W, and Dauskardt R H (2006b) Mechanical properties of human stratum corneum: Effects of temperature, hydration, and chemical treatment. *Biomaterials* 27: 785-795.

Xie Y, Xu B, and Gao Y (2005) Controlled transdermal delivery of model drug compounds by MEMS microneedle array. *Nanomedicine: Nanotechnology, Biology and Medicine* 1: 184-190.

Yan G, Warner K S, Zhang J, Sharma S, and Gale B K (2010) Evaluation needle length and density of microneedle arrays in the pretreatment of skin for transdermal drug delivery. *International Journal of Pharmaceutics* In Press, Uncorrected Proof.

Yang M, and Zahn J D (2004) Microneedle insertion force reduction using vibratory actuation. *Biomedical Microdevices* 6: 177-182.

Yeoh O H (1993) Some forms of the strain energy function for rubber. *Rubber Chemistry and Technology* 66: 754-771.

Yuan Y, and Verma R (2006) Measuring microelastic properties of stratum corneum. *Colloids and Surfaces B: Biointerfaces* 48: 6-12.

Zahouani H, Pailler-Mattéi C, Sohm B, Vargiolu R, Cenizo V, and Derbret R (2008) Characterization of Mechanical Properties of a Dermal Equivalent Compared with Human in-vivo by Indentation and Static Friction Tests. *Skin Research and Technology* 14: 1-9.

Zahouani H, Pailler-Mattéi C, Sohm B, Vargiolu R, Cenizo V, and Derbret R (2009) Characterization of Mechanical Properties of a Dermal Equivalent Compared with Human in-vivo by Indentation and Static Friction Tests. *Skin Research and Technology* 14: 68-76.

Zhang W, Gao J, Zhu Q G, Zhang M, Ding X Y, Wang X Y, Hou X M et al. (2010) Penetration and distribution of PLGA nanoparticles in the human skin treated with microneedles. *International Journal of Pharmaceutics* 402: 205-212.

Zhou C-P, Liu Y-L, Wang H-L, Zhang P-X, and Zhang J-L (2010) Transdermal delivery of insulin using microneedle rollers in vivo. *International Journal of Pharmaceutics* 392: 127-133.

Zhou H, Li G, Sun X, Zhu Z, Xu B, Jin Q, Zhao J et al. (2009) A new process for fabricating tip-shaped polymer microstructure array with patterned metallic coatings. *Sensors and Actuators A: Physical* 150: 296-301.

Zhu M W, Li H W, Chen X L, Tang Y F, Lu M H, and Chen Y F (2009) Silica needle template fabrication of metal hollow microneedle arrays. *Journal of Micromechanics and Microengineering* 19: 1-6.

# APPENDIX A

# PUBLICATIONS & CONFERENCES

## Publications

**2011** Groves, R.B, Coulman, S.A., Birchall, J.C., Evans, S.L. (2011) Quantifying the mechanical properties of skin to optimise future microneedle device design. *Computer Methods in Biomechanics and Biomedical Engineering: 14(12) 1-11*

## Conferences

**2009** **The Third International Conference on Mechanics of Biomaterials and Tissues,** Clearwater Beach, Florida, USA
Groves, R.B, Evans, S.L., Coulman, S.A., Birchall, J.C. *"Mechanics of skin penetration by microneedles"* (oral presentation)

**2010** **Computer Methods in Biomaterials and Biomedical Engineering,** Valencia, Spain
Groves, R.B, Evans, S.L., Coulman, S.A., Birchall, J.C. *"Mechanics of skin penetration by microneedles"* (oral presentation)

**The 17th Congress of the European Society of Biomechanics**, Edinburgh, UK
Groves, R.B, Evans, S.L., Coulman, S.A., Birchall, J.C. *"Quantifying the mechanical properties of human skin to optimise future microneedle device design"* (oral presentation)
**First International Conference on Microneedles, Atlanta, USA**
Groves, R.B., Evans, S.L., Coulman, S.A., Birchall, J.C. *"Optimising microneedle device design through finite element modelling"* (poster presentation)

**2011** **The Fourth International Conference on Mechanics of Biomaterials and Tissues,** Hawaii, USA
Groves, R.B, Coulman, S.A., Birchall, J.C., Evans, S.L. *"Using inverse finite element modelling to identify the anisotropic mechanical properties of human and mouse skin in tension"* (poster presentation

# APPENDIX B

# INVERSE ANALYSIS PROGRAM FOR MULTILAYERED FINITE ELEMENT MODEL OF HUMAN SKIN

```
function rmserr=runfebiosphcyl(c0,m0,c01,m01,c02,m02);

%FOR SKIN INDENTATION ONLY

%CO = mu for epidermis, M0 = alpha for epidermis, C1 = mu for dermis,
M1 =
%alpha for dermis, C2 = mu for epidermis, M2 = alpha for dermis

%SPHERE (DERMIS)

%Importing .feb file.
FEBio_file=importdata('skin_1_16thball.feb');

%split file into seperate files and add the material property
sections
FEBio_part1=FEBio_file(1:32,:);
FEBio_part2=FEBio_file(36:37,:);
FEBio_part3=FEBio_file(41:42,:);
FEBio_part4=FEBio_file(46:32219,:);


%EPIDERMIS
%Shear Stiffness
c1='<c1>';
c2='</c1>';
c0=num2str(c0);
C0=strcat(c1,c0,c2);
%Non-linearity coefficient
m1='<m1>';
m2='</m1>';
m0=num2str(m0);
M0=strcat(m1,m0,m2);
%bulk modulus
k1='<k>';
k2='</k>';
k01=1000;
k0=num2str(k01);
K0=strcat(k1,k0,k2);

%DERMIS
%Shear Stiffness
c1='<c1>';
c2='</c1>';
```

```
c01=num2str(c01);
C1=strcat(c1,c01,c2);
%Non-linearity coefficient
m1='<m1>';
m2='</m1>';
m01=num2str(m01);
M1=strcat(m1,m01,m2);
%bulk modulus
k1='<k>';
k2='</k>';
k011=12;
k01=num2str(k011);
K1=strcat(k1,k01,k2);

%HYPODERMIS
%Shear Stiffness
c1='<c1>';
c2='</c1>';
c02=num2str(c02);
C2=strcat(c1,c02,c2);
%Non-linearity coefficient
m1='<m1>';
m2='</m1>';
m02=num2str(m02);
M2=strcat(m1,m02,m2);
%bulk modulus
k1='<k>';
k2='</k>';
k012=5;
k02=num2str(k012);
K2=strcat(k1,k02,k2);

%produce output files
O='<Output>';
O1='<logfile file="data">';
O2='<rigid_body_data data="Fz" name = " " file="Sphere_Fz.txt"
delim=" = " >1</rigid_body_data>';
O3='<rigid_body_data data="z" name = " " file="Sphere_z.txt" delim="
= " >1</rigid_body_data>';
O4='</logfile>';
O5='</Output>';
O6='</febio_spec>';


%Attach file back together
FEBIO=[FEBio_part1;C0;M0;K0;FEBio_part2;C1;M1;K1;FEBio_part3;C2;M2;K2
;FEBio_part4;O;O1;O2;O3;O4;O5;O6];

[nrows,ncols]= size(FEBIO);

filename = 'C:\febiofileball.feb';
fid = fopen(filename, 'w');

for row=1:nrows
    fprintf(fid, '%s\n', FEBIO{row,:});
end

fclose(fid);
```

```
%To run FEBio in MATLAB
dos('febio -i C:\febiofileball.feb > febiooutputball.txt');

%output from FEBio
Fz = importdata('Sphere_Fz.txt');
z = importdata('Sphere_z.txt');
fZ = Fz.data;
Z = z.data;
FE_LoadBall = fZ(4:4:end)*-4;
FE_DisplacementBall = Z(4:4:end)*-1;
%change displacement depending on COG position

% experimental results
%Filter first
ex_LoadBall = importdata('Load1_16th.txt');
ex_DisplacementBall = importdata('dis1_16th.txt');
[B,A]=butter(2,0.1,'low');
EX_LoadBall = filtfilt(B,A,ex_LoadBall);
EX_DisplacementBall = filtfilt(B,A,ex_DisplacementBall);

%interpolate
intEX_LoadBall=interp1(EX_DisplacementBall,EX_LoadBall,FE_Displacemen
tBall,'pchip');

%Calculating R squared value

%R squared value
diff=(intEX_LoadBall-FE_LoadBall).^2;
sqIntEX_LoadBall=intEX_LoadBall.^2;
sumIntEX_LoadBall=(sum(intEX_LoadBall)).^2;

%Calculation from R squared. Namani et al
rsquaredball=((sum(diff)/((sum(sqIntEX_LoadBall))-
(sumIntEX_LoadBall/numel(FE_LoadBall)))));
Rsquaredball=abs(rsquaredball)


%CYLINDER (HYPODERMIS)

%Importing .feb file.
FEBio_file=importdata('skin_cylinder.feb');

%split file into seperate files and add the material property
sections

FEBio_part1=FEBio_file(1:32,:);
FEBio_part2=FEBio_file(36:37,:);
FEBio_part3=FEBio_file(41:42,:);
FEBio_part4=FEBio_file(46:10231,:);

%EPIDERMIS
%Shear Stiffness
c1='<c1>';
c2='</c1>';
c0=num2str(c0);
C0=strcat(c1,c0,c2);
%Non-linearity coefficient
```

```
m1='<m1>';
m2='</m1>';
m0=num2str(m0);
M0=strcat(m1,m0,m2);
%bulk modulus
k1='<k>';
k2='</k>';
k01=1000;
k0=num2str(k01);
K0=strcat(k1,k0,k2);

%DERMIS
%Shear Stiffness
c1='<c1>';
c2='</c1>';
c01=num2str(c01);
C1=strcat(c1,c01,c2);
%Non-linearity coefficient
m1='<m1>';
m2='</m1>';
m01=num2str(m01);
M1=strcat(m1,m01,m2);
%bulk modulus
k1='<k>';
k2='</k>';
k011=12;
k01=num2str(k011);
K1=strcat(k1,k01,k2);

%HYPODERMIS
%Shear Stiffness
c1='<c1>';
c2='</c1>';
c02=num2str(c02);
C2=strcat(c1,c02,c2);
%Non-linearity coefficient
m1='<m1>';
m2='</m1>';
m02=num2str(m02);
M2=strcat(m1,m02,m2);
%bulk modulus
k1='<k>';
k2='</k>';
k012=5;
k02=num2str(k012);
K2=strcat(k1,k02,k2);

%produce output files
O='<Output>';
O1='<logfile file="data">';
O2='<rigid_body_data data="Fz" name = " " file="Cylinder_Fz.txt"
delim=" = " >1</rigid_body_data>';
O3='<rigid_body_data data="z" name = " " file="Cylinder_z.txt"
delim=" = " >1</rigid_body_data>';
O4='</logfile>';
O5='</Output>';
O6='</febio_spec>';


%Attach file back together
```

```
FEBIO=[FEBio_part1;C0;M0;K0;FEBio_part2;C1;M1;K1;FEBio_part3;C2;M2;K2
;FEBio_part4;O;O1;O2;O3;O4;O5;O6];

[nrows,ncols]= size(FEBIO);

filename = 'C:\febiofilecylinder.feb';
fid = fopen(filename, 'w');

for row=1:nrows
    fprintf(fid, '%s\n', FEBIO{row,:});
end

fclose(fid);

%To run FEBio in MATLAB
dos('febio -i C:\febiofilecylinder.feb > febiooutputcylinder.txt');


%output from FEBio
Fz = importdata('Cylinder_Fz.txt');
z = importdata('Cylinder_z.txt');
fZ = Fz.data;
Z = z.data;
FE_LoadCyli = fZ(4:4:end)*-4;
FE_DisplacementCyli = (Z(4:4:end)-0.96)*-1;
%change displacement depending on COG position

% experimental results
ex_LoadCyli = importdata('Load05mm.txt');
ex_DisplacementCyli = importdata('Dis05mm.txt');
[B,A]=butter(2,0.1,'low');
EX_LoadCyli = filtfilt(B,A,ex_LoadCyli);
EX_DisplacementCyli = filtfilt(B,A,ex_DisplacementCyli);

%interpolate
intEX_LoadCyli=interp1(EX_DisplacementCyli,EX_LoadCyli,FE_Displacemen
tCyli,'pchip');

%Calculating R squared value

%R squared value
diff=(intEX_LoadCyli-FE_LoadCyli).^2;
sqIntEX_LoadCyli=intEX_LoadCyli.^2;
sumIntEX_LoadCyli=(sum(intEX_LoadCyli)).^2;

%Calculation from R squared. Namani et al
rsquaredcyli=((sum(diff)/((sum(sqIntEX_LoadCyli))-
(sumIntEX_LoadCyli/numel(FE_LoadCyli)))));
Rsquaredcyli=abs(rsquaredcyli)

%Comparing FEM to Experiment
plot(FE_DisplacementBall, FE_LoadBall, EX_DisplacementBall,
EX_LoadBall, FE_DisplacementCyli, FE_LoadCyli, EX_DisplacementCyli,
EX_LoadCyli);
ylabel('Force (N)');
xlabel('Displacement (mm)');
legend( 'FEM-Spherical Indenter', 'Experiment-Spherical Indenter',
'FEM-Cylindrical Indenter', 'Experimental- Cylindrical Indenter');
```

```
axis([0 0.4 0 0.018]);
rmserr=( Rsquaredball + Rsquaredcyli)/2
```

# APPENDIX C

# INVERSE ANALYSIS PROGRAM FOR ANISOTROPIC FINITE ELEMENT MODEL OF HUMAN & MURINE SKIN

```
function
rmserr=runmurineskintensilefibre3families(c1,c2,c31,c41,lam_max1,c32,
c42,lam_max2,c33,c43,lam_max3,a1,a2,a3)

%FOR TENSILE TESTS OF SKIN
%INPUT PARAMETERS WHICH WERE OPTIMISED USING "RUNHUMANSKINTENSILE"
THEN
%OPTIMISE FOR 0,45 AND 90 DEG TO SEE EFFECT OF FIBRE ORIENATATION

%USE THREE LAYER OF FIBRES DEFINIED UNDER DIFFERENT MATERAILS. ALL
%VERONDA-WESTMANN TRANSVERSLY ISOTROPIC. TRANSFORMS VECTORS FOR EACH
%DIRECTION.  VERONDA-WESTMANN CONSTANTS ARE THE SAME FOR ALL THREE
LAYERS,
%HOWEVER THE CONSTANTS C3-LAMDA ARE CHANGED FOR EACH DIRECTION.
VECTORS OF
%FIBRES ARE WRITENS AS ANGLES AND CHANGED TO VETCORS WITHIN THE
PROGRAM.
%VECTORS ARE ASSUMED TO HAVE A LENGTH OF 1


%PARAMETERS THAT REMAIN CONSTANT FOR ALL THREE FIBRE FAMILIES

%C1= VERONDA-WESTMANN COEF 1:
C1='<c1>';
C11='</c1>';
c1=num2str(c1);
C01=strcat(C1,c1,C11);

%C2 = VERONDA-WESTMANN COEF 2:
C2='<c2>';
C22='</c2>';
c2=num2str(c2);
C02=strcat(C2,c2,C22);

%K = BULK MODULUS: do not optimise for now
K1='<k>';
K3='</k>';
K2='10';
K=strcat(K1,K2,K3);

%.....
......
```

```
%FIBRE FAMILY ONE
%C5 = MODULUS OF STRAIGHTENED FIBRES:
l1=lam_max1-1;
C51=c31*c41*lam_max1*exp(c41*l1);
C5='<c5>';
C55='</c5>';
c51=num2str(C51);
C051=strcat(C5,c51,C55);

%C3 = EXPONENTIAL FIBRE STRESS COEF: scales the exponential stresses
C3='<c3>';
C33='</c3>';
c31=num2str(c31);
C031=strcat(C3,c31,C33);

%C4 = FIBRE UNCRIMPING COEF: rate of the uncrimping fibers
C4='<c4>';
C44='</c4>';
c41=num2str(c41);
C041=strcat(C4,c41,C44);

% LAM_MAX = FIBRE STRETCH FOR STRAIGHTENED FIBERS: the stretch at
which the
% fibers are straight
L1='<lam_max>';
L3='</lam_max>';
%fill in lamda max
lam_max1=num2str(lam_max1);
L01=strcat(L1,lam_max1,L3);

%VECTOR OF FIBRE
fibre1='<fiber type="vector">';
ang1 = a1*(pi/180);
X01=sin(ang1);
Y01=cos(ang1);
X0L1=num2str(X01);
Y0L1=num2str(Y01);
fibre2='</fiber>';

%.....................................................................
......
%FIBRE FAMILY TWO

%C5 = MODULUS OF STRAIGHTENED FIBRES:
l2=lam_max2-1;
C52=c32*c42*lam_max2*exp(c42*l2);
c52=num2str(C52);
C052=strcat(C5,c52,C55);

%C3
c32=num2str(c32);
C032=strcat(C3,c32,C33);

%C4
c42=num2str(c42);
C042=strcat(C4,c42,C44);


%LAM_MAX
```

```
lam_max2=num2str(lam_max2);
L02=strcat(L1,lam_max2,L3);

%VECTOR OF FIBRE
ang2 = a2*(pi/180);
X02=sin(ang2);
Y02=cos(ang2);
X0L2=num2str(X02);
Y0L2=num2str(Y02);

%.....
......
%FIBRE FAMILY THREE
%C5 = MODULUS OF STRAIGHTENED FIBRES:
l3=lam_max3-1;
C53=c33*c43*lam_max3*exp(c43*l3);
c53=num2str(C53);
C053=strcat(C5,c53,C55);

%C3
c33=num2str(c33);
C033=strcat(C3,c33,C33);

%C4
c43=num2str(c43);
C043=strcat(C4,c43,C44);

%LAM_MAX
lam_max3=num2str(lam_max3);
L03=strcat(L1,lam_max3,L3);

%VECTOR OF FIBRE
ang3 = a3*(pi/180);
X03=sin(ang3);
Y03=cos(ang3);
X0L3=num2str(X03);
Y0L3=num2str(Y03);

%produce output files
O='<Output>';
O1='<logfile file="data">';
O2='<rigid_body_data data="Fx" name = " " file="load_on_grip_0.txt"
delim=" = " >1</rigid_body_data>';
O3='<rigid_body_data data="x" name = " "
file="displacement_of_grip_0.txt" delim=" = " >1</rigid_body_data>';
O4='</logfile>';
O5='</Output>';
O6='</febio_spec>';


%IMPORT FEBio FILE
FEBio_file=importdata('humanskintensile0deg.feb');

%split file into seperate files and add the material property
sections
FEBio_part1=FEBio_file(1:24,:);
FEBio_part2=FEBio_file(33);
FEBio_part3=FEBio_file(35);
FEBio_part4=FEBio_file(44);
```

```
FEBio_part5=FEBio_file(46);
FEBio_part6=FEBio_file(55);
FEBio_part7=FEBio_file(34);
FEBio_part8=FEBio_file(56:24135,:);


%Attach file back together
FEBIO=[FEBio_part1;C01;C02;C031;C041;C051;K;L01;fibre1;X0L1;',';Y0L1;
',';'0';fibre2;FEBio_part2;FEBio_part3;C01;C02;C032;C042;C052;K;L02;f
ibre1;X0L2;',';Y0L2;',';'0';fibre2;FEBio_part4;FEBio_part5;C01;C02;C0
33;C043;C053;K;L03;fibre1;X0L3;',';Y0L3;',';'0';fibre2;FEBio_part6;FE
Bio_part7;FEBio_part8;O;O1;O2;O3;O4;O5;O6];

[nrows,ncols]= size(FEBIO);

filename = 'C:\febiofile0deg.feb';
fid = fopen(filename, 'w');

for row=1:nrows
    fprintf(fid, '%s\n', FEBIO{row,:});
end

fclose(fid);


%To run FEBio in MATLAB
dos('febio -i C:\febiofile0deg.feb > febiooutput0deg.txt');

%OUTPUT FROM FEBio
Fz = importdata('load_on_grip_0.txt');
z = importdata('displacement_of_grip_0.txt');
fZ = Fz.data;
Z = z.data;
FE_LOAD0DEG = fZ(4:4:end)*2;
FE_DIS0DEG = Z(4:4:end)*2;
%change displacement depending on COG position

% EXPERIMENTAL RESULTS: no need to filter
EX_LOAD0DEG = importdata('load0deg.txt');
EX_DIS0DEG = importdata('dis0deg.txt');

%interpolate
intEX_LOAD0DEG=interp1(EX_DIS0DEG,EX_LOAD0DEG,FE_DIS0DEG,'pchip');

%CALCULATING R SQUARED VALUE FOR 0 DEG

%R squared value
diff=(intEX_LOAD0DEG-FE_LOAD0DEG).^2;
sqIntEX_LOAD0DEG=intEX_LOAD0DEG.^2;
sumIntEX_LOAD0DEG=(sum(intEX_LOAD0DEG))^2;

%Calculation from R squared. Namani et al
r_0deg=((sum(diff)/((sum(sqIntEX_LOAD0DEG))-
(sumIntEX_LOAD0DEG/numel(FE_LOAD0DEG)))));
R_0deg=abs(r_0deg)
```

```
%.....................................................................
......
%CALCULATE DIRECTION FOR 45 AND 90 DEGREES
%Only work with vectors in the x and y directions as sample is not
moved in
%the z direction

%angles of rotation
THETA45=45*(pi/180);
THETA90=90*(pi/180);

%FIBRE LAYER 1
%components at 45 degrees
x45lay1=(X01*cos(THETA45))-(Y01*sin(THETA45));
y45lay1=(X01*sin(THETA45))+(Y01*cos(THETA45));
%components at 90 degrees
x90lay1=(X01*cos(THETA90))-(Y01*sin(THETA90));
y90lay1=(X01*sin(THETA90))+(Y01*cos(THETA90));


%FIBRE LAYER 2
%components at 45 degrees
x45lay2=(X02*cos(THETA45))-(Y02*sin(THETA45));
y45lay2=(X02*sin(THETA45))+(Y02*cos(THETA45));
%components at 90 degrees
x90lay2=(X02*cos(THETA90))-(Y02*sin(THETA90));
y90lay2=(X02*sin(THETA90))+(Y02*cos(THETA90));


%FIBRE LAYER 3
%components at 45 degrees
x45lay3=(X03*cos(THETA45))-(Y03*sin(THETA45));
y45lay3=(X03*sin(THETA45))+(Y03*cos(THETA45));
%components at 90 degrees
x90lay3=(X03*cos(THETA90))-(Y03*sin(THETA90));
y90lay3=(X03*sin(THETA90))+(Y03*cos(THETA90));


%.....................................................................
......
%RUN FEBIO FILE FOR 45 DEGREES

%IMPORT FEBio FILE
FEBio_file=importdata('humanskintensile45deg.feb');

%split file into seperate files and add the material property
sections
FEBio_part1=FEBio_file(1:24,:);
FEBio_part2=FEBio_file(33);
FEBio_part3=FEBio_file(35);
FEBio_part4=FEBio_file(44);
FEBio_part5=FEBio_file(46);
FEBio_part6=FEBio_file(55);
FEBio_part7=FEBio_file(34);
FEBio_part8=FEBio_file(56:24135,:);

%VECTOR OF FIBRE LAYER 1
X45L1=num2str(x45lay1);
Y45L1=num2str(y45lay1);
```

```
%VECTOR OF FIBER LAYER 2
X45L2=num2str(x45lay2);
Y45L2=num2str(y45lay2);

%VECTOR OF FIBER LAYER 3
X45L3=num2str(x45lay3);
Y45L3=num2str(y45lay3);

%produce output files
O='<Output>';
O1='<logfile file="data">';
O245='<rigid_body_data data="Fx" name = " "
file="load_on_grip_45.txt" delim=" = " >1</rigid_body_data>';
O345='<rigid_body_data data="x" name = " "
file="displacement_of_grip_45.txt" delim=" = " >1</rigid_body_data>';
O4='</logfile>';
O5='</Output>';
O6='</febio_spec>';

%Attach file back together
FEBIO=[FEBio_part1;C01;C02;C031;C041;C051;K;L01;fibre1;X45L1;',';Y45L
1;',';'0';fibre2;FEBio_part2;FEBio_part3;C01;C02;C032;C042;C052;K;L02
;fibre1;X45L2;',';Y45L2;',';'0';fibre2;FEBio_part4;FEBio_part5;C01;C0
2;C033;C043;C053;K;L03;fibre1;X45L3;',';Y45L3;',';'0';fibre2;FEBio_pa
rt6;FEBio_part7;FEBio_part8;O;O1;O245;O345;O4;O5;O6];

[nrows,ncols]= size(FEBIO);

filename = 'C:\febiofile45deg.feb';
fid = fopen(filename, 'w');

for row=1:nrows
    fprintf(fid, '%s\n', FEBIO{row,:});
end

fclose(fid);


%To run FEBio in MATLAB
dos('febio -i C:\febiofile45deg.feb > febiooutput45deg.txt');


%OUTPUT FROM FEBio
Fz = importdata('load_on_grip_45.txt');
z = importdata('displacement_of_grip_45.txt');
fZ = Fz.data;
Z = z.data;
FE_LOAD45DEG = fZ(4:4:end)*2;
FE_DIS45DEG = Z(4:4:end)*2;
%change displacement depending on COG position

%EXPERIMENTAL RESULTS: no need to filter
EX_LOAD45DEG = importdata('load45deg.txt');
EX_DIS45DEG = importdata('dis45deg.txt');


%interpolate
```

```
intEX_LOAD45DEG=interp1(EX_DIS45DEG,EX_LOAD45DEG,FE_DIS45DEG,'pchip');

%CALCULATING R SQUARED VALUE FOR 45 DEG

%R squared value
diff=(intEX_LOAD45DEG-FE_LOAD45DEG).^2;
sqIntEX_LOAD45DEG=intEX_LOAD45DEG.^2;
sumIntEX_LOAD45DEG=(sum(intEX_LOAD45DEG)).^2;

%Calculation from R squared. Namani et al
r_45deg=((sum(diff)/((sum(sqIntEX_LOAD45DEG))-
(sumIntEX_LOAD45DEG/numel(FE_LOAD45DEG)))));
R_45deg=abs(r_45deg)



%.....................................................................
......
%RUN FEBIO FILE FOR 90 DEGREES

%IMPORT FEBio FILE
FEBio_file=importdata('humanskintensile90deg.feb');

%split file into seperate files and add the material property
sections
FEBio_part1=FEBio_file(1:24,:);
FEBio_part2=FEBio_file(33);
FEBio_part3=FEBio_file(35);
FEBio_part4=FEBio_file(44);
FEBio_part5=FEBio_file(46);
FEBio_part6=FEBio_file(55);
FEBio_part7=FEBio_file(34);
FEBio_part8=FEBio_file(56:24135,:);

%VECTOR OF FIBRE DIRECTION 1
X90L1=num2str(x90lay1);
Y90L1=num2str(y90lay1);

%VECTOR OF FIBER DIRECTION 2
X90L2=num2str(x90lay2);
Y90L2=num2str(y90lay2);

%VECTOR OF FIBER DIRECTION 3
X90L3=num2str(x90lay3);
Y90L3=num2str(y90lay3);


%produce output files
O='<Output>';
O1='<logfile file="data">';
O290='<rigid_body_data data="Fx" name = " "
file="load_on_grip_90.txt" delim=" = " >1</rigid_body_data>';
O390='<rigid_body_data data="x" name = " "
file="displacement_of_grip_90.txt" delim=" = " >1</rigid_body_data>';
O4='</logfile>';
O5='</Output>';
O6='</febio_spec>';
```

```
%Attach file back together
FEBIO=[FEBio_part1;C01;C02;C031;C041;C051;K;L01;fibre1;X90L1;',';Y90L
1;',';'0';fibre2;FEBio_part2;FEBio_part3;C01;C02;C032;C042;C052;K;L02
;fibre1;X90L2;',';Y90L2;',';'0';fibre2;FEBio_part4;FEBio_part5;C01;C0
2;C033;C043;C053;K;L03;fibre1;X90L3;',';Y90L3;',';'0';fibre2;FEBio_pa
rt6;FEBio_part7;FEBio_part8;O;O1;O290;O390;O4;O5;O6];

[nrows,ncols]= size(FEBIO);

filename = 'C:\febiofile90deg.feb';
fid = fopen(filename, 'w');

for row=1:nrows
    fprintf(fid, '%s\n', FEBIO{row,:});
end

fclose(fid);


%To run FEBio in MATLAB
dos('febio -i C:\febiofile90deg.feb > febiooutput90deg.txt');


%OUTPUT FROM FEBio
Fz = importdata('load_on_grip_90.txt');
z = importdata('displacement_of_grip_90.txt');
fZ = Fz.data;
Z = z.data;
FE_LOAD90DEG = fZ(4:4:end)*2;
FE_DIS90DEG = Z(4:4:end)*2;
%change displacement depending on COG position

% EXPERIMENTAL RESULTS: no need to filter
EX_LOAD90DEG = importdata('load90deg.txt');
EX_DIS90DEG = importdata('dis90deg.txt');


%interpolate
intEX_LOAD90DEG=interp1(EX_DIS90DEG,EX_LOAD90DEG,FE_DIS90DEG,'pchip');

%CALCULATING R SQUARED VALUE FOR 90 DEG

%R squared value
diff=(intEX_LOAD90DEG-FE_LOAD90DEG).^2;
sqIntEX_LOAD90DEG=intEX_LOAD90DEG.^2;
sumIntEX_LOAD90DEG=(sum(intEX_LOAD90DEG)).^2;

%Calculation from R squared. Namani et al
r_90deg=((sum(diff)/((sum(sqIntEX_LOAD90DEG))-
(sumIntEX_LOAD90DEG/numel(FE_LOAD90DEG)))));
R_90deg=abs(r_90deg)



%PLOT
plot(FE_DIS0DEG, FE_LOAD0DEG, EX_DIS0DEG, EX_LOAD0DEG, FE_DIS45DEG,
FE_LOAD45DEG, EX_DIS45DEG, EX_LOAD45DEG, FE_DIS90DEG, FE_LOAD90DEG,
EX_DIS90DEG, EX_LOAD90DEG);
```

```
ylabel('Force (N)');
xlabel('Displacement (mm)');
legend('FEM 0 degrees', 'Experiment 0 degrees','FEM 45 degrees',
'Experiment 45 degrees','FEM 90 degrees', 'Experiment 90 degrees');
axis([0 6 0 2.5]);

rmserr=(R_0deg+R_45deg+R_90deg)/3
```

# APPENDIX D

# VOLUNTEER INFORMATION SHEET FOR INDENTATION TESTS

## VOLUNTEER INFORMATION SHEET

**Study Title:**
**A Study to Assess the Mechanical Properties of Human Skin**

You are being invited to take part in a research study. Before you decide it is important for you to understand why the research is being done and what it will involve. Please take time to read the following information carefully and discuss it with others if you wish. Ask us if there is anything that is not clear or if you would like more information. Take time to decide whether or not you wish to take part.

**Purpose of study:**
Tiny microneedles, which are able to pierce the outermost barrier layer of skin without stimulating the underlying pain receptors or blood vessels, have been developed and exploited at the Welsh School of Pharmacy as a new method of delivering medicaments and vaccines through the skin. However in order to optimise future designs, it is important to understand the mechanics involved in the insertion of microneedles and the resultant deflection of the skin. This study aims to give an insight into the mechanisms involved as the microneedle is inserted and what effects the underlying tissue may have on the force required. To achieve this, indentation tests will be performed on the subjects' skin to help determine the skin's elastic properties.

**What the study will involve:**
For this study, a series of indentation tests will be performed on the volar aspect of the forearm. Three indenters with varying geometries will be applied to the skin with a maximum load of 0.1N. Each indentation cycle will be performed up to 7 times, per indenter. All indenters will be thoroughly cleaned before use.

You may be asked to participate in a second study where a single, sterilised microneedle will be applied to the same skin site. Prior to testing, the skin site will be thoroughly cleaned with an alcohol wipe to prevent infection

**Do I have to take part?**
Participation in this study is voluntary and anonymous. You may withdraw from the study at any time without stating a reason.

Many thanks for taking part in this study.

If participating in this study you will be provided with a copy of the Volunteer Information Sheet and the signed Consent Form to keep.

# APPENDIX E

# VOLUNTEER INFORMATION SHEET FOR MICRONEEDLE INSERTION TESTS

## VOLUNTEER INFORMATION SHEET

**Study Title:**
**Assessing microneedle puncture using a new microneedle device**

You are being invited to take part in a research study. Before you decide it is important for you to understand why the research is being done and what it will involve. Please take time to read the following information carefully and discuss it with others if you wish. Ask us if there is anything that is not clear or if you would like more information. Take time to decide whether or not you wish to take part.

**Purpose of study:**
Tiny microneedles, which are able to pierce the outermost barrier layer of skin without stimulating the underlying pain receptors or blood vessels, have been developed and exploited at the Welsh School of Pharmacy as a new method of delivering medicaments and vaccines through the skin. However, concerns have been raised regarding the consistency of individual microneedle puncture across the entire array. Hence a new curved microneedle array has been developed which aims to evenly distributes the load over all microneedles with to increase microneedle penetration consistency. This study aims to apply the improved microneedle devices to *in vivo* human skin, and by using a dye on the application site, affective skin penetration can be quantified.

**What the study will involve:**
For this study, the microneedle array will adhered to a force gauge and the microneedles will be applied to the volar aspect of the volunteer's forearm. The force gauge will record the load on the microneedle array during application to the skin site. After which, a dying agent called methylene blue will applied to the tested skin site to quantify skin puncture.

**Do I have to take part?**
Participation in this study is voluntary and anonymous. You may withdraw from the study at any time without stating a reason.

Many thanks for taking part in this study.

If participating in this study you will be provided with a copy of the Patient Information Sheet and the signed Consent Form to keep.